# F2 extraction from Inclusive Cross Section Data at Large Bjorken x

A Dissertation Presented

by

**Fernando Araiza Gonzalez**

to

The Graduate School

in Partial Fulfillment of the Requirements

for the degree of

**Doctor of Philosophy**

in

**Physics**

Stony Brook University

2020

# Stony Brook University

The Graduate School

**Fernando Araiza Gonzalez**

We, the dissertation committee for the above candidate for the
Doctor of Philosophy degree, hereby recommend
acceptance of this dissertation

**Prof. Abhay Deshpande - Advisor**
**Professor, Department of Physics and Astronomy**

**Prof. George Sterman - Chairperson of Defense**
**Professor, Department of Physics and Astronomy**

**Prof. Xu Du - Committee Member**
**Associate Professor, Department of Physics and Astronomy**

**Prof. Alberto Accardi - External Member**
**Assistant Professor, Hampton University School of Science**

This dissertation is accepted by the Graduate School

Eric Wertheimer
Dean of the Graduate School

Abstract of the Dissertation

# F2 extraction from Inclusive Cross Section Data at Large Bjorken x

by

**Fernando Araiza Gonzalez**

**Doctor of Philosophy**

in

**Physics**

Stony Brook University

2020

While we have made significant progress in probing nuclear structure at low Bjorken $x$ and high $Q^2$, we still have gaps in our knowledge regarding the high Bjorken $x$ and intermediate $Q^2$ kinematic region. This is not an accident, but instead due to the difficulty in assessing the non-perturbative region of nuclear physics. For this reason, the E12-10-002 experiment measured the H(e,e') and D(e,e') inclusive cross section in the resonance region. This will allow us to study both perturbative and non-perturbative physics in a kinematic region that lacks precision measurements. Measurements were made up to a Bjorken $x$ of 0.99 and $Q^2$ up to 17 GeV$^2$. These measurements are made using the independent HMS and SHMS spectrometers at the upgraded beam energy of 11 GeV in Hall C at Jefferson Lab. Further, we extract $F_2$ structure functions from the measured data and study the effect of their inclusion in a global Parton Distribution Function analysis.

# Contents

# List of Figures

# List of Tables

# Chapter 1

# Introduction

The motivation for the E12-10-002 experiment follows in the footsteps established predominantly at SLAC in the 1960s – we still don't have a satisfactory understanding about the inner dynamics of the proton and neutron. Indeed, some 60 years later, we still have yet to answer fundamental questions about the nature of nuclear matter. Questions like, "How is the momentum and position of the quarks and gluons distributed inside of the nucleons?", "How is the spin of the quarks and gluons tied to the spin of the nucleons?", and "How do the nucleons acquire their mass from quarks and gluons?". It is emphasized that these questions are extremely simple. They are simple in the sense that one does not even have to be a scientist to understand what the question is asking. This exemplifies the sorts of challenges that the field of nuclear physics faces. On these fundamental questions, the E12-10-002 experiment, taken together with the whole of the JLab experimental data set, is expected to make some contribution.

Regarding the momentum distribution of the partons in the nucleons, special interest is taken in behavior of $\frac{d}{u}$, where $d$ refers to the momentum distribution of the down quark and $u$ refers to the momentum distribution of the up quark. As one approaches a kinematic region where valence effects dominate, that is, where nucleons can be appropriately described by a model consisting of three quarks, the behavior of $\frac{d}{u}$ can change depending on the choice of model used to describe the mechanism that breaks spin-flavor symmetry. Spin-flavor is a symmetry whose conclusion suggests the up (down) quarks in the proton can simply be mapped to the down (up) quarks in the nucleon. This is a symmetry that nature does not hold itself to, but the way in which this symmetry is broken is

fundamentally related to the quantity $\frac{d}{u}$ in the valence region; a kinematic region where a valence model is valid.

The question regarding the source of the nucleons spin and how it is related to the spin of the partons is another interesting puzzle. It came as a surprise in the 80's when experiments at CERN showed that the quarks carried only about $12 \pm 17\%$ of the nucleon's total spin. This was in clear contradiction to models at the time that suggested quarks carried about 75% of the nucleon's spin, with the remaining 25% accounted for by the orbital angular momentum of the quarks. Current estimates have the quark contribution to the nucleon's spin at about $20 - 30\%$, with remaining spin contributions presumably coming fromsea quark and gluons, where sea quarks constitute quark-antiquark pairs that are present in the structure of nucleons as one moves away from the valence region. But the valence region is precisely where E12-10-002 is situated kinematically. Here, sea quarks and gluons are scarce, and therefore, one need not worry about the complications they represent elsewhere. There are three additional JLab experiments, E12-06-109, E12-06-111, and E12-06-122, that are attempting to study spin dynamics in the valence region. And while E12-10-002 involved an unpolarized electron beam and unpolarized target, the machinery needed to study the distribution of quarks in the nucleons remains very similar, and could provide assistance in this endeavor.

Another large motivation for performing the E12-10-002 experiment deals with the attempt to elucidate fundamental properties about the theory that we use to describe quarks and gluons, namely, Quantum Chromodynamics (QCD). This theory has the interesting property that at high energy scales, or small distance scales, the quarks and gluons can be treated as unbound quasi-free particles. More concretely, the coupling of QCD becomes small at small distance scales. This property is called asymptotic freedom and can be explicitly demonstrated as a feature of QCD within the QCD framework. However, at large distance scale the opposite is true. As the distance between quarks increases, the QCD coupling also increases, enhancing the attraction between them. At a large enough distance scale, it becomes energetically favorable to produce a quark-

antiquark pair, producing now two quark bound states. In essence, by trying to isolate two pairs of quarks, we have simply produced a second pair. This observation that we cannot isolate quarks and gluons is referred to as confinement. Clearly, asymptotic freedom and confinement represent two extremes of the strength of the QCD coupling, and the study of the transition from one extreme to the other is referred to as Quark Hadron Duality (QHD). QHD was a phenomenon first observed in the 70's, but it has been revitalized in the present day by the ability to perform precision experiments in this transition region, of which E12-10-002 is a prime candidate.

These questions and the role of E12-10-002 in addressing them will form the basis of this thesis. An in-depth discussion of QCD and it's history from the 1900's to present day is presented in Chapter 2, where ideas about what quarks are and how they behave will be explored. Chapter 3 will go through the necessary step of explaining how the E12-10-002 made it's measurement. We will discuss the Hall C spectrometers in detail and give special attention to the detectors that make up the detector package. Chapter 4 discusses primarily the analysis of the E12-10-002 data. This includes the calibrations of the spectrometer detectors as well as their associated efficiencies. Additionally, we cover the major sources of backgrounds and systematics associated with E12-10-002 and how they are addressed. Finally, Chapter 5 will explore how the cross section measurements were utilized to extract information about the parton distribution functions of the up quarks, down quarks, and gluons, as well a perspective for the future of nuclear physics at the Electron Ion Collider (EIC).

To begin, we present some information about the E12-10-002 experiment. E12-10-002 used an unpolarized electron beam at 10.6 $GeV$ on hydrogen and deuterium cryogenic targets. E12-10-002 took measurements ranging in scattering angle from $21 - 39$ degrees and for scattering energies ranging from $1.6 - 5.1$ $GeV$. Measurements were taken with the new Super High Momentum Spectrometer (SHMS) and the High Momentum Spectrometer (HMS). The SHMS and HMS did not take measurements at identical kinematic settings, but the measurements do overlap kinematically. This allows for a cross-check for the

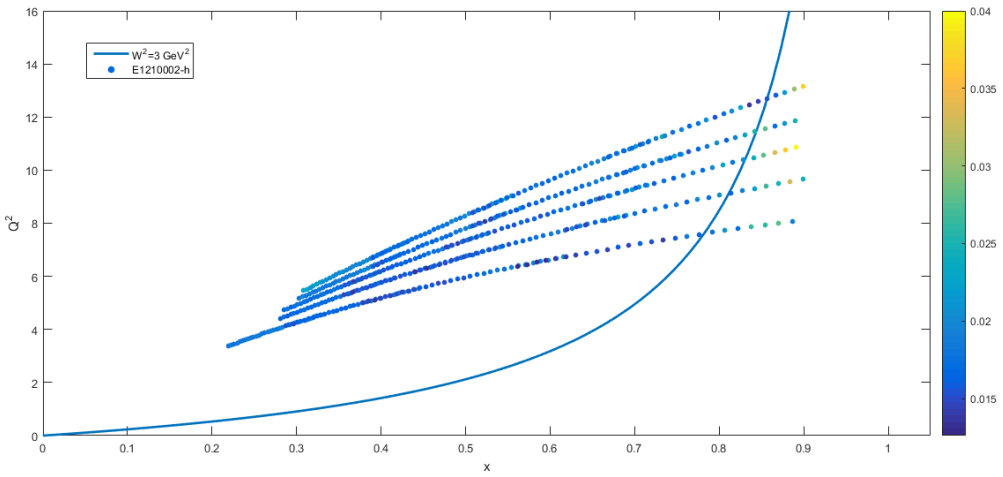


**Figure 1.1:** Kinematics plot of data measured for the Hydrogen target in the SHMS. The color scale indicates the relative uncertainty of the data point. The blue curve indicates the data at greater than and less than $W^2 = 3\ GeV^2$. It is noted that the highest $x$ values for E12-10-002 were achieved by the HMS, therefore, the range in $x$ for the SHMS do not reach $x \approx 0.99$

new SHMS spectrometer. Figure 1.1 shows the kinematic coverage of the data taken on the hydrogen target for the SHMS spectrometer. It should be noted that the anaylsis presented in this thesis was performed only on the data acquired by the SHMS.

# Chapter 2

# Theoretical Overview

## 2.1 Kinematics

E12-10-002 is an inclusive electron-proton and electron-deuteron experiment that measures the inelastic cross section of hydrogen and deuterium at relatively high Bjorken $x$ – up to 0.99.

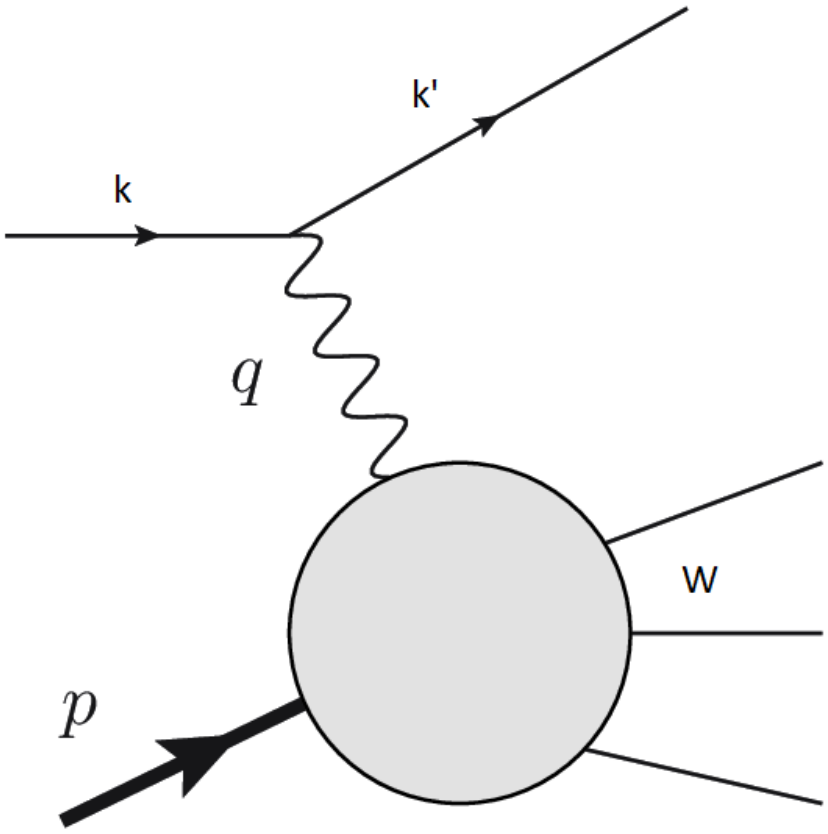


**Figure 2.1:** Inelastic scattering of an electron from a proton.

Figure 2.1 shows the single photon exchange Feynman diagram of an unpolarized

electron with momentum $k$, interacting with a proton via exchange of a photon with momentum $q$. The interaction is inelastic, so the final state of the proton is represented by the invariant mass $W$, and the electron is scattered with momentum $k'$ at angle $\theta$. Of course, in the case of deuterium, the interacting nucleon can be either a proton or a neutron.

A standard base of kinematic variables are used in the analysis of the interaction. Firstly, the incoming and outgoing four-momentum of the electron in the lab-frame are given respectively by

$$k = (E, \overrightarrow{k}) \tag{2.1}$$

$$k' = (E', \overrightarrow{k'}) \tag{2.2}$$

Thus, the momentum transfer of the exchange photon is given by

$$q^u = (E - E', \overrightarrow{k} - \overrightarrow{k'}) \tag{2.3}$$

And the energy of the photon is

$$\nu = E - E' \tag{2.4}$$

Because this is a fixed target experiment, the four-momentum of the nucleon is simply

$$P^u = (M, 0) \tag{2.5}$$

Where $M$ is the mass of the nucleon. The above quantities can be used to calculate the kinematic variables most commonly used to characterize a nuclear system, namely the square of the momentum transfer, $Q^2$ and Bjorken $x$. The momentum transfer of the exchange photon determines the resolution to which the nucleon is probed, and

goes approximately as the inverse of $Q$. Bjorken $x$ is the ratio of the momentum of the interacting parton divided by the momentum of the entire nucleon. In terms of the above quantities, these variables are given by

$$Q^2 = -q^2 = 4EE'sin^2(\frac{\theta}{2}) \tag{2.6}$$

$$x = \frac{Q^2}{2M\nu} \tag{2.7}$$

Finally, the invariant mass $W$ can be written as

$$W^2 = M^2 - Q^2 + 2M\nu \tag{2.8}$$

## 2.2 Unpolarized Cross Sections and Structure Functions

The cross section for lepton-nucleon scattering at leading order can be written as

$$\frac{d^2\sigma}{d\Omega dE'} = \frac{\alpha^2}{Q^4}\frac{E'}{E}L_{\mu\nu}W^{\mu\nu}, \tag{2.9}$$

where $L^{\mu\nu}$ is the leptonic tensor, readily calculable from QED. The leptonic part of the cross section is given by

$$L_{\mu\nu} = 2(k_\mu k'_\nu + k'_\mu k_\nu - g_{\mu\nu}kk') \tag{2.10}$$

The hadronic part of the cross section is represented by $W_{\mu\nu}$. In fact, the hadronic tensor is the part of the cross section that represents our ignorance about the structure of the nucleon. Within a broad field theory formalism, the hadronic tensor can be written as

$$W_{\mu\nu} = \frac{1}{2}\sum_n \langle p|[J^+_\mu J_\nu]|p\rangle (2\pi)^3 \delta^4(p+q-p_n). \tag{2.11}$$

It is precisely our inability to analytically write down the states of the nucleon $|p\rangle$ that represents the difficulty of understanding the structure of the nucleon. Instead, if we impose gauge and Lorentz invariance on the hadronic tensor we can a priori write down its functional form as

$$W^{\mu\nu} = W_1(\nu, q^2)(-g^{\mu\nu} + \frac{q^\mu q^\nu}{q^2}) + \frac{W_2(\nu, q^2)}{M^2}(p^\mu - \frac{p\cdot q}{q^2}p^\mu)(p^\nu - \frac{p\cdot q}{q^2}p^\nu). \tag{2.12}$$

We can substitute this into the expression for the differential cross section and write it as

$$\frac{d^2\sigma}{d\Omega dE'} = \frac{4\alpha^2 E'^2}{Q^4}\left[2W_1(\nu, Q^2)\sin^2(\frac{\theta}{2}) + W_2(\nu, Q^2)\cos^2(\frac{\theta}{2})\right]. \tag{2.13}$$

Further, we can introduce dimensionless quantities called structure functions, defined as

$$F_2 = \nu W_2 \tag{2.14}$$

$$F_1 = MW_1; \tag{2.15}$$

thus, the cross section is now

$$\frac{d^2\sigma}{d\Omega dE'} = \frac{4\alpha^2 E'^2}{Q^4}\left[\frac{2}{M}F_1(\nu, Q^2)sin^2(\frac{\theta}{2}) + \frac{1}{\nu}F_2(\nu, Q^2)cos^2(\frac{\theta}{2})\right]. \tag{2.16}$$

Finally, the cross section is sometimes written a function of $x = \frac{Q^2}{2M\nu}$ and $y = 1 - \frac{E'}{E}$ as

$$\frac{d^2\sigma}{dxdQ^2} = \frac{4\alpha^2}{Q^4}\left[(1-y)\frac{F_2(x,Q^2)}{x} + \frac{1}{2}y^2\frac{F_1(x,Q^2)}{y}\right]. \tag{2.17}$$

However, for our purpose it is most useful to express the differential cross section in terms of the longitudinal and transverse cross sections. This will facilitate an intuitive and simple extraction of the $F^2$ structure function from the cross section through a technique called Rosenbluth separation[Ros50]. To begin, we consider the helicity of the photon in 2.1. For a given energy $\nu$ and squared transfer momentum $Q^2$ traveling in the z-direction, the photon can have a transverse helicity given by it's polarization vector

$$\epsilon(\pm 1) = \frac{1}{\sqrt{2}}(0, \pm 1, -i, 0) \tag{2.18}$$

Because this is a virtual photon, it may also have a longitudinal momentum, with a polarization given by

$$\epsilon(0) = \frac{1}{Q^2}(\sqrt{Q^2+\nu^2}, 0, 0, \nu) \tag{2.19}$$

Then, the so-called photo-absorption cross section can be decomposed in terms of its transverse and longitudinal components as

$$\sigma_{\pm,0} = \frac{4\pi\alpha}{\sqrt{Q^2+\nu^2}}\epsilon^{\mu}_{\pm,0}W_{\mu\nu}\epsilon^{\nu}_{\pm,0}. \tag{2.20}$$

Likewise, the functions $W_1$ and $W_2$ can also be expressed in terms of the transverse and longitudinal photo-absorption cross section as

$$W_1 = \frac{\sqrt{Q^2+\nu^2}}{4\pi^2\alpha}\sigma_T \tag{2.21}$$

$$W_2 = \frac{1}{4\pi^2\alpha}(\sigma_T + \sigma_L)\frac{Q^2}{\sqrt{Q^2+\nu^2}} \tag{2.22}$$

These can be substituted into the differential cross section to give

$$\frac{d^2\sigma}{d\Omega dE'} = \Gamma(\sigma_T + \epsilon\sigma_L) \tag{2.23}$$

Where $\Gamma$ is the flux of incident virtual photon given by

$$\Gamma = \frac{\sqrt{Q^2+\nu^2}}{2\pi^2 Q^2}\frac{E'}{E}\frac{1}{1-\epsilon} \tag{2.24}$$

and $\epsilon$ is the relative flux of longitudinally polarized photons

$$\epsilon = (1 + 2\frac{Q^2+\nu^2}{Q^2}\tan^2(\frac{\theta}{2}))^{-1} \tag{2.25}$$

It is then useful to introduce the reduced cross section, defined as

$$\sigma_R = \frac{1}{\Gamma}\frac{d^2\sigma}{d\Omega dE'} = \sigma_T + \epsilon\sigma_L \tag{2.26}$$

Thus, one can measure the cross section and plot it as a function of $\epsilon$. The result is linear relationship where $\sigma_T$ is the y-intercept and the slope is given by $\sigma_L$.

## 2.3 Development of Quantum Chromodynamics

The motivation for the E12-10-002 experiment rests upon the simple question first proposed in the late 1940s when the field of nuclear physics was in its infancy – what is the nature of nuclear structure? It is perhaps surprising that such a question still weighs so heavy after 70 years, but this only speaks to the perplexing nature of the strong interaction.

### 2.3.1 The Strong Interaction

In a sense, the existence of the strong nuclear force was first implied after Rutherford's discovery of the proton in 1917 and the discovery of the neutron by James Chadwick in 1932[Rut19 Cha32]. These results prompted Chadwick to construct a model which saw

protons and neutrons tightly bound together in the center of atoms – the birth of the nuclei. However, this immediately posed a problem. The electrostatic repulsion between protons at such close proximity should make all atoms unstable. Therefore, there must be a "strong" enough force to keep the nuclei intact. One of the first attempts at a solution came from Hideki Yukawa in 1935 [Yuk35]. He proposed the existence of a new particle that would communicate the force of attraction between protons and neutrons. Based on the length scale of this interaction, the new particle would have to have a mass of about 100 MeV. Indeed, the pion was discovered in 1947 by use of nuclear emulsion plates and cosmic rays [GPSO47].

With this, the era of particle physics had begun, and the use of bubble chambers and emulsion plates saw the discovery of a growing list of new particles. This was seen as troubling by many, as it had been taken for granted that these new particles were elementary. George Zweig, independent creator of the quark/ace model, credits a 1939 paper by Fermi and Yang as a natural starting point for the conceptual existence of quarks. In this paper, Fermi and Yang make the bold claim that the pion is not fundamental, but instead a composite particle of a nucleon and anti-nucleon – ultimately incorrect, but a step in the right direction [EF49].

### 2.3.2 The Quark Model

With the advent of the first particle accelerators, the 1950s saw an explosion of new particles and it became necessary to construct a formalism to make sense of these new particles' properties. It was noticed by Murray Gell-Mann and others that these newly discovered baryons and mesons had suggestive symmetries. In particular, Gell-Mann and Nishijima independently noticed that these particles' electromagnetic charge would be given by the following relation

$$Q = I_3 + \frac{1}{2}Y$$

where $I_3$ is the isospin and is the third component of the hadron's spin and $Y$ is the hyperchage, an additional quantum number of the hadron that is conserved by the strong interaction. This led Gell-Mann to formulate a more robust organizational scheme called the Eightfold Way[GM61]. This phenomenological scheme was based on the observation that baryons and mesons could be grouped in a way that explained their masses, isospin, and charges if one assumed the existence of three "flavors" of constituent particles. The model was presented by Gell-Mann at Caltech in 1961, where the baryons are expressed in terms of the SU(3) generators $\lambda_i$ in figure 2.2 and shown schematically in figure 2.3.

$$\Sigma^+ \sim \tfrac{1}{2}\,\bar{L}(\lambda_1 - i\lambda_2)\ell \sim D^+\nu$$

$$\Sigma^- \sim \tfrac{1}{2}\,\bar{L}(\lambda_1 + i\lambda_2)\ell \sim D^0 e^-$$

$$\Sigma^0 \sim \frac{1}{\sqrt{2}}\,\bar{L}\,\lambda_3\,\ell \sim \frac{D^0\nu - D^+e^-}{\sqrt{2}}$$

$$p \sim \tfrac{1}{2}\,\bar{L}(\lambda_4 - i\lambda_5)\ell \sim S^+\nu$$

$$n \sim \tfrac{1}{2}\,\bar{L}(\lambda_6 - i\lambda_7)\ell \sim S^+e^-$$

$$\Xi^0 \sim \tfrac{1}{2}\,\bar{L}(\lambda_6 + i\lambda_7)\ell \sim D^+\mu^-$$

$$\Xi^- \sim \tfrac{1}{2}\,\bar{L}(\lambda_4 + i\lambda_5)\ell \sim D^0\mu^-$$

$$\Lambda \sim \frac{1}{\sqrt{2}}\,\bar{L}\,\lambda_8\,\ell \sim (D^0\nu + D^+e^- - 2S^+\mu^-)/\sqrt{6}$$

**Figure 2.2:** Table from Gell-Mann's Caltech Synchotron Report, "The Eightfold Way: A Theory of Strong Interaction Symmetry", showing baryons represented by an SU(3) isospin symmetry.

It worked surprisingly well, and even led to the prediction of the omega baryon $\Omega^-$ made up of three strange quarks[Fow64]. It was discovered in 1964 at Brookhaven – Gell-Mann subsequently won the Nobel Prize in Physics in 1969. The success of this scheme naturally led to the search for an SU(3) symmetry on more stable ground. Gell-Mann realized that if one presumed the existence of objects called "quarks" that came in three "flavors" – up, down, and strange, one could impose an SU(3) flavor symmetry.

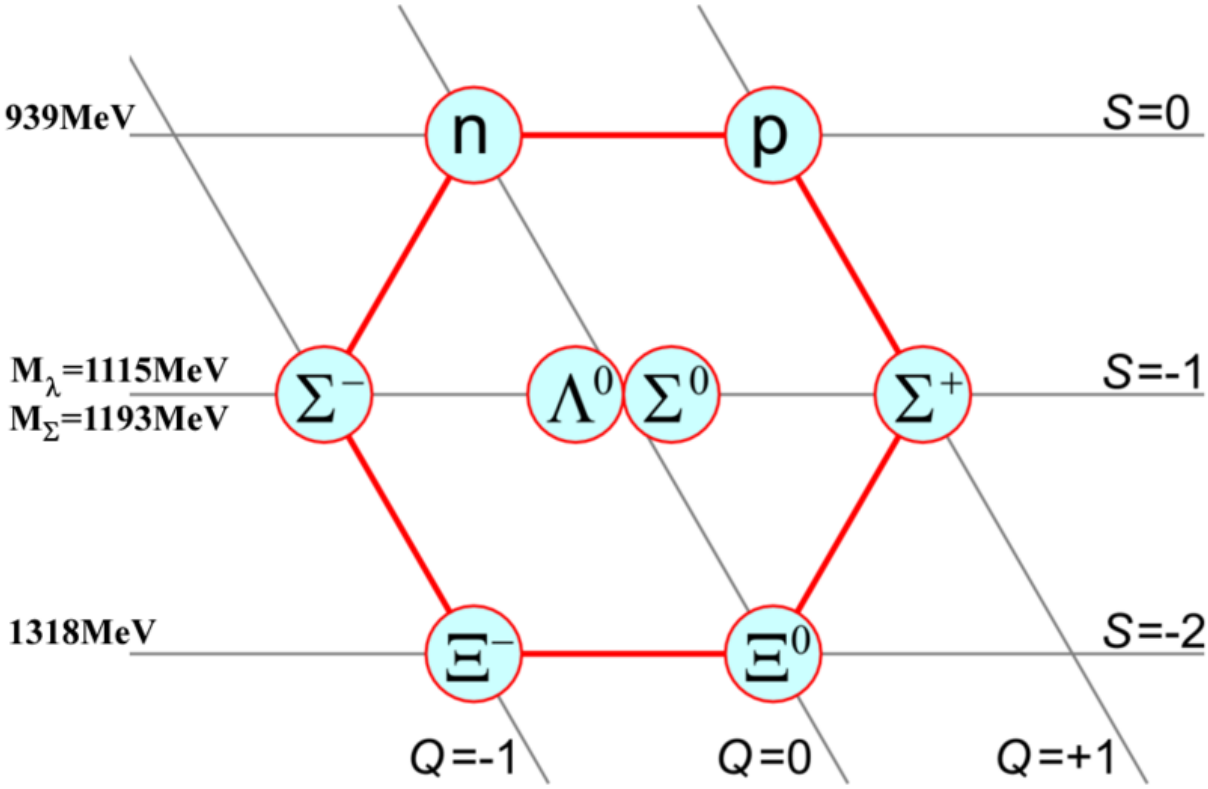


**Figure 2.3:** A schematic figure showing Gell-Mann's quark model in which the eight baryons are grouped according to their charge $Q$ and strangeness $S$, a quantity related to the hyperchage $Y$.

However, it is important to make clear that Gell-Mann saw quarks merely as a useful mathematical concept rather than as physical particles. Gell-Mann was not alone in this estimation, perhaps due to the fact that within the great number of particles discovered, none appeared with the properties assigned to quarks. While the consensus that quarks were not physical would remain throughout the 1960s, others were beginning to see the benefit of considering quarks as real particles described by a field theory.

### 2.3.3 The Parton Model & Bjorken Scaling

In the late 1960s, experimental particle physics had matured to the point that exploring the structure of nucleons was within reach. In particular, this time saw a major program of Deep Inelastic Scattering in experimental laboratories, primarily at the Stanford Linear Accelerator (SLAC). However, this abundance of experimental data was still waiting for a qualitative explanation. While Gell-Mann's quark model worked well to explain the static properties of nucleons, such as their mass and isospin, it was not well suited for application in high energy scattering experiments. Looking for a way to interpret this data, Richard Feynman postulated that nucleons were instead made up of "partons". At SLAC, Bjorken and Pachos considered how Feynman's Parton Model could be applied to inelastic electron-proton scattering[JDB69].

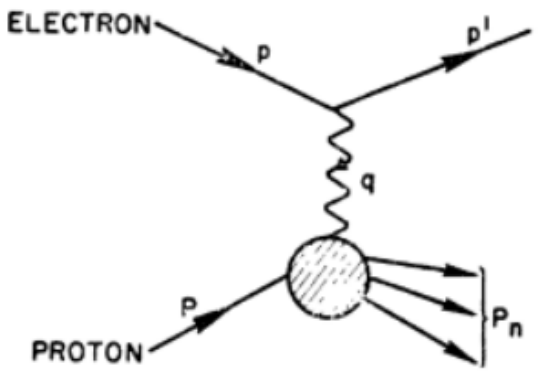


**Figure 2.4:** Inelastic electron-proton scattering being studied by Bjorken and Pachos.

The key insight to the parton model in DIS processes, shown schematically in figure 2.4, is to realize that in the infinite momentum frame, time dilation implies that the partons are essentially free – only one of the partons interacts with the lepton while the others remain spectators. Carrying out the calculation, Bjorken and Pachos realized that the parton model predicted the structure functions were a function of a single dimensionless variable, now called bjorken $x$. They started with the electron–proton inelastic scattering cross section

$$\frac{d\sigma}{d\Omega dE'} = \frac{\alpha^2}{4E'^2 sin^4(\frac{\theta}{2})}[W_2(v,Q^2)cos^2(\frac{\theta}{2}) + 2W_1(v,Q^2)sin^2(\frac{\theta}{2})] \tag{2.27}$$

Using a small angle approximation,

$$\frac{d\sigma}{d\Omega dE'} \simeq \frac{\alpha^2}{4E'^2 sin^4(\frac{\theta}{2})}W_2(v,Q^2)[1 + (\frac{\sigma_t}{\sigma_t + \sigma_l})\frac{v^2}{2EE'}], \tag{2.28}$$

where $\sigma_t$ and $\sigma_l$ are the transverse and longitudinal photo–absorption cross section respectively. Four assumptions based around the parton model are then presented. First, it is assumed that the proton is made of N partons that are free, with probability $P(N)$. Second, the partons have a longitudinal momentum that is a fraction of the proton given by

$$p_i = x_i P, \tag{2.29}$$

where the index $i$ refers to the $i^{th}$ parton. Third, the mass of the parton is assumed to be small. Finally, the transverse momentum of the partons is small, so that the following relation is true

$$p_i^\mu = x_i P^\mu \tag{2.30}$$

With these assumptions, Bjorken and Pachos derived

$$W_2(v,Q^2) = \sum_N P(N)\langle\sum_i Q_i^2\rangle \int_0^1 dx F_N(x)\delta(v - \frac{Q^2}{2xM}) \equiv F(x) \tag{2.31}$$

Where P(N) is the probability of finding the N partons at some configuration and $< \sum_i e_i^2 >$ is the average charge of the partons. Thus, the final result demonstrates that the structure function of the proton depends only on the dimensionless variable $x$. This suggests that increasing $Q^2$ does not resolve any more structure in the proton. The conclusion is that the partons have no further structure, and are therefore point-like

particles. Figure 2.5 demonstrates one of the first experimental observations by SLAC-MIT of what is now called Bjorken scaling and it is representative of the strong interaction being described by a field theory with a property called asymptotic freedom.

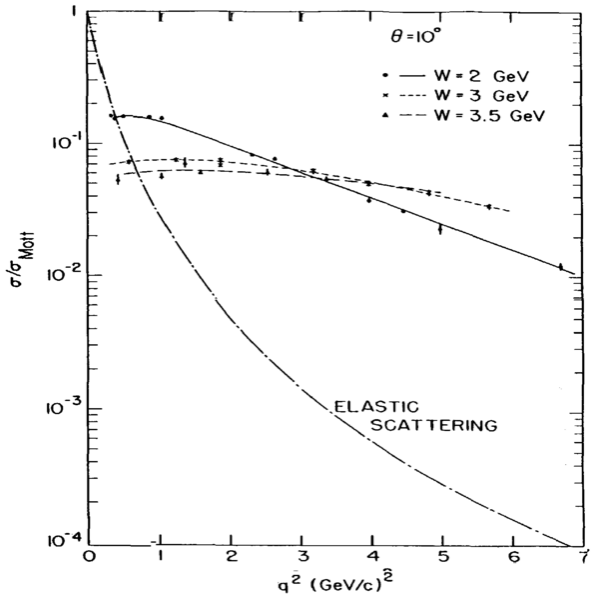


**Figure 2.5:** One of the first hints of Bjorken scaling from DIS data from the SLAC-MIT experiment.

### 2.3.4 Asymptotic Freedom

With the experimental observation of Bjorken scaling, people began to explore field theories which could accommodate the strong force becoming asymptotically weak at high energies. Another reason to pursue a new theory was the realization that a spin-statistics paradox had to be addressed. It was known that spin-$\frac{1}{2}$ particles had to obey Fermi statistics; under a permutation of identical quarks, the wavefunction must change sign. Baryons, being fermions must also be described by antisymmetric wavefunctions. This was in contradiction to a relatively successful model by Gursey and Radicati in 1964[FG64]. This model saw an extension of the $SU(3)_{flavor}$ to an SU(6) symmetry by combining it with an SU(2) spin symmetry. This model was able to organize the hadrons into a totally symmetric 56-dimensional representation with 8 spin-$\frac{1}{2}$ particles and 40 spin-$\frac{3}{2}$ particles[Gre15]. This paradox inspired Greenberg to propose a hidden quark quantum number called color. This

new quantum number would have three values – or colors, to generate a new $SU(3)_{color}$ symmetry that would be antisymmetric under quark permutation[Gre64]; this would make the baryonic and mesonic wavefunctions antisymmetric in accordance with Fermi statistics.

At this point, quarks were still believed to be nothing more than a mathematical construct. Thus, Greenberg's insight to imbue them with a color charge was a bold move towards our modern understanding of the strong interaction as an SU(3), non-abelian gauge theory. Greenberg gave QCD it's color, but it's non-abelian character would be explored only a year later in 1965 by Han and Nambu[MYH65]. Han and Nambu were incorrectly guided to an SU(3) theory with 9 quarks because it could allow for integer electric charges. But more importantly, they showed that their theory for the strong interaction included an octet of force-carrying bosons. Indeed, a general gauge group will have a number of gauge bosons equal to the dimension of the adjoint representation – in the case of an SU(3) theory, eight gauge bosons. Here, nuclear physics is on the precipice of QCD, and Gross and Wilczek pushed it over the edge.

Gross and Wilczek demonstrated the high energy limit behavior of the coupling for a Yang-Mills (non-Abelian) theory[DJG73]. Starting with the renormalization group equations

$$[m\frac{\partial}{\partial m} + \beta(g)\frac{\partial}{\partial g} - n\gamma(g)]\Gamma^{(n)}_{asy}(g; P_1, ..., P_n) = 0, \tag{2.32}$$

where $\Gamma_{Asy}$ is the asymptotic part of the renormalized n-particle Green's function, and where the invariant coupling determined by the solution to

$$\frac{d\bar{g}}{d\ln\lambda} = \beta(\bar{g}) \qquad \bar{g}(g, 0) = 0 \tag{2.33}$$

where $\lambda$ is an arbitrary energy scale. The Yang-Mills theory they considered is given by the Lagrangian

$$\begin{aligned} \mathcal{L} &= -\frac{1}{4} F^a_{\mu\nu} F^{\mu\nu}_a \\ F^a_{\mu\nu} &= \partial_\mu A^a_\nu - \partial_\nu A^a_\mu - g C_{abc} A^b_\mu A^c_\nu \end{aligned} \tag{2.34}$$

Solving for $\bar{g}$, they find

$$\bar{g}^2(\ln \lambda) = \frac{g^2}{1 - 2\beta_V g^{-1} \ln \lambda} \tag{2.35}$$

Thus, $\bar{g} \to 0$ as $\ln \lambda \to \infty$ and the theory is asymptotically free; that is, the coupling goes to zero as the energy scale $\lambda$ is increased. While non-Abelian gauge theories had been studied for some time, Gross and Wilczek showed explicitly that one could construct an $SU(3)_{color}$ non-Abelian gauge theory that was asymptotically free, and therefore, describe Bjorken scaling in a natural way.

Only a year later the $J/\psi$ particle, a charm quark meson, was discovered simultaneously at Brookhaven and SLAC[Tin74]. After a decade from it's first proposal and the confirmation of the existence of a fourth quark through the discovery of $J/\psi$, physics could no longer deny the reality of quarks. And in 1979, the PLUTO collaboration found the first instance of jets, hadrons following a narrow cone of production, from electron–positron scattering[Col79]. A year later, a Monte Carlo analysis demonstrated that the observation and measurements of the jets could be attributed to the formation of hadrons along the trajectories of the struck quarks and gluons. The process by which hadrons are formed can be briefly explained by considering two quarks as their distance is increased. Indeed, we know that at large distances the coupling between quarks and gluon also increases. Thus, if the distance is sufficiently increased, it becomes energetically favorable to simply produce a quark and anti-quark pair in order to keep the system color-neutral. This process is referred to as hadronization. Although confinement, the idea that quarks and gluons may not be measured in isolation but rather as constituents in color-neutral objects, meant that the quarks and gluons could not be directly measured, the observation of jets

served as the strongest evidence for their existence.

## 2.4 Parton Distribution Functions

With the establishment of QCD as the theory of the strong interaction firmly on solid ground, the consequences of its fundamental properties needed to be addressed. Confinement and asymptotic freedom are the defining properties of QCD. They describe the long-distance and short-distance behavior of QCD respectively. Confinement dictates that as the distance between quarks increases, the force between them increases as well. At a distance around the size of the nucleon, the energy content of the gluon field between the quarks is enough to spontaneously create a new quark-antiquark pair, thereby keeping the system color-neutral. On the other hand, asymptotic freedom means that at short distances the force between quarks goes to zero, and quarks behave as free particles.

Much progress has been made in studying nuclear processes at higher energy when the QCD coupling is small. Indeed, DIS experiments have been stunningly corroborated by QCD. However, at lower energies, where the coupling is large, QCD remains less explored. At this cross roads, we rely more heavily on experimental results to lead the way. In attempting to characterize the dynamic structure of nucleons, we make use of the idea of Parton Distribution Functions (PDF). Here, the parton model is useful in gaining an intuitive understanding of PDFs. In the parton model, the structure functions are simply given by the sum of the PDFs in the nucleon

$$\begin{aligned} F_1(x) &= \frac{1}{2}\sum_i Q_1^2 f_i(x) \\ F_2(x) &= \sum_i x Q_1^2 f_i(x) \end{aligned} \tag{2.36}$$

Where $Q_i$ is the charge of the parton and $f_i(x)$ is the PDF, which represents the probability to find the $i^{th}$ parton with momentum fraction $x$. Thus, PDFs are probability

densities that characterize the momentum distribution of partons inside nucleons. An additional benefit of PDFs is that they are universal. That is, PDFs are independent of the specific process, and the $x$ and $Q^2$ dependence of a given PDF is an inherent description of the parton. However, as mentioned previously, the parton model has a limited window of applicability. In fact, due to the strong coupling behavior of QCD, it is still not currently possible to analytically calculate PDFs. But hope is not completely lost. In the 1970s, efforts were made to extend PDFs to arbitrary energy scales, culminating in the DGLAP equations[Dok77]. A few years later, Gribov, Lipatov, and independently Altarelli, and Parisi presented similar results in 1977[VG72]. Their work showed that one could "evolve" the $Q^2$ dependence of the quark and gluon PDFs. Unfortunately, the Bjorken $x$ dependence cannot be analytically determined.

$$\begin{aligned}\frac{dq^i(x,t)}{dt} &= \frac{\alpha(t)}{2\pi}\int_x^1 \frac{dy}{y}[\sum_j^{2f} q^j(y,t)P_{qq}(\frac{x}{y}) + G(y,t)P_{qG}(\frac{x}{y})] \\ \frac{dG(x,t)}{dt} &= \frac{\alpha(t)}{2\pi}\int_x^1 \frac{dy}{y}[\sum_j^{2f} q^j(y,t)P_{Gq}(\frac{x}{y}) + G(y,t)P_{GG}(\frac{x}{y})]\end{aligned} \tag{2.37}$$

Where $t = \ln\frac{Q^2}{Q_0^2}$, and $Q_0$ is the renormalization scale. The function $P(\frac{x}{y})$ is called a splitting function and represents the probability of emitting a gluon with fractional momentum $\frac{x}{y}$. The indices $i$ and $j$ run over quarks and anti-quarks of every flavor[GA77]. The DGLAP evolution equations allows one to take PDFs at some known energy scale, $Q_0^2$ and evolve them to an arbitrary energy scale $Q^2$.

However, even with the DGLAP equations, one still needs a way to relate observable quantities, such as cross sections, to PDFs. In general, cross sections include both short-distance and long-distance behavior. Work carried out by Collins, Soper, and Sterman showed that the cross section could be factorized into precisely these two type of behaviors[JC89]. For DIS, the structure functions are written as,

$$F_1(x, Q^2) = \sum_a \frac{d\xi}{\xi} f_{\frac{a}{A}}(\xi, \mu) H_{1a}(\frac{x}{\xi}, \frac{Q}{\mu}, \alpha_s(\mu)) + remainder \tag{2.38}$$

$$\frac{1}{x} F_2(x, Q^2) = \sum_a \frac{d\xi}{\xi} f_{\frac{a}{A}}(\xi, \mu) \frac{\xi}{x} H_{1a}(\frac{x}{\xi}, \frac{Q}{\mu}, \alpha_s(\mu)) + remainder, \tag{2.39}$$

where $f_{\frac{a}{A}}$ is the PDF of a parton $a$ from a hadron of type $A$, $\mu$ is called the factorization scale, typically taken to be $Q$, and $H_a$ is called the hard scattering coefficient. This result is referred to as the factorization theorem, and it says that short-range behavior is contained within $f_{\frac{a}{A}}$, while long-range behavior is described by $H_a$. However, as previously mentioned, the evolution equations do not give us the functional dependence of the PDFs on Bjorken $x$. Thus, we rely on experimental data to determine the $x$ dependence of PDFs. For this, software is used to parameterize and fit the form of $f(x)$ to a variety of data.

And with that, we now have a systematic procedure for characterizing PDFs. First, we acquire a data set of cross sections across a large as possible kinematic range. Then, a $Q^2 = Q_0^2$ value is chosen to be low, but still large enough that perturbation methods are available, and the PDF behavior is evolved to higher $Q^2$ through the DGLAP equations – this determines their $Q^2$ dependence. Of course, fitting the functional dependence of $f(x)$ is not trivial and there are a multitude of groups around the world dedicated to this kind of PDF analysis program, each with their own methodology and data sets chosen to constrain their fit. Figure 2.6 demonstrates the choice and kinematic coverage of one such group fitting PDFs with a multitude of data sets. Such an analysis is referred to as a global PDF analysis, named for the data sets accumulated from a wide array of independent experiments.

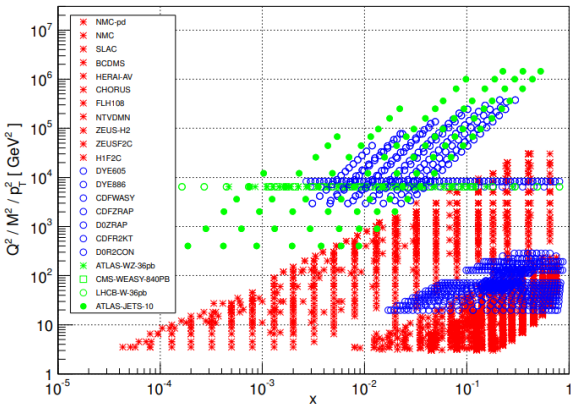


**Figure 2.6:** An example of the kinematic coverage of the data sets used in the PDF fit called NNPDF2.3. In fact, almost every PDF fitting group relies on data largely from SLAC and the Tevatron to reach the large $x$ region, and so it is a representative example of lack of precision data here.

And while global data sets are heavily populated at with precision data sets at low $x$, there remains a gap in our knowledge regarding high precision data sets at large $x$. And here we emphasize that even though there exists data at large $x$, primarily from SLAC and the Tevatron, as seen in figure 2.6, the uncertainty for these data points is insufficient to properly constrain certain PDFs, such as for the down quark and the gluon. This is shown in figures 2.7 and 2.8, where PDF fits from different groups are compared to the fit called CJ15, to be discussed in depth in Chapter 5[AA16]. The differences between the PDF fits is made more clear by plotting the ratio of the PDF to CJ15, and it is noted that as $x$ becomes large the uncertainty band begins to grow, signifying that these PDFs remain relatively unconstrained in this region.

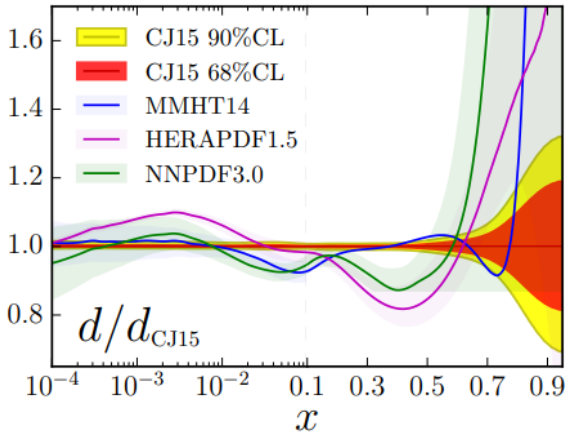


**Figure 2.7:** Plot of the down quark PDF ratio to CJ15 with, MMHT14, HERAPDF1.5, NNPDF3.0. The red bands on CJ15 indicate a 68% confidence level and the yellow bands indicate a 90% confidence level.

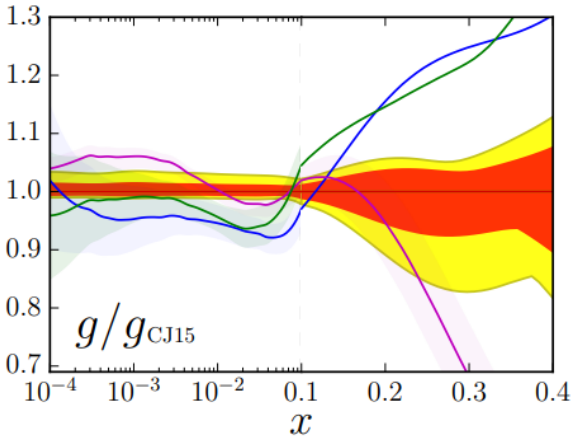


**Figure 2.8:** Plot of the gluon PDF ratio to CJ15 with, MMHT14, HERAPDF1.5, NNPDF3.0. The red bands on CJ15 indicate a 68% confidence level and the yellow bands indicate a 90% confidence level.

Here, the E12-10-002 experiment at Jefferson Lab is well suited to make an important contribution, providing precision measurements on hydrogen and deuterium cross sections. For that reason, CTEQ-JLab, commonly referred to as CJ, was created as a collaboration between the global PDF analysis efforts of CTEQ and Jefferson Lab experiments at large $x$ to provide a unique addition to the world data set in this large $x$ region.

# Chapter 3

# Experimental Setup

## 3.1 Overview

The heart of Jefferson Lab is the Continuous Electron Beam Accelerator Facility (CEBAF) shown in figure 3.1. It was proposed in the mid 1980s and motivated by the need to explore the still-mysterious region of QCD where interactions are described by quarks and gluons on one hand, and by strongly interacting hadrons on the other. An accelerator that could be capable of exploring these fundamental questions about the structure of matter would have to meet a few critical criteria. First, the accelerator would need to deliver multiple-GeV beam energy for high spatial resolution. It would also need high beam intensity to attain the necessary precision on the small cross sections being measured. Finally, the accelerator would need to be flexible enough to allow coincident experiments, each focused on independent, but important aspects of this region of QCD. Unless alternately cited, figures and information about the detailed operations of CEBAF may be assumed to be referenced from the "Jefferson Lab Hall C Standard Equipment Manual",[SW16].

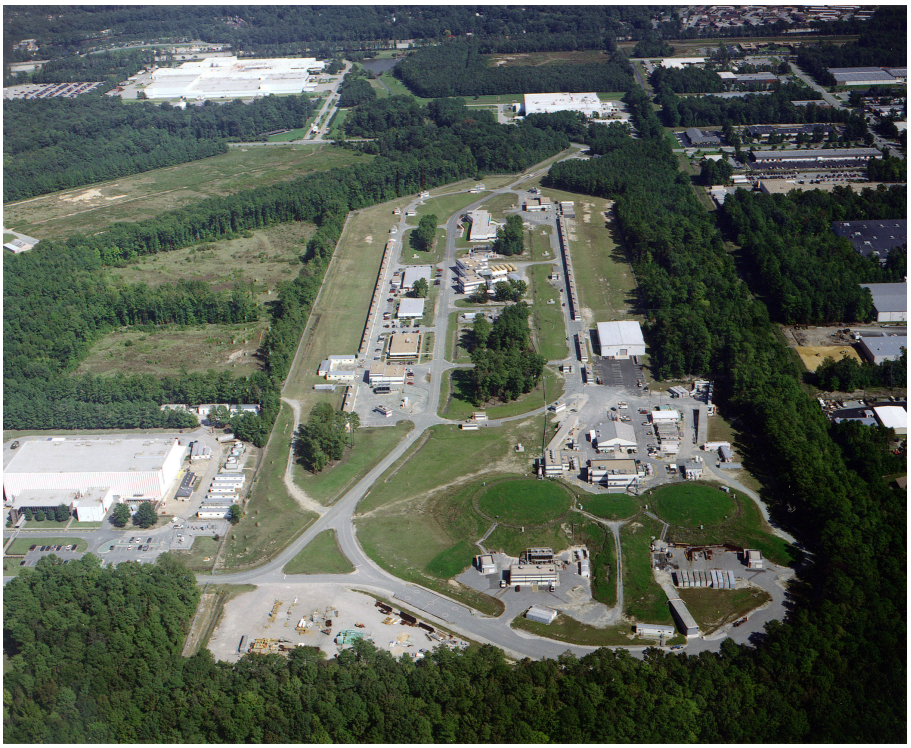

**Figure 3.1:** Aerial view of the CEBAF accelerator facility.

To begin, the accelerator was designed using superconducting radiofrequency (SRF) cavity technology in mind, shown in figure 3.2. As their name implies, SRF cavities use radio frequencies within a resonant superconducting structure in order to transfer energy to a beam of charged particles; this is done by creating an accumulation of negative charges in the conductor behind the beam electrons and positive charges in front of them. The electric field produced by the charge distribution serves to accelerate the beam. Its superconducting nature both allows a larger amount of the RF energy to go into the acceleration of the beam as well as eliminating the need to employ a water cooling system. Of course, the niobium superconducting cavities must be super cooled to a temperature of 2 kelvin, which is achieved by 400 gallons of liquid helium.

**Figure 3.2:** SRF cavity pair in the CEBAF.

The CEBAF accelerator operates by first producing electrons from a photocathode and introduces the electrons into the beam line by using a 100kV electron gun. From here, the electrons encounter two linacs made up of 25 cryomodules; each of these cryomodules subsequently contain 8 RF cavities each. Recirculation arcs transport the beam between the two linacs[CL01]. Depending on the requested beam energy, the beam may make five passes through the accelerator, for a total beam energy of 11 GeV for Halls A, B, and C, and Hall D capable of receiving 12 GeV, with operation currents up to $200\mu A$. A schematic of the CEBAF design is presented in figure 3.3.

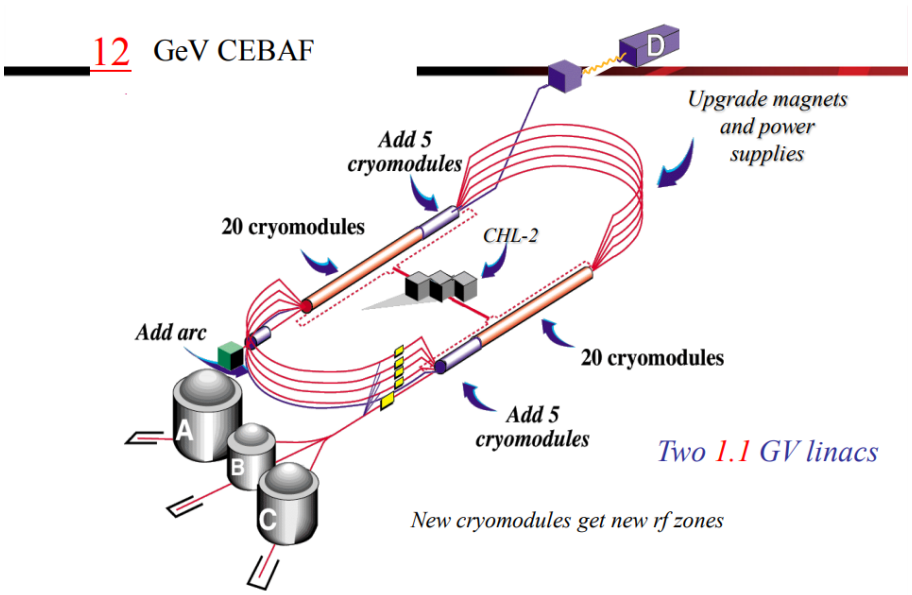


**Figure 3.3:** CEBAF showig 12 GeV upgrade.

In 2005, the first proposals were made to update both the technical capabilities of

Jefferson Lab's accelerator facility, called CEBAF, and also it's physics program. Originally, CEBAF was commissioned to provide a 4 GeV beam to its experimental halls, however, it outperformed it's original design specifications and was capable of providing up to 6 GeV. But, the need for higher beam energies soon became apparent. Indeed, increasing the accelerator beam energy opens the door to experiments at new kinematics with the same high luminosity as before.

After more than 10 years of commissioning, work on the CEBAF upgrade began in 2017. The upgrade installed 10 additional cryomodules into the accelerator track. These cryomodules are responsible for the acceleration of the electrons of the beam, and with the additional cryomodules, CEBAF is now able to achieve beam energies up to 12 GeV. Along with these cryomodules, stronger magnets were necessary to keep the beam in the recirculation arc. In order to make full use of the 12 GeV upgrade, the Hall C experimental hall also underwent some upgrades. Most prominently, a new spectrometer was added to the hall to account for the increased beam energy. In particular, the Super High Momentum Spectrometer (SHMS) is able to reach very forward scattering angles – down to 5.5 degrees. It's momentum acceptance was also increased above it's predecessor, the High Momentum Spectrometer (HMS).

During the E12-10-002 run time, data was taken simultaneously using the independent SHMS and HMS spectrometers. The kinematic ranges covered by the two spectrometers are both complimentary and overlapping. This allows for an independent cross check for the first time use of the SHMS, as well as providing improved statistics for the experiment.

## 3.2 Hall C

### 3.2.1 Beam Line

#### Beam Position Monitors

In order to precisely determine the position of the beam in Hall C, various diagnostic elements are used. Three beam position monitors are used in total, called IPM3H07A, IPM3H07B, and IPM3H07C. The BPMs are located 3.71 meters, 2.25 meters, and 1.23 meters upstream respectively from the beam target. The BPMs are of a stripline design, shown schematically in figure 3.4, and consist of an array of four antennas tuned to the fundamental RF frequency of the 1.497 GHz beam.

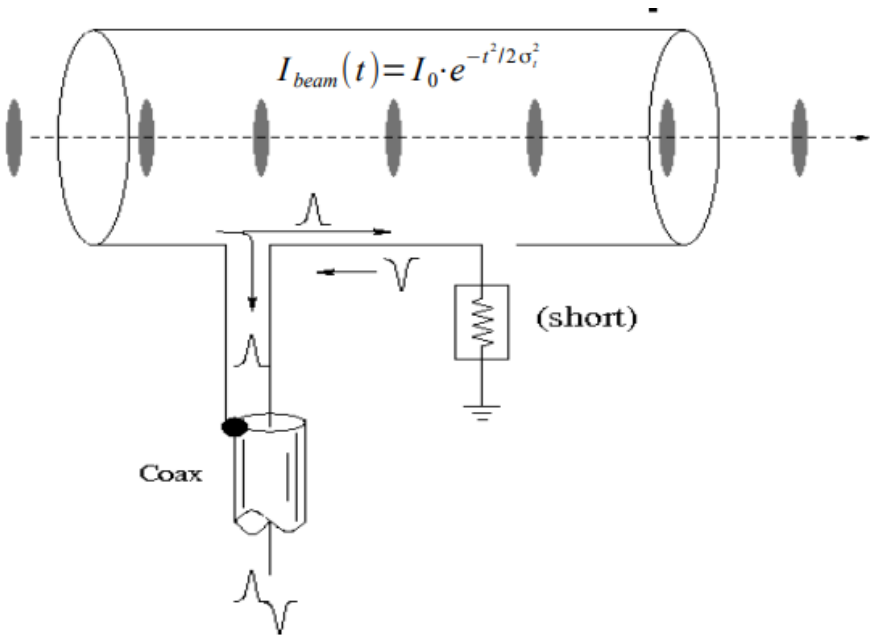


**Figure 3.4:** Stripline beam position monitor.

As the beam passes through the BPM, a current and voltage is induced in the thin wire striplines, given by

$$j_3(\phi) = \frac{I_{beam}}{2\pi a} \frac{a^2 - r^2}{a^2 + r^2 - 2ar \cdot cos(\phi - \theta)} \tag{3.1}$$

$$I_3 = \int_{-\frac{\alpha}{2}}^{+\frac{\alpha}{2}} a \cdot j_3(\phi) d\phi \tag{3.2}$$

and

$$V_1(t) = \frac{1}{2}\frac{\alpha}{2\pi} R_1 (I_{beam}(t) - I_{beam}(t - \frac{2l}{c})) \tag{3.3}$$

where the geometric variables are defined in figure 3.5.

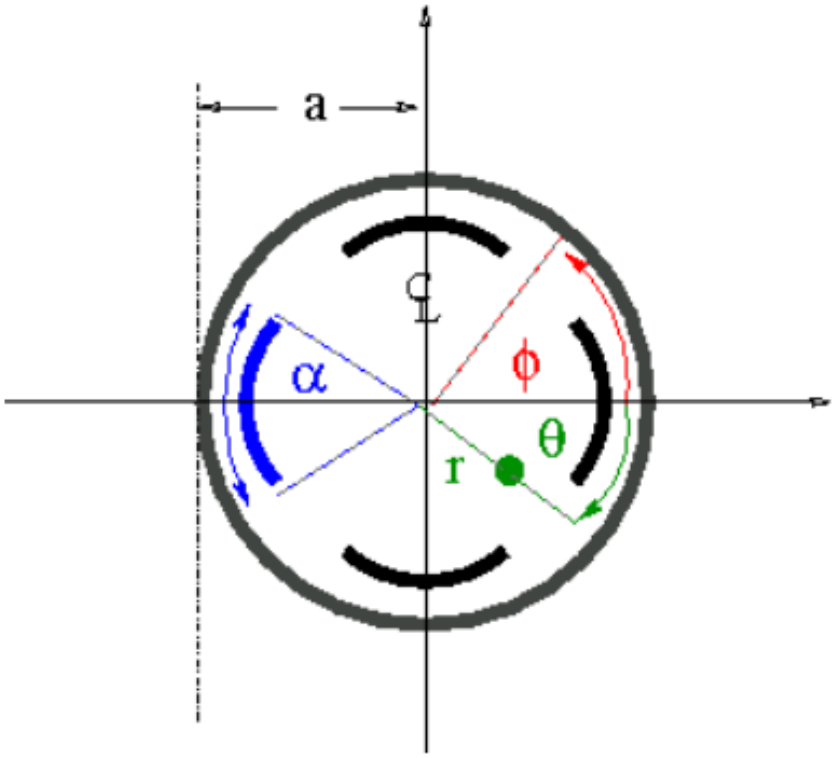


**Figure 3.5:** Figure demonstrating the geometric variables of the BPM design.

The resolution of the BPM is determined through a difference-over-sum resolution analysis, explained below. The beam position in the x-direction is expressed in terms of the voltage as

$$x = \frac{a}{2}\frac{V_L - V_R}{V_L + V_R} \tag{3.4}$$

where the resolution is given by

$$\sigma_x = \frac{a}{(V_R + V_L)^2}\sqrt{V_L^2 \delta V_R^2 + V_R^2 \delta V_L^2} \tag{3.5}$$

and finally in terms of the signal-to-noise ratio.

$$\sigma_x = \frac{a}{2\sqrt{2}}\frac{1}{\sqrt{SNR}} \tag{3.6}$$

With these beam position monitors, a resolution of $\sigma = 100\mu m$ can be reached for beam currents above $100nA$. However, measurements from the stripline style BPMs are relative, and they must first be calibrated by the use of another type of beam position diagnostic called superharps, shown in figure 3.6. There are two superharps located adjacent to the further two downstream BPMs.

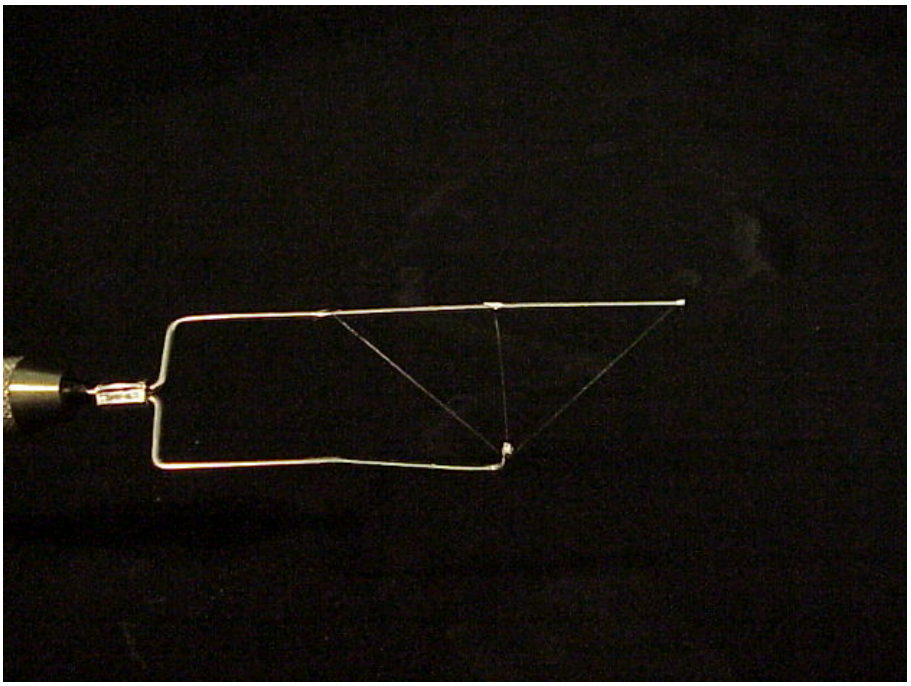

**Figure 3.6:** CEBAF harp design showing three Tungsten Rhenium wires stretched across a fork.

Mechanically, harps consist of Tungsten Rhenium wires that are passed through the electron beam. This is controlled through a computer automated measurement and control (CAMAC) system that operates stepper motors to move the harps in a precise and controlled manner through the beam. As the beam interacts with the wire, charge is

accumulated and the signal is recorded. A harp is fitted with several such wires onto a rigid frame called a fork, and from the charge measurements the beam position may be determined. Harp measurements are inherently destructive to the beam, thus, they are used primarily for calibration of the standard BPMs[SW16].

### Beam Current Monitors

Hall C also utilizes several beam current monitors that are used for analysis purposes but also for beam operation needs. The main beam current monitor (BCM) consists of a parametric current transformer, an unser monitor and two rf cavities. A triplet of rf cavities are also optionally used downstream of the main BCM unit. This is shown schematically in figure 3.7.

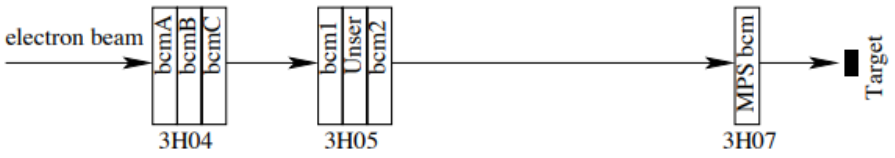


**Figure 3.7:** Schematic of the beam current monitors used in Hall C.

In particular, the unser monitor is a toroidal transformer coupled into a feedback loop of an operational amplifier. The drawbacks of such a system are that it is extremely sensitive to external magnetic fields and temperature and it is susceptible signal drifts. To minimize the unser monitor is magnetically shielded from the outside environment. Due to the signal drift of the unser, it's not possible to make current measurements over a long time scale (minutes). For this reason, the BCM also utilizes two additional rf cavities. The cavities are cylindrical, high Q-factor waveguides tuned to the beam frequency. As the beam passes through the cavities, a voltage is induced which is proportional to the current of the beam. The unser monitor and rf cavities are thus used in tandem – when the beam is off the zero-current signal drift is measured in the unser monitor and removed in the BCM cavity calibration[Uns91].

### Beam Raster

Due to the high current, high luminosity beam in Hall C the use of a beam raster is necessary. Additionally, an unrasterd beam has a profile of less than $200\mu m$. Leaving the beam unrastered would deposit a large amount of power into the target, causing it to boil. As will be discussed in a Chapter four, boiling of the target is an undesired systematic effect that must by determined and accounted for. Additionally, an unrastered beam is possibly dangerous and damaging to the Hall C equipment. Thus, two air-core magnets are used to raster the beam vertically and horizontally into a $2mmx2mm$ Lissajous raster pattern[Yan03]. Figure 3.8 shows a diagnostic screenshot of a properly rastered beam.

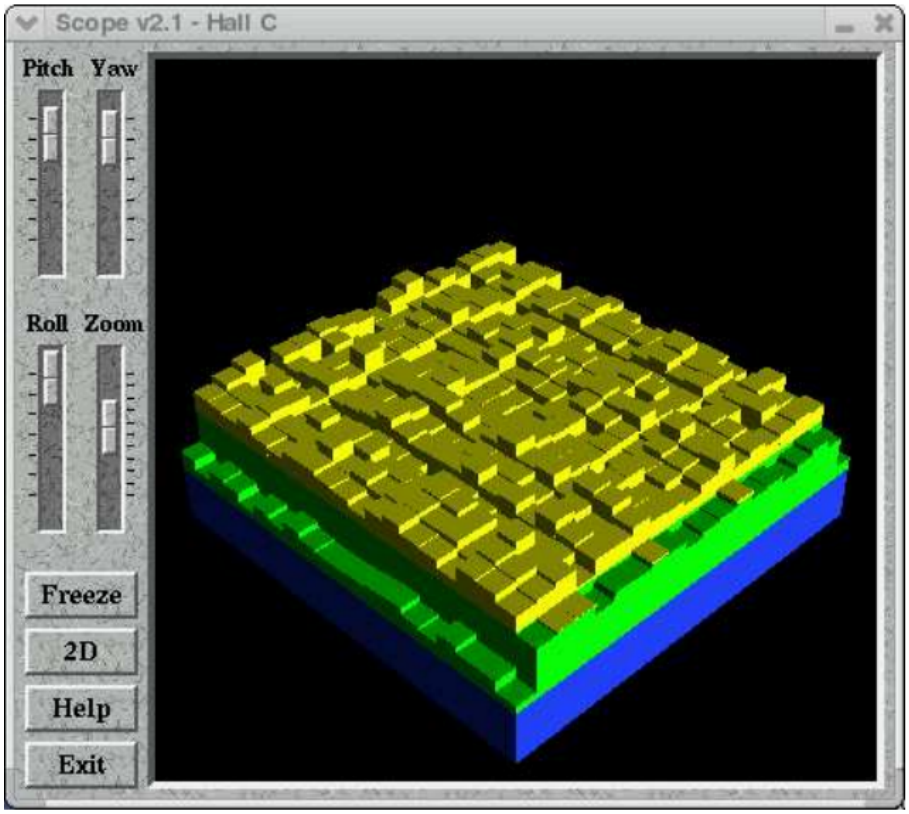


**Figure 3.8:** Raster diagnostics used by accelerator operators.

## 3.3 Target

The targets used in E12-10-002 are housed in a vacuum pumped target chamber specifically designed for Hall C. The vacuum in the chamber is created by a Leybold 1000 $Hz$ turbomolecular pump and the held vacuum ranges from $10^{-6}$ Torr to $10^{-7}$ Torr when a cryotarget is used. The target chamber was designed to accommodate the acceptance of both the SHMS and HMS spectrometers, shown schematically in figure 3.9. Indeed, on the HMS side the horizontal angular range of the chamber is 3.2 to 77.0 degrees and on the SHMS side the horizontal range is 3.2 to 47.0 degrees. This allows for the specified range of the HMS of 10.5 to 80.0 degrees for the HMS and 5.5 to 40.0 degrees for the SHMS.

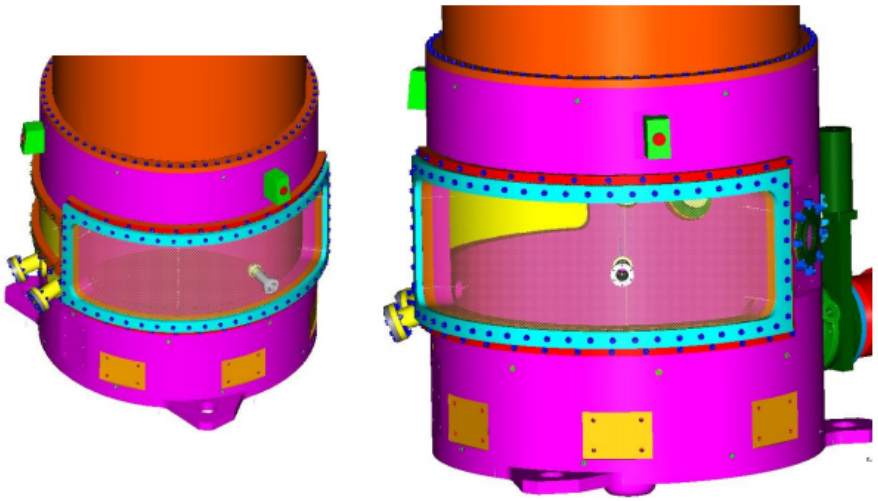

**Figure 3.9:** CAD schematic of the target chamber designed in 2006.

The primary targets used in E12-10-002 are liquid hydrogen ($H_2$) and liquid deuterium ($D_2$). Additional solid targets are used, such as the carbon hole target used for beam centering purposes. An aluminum dummy target is also used to account for the portion of the electron yield coming from the aluminum walls of the cryotarget cells. Cryogenic targets are used to increase the density of the target, and therefore the yield of the experiment. This presents additional challenges, as the temperature and pressure of the cryotargets must be monitored to ensure changes in density can be accounted for. The

ideal thermal state for the targets is presented in table 3.1.

| Target | Temperature | Pressure | Freezing T | Boiling T |
|---|---|---|---|---|
| $H_2$ | $19 \pm 0.1$ | $24 \pm 2$ | 13.86 | 22.24 |
| $D_2$ | $22 \pm 0.1$ | $24 \pm 2$ | 18.73 | 25.13 |

**Table 3.1:** Operating temperature and pressure of cryotargets.

The cryogenic targets are supplied with a set flow of liquid helium supplied from the end station refrigerator (ESR). This supply is determined by the demand of the several Halls in the CEBAF. Thus, the temperature of the cryotargets is regulated by a Proportional-Integral-Differential (PID) feedback loop coupled to a heating system. The PID system monitors the output temperature of the cryotargets and adjusts the heating power accordingly to keep the temperature constant. During production running, a target operator is necessary to monitor the inlet and outlet temperature of the cryotargets, as well as adjust the power feeding the heating system.

As previously mentioned, the target cells are made of aluminum. The target cells used in E12-10-002 utilize the "cigar" target cell design as opposed to previous "tuna can" designs, shown in figure 3.10. The cells are $10cm$ long, with the outer wall measuring $0.006in$ thick and the exit window measuring $0.004in$

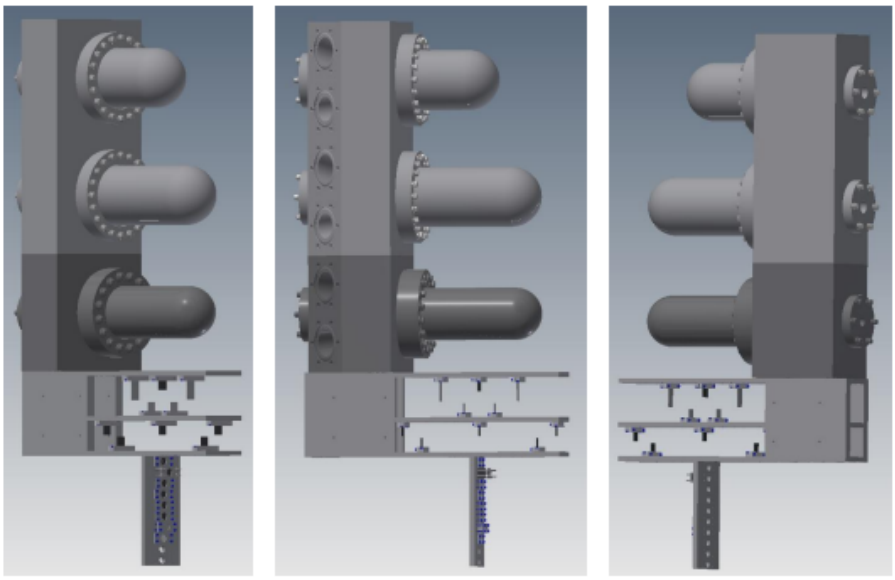

**Figure 3.10:** Schematic of the $H_2$ and $D_2$ aluminum "cigar" cryotarget cells.

## 3.4 Super High Momentum Spectrometer

The SHMS spectrometer was built between 2009 and 2016 in order to accommodate the 12 GeV update, and its design parameters are presented in table 3.2. It was designed to be used in conjunction with the existing HMS spectrometer. For the $F_2$ experiment, both spectrometers were set to measure primarily electrons, and for the charge symmetric background systematic, positrons.

| Parameter | SHMS Design |
|---|---|
| Range of Central Momentum | 2 to 11 GeV/c |
| Momentum Acceptance $\delta$ | -10% to +22% |
| Scattering Angle Range | 5.5 to 40 degrees |
| Solid Angle Acceptance | $>$ 4.0 millisteridians |
| Horizontal Angle Resolution | 0.5 - 1.2 mrad |
| Vertical Angle Resolution | 0.3 - 1.1 mrad |
| Vertex Length Resolution | 0.1 - 0.3 cm |
| Tracking Rate Capability | 5 MHz |
| Beam Capability | Up to 90$\mu A$ |

**Table 3.2:** SHMS design specifications.

As shown in figure 3.11, as the electron beam approaches the SHMS detector package it is first bent by a horizontal-bending (HB) magnet. The HB allows the SHMS to reach it's most forward scattering angles. Next, the beam is focused by three separate quadrupole magnets. The quadrupole magnets ensure the beam is properly focused at the focal plane of the detector package. Finally, a dipole magnet is tuned to select primary electrons of a given momentum.

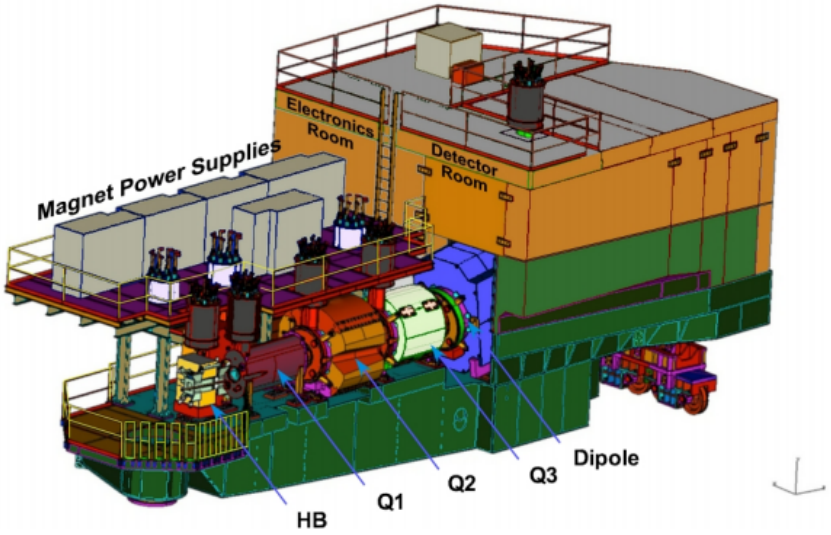


**Figure 3.11:** CAD of the SHMS design.

## 3.5 High Momentum Spectrometer

The High Momentum Spectrometer (HMS) has a detector package that is very similar to the SHMS detector package, and its design parameters are presented in table 3.3. Like the SHMS, the HMS uses a drift chamber to track primary events, a hodoscope to determine the TOF of events and create triggers, a gas Cerenkov detector to identify and separate electrons from pions, and a calorimeter to determine energy deposition as well as particle identification. There are minor differences between the SHMS and HMS detector package which will be addressed, but the detectors fundamentally function on the same principles.

| Parameter | HMS Design |
|---|---|
| Range of Central Momentum | 0.4 to 7.3 GeV/c |
| Scattering Angle Range | 10.5 to 90 degrees |
| Solid Angle Acceptance | $>$ 8.0 millisteridians |

**Table 3.3:** HMS design specifications.

### 3.5.1 Spectrometer Detector Packages

#### Drift Chamber

The drift chambers in the SHMS detector package are used to determine the position and angle of the electron beam within the detector package, shown in figure 3.12. From this information, it is possible to reconstruct the trajectory of primary electrons. Combined with knowledge of the spectrometer magnets, it is possible to infer their momenta. The drift chamber is composed of two identical gas chambers, connected by a rigid aluminum support structure.

An individual chamber is constructed from a printed circuit board 1/8 in thick, sandwiched between two aluminum plates to provide structure. The chamber is further bisected by a fiberglass board, and a vacuum is held in the chamber. Each chamber

encloses 6 planes of wires, consisting of alternating $20\mu m$ gold tungsten anode wires and $80\mu m$ copper plated beryllium field wires. The planes in first chamber are labeled and ordered as (U, U', X, X', V, V'), where the X and X' planes consist of horizontally oriented wires, the U and U' planes are rotated $+60°$ relative to the X plane, and the V and V' planes are rotated $-60°$ relative to the X plane. The second chamber is identical to the first, however, it is rotated $+180°$ relative to the first around the vertical axis; this flips the orientation to (V', V, X', X, U', U). Additionally, the rotation introduces a half-cell shift in the wires, allowing for cross-checking left/right differences.

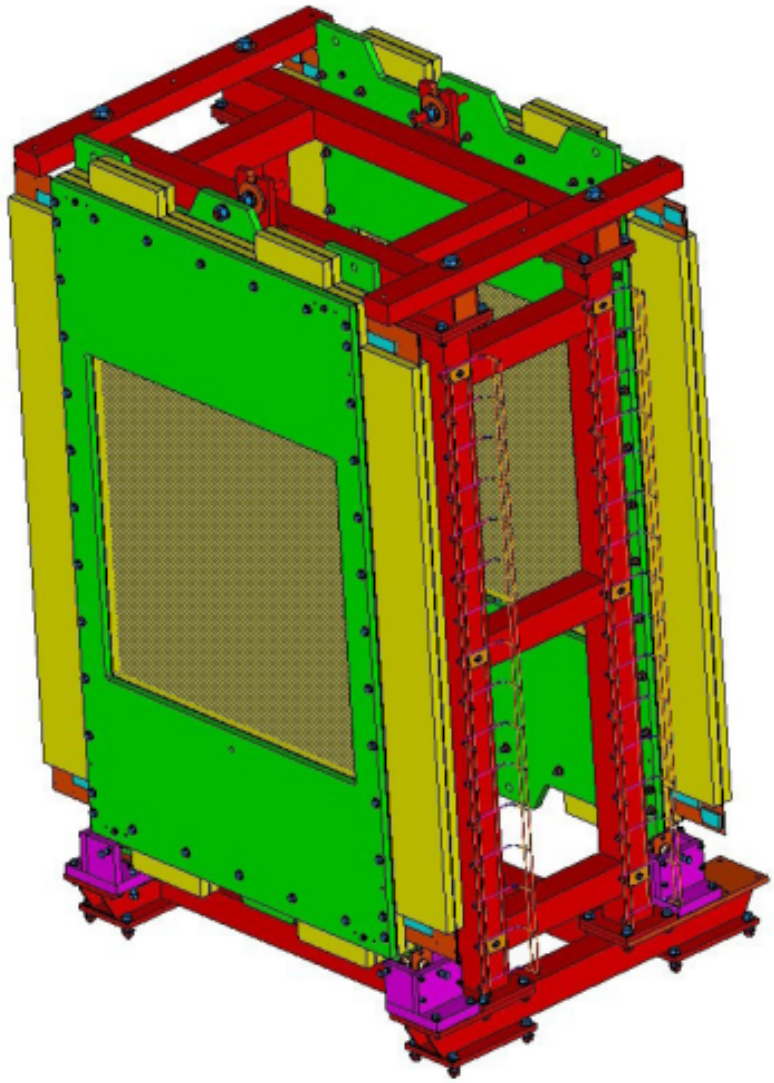

**Figure 3.12:** Drift chamber package in the SHMS.

The operational principle of the drift chambers is quit simple. The gas chambers are filled with a 50/50 mixture of ethane and argon; this acts as a ionizing gas. As the electron beam passes through the gas chamber, the gas becomes ionized and is drawn toward the sensing wires directed by the field wires. The wires collect and measure the charge and the readout is sent to preamplifier and discriminator cards. The readout values are in fact TDC values, and the drift distance must be calculated using the relation,

$$t_{drift} = \int_{track}^{anode} \frac{ds}{v(t)} \tag{3.7}$$

However, if the field wires are such that the electric field within the volume of the drift chamber is near constant, the drift velocity of the ions will not be time-dependent and the relationship between drift time and drift distance is simple. A schematic of the wires is shown in figure 3.13.

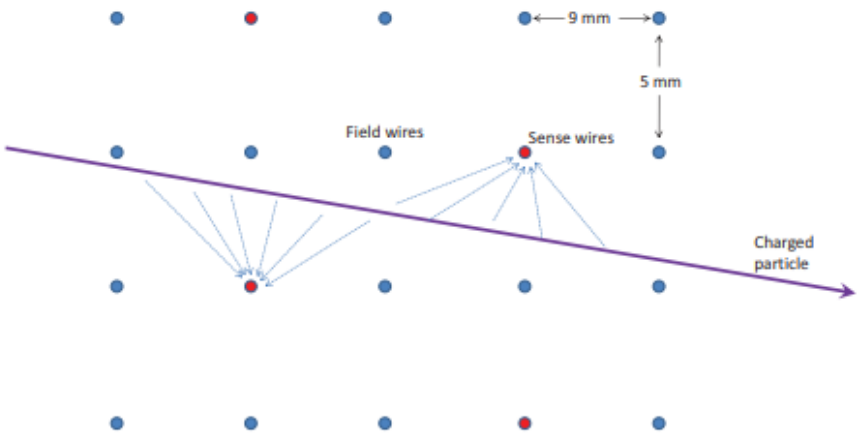


**Figure 3.13:** Diagram demonstrating operation of a general principle drift chamber.

Like the SHMS, the HMS uses two, 6 wire plane gas chambers. The two chambers are rotated about the vertical axis with respect to each other, and the planes are represented by (U, U', X, X', V, V') and (V, V', X', X, U', U). The use of the drift chamber is identical to the SHMS; field wires are operated at high voltage and are used to direct the ions to sensing wires. A 50/50 mixture of ethane and argon is used as the ionizing gas.

### Hodoscopes

The hodoscope detectors, shown in figure 3.14, are used to keep time for the experiment. There are a total of four hodoscope planes; the first two, called S1X and S1Y, consist of 13 paddles of RP-408 scintillating material each. Each paddle is attached to XP2262 and ET9214B PMTs to collect the scintillation signal. These hodoscope planes are located directly after the drift chamber. The second two hodoscope planes, called S2X and S2Y, are comprised of 13 and 21 paddles respectively. While S2X is of the same design as the first two hodoscope planes, S2Y uses a quartz bar paddle design. The S2Y plane uses 21 Corning HPFS 7980 Fused Silica measuring 125 x 5.5 x 2.5 cm.

The last hodoscope was designed to use quartz bars to address the sensitivity of the first three scintillating planes to low energy backgrounds due to knock-on electrons. The quartz bar, however, will only emit light through Cerenkov radiation, and therefore it is much less sensitive to low energy backgrounds.

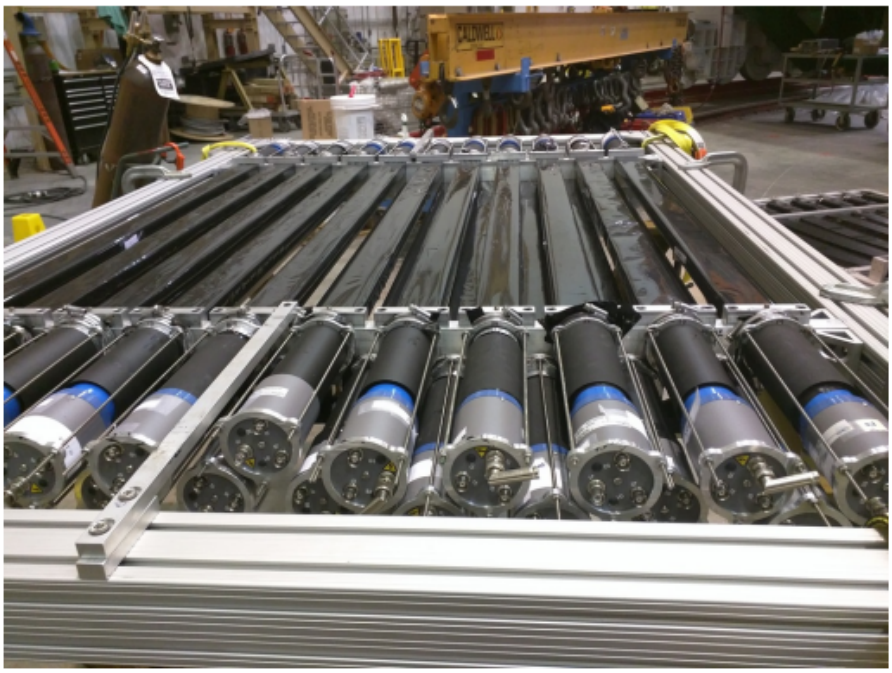

**Figure 3.14:** The S2Y quartz hodoscope detector with PMTs attached at each end of a quartz block.

In general, hodoscopes operate through the scintillation of a material as the beam

passes through it. A signal is measured and a start time is recorded. A second set of scintillating material is placed downstream and a second time value is recorded. From this information, a time of flight is derived. The SHMS hodoscope detector uses two planes for each stage, one in the x-direction and one in the y-direction. This is done to remove the position dependence from the efficiency of the detector. Indeed, the detector achieves a greater than 99% efficiency with about 100 ps of time resolution.

In addition, the hodoscope is responsible for the creating of the triggers used by the DAQ systems of the rest of the detectors in the detector package of the SHMS. Some of the basic triggers utilized by the DAQ system is the 3/4 SCIN trigger, the CER trigger, the STOF trigger, and the PSh_Hi and PSh_Lo triggers. These triggers are derived from their corresponding detectors and are used to construct final physics triggers. The 3/4 scintillator trigger requires 3 out of the 4 S1X, S1Y, S2X, or S2Y scintillator planes to record a signal, and similarly for the rest of the detector triggers. From these basic triggers, EL_HI and EL_LO are derived. They are

$$EL\_HI = SCIN \& PSh\_Hi \tag{3.8}$$

$$EL\_LO = 2/3\{SCIN \wedge STOF \wedge PSh\_Lo\} \wedge CER \tag{3.9}$$

The final physics triggers are EL_CLEAN and EL_REAL; these triggers are derived as

$$EL\_CLEAN = EL\_HI \wedge EL\_LO \tag{3.10}$$

$$EL\_REAL = EL\_HI \& EL\_LO \tag{3.11}$$

The hodoscope provides a trigger for the HMS DAQ system as well as determining the TOF for events, allowing for particle identification. The general design is similar to the

SHMS hodoscope; it uses four total hodoscope planes, grouped together in sets of two. The first two, S1X and S1Y are placed before the dirft chamber and S2X and S2Y are placed after the drift chamber. The hodoscope plane utilizes BC404 Plyvinyltoluene scintillating material for the paddles, and two Philips XP2282B 8-stage PMTs are attached to each paddle to read out the scintillating signal.

### Gas Cerenkov Detectors

The SHMS detector package includes two threshold gas Cerenkov detectors – primarily a noble gas Cerenkov is used, but a heavy gas Cerenkov was also installed during the running of E12-10-002. Due to the fact that the SHMS can cover a large kinematic range; 5.5 degrees to 40.0 degrees, and scattering momenta up to 11 GeV/c, the noble gas Cerenkov detector must be able to separate electrons from pion in kinematic regions where pion production dominates electron production 1000:1.

Both gas Cerenkov detectors work under the principle of Cerenkov radiation. When a charged particle passes through a gas medium with index of refraction $n$ with a speed greater than that of light, a cone of radiation is produced with an opening angle, $\theta$, given by

$$cos(\theta) = \frac{1}{\beta n} \tag{3.12}$$

Thus, Cerenkov radiation is produced only if

$$n > \frac{1}{\beta} \tag{3.13}$$

However, we only want electrons to primarily produce radiation instead of pions. For this condition to be met, a gas with index of refraction $n$ must be chosen so that

$$n < \frac{1}{\beta_{\pi,max}} \tag{3.14}$$

and

$$n > \frac{1}{\beta_{e^-,min}} \tag{3.15}$$

The first condition ensures that pions up to their highest possible speed will not radiate. The second condition ensures that electrons down to their lowest possible speed will still radiate. Since

$$\frac{1}{\beta_{e^-,min}} < \frac{1}{\beta_{\pi,max}} \tag{3.16}$$

only one gas with index of refraction $n$ can be chosen to separate pions and electrons over the entire kinematic range of the experiment. For a gas Cerenkov detector filled with Argon at 1 ATM, pions with momenta less than 6 GeV/c will not produce Cerenkov radiation. In fact, the gas mixture used in the experiment is a 50/50 mixture between Argon and Neon. Figure 3.15 shows the Cerenkov threshold for a variety of charged particles and different gasses.

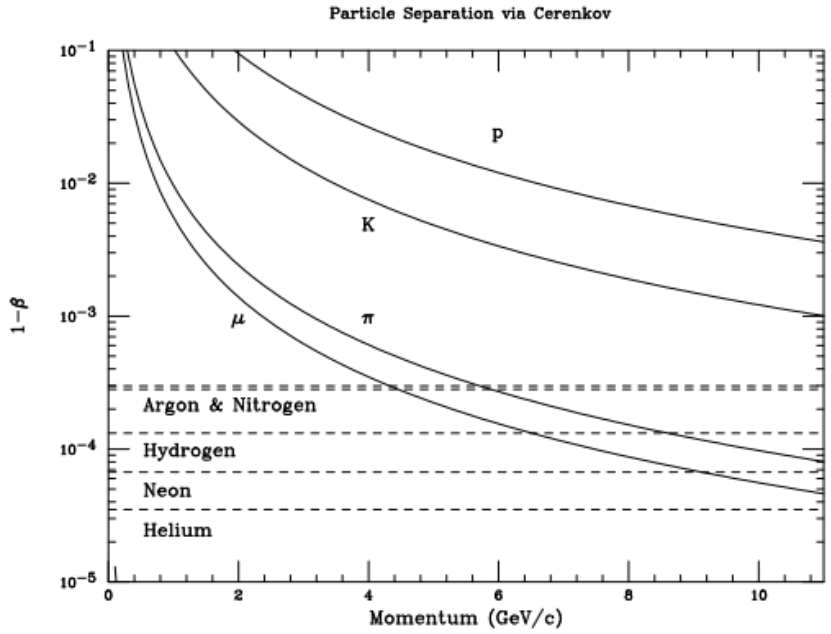


**Figure 3.15:** Plot demonstrating particle identification with a threshold Cerenkov detector. Dotted lines indicate the value $(n-1)$ of gasses at 1 ATM. Only when $(1-\beta)>(n-1)$ will Cerenkov radiation be produced.

The noble gas Cerenkov detector consists of a tank with an internal aluminum frame. The detector measures 2m along the beam direction and 90 cm in the perpendicular direction. The gas Cerenkov detector was designed so that the PMTs used to measure the Cerenkov detector would be out of the way of the active area of the beam. Thus, four 135 cm radius spherical glass mirrors are used to collect, focus, and reflect the produce Cerenkov radiation into four 9823QKB04 quartz window PMTs. A schematic of the noble gas Cerenkov detector is presented in figure 3.16

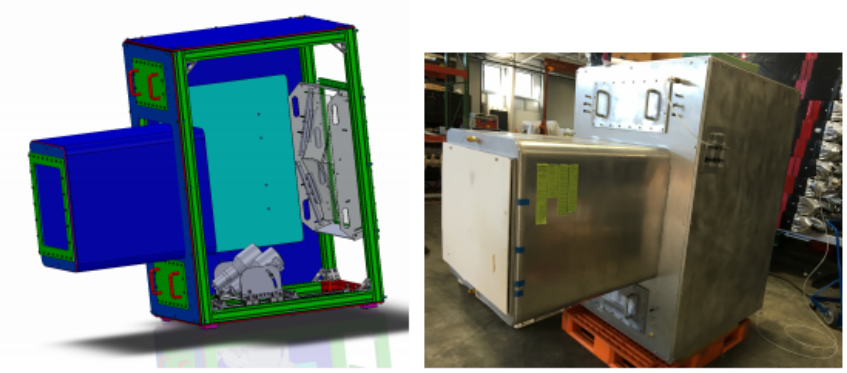

**Figure 3.16:** CAD and photograph of the noble gas Cerenkov detector showing the four PMTs and four spherical glass mirrors.

It should be mentioned that the lower left glass mirror of the noble gas Cerenkov detector was found to be damaged during the running of E12-10-002. The damaged mirror needs to be accounted for as a systematic uncertainty, and will be discussed in a later chapter.

As mentioned previously, a heavy gas Cerenkov detector was used in conjunction with the noble gas Cerenkov. Of course, the heavy gas Cerenkov detector operates under the same fundamental principles as the noble gas Cerenkov detector. However, it's overall design differs significantly to the noble gas Cerenkov detector. In particular, four spherical mirrors are used to direct Cerenkov radiation to four independent R1584 Hamamatsu PMTs. As it's name suggests, the heavy gas Cerenkov detector is filled with a $C_4F_8$ gas. It can also be filled with $C_4F_{10}$.

The HMS gas Cerenkov detector is a threshold Cerenkov detector and so it operates

on the same basis as the SHMS Cerenkov detector. It differs from the SHMS detector in its desgin. While the SHMS detector had four spherical glass mirrors and four PMTs, the HMS Cerenkov detector uses only two mirrors that direct Cerenkov radiation into two 5 inch Burle 8854 PMTs. The HMS Cerenkov detector is filled with $C_4F_{10}$ gas and was used as a $e\pi$ discriminator.

**Calorimeter**

The calorimeter used in the SHMS spectrometer is a lead glass calorimeter consisting of two parts. Along the beam direction, the first section is the preshower. The preshower is constructed from 28 TF-1 lead glass blocks measuring 10 x 10 x 70 cm arranged as two columns and 14 rows – these two columns constitude the "negative" and "positive" side of the preshower. After the preshower is the shower, or fly's eye array. The fly's eye array consists of 224 F-101 blocks measuring 9 x 9x 50 cm stacked in a 14 column by 16 row arrangement, shown schematically in figure 3.17. As the beam traverses through the lead glass blocks the electrons radiate photons primarily through bremmshtralung. These photons are measured by Photonis XP3462B PMTs in the preshower and XP3461 PMTs in the shower. The lead blocks in the preshower are individually wrapped in $50\mu m$ aluminum Mylar and $50\mu m$ Tedlar in order to optically isolate them. The lead glass blocks are optically coupled to the PMTs by use of a thin layer of Bicron ND-703 optical grease. In the shower, the blocks are wrapped in $50\mu m$ of Mylar and $125\mu m$ of Tedlar.

The redesign of the SHMS calorimeter compared to the HMS calorimeter was primarily motivated by the fact that the SHMS was built to take advantage of the 12 GeV beam upgrade and forward scattering kinematics. For this reason, the SHMS is capable of accepting higher momenta electrons, and it must be ensured that these high energy electrons will deposit all of their momenta into the calorimeter. Thus, the fly's eye array is arranged so that the long side of the lead glass blocks is along the beam direction. In this way, the shower is 18 radiation lengths long, increasing the effective volume of the shower substantially.

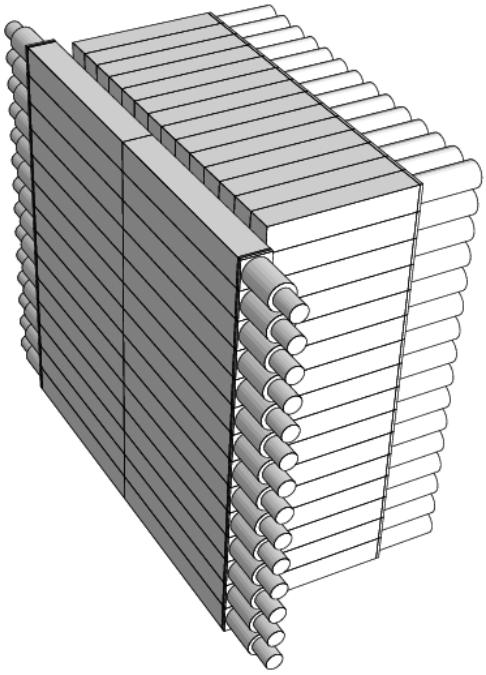

**Figure 3.17:** CAD of the SHMS calorimeter. The negative and positive sides of the preshower are shown, with the fly's eye shower array placed behind it.

The HMS calorimeter is a lead-glass calorimeter comprised of TF-1 blocks arranged in a 4x13 layout for a total of 52 modules; the lead block measure 10 x 10 x 70 cm and attach to a XP3462B PMT as shown in figure 4.6.

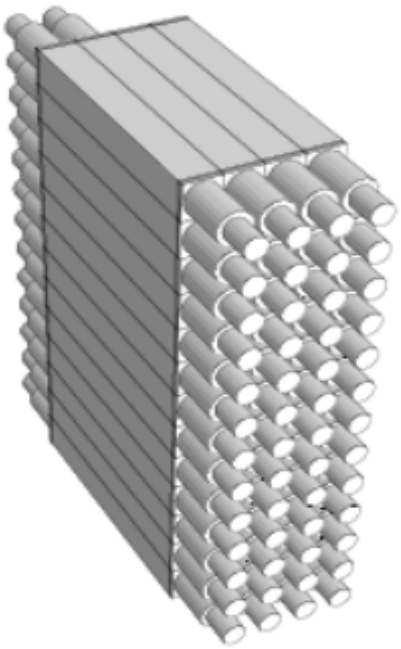

**Figure 3.18:** Design of the HMS calorimeter detector.

## 3.6 Electronics & Data Acquisition

All of the electronics and data acquisition in Hall C is handled by a system called CODA (CEBAF Online Data Acqusition) developed by the data acquisition group. CODA handles the ADC signals, primarily from PMTs, from all of the detectors of the specrometer in Hall C, as well as the TDCs signals from the hodoscopes and drift chambers. A trigger diagram for the SHMS and HMS hodoscope is shown in figure 3.19. The TDCs are CAEN V1190A TDC modules, with 128 channels each with a 100 ps time resolution. The ADC signals are treated by FADC250 modules that digitize the trigger signals read into it.

The electronics themselves are housed in an electronics house in the counting room as well as an electronics bunker attached to the spectrometers themselves. These electronics are housed in 5 VXS and VME64X crates. Indeed, the HMS detector hut houses a VXS create that runs the CAEN1190 TDC for the HMS dfift chamber detector. The SHMS detector hut contains one VMXE64X crate to hold another CAEN1190 module for the SHMS dirft chamber as well as a VXS create with FADC250 modules that handle the

SHMS pre-shower and shower counter PMT signals. In the counting house, a VXS crate houses a FADC250 and CAEN1190 modules for the HMS hodoscope, shower counter, and Cerenkov detector. Also, a separate VXS crate houses another set of FADC250 and CAEN1190 modules for the SHMS hodoscope and Cerenkov detector.

The ADCs and TDCs from the various detectors turn their respective analogue signals into digital signals, which are then fed into CODA read out controllers (ROCs). The ROCs are responsible for converting trigger signals into a format usable by the CODA event builder (EB). In addition to trigger event information, scaler and EPICS information is built into the DAQ data structure. Scalers record raw PMT counts, as well as charge and trigger type. Approximately every 30 seconds, EPICS data is recorded, including beam position and current, as well as magnet settings in the spectrometer.

The ADC and TDC modules are also used to create the trigger logic for the detectors. The trigger logic for both spectrometers is presented below in figures 3.19 through 3.22.

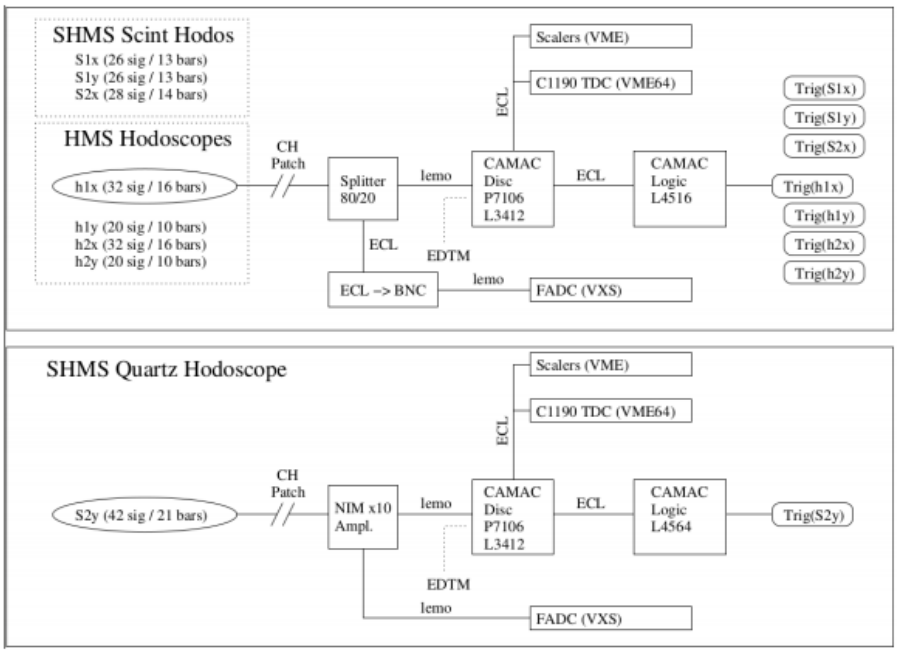


**Figure 3.19:** Trigger diagram for the SHMS scintillator and quartz hodoscopes as well as the HMS hodoscope.

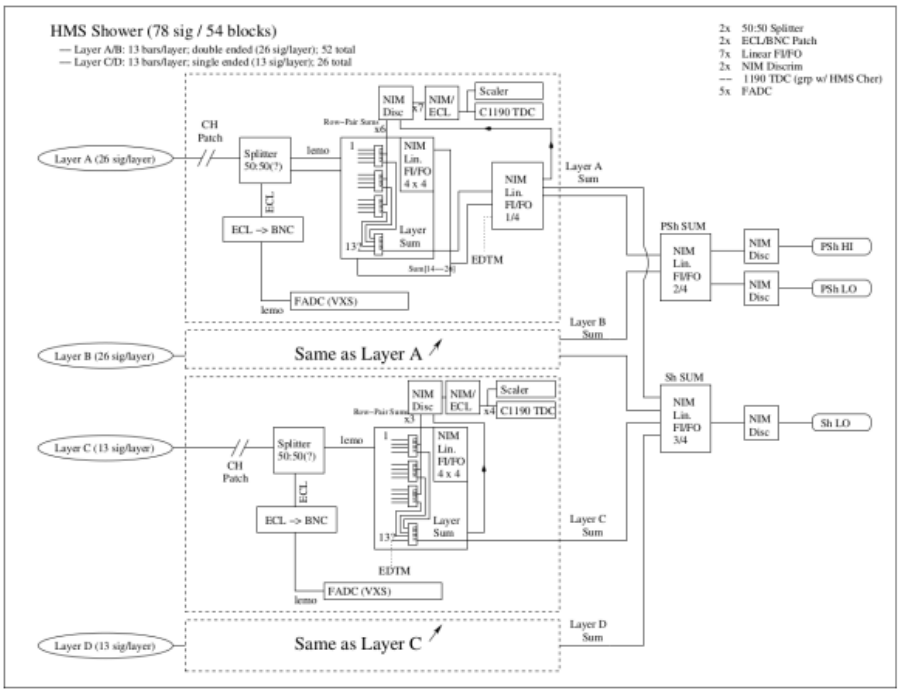


**Figure 3.20:** Trigger diagram for the HMS shower counter. The final logic triggers are PSh_HI, PSh_LO, and Sh_LO; these triggers can be used to create addtional event triggers by the user.

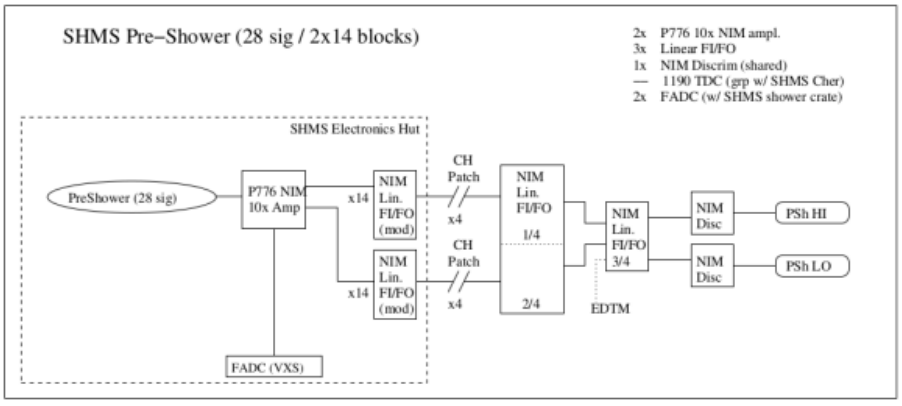


**Figure 3.21:** Trigger diagram for the SHMS pre-shower.

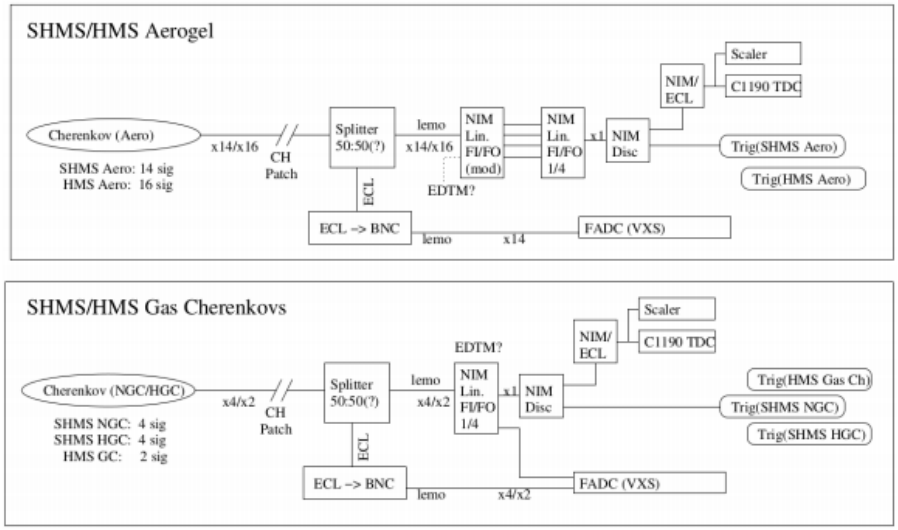


**Figure 3.22:** Trigger diagram for the SHMS and HMS gas Cerenkov and aerogel detectors.

# Chapter 4

# Data Analysis

## 4.1 Analysis Software

The analysis software used for event reconstruction is called HCANA. HCANA is an object-oriented software package based on CERN's ROOT programming framework. ROOT was built for large scale data analysis, allowing for efficient data manipulation, statistical analysis, and data visualization. More specifically, HCANA is a C++ software package built upon previous FORTRAN based codes used in Hall A. Raw data recorded by CODA is accessible to HCANA where it is decoded and interfaced with the underlying HCANA framework. This framework relies on three major class types: Apparatuses, Detectors, and Physics Modules. The spectrometers (SHMS, HMS) are defined by an Apparatus type, and drift chambers, hodoscopes, Cerenkov detectors, and calorimeters will each be determined by classes of their detector type. The Physics Modules type generally handle vertex and kinematic determinations of physics events.

Of particular importance is the determination of focal plane variables that are used to determine the momentum of events, as well as acting as a direct cross check with monte carlo simulations. These variables are $x_{fp}$, $y_{fp}$, $x'_{fp}$, and $y'_{fp}$, and they represent the position and slope of a given track respectively; this slope is with respect to the z-direction, so that

$$x'_{fp} = \frac{dx_{fp}}{dz} \tag{4.1}$$

$$y'_{fp} = \frac{dy_{fp}}{dz} \tag{4.2}$$

Information about the focal plane variables are extracted from the drift chambers, and from this target variables can be reconstructed through a so-called reconstruction matrix transformation

$$T_{tar} = \sum_{i,j,k,l} R^{y}_{i,j,k,l} (x_{fp})^i (y_{fp})^j (x'_{fp})^k (y'_{fp})^l \tag{4.3}$$

and the reconstructed target variables are $y_{tar}$, $x'_{tar}$, $y'_{tar}$, and $\frac{\delta p}{p}$, where

$$\frac{\delta p}{p} = \frac{p_{recon} - p_0}{p_0} \tag{4.4}$$

and $p_{recon}$ is the reconstructed momentum. An apparatus class, THcHallCSpectrometer, is responsible for determining the focal plane variables from the CODA data files, at which point tracks can be reconstructed via the reconstruction matrix. Likewise, detector classes read from raw CODA files and can perform pedestal subtraction, cluster reconstruction, and gain multiplication in the case of the shower class, or event counting for the Cerenkov detector class.

## 4.2 Detector Calibrations

In addition to HCANA, there is also a collection of codes used for the calibration of the detectors. The purpose of the codes is to produce parameter files that are used by HCANA to produce a ROOTfile suitable for analysis. This becomes an iterative process – HCANA is used to produce a ROOTfile, and the ROOTfile serves as an input to the calibration codes which produces parameter files. The new parameter files are used in HCANA and an updated ROOTfile is produced. The procedure continues until all of the spectrometer detectors behave as expected. In the following sections, the calibration

codes will be discussed and calibration results presented.

### 4.2.1 Electromagnetic Calorimeter Calibration

The calorimeter calibration code function identically for the SHMS and HMS, and it's purpose is to calculate gain calibration constants for each of the PMTs in the calorimeter shower and pre-shower. The file containing these calibration constants constitutes the parameter file produced by the calibration code.

The calibration constants are calculated by minimizing the difference between the reconstructed energy deposition $E_R$ and the known energy deposition $E$, given by

$$f(\overrightarrow{c}) = (E_R - E)^2 \tag{4.5}$$

where $\overrightarrow{c}$ represents a vector of the calibration constants. This minimization is subject to the constraint that the calibration constants can properly reconstruct the mean energy deposition $e_0$, such that

$$g(\overrightarrow{c}) = c^{(\overrightarrow{T})}\overrightarrow{q_0} = e_0 \tag{4.6}$$

where $\overrightarrow{q_0}$ is the mean PMT signal. The function $f(\overrightarrow{c})$ may also be expressed as

$$\sum_{n}^{N}(\sum_{i} C_i A_i^n - E^n)^2 \tag{4.7}$$

thus, the system of equations may be solved using the method of Lagrange multipliers. Therefore, the Lagrangian is

$$\mathcal{L}(\overrightarrow{c}, \lambda) = f(\overrightarrow{c}) - \lambda \cdot g(\overrightarrow{c}) \tag{4.8}$$

From $\frac{\partial \mathcal{L}}{\partial(c_j, \lambda_j)} = 0$, one can solve for $\overrightarrow{c}$ and $\lambda$,

$$\lambda = \frac{e_0 - Q^{-1}\overrightarrow{q_e}\overrightarrow{q_0}}{\overrightarrow{q_0}Q^{-1}\overrightarrow{q_0}} \tag{4.9}$$

$$\overrightarrow{c} = \frac{e - \overrightarrow{c_U}\overrightarrow{q_0}}{\overrightarrow{q_0}Q^{-1}\overrightarrow{q_0}}Q^{-1}\overrightarrow{q_0} + \overrightarrow{a_U} \tag{4.10}$$

where $\overrightarrow{C_U}$ is the unconstrained calibration constants derived from the condition that $\frac{df}{dC_j} = 0$, and Q is the calorimeter PMT signal, determined by $Q_{ij} = A_i A_j$. The unconstrained calibration may be solved from,

$$\overrightarrow{c_U} = Q^{-1}\overrightarrow{q_e} \tag{4.11}$$

thus, the the values for $\overrightarrow{c}$ is fully determined.

Of utmost importance for the calibration to be done properly, electron events should be selected to the exclusion of everything else. In practice, this is difficult to achieve and therefore several selection cuts are made to attempt select only electrons. This is done by requiring that events to be calibrated also have at least two photo-electrons were produced and measured by the noble gas Cerenkov detector for the SHMS, and four photo-electrons for the HMS. Additionally, a $-10\% < \delta p < 22\%$ cut is placed for the SHMS and $-10\% < \delta p < 10\%$ for HMS. After calibration, four diagnostic plots are produced. The first shows a one-dimensional distribution of the momentum normalized energy deposition of events. Because electrons carry most of their energy in their momentum, electron events will be found near unity. Pions, however, will be distributed closer to zero.

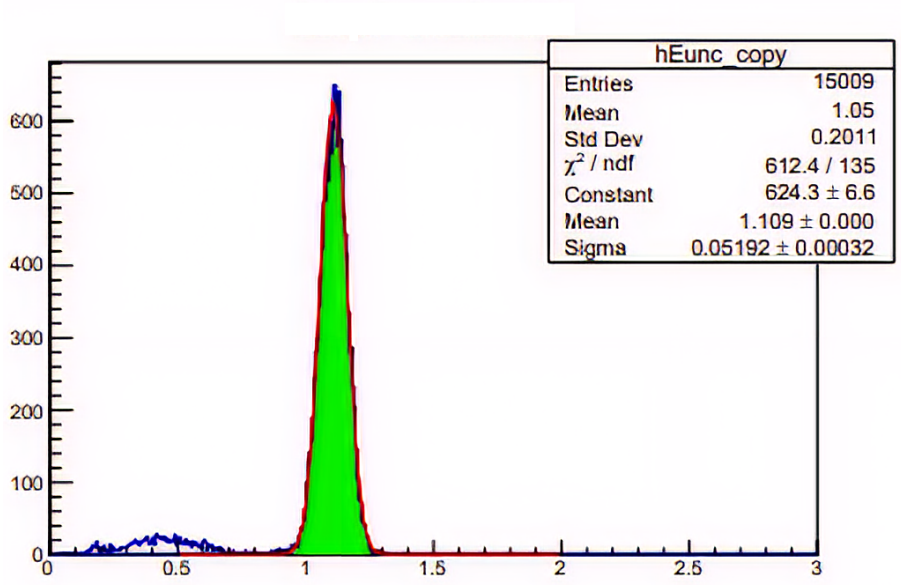


**Figure 4.1:** Uncalibrated momentum normalized energy deposition.

The example in figure 4.1 shows the events to be calibrated shaded in green, and it is clear that the electron events and pion events are separated. Of course, the distribution is uncalibrated, and therefore the mean electron peak does not sit exactly at one.

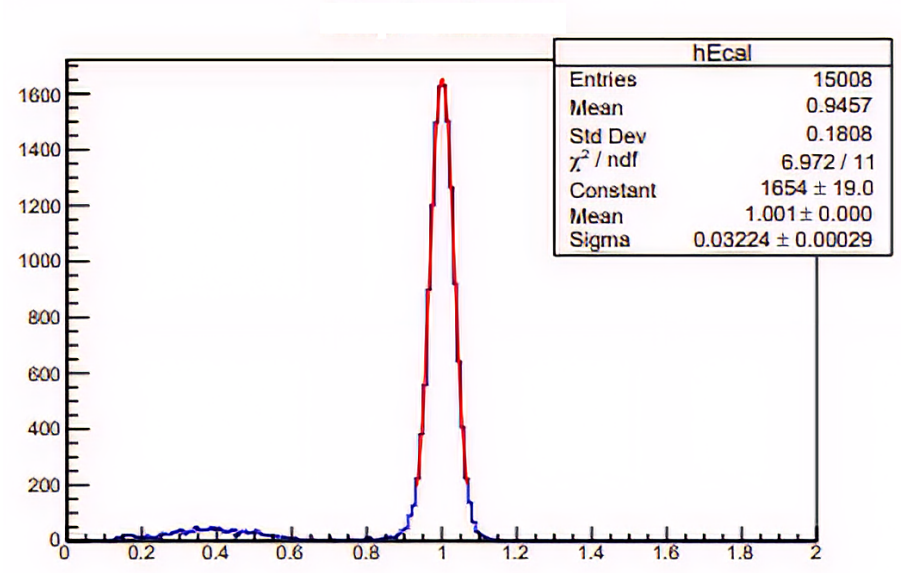


**Figure 4.2:** Calibrated momentum normalized energy deposition.

As shown in figure 4.2, after calibration, the electron peak is fit as a Gaussian distribution around one – this suggests the calibration was successful. Additionally, two

other plots are used for diagnostics. One such plot is the energy deposited in the shower versus the energy deposited in the pre-shower, shown in figure 4.3.

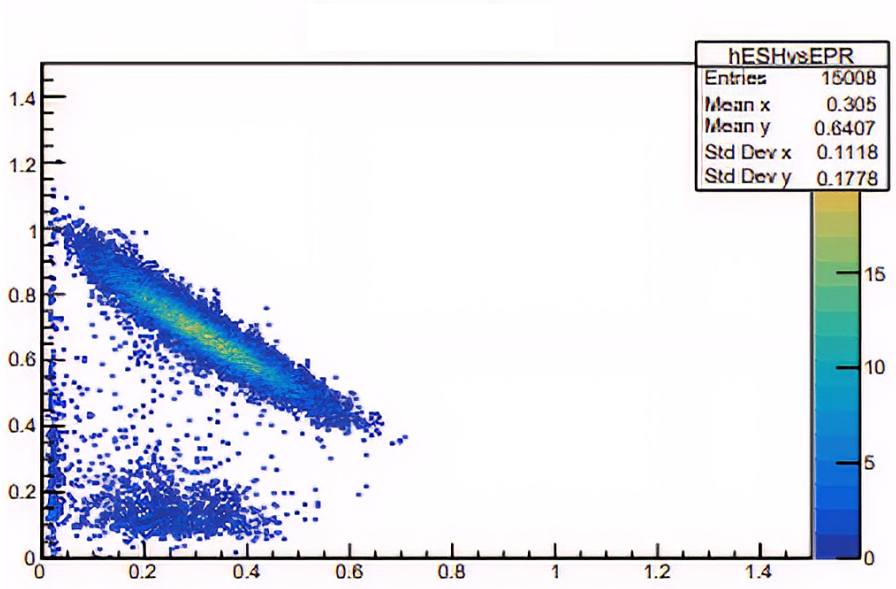


**Figure 4.3:** Energy deposited in the shower versus the energy deposited in the pre-shower.

This plot ensures that all of a particle's energy is deposited somewhere in the calorimeter, either in the shower or in the pre-shower. The fourth plot produced, is shown in figure 4.4, and is used to make sure there is no $\delta p$ dependence on the momentum normalized energy deposition.

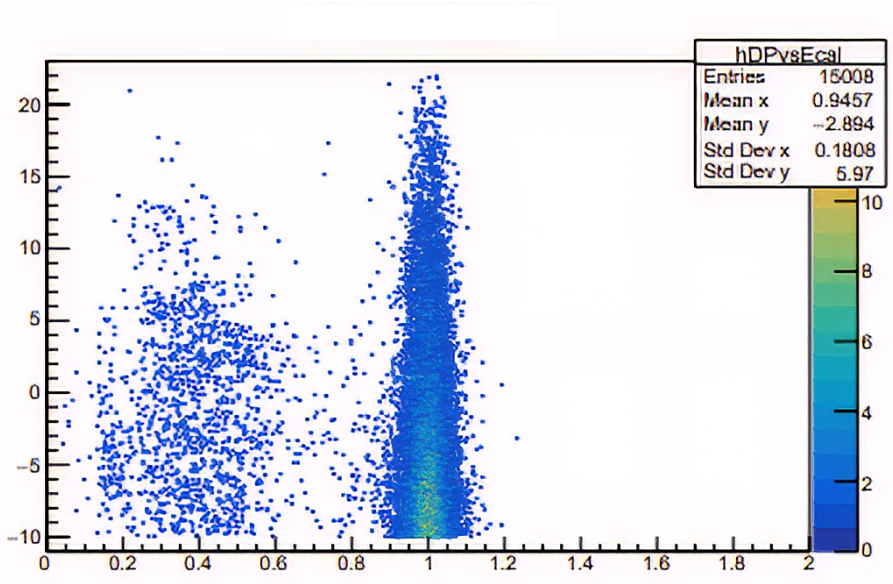


**Figure 4.4:** $\delta p$ versus $\frac{E_{dep}}{p}$.

Of course, pion and electron production is dependent on the scattering angle and final momentum, and therefore, the calculated calibration constants in the parameter files also carry this dependence. For this reason, calibrations need to be done for all of the kinematic settings of the experimental run. In this way, each run can be replayed with HCANA with a parameter file corresponding to it's angle and momentum setting. Thus, we can compile the mean peak of the momentum normalized energy deposition for all kinematic settings taken during the experimental run as a sanity check for the parameter files.

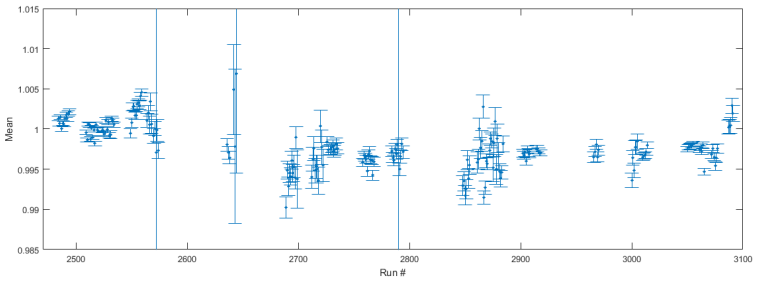


**Figure 4.5:** Mean of the momentum normalized energy deposition Gaussian distribution for all unique SHMS kinematic settings. Several runs in a given setting are considered.

It should be noted in figure 4.5 that a few runs show large error bars; this is due to

small statistics in the run. This can be mitigated by combining runs in a given kinematic setting into a single "run". Similarly, we check the means for all unique kinematic settings in the HMS in figure 4.6.

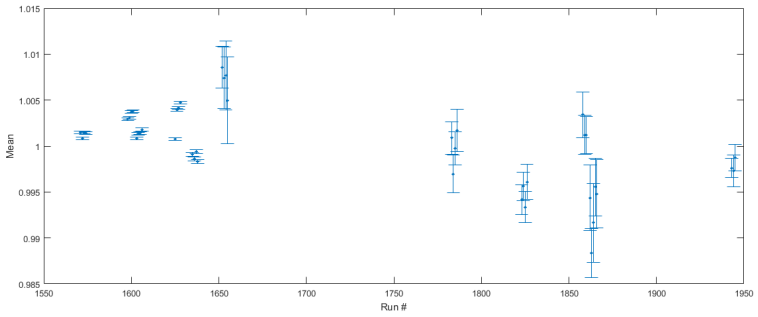


**Figure 4.6:** Mean of the momentum normalized energy deposition Gaussian distribution for all unique HMS kinematic settings. Several runs in a given setting are considered.

In our calibration study, we also investigate the $\delta p$ dependence on the mean peak of $\frac{E_{dep}}{p}$. To do this, we divide the $-10\%, +22\%$ $\delta p$ region into four equal regions, and see how the mean peak changes with respect to electron events in different regions. The results are presented in figure 4.7.

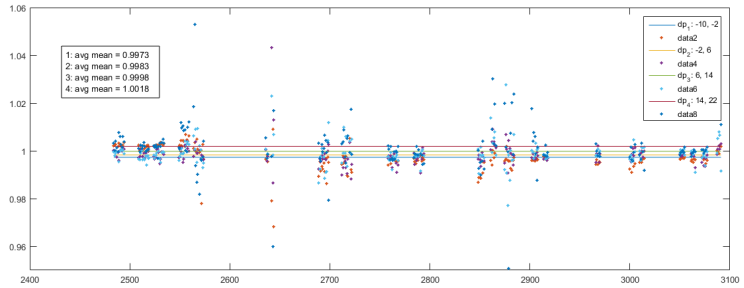


**Figure 4.7:** Mean of the momentum normalized energy deposition Gaussian distribution for events in four distinct $\delta p$ regions. Generally, we see that the mean peak has little $\delta p$ dependence.

Apart from the mean peak of the Gaussian distribution of $\frac{E_{dep}}{p}$, the RMS of the Gaussian distribution is an important figure of merit. In particular, the RMS as a function of $E'$ determines the resolution of the calorimeter detector. In ideal detector, where all of a particle's energy is deposited into the detector, the resolution of the calorimeter

is limited by fluctuations in the track length, and so the development of the shower is stochastic. Thus, one expects sigma to be proportional to the square of the track length, which is in turn proportional to the energy. Thus, we expect the calorimeter resolution to be proportional to the inverse of the square root of the energy. First, we plot the RMS across all of the runs taken, as shown by figure 4.8.

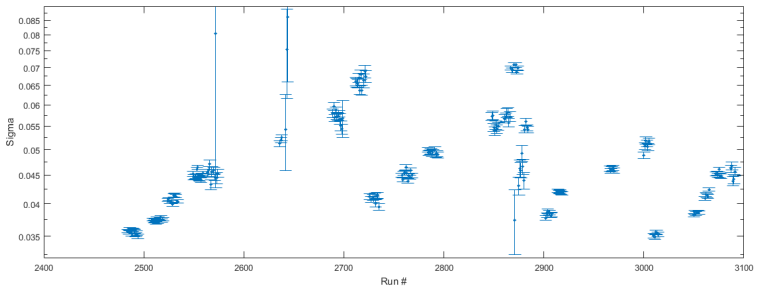


**Figure 4.8:** RMS of the momentum normalized energy deposition Gaussian distribution for the SHMS.

And likewise for the HMS, as shown in figure 4.9.

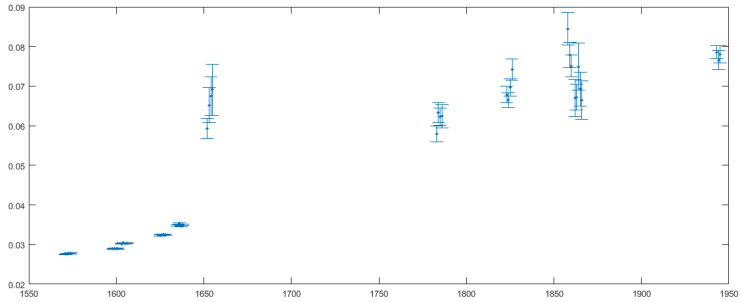


**Figure 4.9:** RMS of the momentum normalized energy deposition Gaussian distribution for the HMS.

As stated previously, plotting the RMS as a function of $E'$ gives the resolution of the calorimeter, demonstrated by figure 4.10.

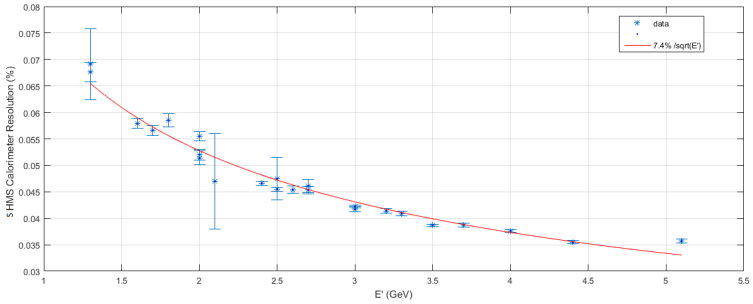


**Figure 4.10:** The resolution of the SHMS is plotted as a function of $E'$. The resolution of the calorimeter is found to be 7.4%.

The same can be done for the HMS and is presented in figure 4.11.

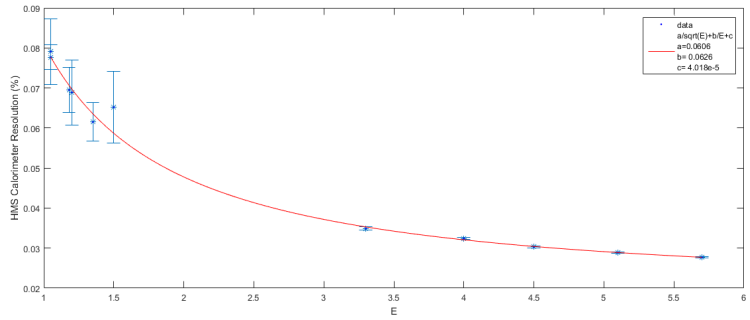


**Figure 4.11:** The resolution of the HMS is plotted as a function of $E'$.

Here, the stochastic term is not enough to fit, thus a noise term and a constant term are added to fully fit the data.

Finally, it is necessary to address a concerning observation made during calibration of the calorimeter. During calibration, it is necessary to use both the gas Cerenkov detector as well as the calorimeter for particle identification as well as separating electron and pion events. Indeed, requiring that an event triggers a certain number of photo-electrons in the Cerenkov, one can select electrons or pions. Typically, electron events trigger around twenty-two photo-electrons while pions will trigger less than five, as shown in figure 4.12.

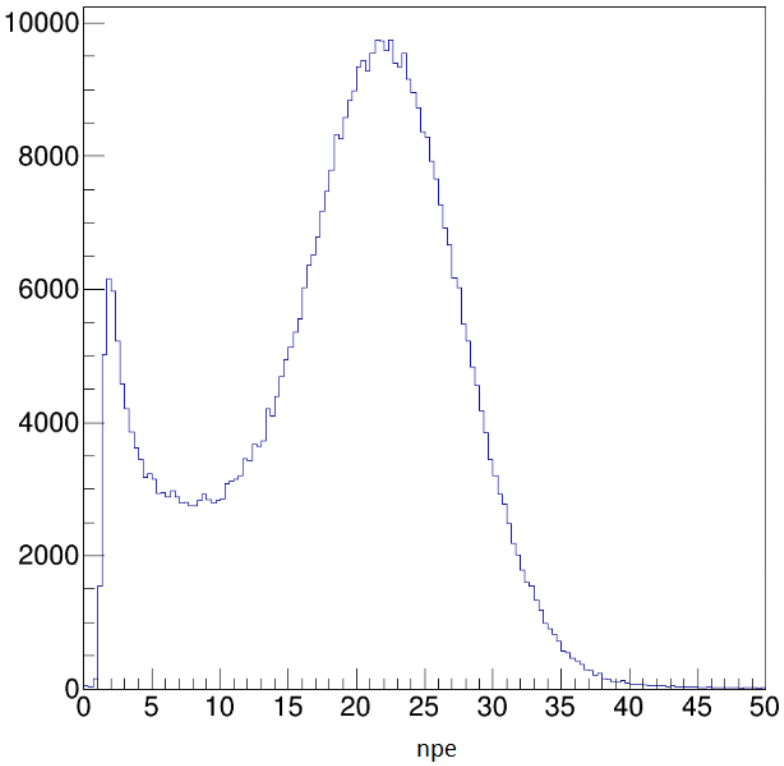


**Figure 4.12:** Distribution of number of photo-electrons in the gas Cerenkov detector.

However, it was found that for events with greater than twenty photo-electrons, many of these events recorded a momentum normalized energy deposition close to, and equal to, zero, as shown in figure 4.13. This, of course, shouldn't be true and suggests a number of issues that could be the cause.

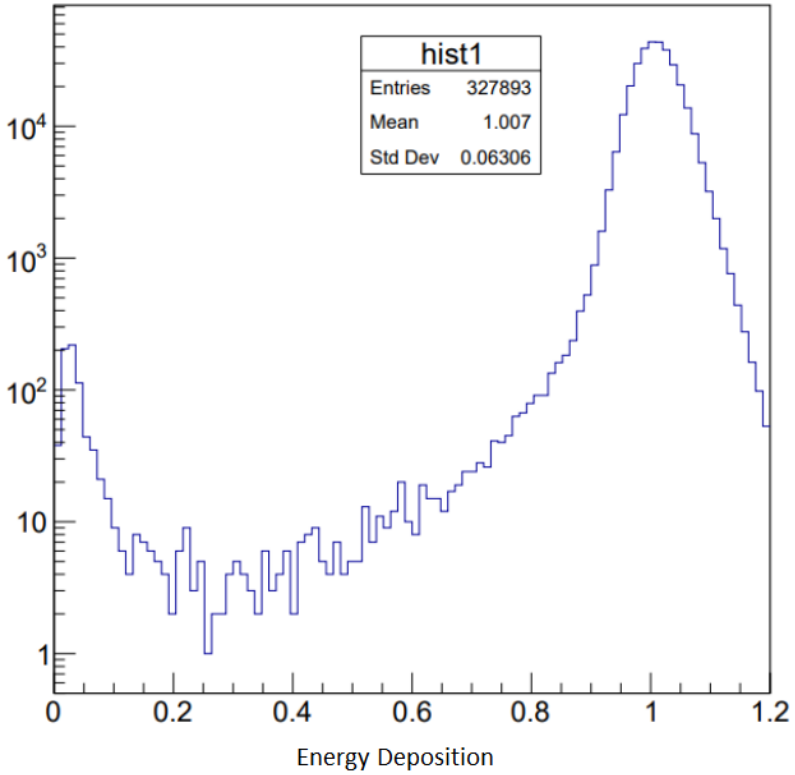


**Figure 4.13:** Distribution of momentum normalized energy deposition. Here, events are associated with greater twenty photo-electrons in the Cerenkov gas detector, i.e., electrons – even still, there are events with zero energy.

First, it could be possible that events are being re-scattered by the dipole and finding their way into the calorimeter. This is addressed by requiring that a track's angle and x-position adhere to the following relation

$$Tr\_th > -0.045 + 0.0025 \cdot Tr\_x \tag{4.12}$$

where, $Tr\_th$ is the theta value of the track and $Tr\_x$ is the x-position of the track.

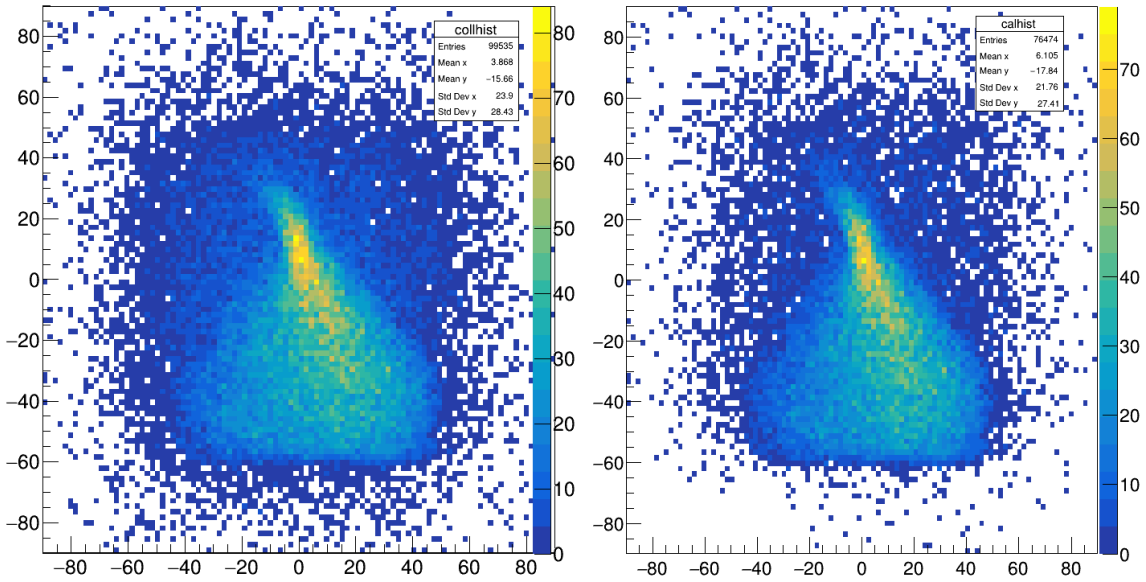


**Figure 4.14:** The effect of adding the "scattcut" condition. A 2D histogram of events at the calorimeter – on the right, no scattering cut is applied, on the left the scattering cut is applied.

In particular for the SHMS, there is an additional concern that events aren't affect by its octagonal collimator. This is confirmed in figure 4.15. As for the scattering condition, the collimator is accounted for through a set of geometric relations on a track's position, angle, and $\delta p$, shown in figure 4.14.

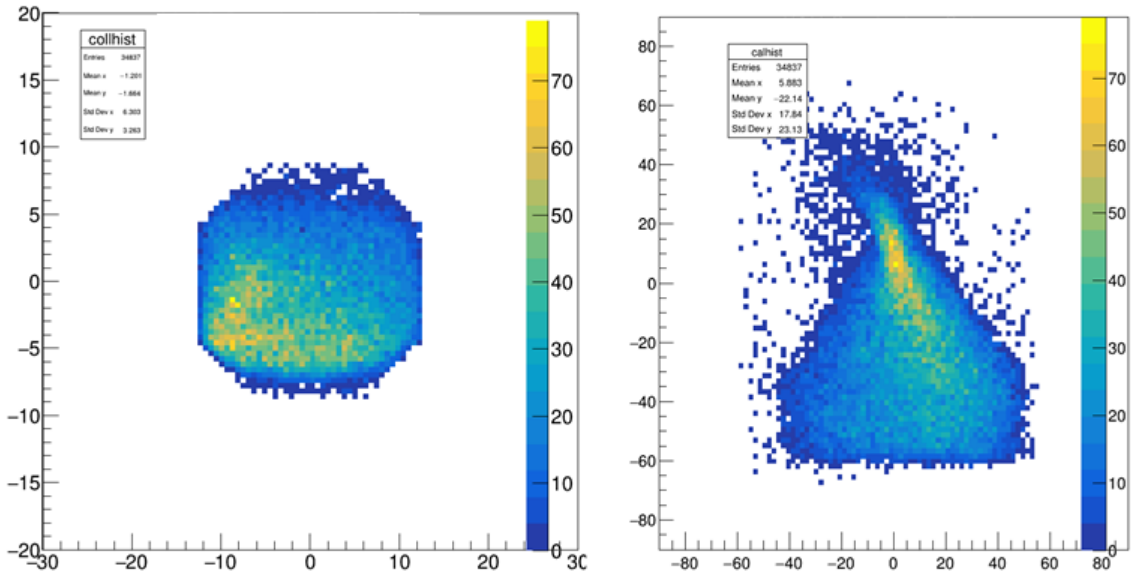


**Figure 4.15:** 2D histogram of events at the collimator demonstrating the collimator condition on the left, and events at the calorimeter with the same collimator condition on the right.

We must also consider the fiducial volume of the calorimeter in order to address the zero energy events. This accounts for the possibility that an electron event hits an edge block with a large angle. For these cases, its possible the event does not deposit all of its energy before it exits the calorimeter. Thus, we apply a fiducial cut such that the edge blocks the calorimeter are not considered, as shown in figure 4.16.

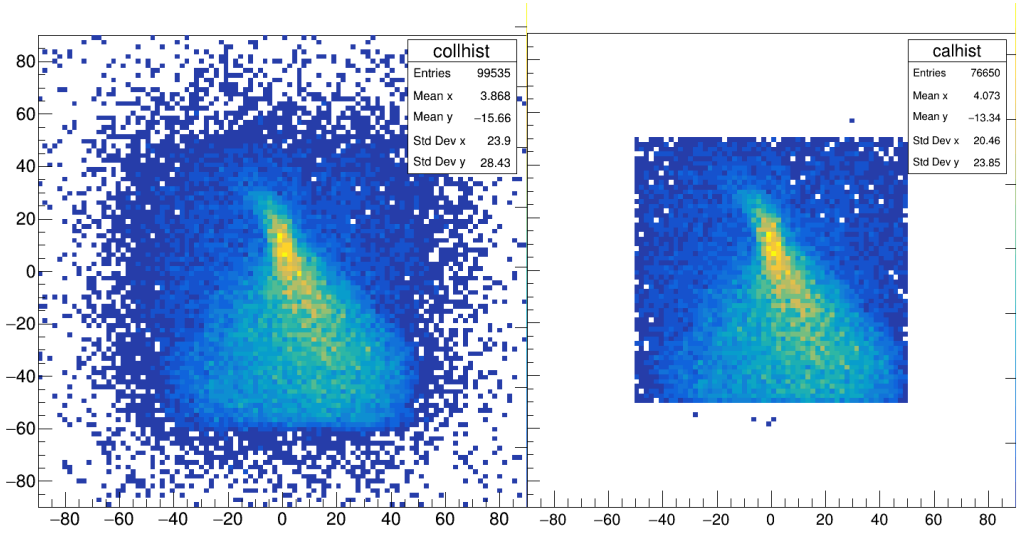


**Figure 4.16:** 2D histogram of events at the calorimeter with and without fiducial cuts applied.

Considering re-scattered events, the SHMS collimator, and the fiducial volume, it is possible to mitigate the zero energy events in the calorimeter, however, it cannot remove them entirely. During this study, it was found that the zero energy events have a peculiar ADC/TDC time behavior. Each PMT in the calorimeters has an associated time window within which events are considered; events that sit outside of this time window do not contribute to the summed energy deposition for the associated block. In particular, it was observed that the zero energy events always sit outside of the time window without exception. This suggests the origin of the issue may not be due to unaccounted physics reasons. However, this method of removing the zero energy events is not satisfactory, as it requires placing a condition on the timing distribution of events. As of the writing of this thesis, this issue has yet to be fully resolved. We do not find a dependence on $E'$ for the zero energy events in the calorimeter, demonstrated by figure 4.17.

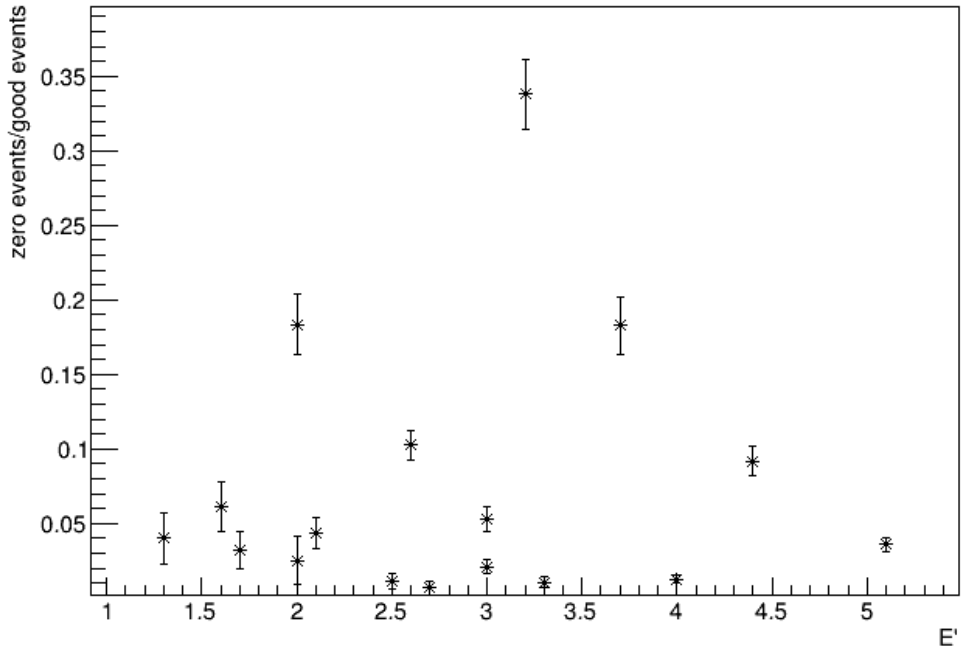


**Figure 4.17:** The ratio of zero energy events in the calorimeter over good events as a function of the final event energy $E'$.

### 4.2.2 Drift Chamber Calibration

As previously stated, the drift chambers serves to reconstruct event tracks for the spectrometers. Briefly, they consist of six planes of wires within a cavity of ionizing gas, namely, $C_4F_8O$. As the electron beam passes through the drift chamber, the gas is ionized. The ions are then attracted to the sensing wires that make up the planes within the drift chamber. In fact, it is TDC values that are output to the preamplifier and discriminator. These time values are used to determine the drift distance, but first it must be ensured that each event, all six planes of the drift chambers agree on the so-called "$t\_zero$" TDC value; this is essentially the start time of the event. The calibration code for the drift chamber serves to mainly to offset the timing distribution of each plane relative to each other so that the drift distance can be correctly calculated.

Calibration first begins by setting the time distribution of each plane to be zero. This constitutes an uncorrected timing distribution for the planes, shown in figure 4.18.

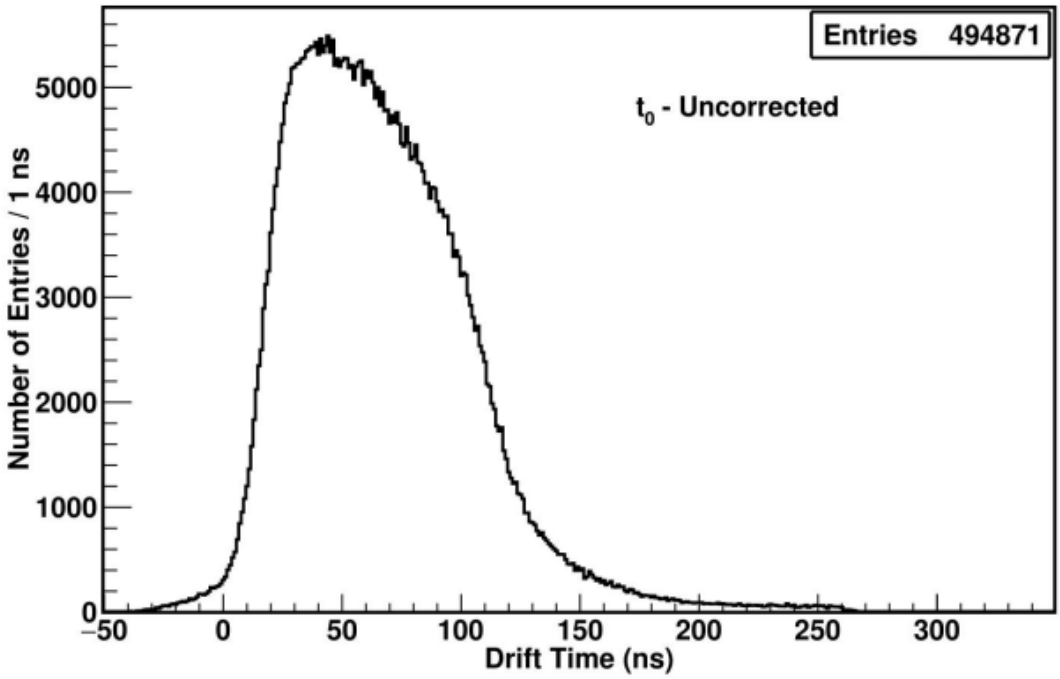


**Figure 4.18:** Uncorrected timing distribution of the V' plane in the drift chamber.

Next, the timing distribution is fitted over a bin range for which the bin content of the range is equal to 20% of the maximum bin content of the distribution. This portion of the distribution is fitted linearly and the x-intercept of the resulting fit is set as the new $t_0$. This procedure is done for all of the sensing wires for each of the planes in the two drift chambers for the spectrometers. For each plane, a weighted average is calculated from each of the wires in the plane, and the plane inherits the weighted $t_0$ offset. The corrected timing distribution is shown in figure 4.19

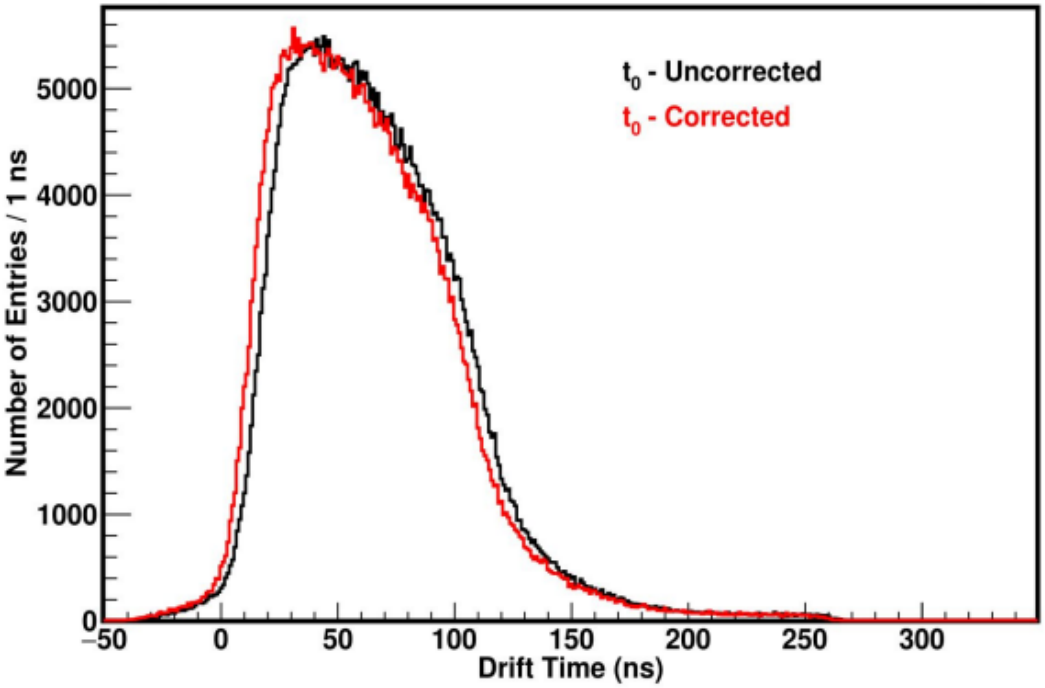


**Figure 4.19:** Corrected timing distribution of the V' plane in the drift chamber.

Finally, using the $t_0$ offset for each plane, a lookup table is created for each wire in the plane. It is here that the drift time TDC values are converted into drift distances that are used to reconstruct event tracks. The calibration can be checked by plotting the distribution of drift distance for a given plane. If the calibration was successful, the drift distance distribution is relatively flat, as is characteristic of a drift chamber of this design. An example of such a drift distance is presented in figure 4.20.

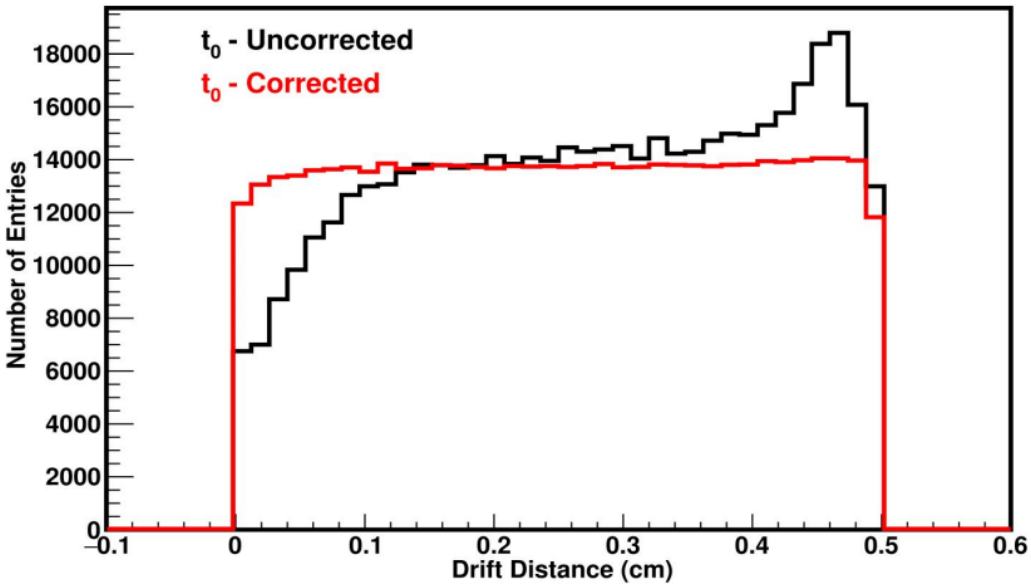


**Figure 4.20:** Comparison between corrected and uncorrected $t_0$ offset of the drift distance distribution for a given plane.

As with the calorimeter calibration, we must check that the drift distance distribution is well calibrated over the entire experimental run. To this end, a useful value is the ratio of the minimum to maximum bin content of the drift distance distribution. If the distribution is sufficiently flat, this ratio should be close to one. Also, it is necessary the timing distributions – this is done by plotting the residuals of these distributions for runs across the entire experimental run. The results are shown in figure 4.21 and 4.22.

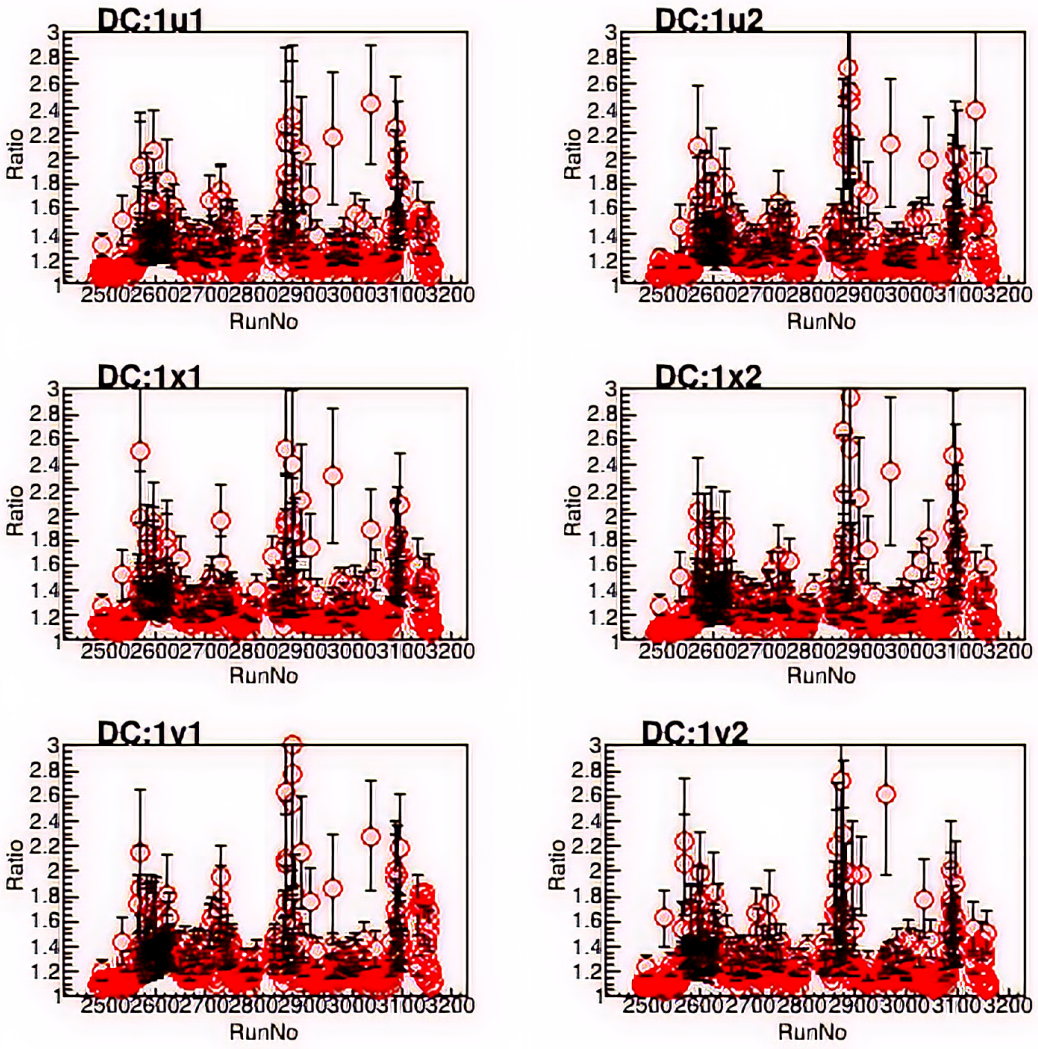


**Figure 4.21:** Result of drift chamber calibration over experimental run. Plotted is the ratio of the minimum to maximum bin content of the the drift distance distribution as a function of run number.

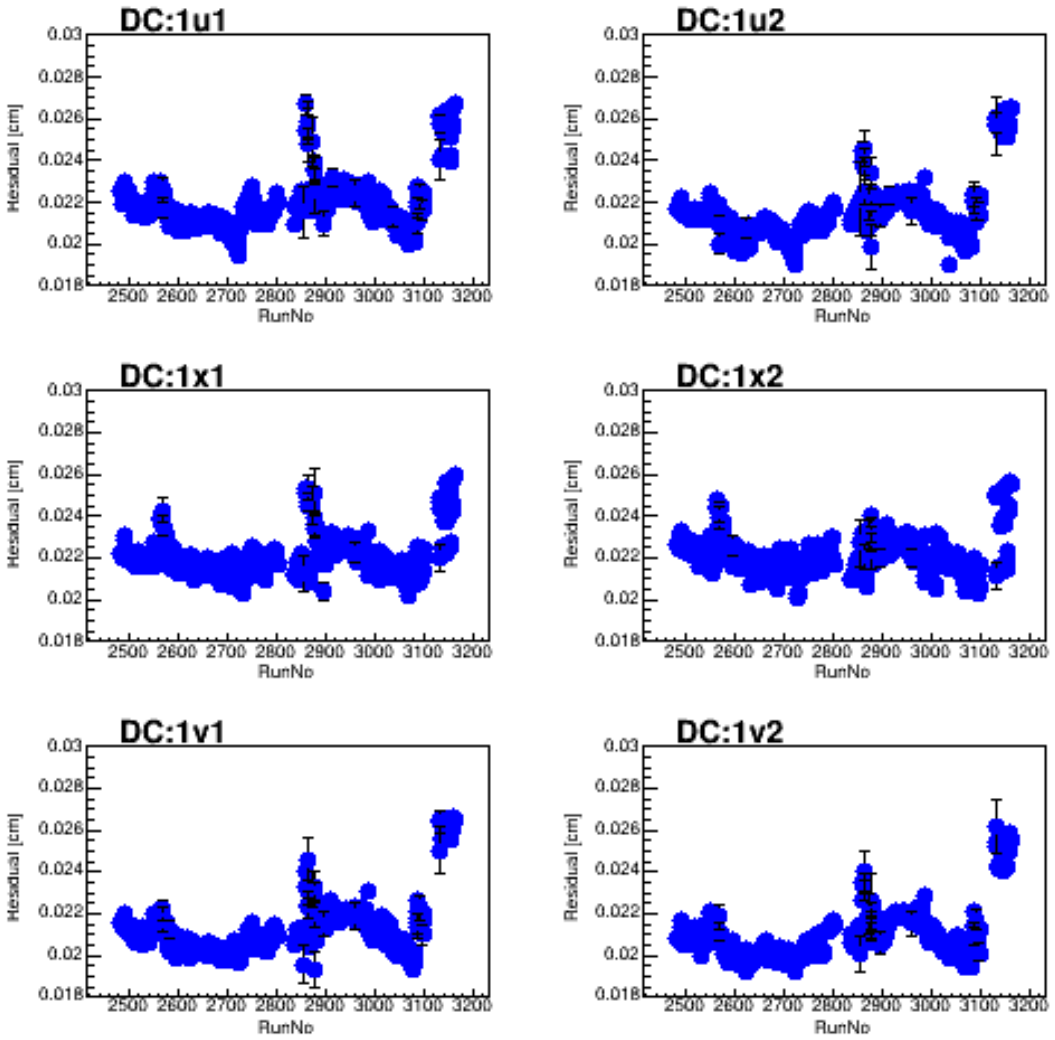


**Figure 4.22:** Plot of residuals of timing distribution as a function of run number.

### 4.2.3 Hodoscope Calibration

As mentioned previously, the hodoscope is used to create the triggers for the DAQ system. As the electron beam travels through the scintillating material of the hodoscope photons are produced and measured as TDC time values when the signal crosses a voltage threshold as determined by discriminators. Because the hodoscope determines the timing and triggers for the rest of the detectors in the detector package, it is absolutely necessary that any systematics be accounted for in the TDC value recorded. Indeed, there are four sources of systematic error that must be addressed to extract the true time values. The corrected time value is given by,

$$t_{corr} = t_{uncorr} - t_{TW} - t_{cable} - t_{prop} - t_{\lambda} \tag{4.13}$$

However, the use of leading edge discriminator introduces a time shift in the measured signals, referred to as a "timewalk" effect, shown in figure 4.23.

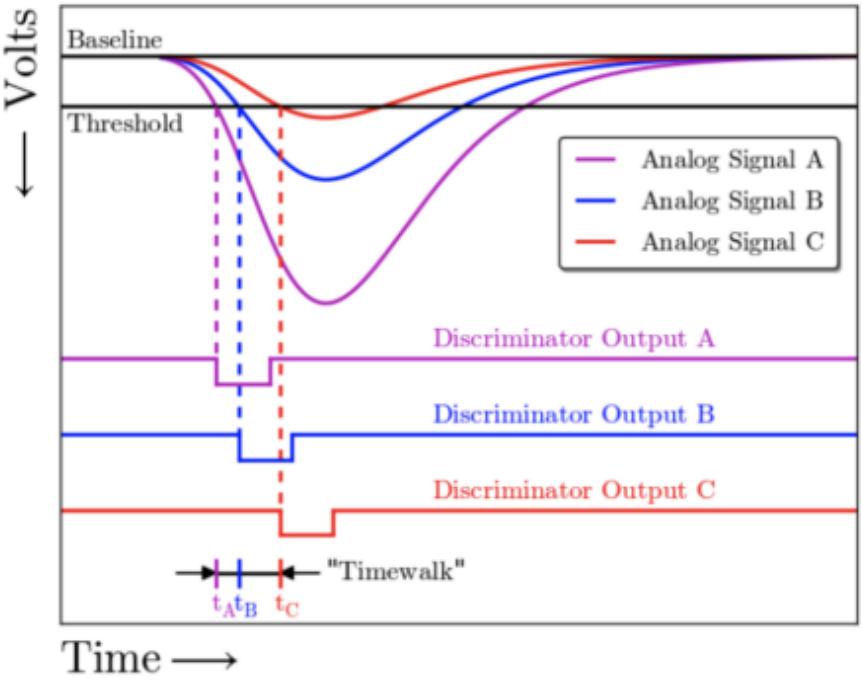


**Figure 4.23:** Figure demonstrating the timewalk effect introduced by leading edge discriminators.

The scintillation photon signal must be carried from the PMT to the TDC discriminator via a cable, which takes a non-negligible amount of time. This systematic, $t_{cable}$, amounts to an offset of a few hundred nanoseconds. The value $t_{prop}$ simply refers to the amount of time it takes for the scintillation photons to reach the PMT after they are produced. And finally, the $t_{\lambda}$ term accounts for the time difference between two hodoscope planes as event passes through them. These corrections are determined by the hodoscope calibration code, and from the time information of events, the velocity of a particle can be calculated. As we are primarily interested in electron events, the value $\beta = \frac{v}{c}$ should be close to one, as shown in figure 4.24.

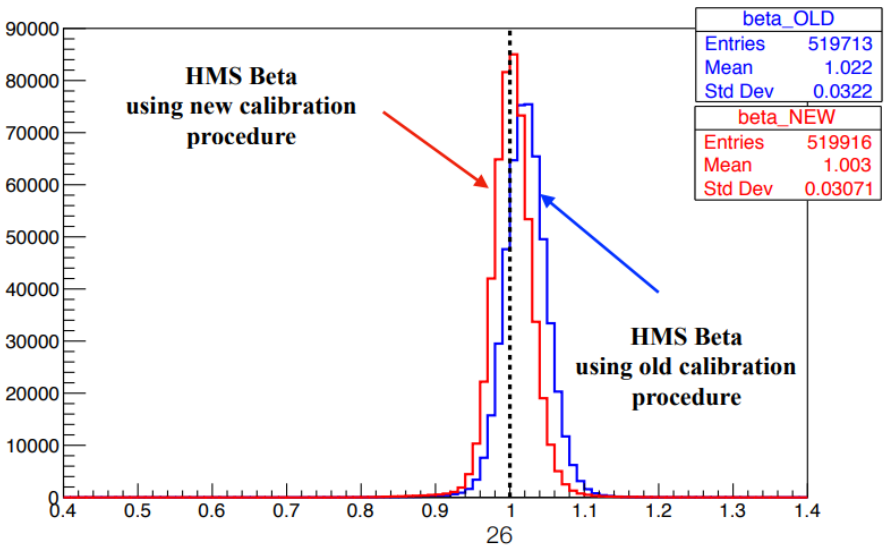


**Figure 4.24:** $\beta$ distribution comparing a calibration accounting for the timewalk effect, and one without.

This value is used to sanity check the calibrations over the experimental run, and the results are presented in figure 4.25.

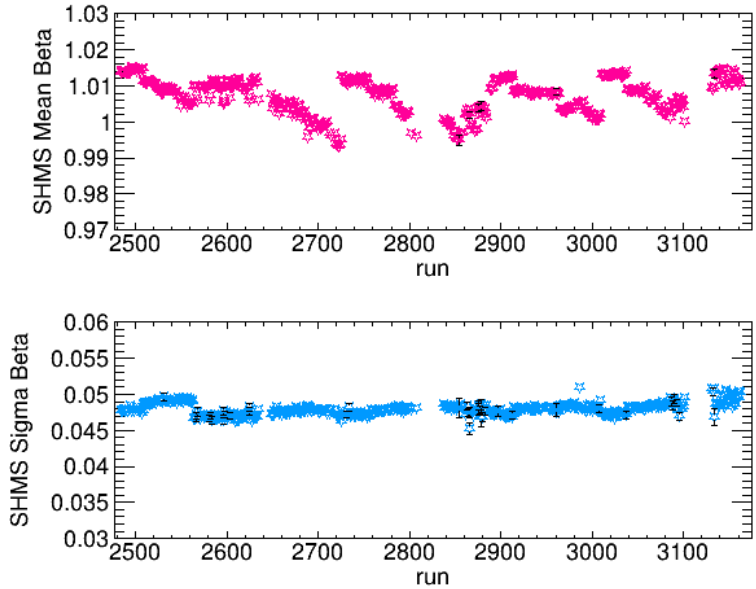


**Figure 4.25:** Plot of the peak mean and sigma value of the beta distribution for runs over the entire experimental run. Image: Simona Malace.

### 4.2.4 Cerenkov Detector Calibration

The Cerenkov detector is used to identify and separate pion and electron events. The design of the gas Cerenkov detector differ between the SHMS and HMS spectrometers, but their function and operation is identical. The separation between pion and electron events is achieved by considering the number of photo-electrons produced in the Cerenkov detector and subsequently measured by its PMTs; electrons will produce more photo-electrons than pions. However, the raw ADC signal measured by the PMTs must first be understood and properly calibrated before it can be interpreted as photo-electrons. This requires that one determine the minimum ADC signal and the crosses the voltage threshold; indeed, this should correspond to the magnitude of the signal for one photo-electron. Because the amplitude of the ADC signal is proportional to the number of photo-electron, we can use this conversion factor to scale the ADC amplitude distribution, shown in figure 4.26, to convert it to a distribution of number of photo-electrons.

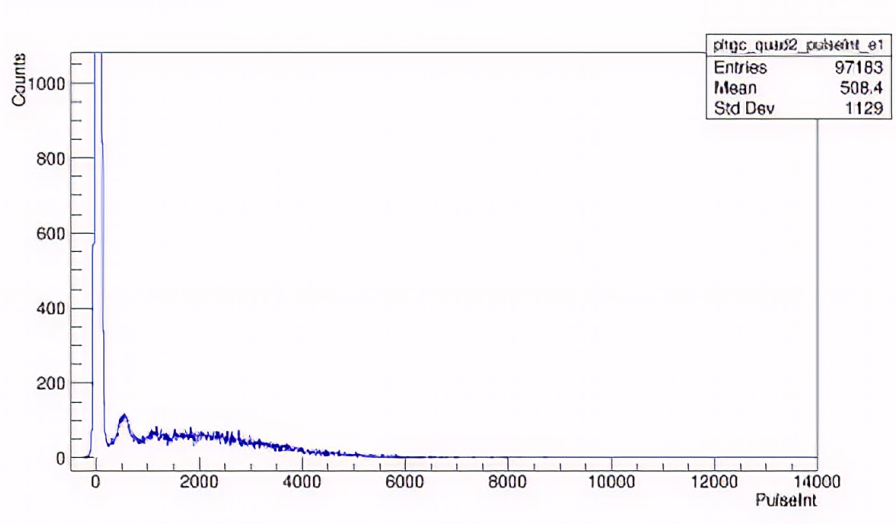


**Figure 4.26:** Raw ADC signal of a Cerenkov detector PMT. The one, two, and three photo-electron peak are somewhat visible.

The raw signal can be cleaned up by removing the Poisson background in the signal. This is shown in figure 4.27.

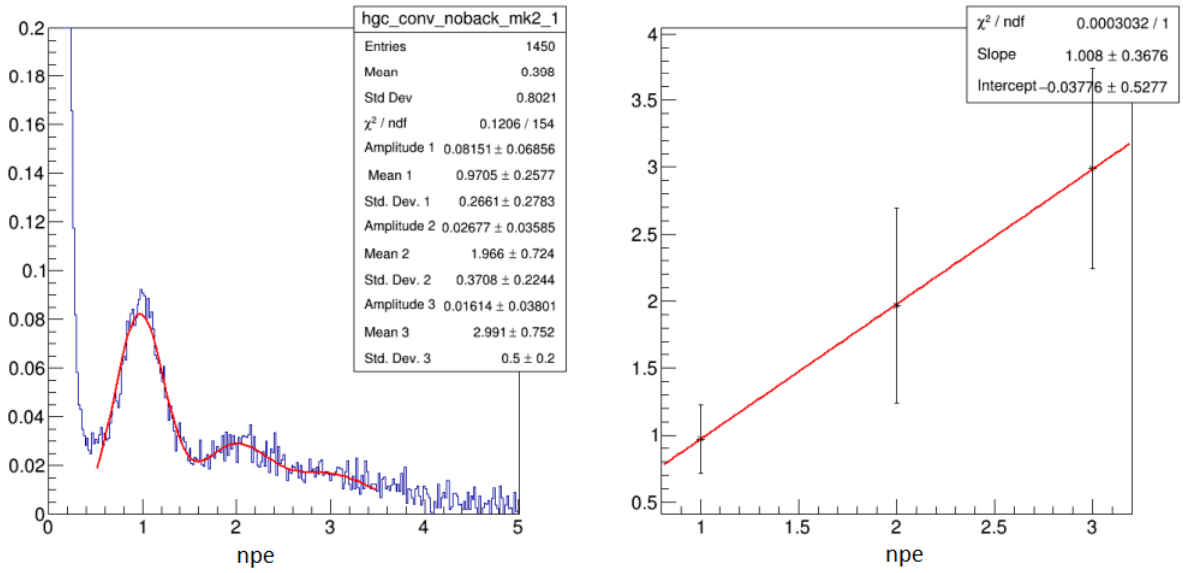


**Figure 4.27:** Cleaned signal distribution with number of photo-electrons (npe) on the $x$-axis, showing the one, two, and three photo-electron peak. The calibration is verified by fitting the mean of the peaks versus number of photo-electrons.

Typically, the Cerenkov detector does not need to be calibrated per kinematic setting. It suffices to calibrate the detector before the experimental run.

### 4.2.5 Beam Current Monitor Calibration

The beam current monitors are responsible for determining the current placed on the target, from which the charge on the target can be calculated by integrating the current over the time. As mentioned in the previous section about the unser and BCMs, while the unser has a fixed gain, its reading can drift over short periods of time. On the other hand, while BCMs typically do not experience a drift offsets, their gain can change over time. For this reason, one usually takes dedicated current calibration runs throughout the run of the experiment. The unser and BCMs are used in conjunction to extract the necessary BCM parameters in order calculate the current and charge on the target. In particular, the unser is used to subtract the gain bias from the BCMs. The BCM response is then plotted as a function of the unser current and a linear fit is applied. The slope of this fit corresponds to the gain of the BCMs.

For the E12-10-002 experiment, it was deemed sufficient to take only one current calibration run. However, it was found that there was a significant systematic shift in response of BCM4A and BCM4B over the course of the experimental run. For this reason, it was necessary to divide the experimental run into six regions, where a "local" calibration could be derived from a chosen run within each region, demonstrated in figure 4.28.

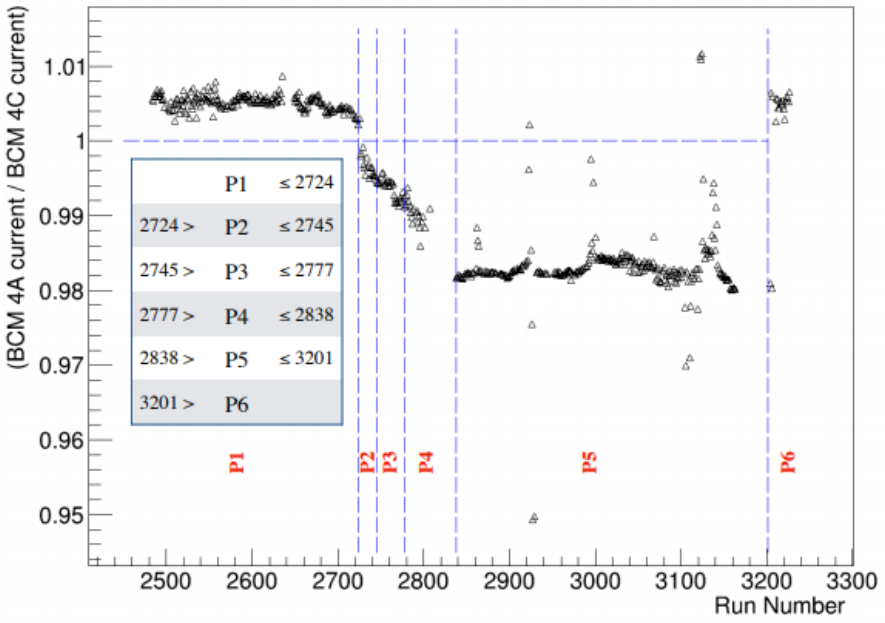


**Figure 4.28:** The experimental run is divided into six periods that will be individually calibrated.

In this way, it was possible to extract consistent gain and offset values for the required BCMs, shown in tables 4.1 and 4.2.

| BCM4A | Gain | ΔGain | Offset | ΔOffset |
|---|---|---|---|---|
| P1 | 13000.0 | 111.1 | 2528 | 4025 |
| P2 | 13370.0 | 310.5 | -20940 | 16290 |
| P3 | 12930.0 | 125.1 | -48.96 | 5424 |
| P4 | 12770 | 189.8 | 10210 | 10120 |
| P5 | 13210 | 277 | -2481 | 13070 |
| P6 | 13150 | 262.2 | -2974 | 13810 |

**Table 4.1:** Parameters for BCM4A.

| BCM4C | Gain | ΔGain | Offset | ΔOffset |
|---|---|---|---|---|
| P1 | 6182 | 54.8 | 1504 | 1941 |
| P2 | 6388 | 153.1 | -823.6 | 8047 |
| P3 | 6222 | 62.52 | 499.8 | 2696 |
| P4 | 6145 | 95.02 | 7451 | 5054 |
| P5 | 6435 | 134.9 | -1078 | 6364 |
| P6 | 6248 | 124.5 | -765.7 | 6540 |

**Table 4.2:** Parameters for BCM4C.

## 4.3 PID Cut Efficiency

A large part of the experimental analysis depends on characterizing the particle identification detectors. Indeed, the particle identification detectors are essential in separating background events, typically pions for E12-10-002, from electron events. However, one must consider the possibility that an electron event is cut out along with the background events. This amounts to the so-called "cut efficiency" of the detector. Ultimately, these efficiencies must be folded into the cross sections. The procedure for the determination of the calorimeter and Cerenkov detector will be discussed briefly and results presented.

### 4.3.1 Calorimeter

The general procedure used to calculate the cut efficiency for the calorimeter first necessitates creating a clean electron sample. It is important that we create a clean sample of electrons because we want to know how likely it is that an electron event will be removed by placing a calorimeter cut on the selected sample. Thus, we must be sure the events we have selected are indeed electrons. However, several methods by which a clean sample is chosen may be employed. During this study, we compared three such methods.

Because it is necessary to remove as many background events from the clean sample as possible, the first method involves a pion to electron ratio extrapolation. First, a cut

efficiency is calculated for several target types. This is because different target types will have different characteristic pi:e ratios. Then, these efficiencies are plotted as a function of pi:e ratio, and the efficiency is extrapolated to zero pi:e ration. In this way we hope to remove as many pion contaminating events in our clean sample. Finally, the extrapolated efficiency is plotted as a function of $E'$. The first efficiency calculation is done by requiring selected events have a large number of photo-electrons associated with the gas Cerenkov detector, as well as making sure events are within the $\delta p$ acceptance of the spectrometer.

$$\epsilon = \frac{ELLO > 100\&\&ngcer > 20\&\& -10 < \delta p < 22\&\&etottracknorm.7}{ELLO > 100\&\&ngcer > 20\&\& -10 < \delta p < 22} \tag{4.14}$$

A visual example of these cuts is presented in figure 4.29, where the red distribution corresponds to the denominator and the blue distribution corresponds to the numerator. Here, "ELLO" corresponds to a specific event triggers that does not use any calorimeter information; we need to use a trigger that does not bias the calorimeter cut efficiency calculation. The "ngcer" condition corresponds to the number of photo-electrons in the noble gas Cerenkov detector, and "etottracknorm" is the momentum normalized energy deposition in the calorimeter. The efficiency contains an explicit calorimeter cut in the numerator, so the denominator corresponds to our clean electron sample. If any electron events are removed from the numerator cut conditions they will be reflected in the efficiency.

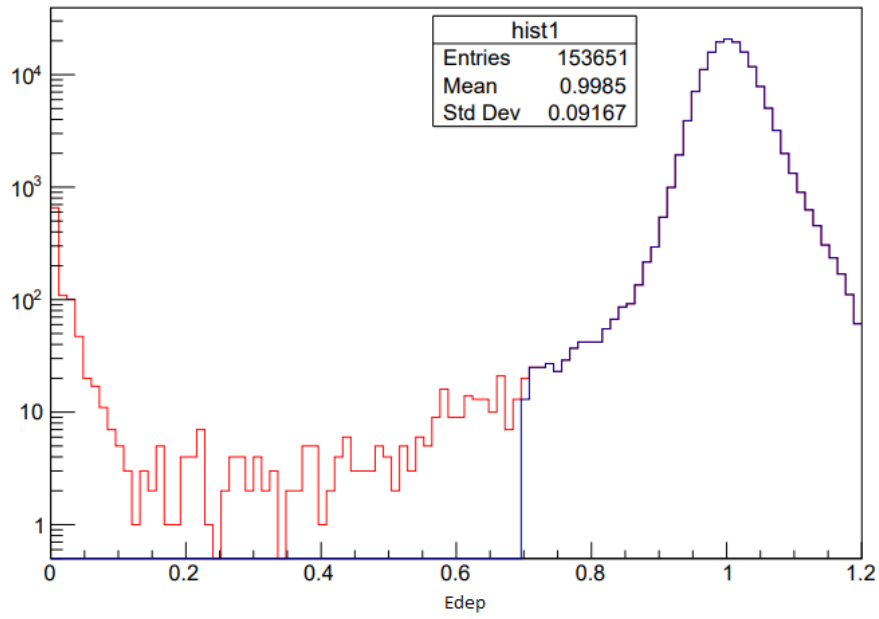


**Figure 4.29:** Plot demonstrating the initial calorimeter cut efficiency. The blue distribution corresponds to the numerator in the efficiency calculation and the red distribution corresponds to the denominator.

As mentioned, this procedure is carried out for a variety of target types, and the efficiency is plotted as a function of pi:e efficiency, as shown in figure 4.30.

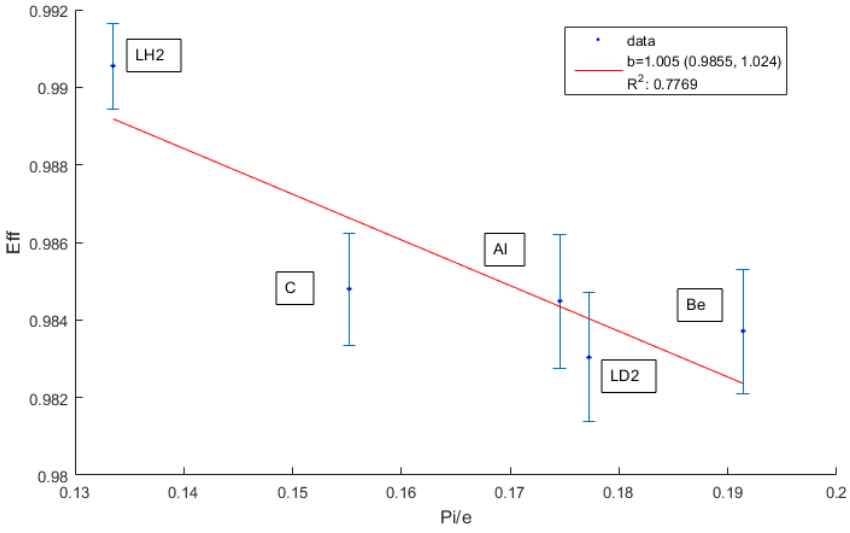


**Figure 4.30:** Plot of calculated efficiency as a function of pi:e ratio for different target types, at $5GeV$. The efficiency is extrapolated to zero pi:e ratio.

This method appeared to work reasonably well for most values of $E'$, however, it was

found that for certain values, the pi:e extrapolation introduced possible systematics that drastically changed the efficiency values.

Another method to ensure to the removal of background events is to place an explicitly calorimeter cut in the denominator. This efficiency is calculated as follows,

$$\epsilon = \frac{ELLO > 100\&ngcer > 20\& - 10 < \delta p < 22\&etottracknorm.7}{ELLO > 100\&ngcer > 20\& - 10 < \delta p < 22\&(etottracknorm > .2 \wedge etottracknorm > .5)} \tag{4.15}$$

The additional condition in the denominator serves to remove events at low $E_{dep}$; as explained before, this corresponds primarily to pion events. Two cuts are chosen – greater than 0.2 and greater than 0.5. Ultimately, the average of the resulting two efficiency calculations is taken, and this average is the final efficiency. Thus, we do not take a pi:e ratio extrapolation.

The third method for creating a clean electron sample involved including a calorimeter time distribution cut. As mentioned in the calorimeter calibration section, it was found that there were an abnormal amount of events at low and zero energy in the calorimeter. These events could be removed by placing a cut on the ADC/TDC timing distribution of events in the calorimeter, but this procedure was hard to justify from physics principles. Nevertheless, these issues at zero energy continued in the analysis of the calorimeter cut efficiency, and so such a timing cut was explored in this context. This efficiency is expressed as,

$$\epsilon = \frac{AdcTdc! = kBig\&ELLO > 100\&\&ngcer > 20\&\& - 10 < \delta p < 22\&\&etottracknorm > .7}{AdcTdc! = kBig\&ELLO > 100\&\&ngcer > 20\&\& - 10 < \delta p < 22} \tag{4.16}$$

where "kBig" is simply a value in HCANA corresponding to the numerical value $10e + 38$.

The three methods for calculating the calorimeter cut efficiencies are shown in figure

4.31.

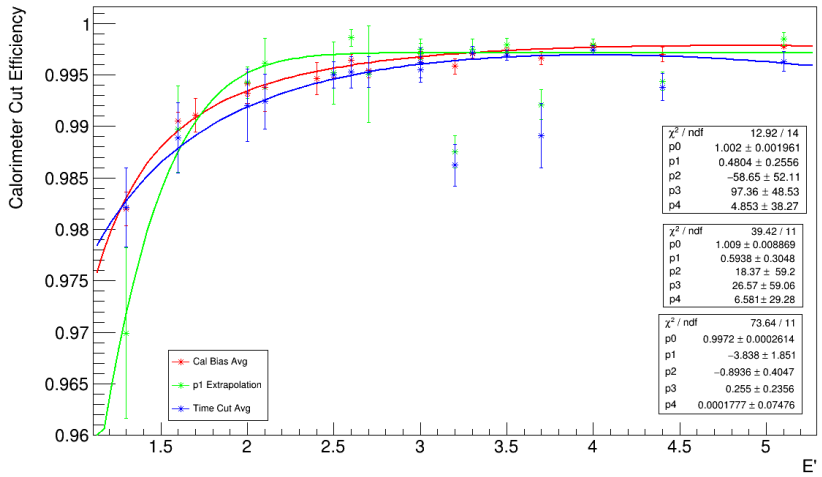


**Figure 4.31:** Comparison between the three methods for the calculation of the calorimeter cut efficiency.

We find that the second method, the calorimeter bias method, provides the best fit for the cut efficiency as a function of $E'$. Thus, the final fit is presented in figure 4.32.

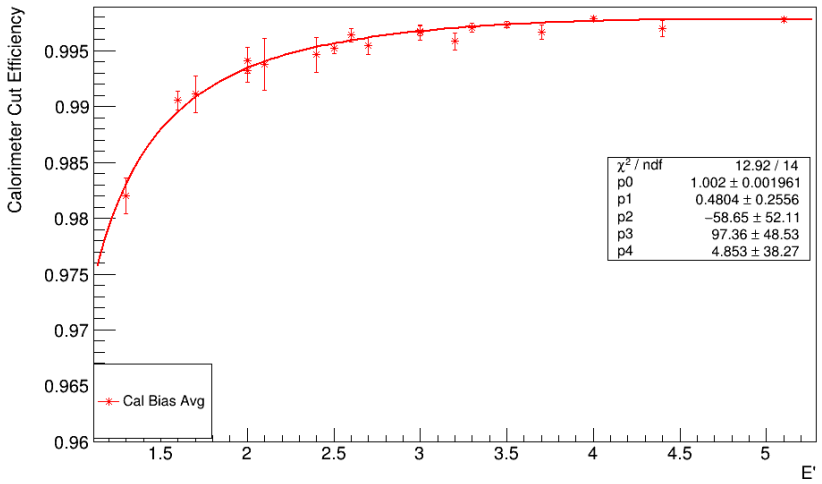


**Figure 4.32:** The final calorimeter cut efficiency as a function of $E'$.

### 4.3.2 Cerenkov Detector

Similar to the calorimeter detector, we must account for the fact that using the gas Cerenkov detector to select electron events carries with it the possibility that we may accidentally be cutting out electrons with abnormally low associated number of photo-electrons. Likewise, the method employed to calculate the cut efficiency rests on the condition that the starting sample of events is as clean as possible; that is, electron events with minimal pion contamination. To this end, pi:e ratio extrapolation is also used. In particular, for the Cerenkov detector, four different methods for extrapolation are carried out. To begin, the Cerenkov cut efficiency is calculated as,

$$\epsilon = \frac{ELHI > 100\&-10 < \delta p < 22\&etottracknorm > 1.0\&eprtracknorm > 0.3\&ngcer > 2}{ELHI > 100\&-10 < \delta p < 22\&etottracknorm > 1.0\&eprtracknorm > 0.3} \tag{4.17}$$

where "ELHI" is an event trigger that does not use the Cerenkov detector, and "eprtracknorm" is the momentum normalized energy deposition in the preshower. As before, the cuts in the denominator are supposed to serve as the clean electron sample. The numerator uses the same set of cuts, but adds an additional cut on the gas Cerenkov detector. Thus, the efficiency is sensitive to the accidental removal of electrons by the detector. Both methods to be discussed use a pi:e extrapolation to find the efficiency at zero pi:e ratio. The first method calculates the pi:e ratio using only the Cerenkov detector. A pion distribution is created by requiring that the number of photo-electrons associated with the events is zero. An electron distribution is created by requiring that the number of photo-electron events is greater than 21. The ratio of the number of these distributions is the pi:e ratio. As with the calorimeter, we calculate the efficiency and pi:e ratio for different target types and plot the relationship, shown in figure 4.33.

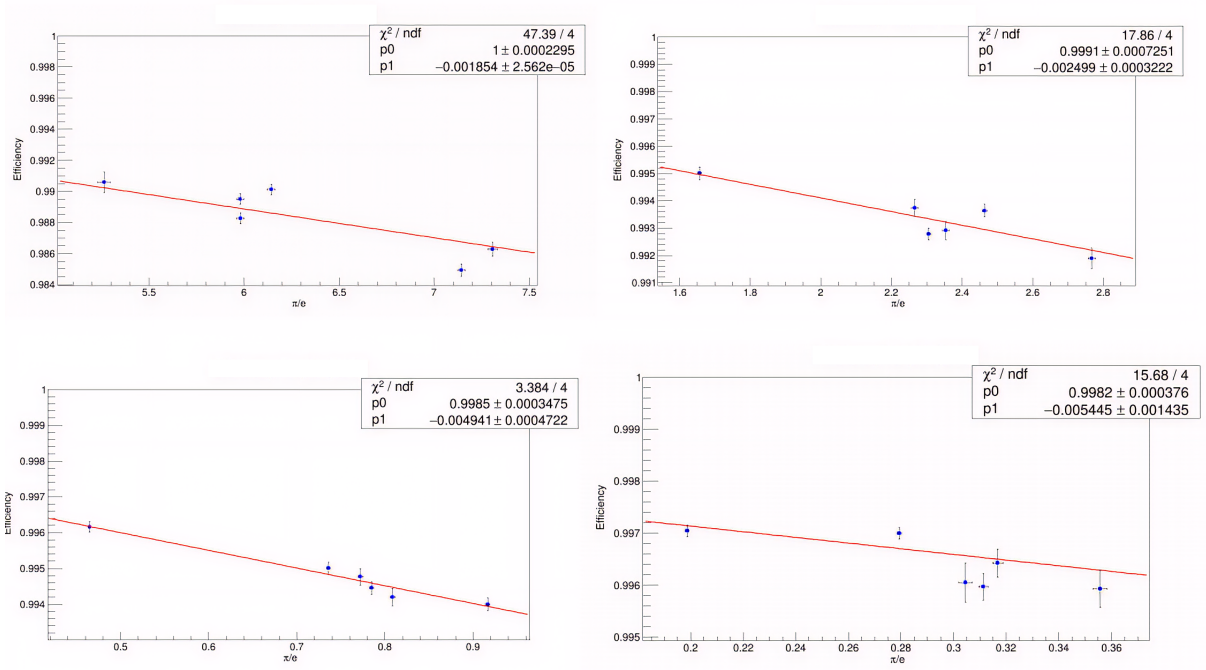


**Figure 4.33:** Calculated efficiency as a function of pi:e ratio. The function is extrapolated to zero pi:e ratio, and the extrapolated efficiency is determined.

For the second method, the pi:e ratio is calculated using only the calorimeter. Here, pions are selected by requiring $etottracknorm < 1.0 \& eprtracknorm < 0.3$, and electrons are selected by requiring $etottracknorm > 1.0 \& eprtracknorm > 0.3$. Likewise, the efficiency and pi:e ratio are calculated and plotted in figure 4.34.

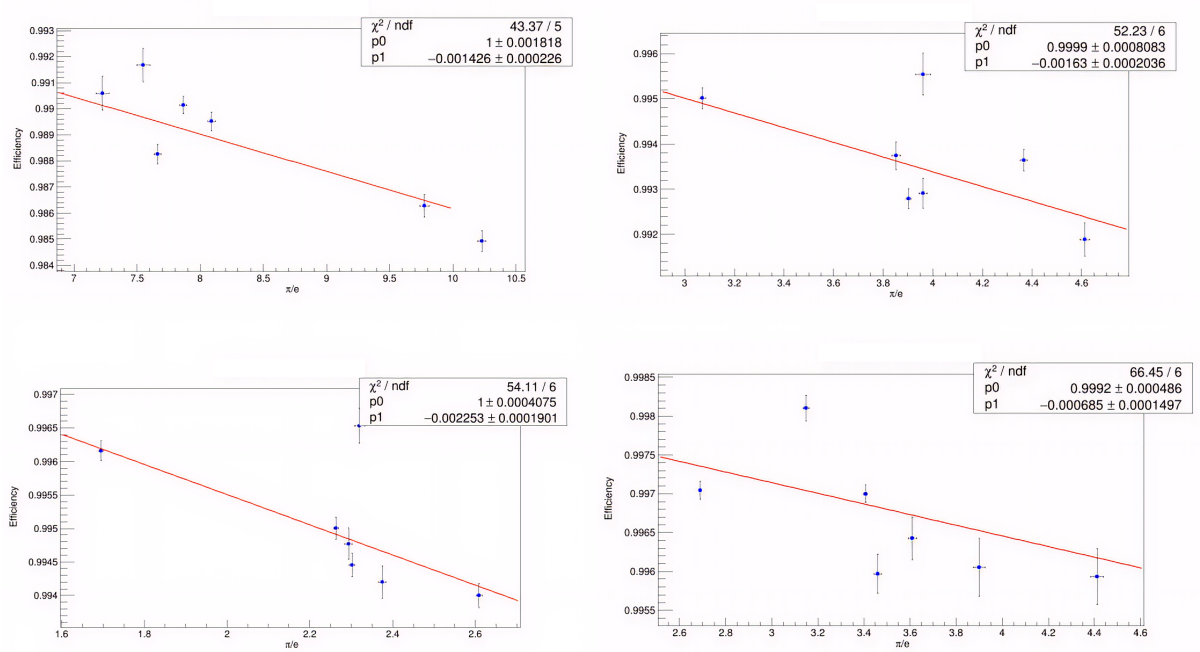


**Figure 4.34:** Calculated efficiency as a function of pi:e ratio. The function is extrapolated to zero pi:e ratio, and the extrapolated efficiency is determined.

For the third method, both the calorimeter and Cerenkov detectors are used in order to calculate the pi:e ratio. The results are presented in figure 4.35

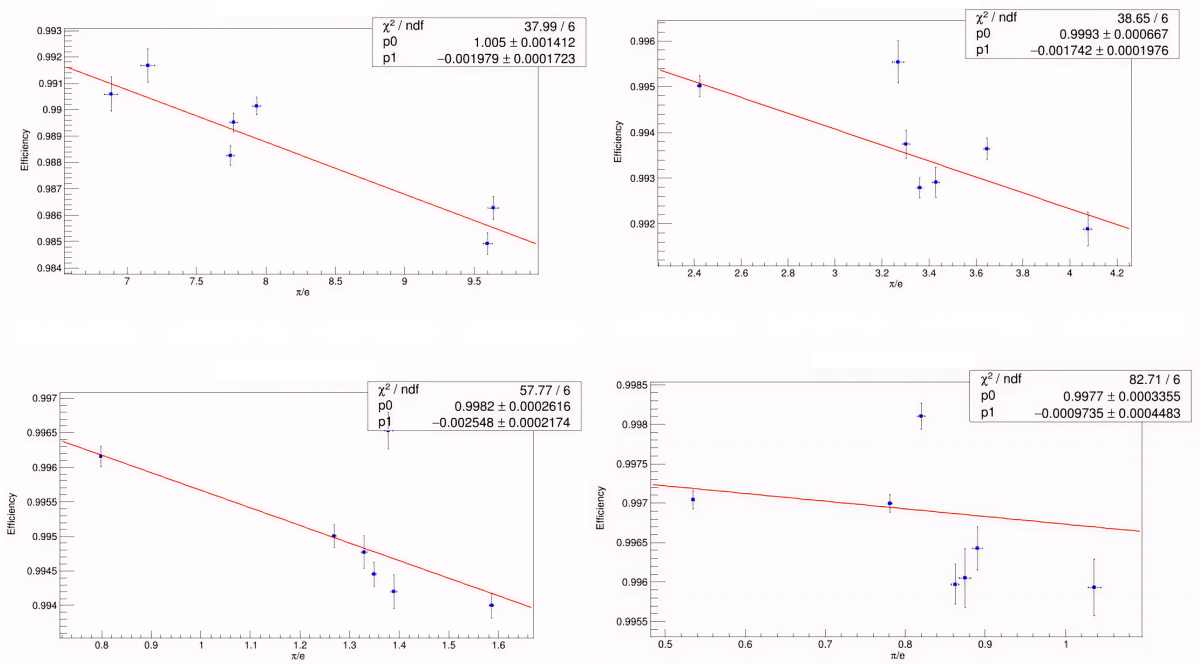


**Figure 4.35:** Calculated efficiency as a function of pi:e ratio. The function is extrapolated to zero pi:e ratio, and the extrapolated efficiency is determined.

A fourth method eschews the pi:e ratio extrapolation, as extrapolated efficiencies carry the same issues encountered with the calorimeter. The fourth method instead employs a pion contamination analysis in order to subtract pion events from the clean electron sample. As of the writing of this thesis, the preferred method has yet to be determined.

In addition to characterizing the Cerenkov efficiencies as a function of $E'$, it is also necessary to characterize the efficiencies as a function the x-position at the Cerenkov detector itself. This is due to the known, systematic effect of the design of the Cerenkov detector having a gap between its mirrors. At these gaps, photo-electrons are not recorded, and therefore the efficiencies are systematically lowered, shown in figure 4.36. Figure 4.37 demonstrates the effect for correcting the efficiency due to the gaps.

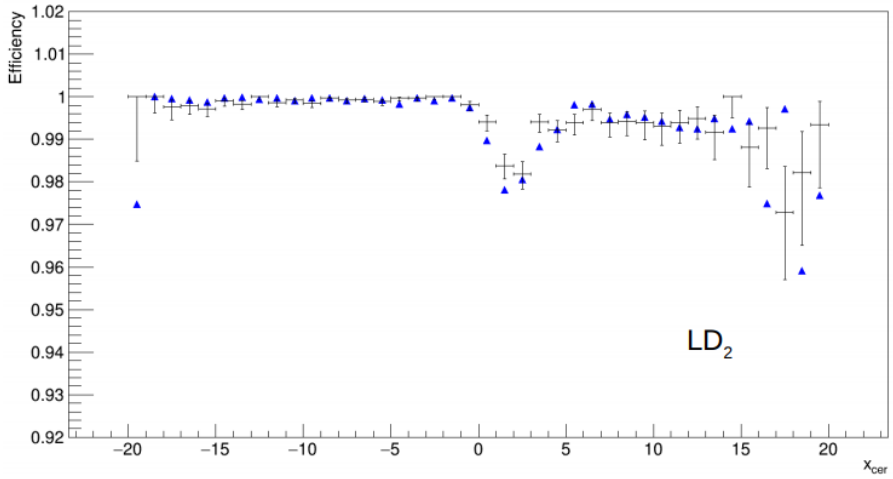


**Figure 4.36:** Efficiency as a function of the x-position at the Cerenkov detector. The characteristic dip around x=0 indicates the gap in the mirrors in the Cerenkov detector.

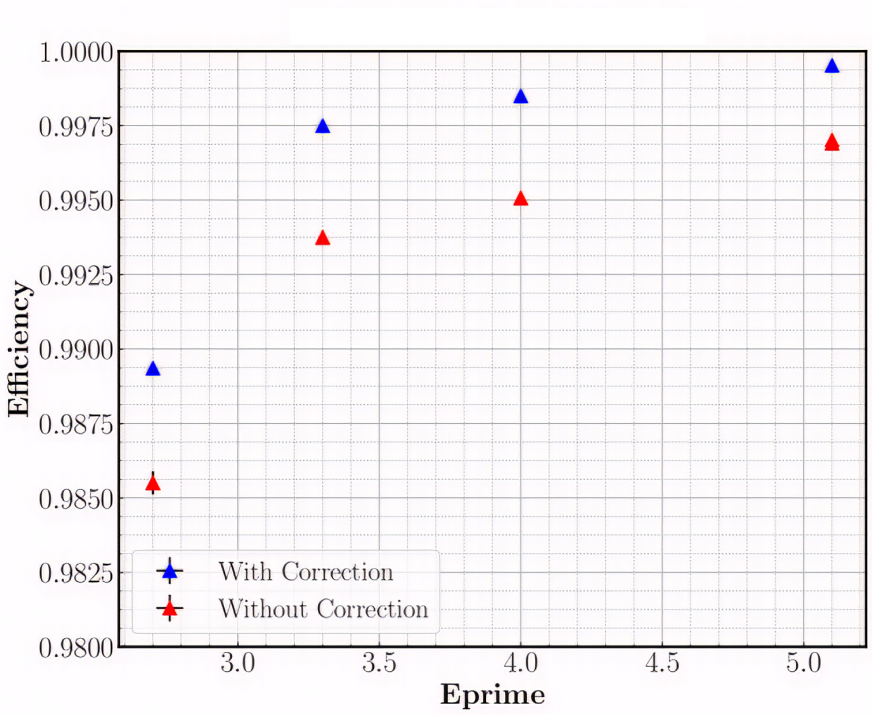


**Figure 4.37:** Efficiency as a function of $E'$, one set with the x-dependence accounted for and one without.

It should be mentioned that one additional step in the Cerenkov cut efficiency must be accounted for in the HMS Cerenkov detector. As mentioned in an earlier section, the bottom left mirror in the HMS Cerenkov detector sustained damage and was broken. This was discovered after the experimental run of E12-10-002, thus, it is believed and corroborated through analysis that the mirror was broken throughout the experiment. This can be seen in figure 4.38, where we can see a decrease in the efficiency at the lower-left corner of the Cerenkov detector. It is planned to account for this systematic by dividing the face of the Cerenkov detector into bins and to calculate the efficiency for each bin for each kinematic setting. In this way, a lookup table can be created and the efficiencies may be corrected for each individual bin. This study is still ongoing.

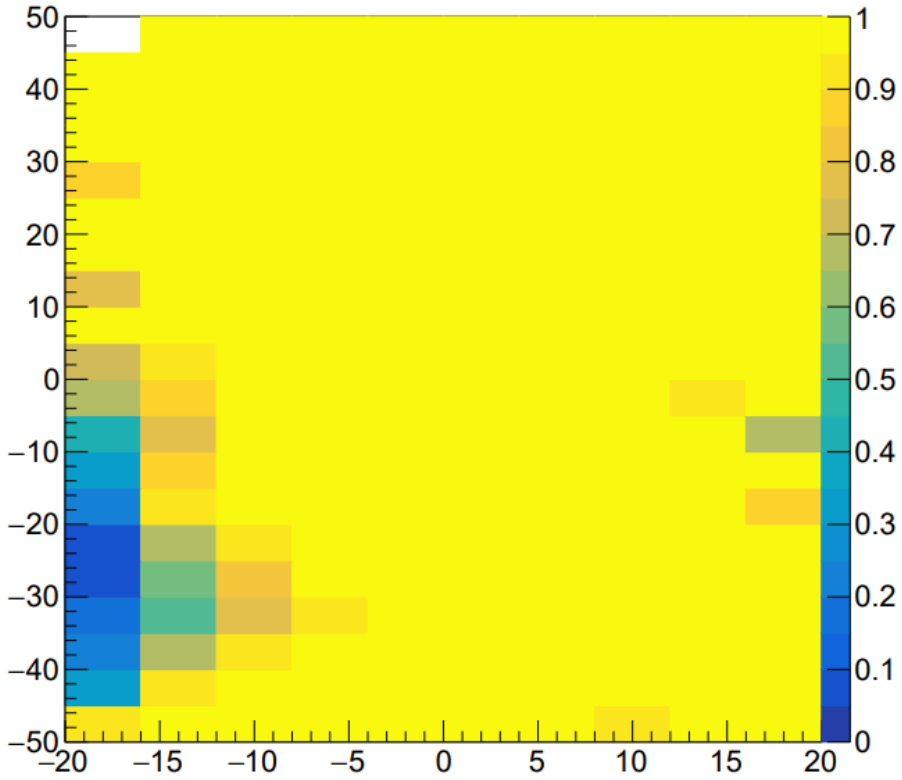


**Figure 4.38:** Efficiency at each bin at the face of the Cerenkov detector at $E' = 5.1GeV$. The effect of the broken mirror is shown in the lower left bins.

## 4.4 Background Subtractions

In addition to the inefficiencies in the particle identification detectors, measures must also be taken to remove unwanted backgrounds in the final electron yield. These backgrounds can take two forms. First, as mentioned in previous sections, pions constitute a dynamic background for the E12-10-002 experiment; at high $E'$ and smaller scattering angles, the pion background can be relatively small. But at lower energies and higher scattering angles, the pion background is quite significant. Another source of backgrounds are electrons that are not produced from the primary interaction. These electrons can be produced in two ways. The first type of electrons are produced when the electron beam scatters off of the aluminum cryogenic target rather than the liquid hydrogen or deuterium.

The second type of electrons can be produced through either photo-production, $\gamma \rightarrow e^- e^+$, or through neutral pion decay, $\pi^0 \rightarrow 2\gamma \rightarrow e^- e^+$.

### 4.4.1 Target Wall Subtraction

Electron events that were scattered from the walls of the cryogenic target constitute a source of background that must be subtracted from the final electron yield. In order to account for these extra events, so-called "Dummy" runs are taken at every kinematic setting. These Dummy runs use empty aluminum targets. In this way, one can correct for the target scattered electrons by subtracting them from the yield of a cryo-target run. As an example, for an LH2 target, the corrected yield is given by,

$$Y_{Corr} = Y_{LH2} - Y_{Dummy} \frac{T_{Walls}}{T_{Dummy}} \frac{RC_{Dummy}}{RC_{Walls}} \tag{4.18}$$

where $T_{Walls}$ and $T_{Dummy}$ are the target thickness of the cyro-target walls and Dummy target walls respectively, and $RC_{Dummy}$ and $RC_{Walls}$ are the radiative corrections for the Dummy and cryo-target respectively. Typically, this subtraction is done within the Monte Carlo simulation. Focal plane variables $x_{tar}$, $y_{tar}$, $y'_{tar}$, and $\delta p$, are checked against the Monte Carlo results before and after the target wall yield correction, as shown in figure 4.39.

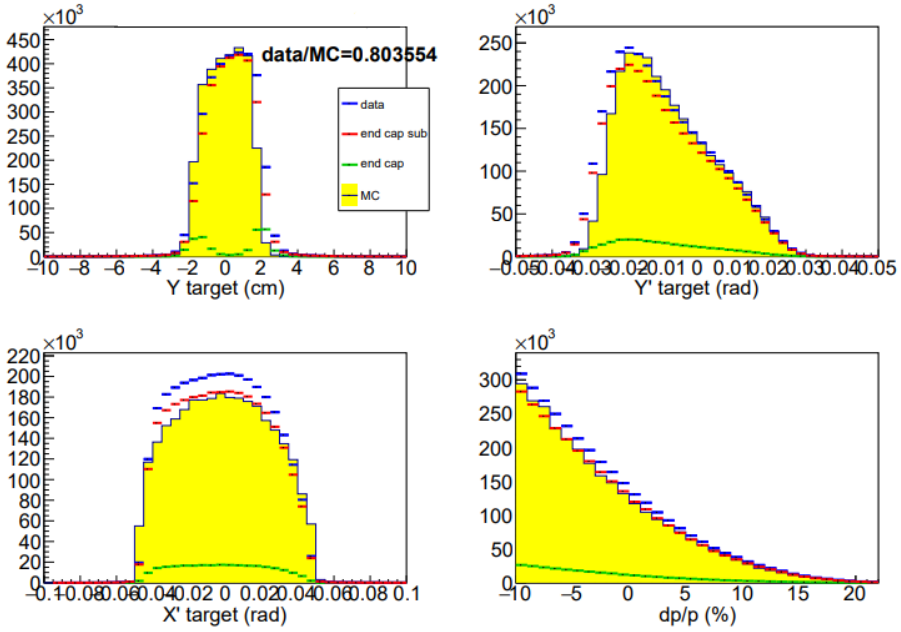


**Figure 4.39:** An example of yields corrected for the target walls and compared to Monte Carlo simulations.

### 4.4.2 Pion Contamination

The Cerenkov and calorimeter detectors are not sufficient to remove all unwanted pion background events, even when their cut efficiencies are accounted for. Indeed, the cut efficiencies are sensitive to occasions when the particle identification detectors remove electron events. Here, we are concerned that applying stringent requirements on the momentum normalized energy deposition and the number of associated photo-electrons will not entirely remove pions from our final yield. As demonstrated in the calorimeter calibration section, when a distribution is plotted in $E_{dep}$, the pion events and electron events are clearly separated. However, the pion distribution has a visible tail that extends to large values of $E_{dep}$; it is these events that we wish to remove.

The procedure for the removal of these events is to create two different distributions. We create one distribution of events that are mostly electron events; this is done by requiring that the number of photo-electrons is greater than 6. A second distribution of mostly pion events in created by requiring that the number of photo-electrons is less than

6.

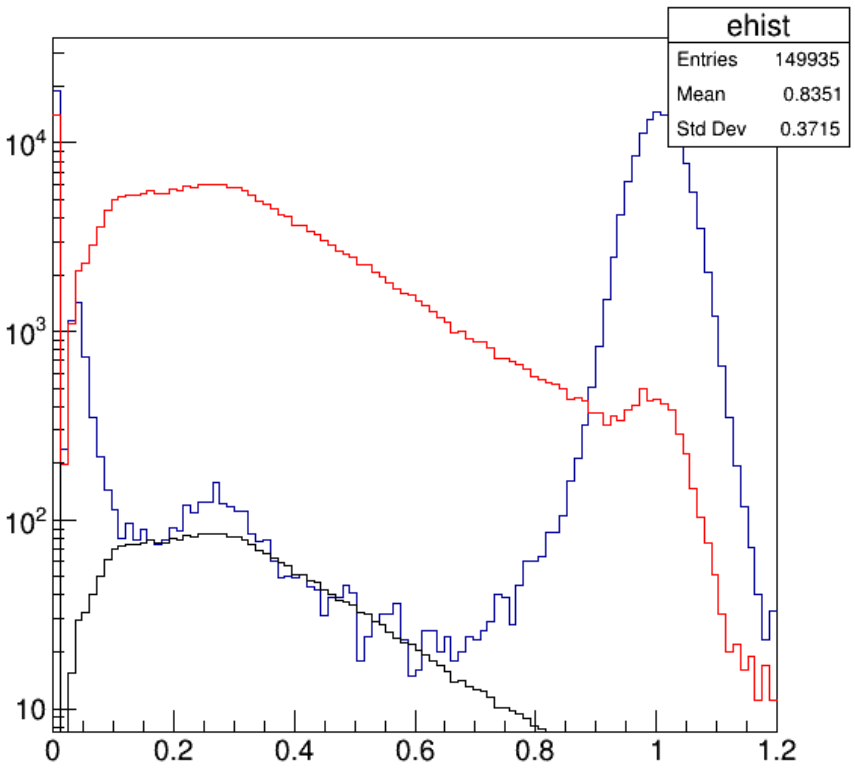


**Figure 4.40:** Electron distribution in blue and pion distribution in red. The scaled pion distribution is in black.

With these two distributions the pion distribution peak is determined in the electron distribution. At this determined bin, a scaling factor is formed by taking the ratio of the bin content between the blue and the red distributions. This scaling factor is applied to the entire pion distribution to produce a scaled pion distribution; this corresponds to the black distribution in figure 4.40. Typically, the calorimeter cut is chosen for $E_{dep} > 0.7$, thus, the events in the black distribution that extend beyond this threshold constitute the pion contamination in the electron sample. As mentioned, pion production is highly dependent on the kinematics, therefore, the pion contamination must be characterized as a function of $E'$, and the results are presented in figure 4.41 for the SHMS and figure 4.42 for the HMS.

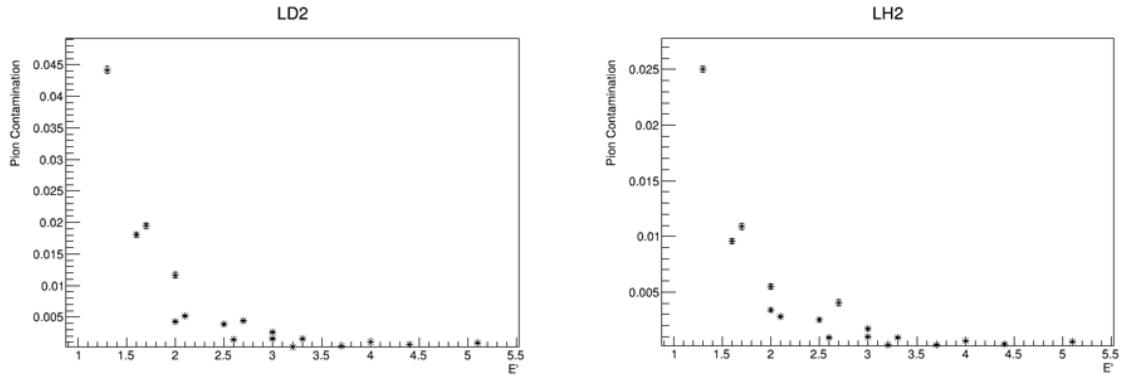


**Figure 4.41:** Pion contamination in percentage, as a function $E'$ for the LH2 and LD2 targets for the SHMS.

For the HMS, there are less kinematic settings and making the fit may take further work.

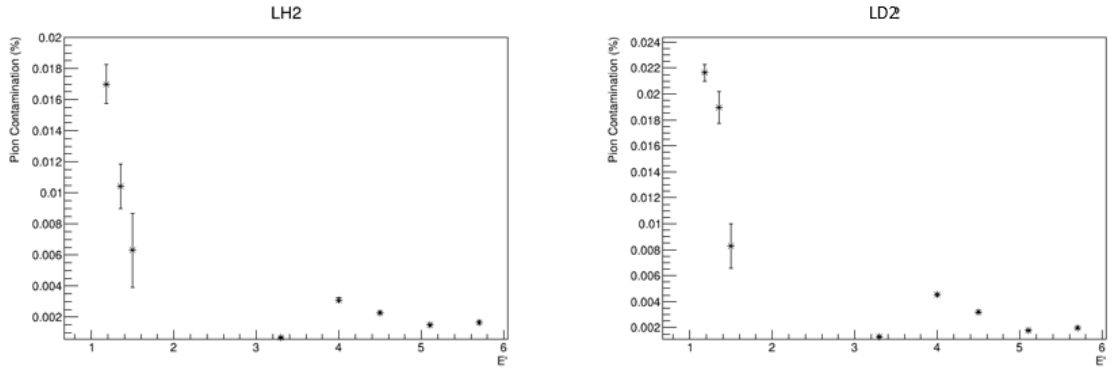


**Figure 4.42:** Pion contamination in percentage, as a function $E'$ for the LH2 and LD2 targets for the HMS.

### 4.4.3 Charge Symmetric Background

The charge symmetric background are unwanted electron events that are produced outside of the primary interaction. Two major sources are the spontaneous creation of a $e^+$ and $e^-$ pair, $\gamma \rightarrow e^+e^-$. Another source of production is from neutral pion decay, $\pi^0 \rightarrow e^+e^-$. This poses the specific issue that our particle identification detectors cannot separate electrons that were produced from the primary interaction and those produced through secondary means. However, we can take advantage of the fact that these unwanted electron events are produced in equal number to the positron $e^+$. Thus, we need only

measure positrons for a given kinematic setting, and we can be sure that the yield number from these events will be equivalent to the yield of unwanted electron events. This was achieved by changing the polarity of the spectrometers to measure positrons instead of electrons. Accounting for the charge symmetric background requires that we extract the cross section for the positron events. Extracting the positron cross section requires all of the same considerations that we make for the final electron cross section. This includes detector efficiencies, pion contamination, target wall backgrounds, etc. However, the magnitude of the charge symmetric background is dependent on the kinematic setting; it increases for increasing scattering angle and decreasing $E'$. For this reason, it is also necessary to parameterize the positron cross sections, as well as using a positron cross section model in conjunction with a Monte Carlo simulation. As of the writing of this thesis, the charge symmetric background has yet to be determined, and therefore this systematic is not accounted for in the results.

## 4.5 Target Density Correction

We must also take into account the effect that beam heating has on the density of the liquid cryogenic targets. As the electron beam passes through the targets, heat can accumulate and change the local density of the target. Of course, this has the immediate effect that the nominal yield is reduced. This effect is non-negligible and the final yield must be corrected. To systematically study the density correction, for two kinematic settings in the SHMS and HMS, dedicated density correction runs were taken. This involved taking runs at different beam currents, from low current to high current. For both the SHMS and HMS, density correction runs were taken at $\theta = 20, E' = 2.0GeV$ and $theta = 25, E' = 4.4GeV$.

To study the target density correction, we calculate the charge normalized yield, given by,

$$Y_{norm} = \frac{\int currentHist \cdot ps}{Q_{ibcm4b} \cdot EtrackEff \cdot CompLt} \tag{4.19}$$

where, "currentHist" is a distribution of events, as shown in figure 4.43, at a given current setting, "ps" is a scaling factor for event rates, "$Q_{ibcm4b}$" is the charge of events as recorded by BCM4B, "EtrackEff" is the tracking efficiency of electron events, and "CompLt" is the computer live-time. Thus, for a given current setting, events that are above a current threshold are accumulated and scaled by an appropriate factor.

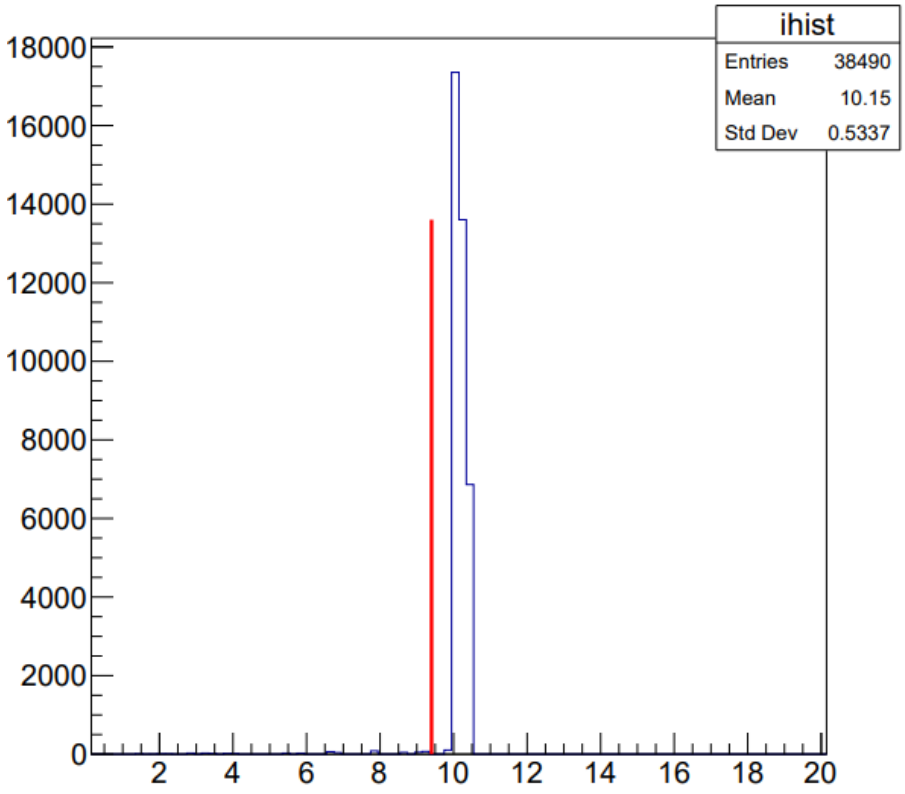


**Figure 4.43:** Current selection for target density correction.

This number is then normalized by the charge of these events, and the yield is corrected for tracking efficiency and computer live-time. This calculation is carried out for several current settings and the charge normalized yield is plotted as a function of current. In particular, this procedure is done for the two cryogenic targets, LH2 and LD2, and also the carbon target, shown in figures 4.44 through 4.47. All other yields are normalized to

the carbon target yield. Additionally, the carbon target is used in order to verify that density corrections have been appropriately applied; if this is the case, the carbon target should not display a correlation with current.

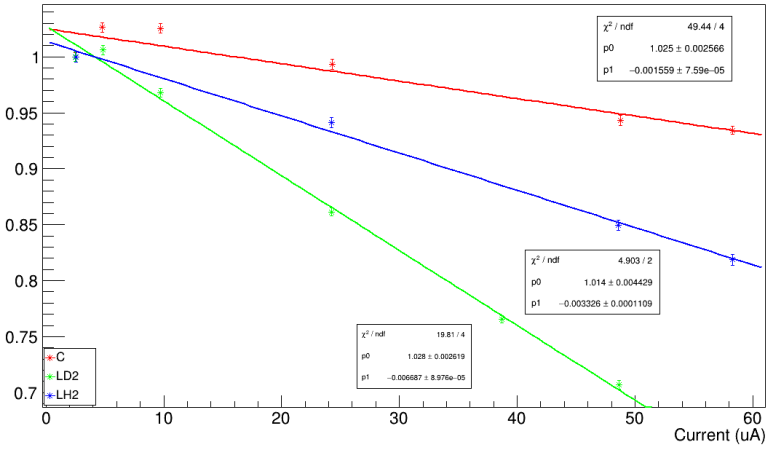


**Figure 4.44:** Target density correction for the SHMS, for scattering angle 15 and $E' = 2.0$ GeV.

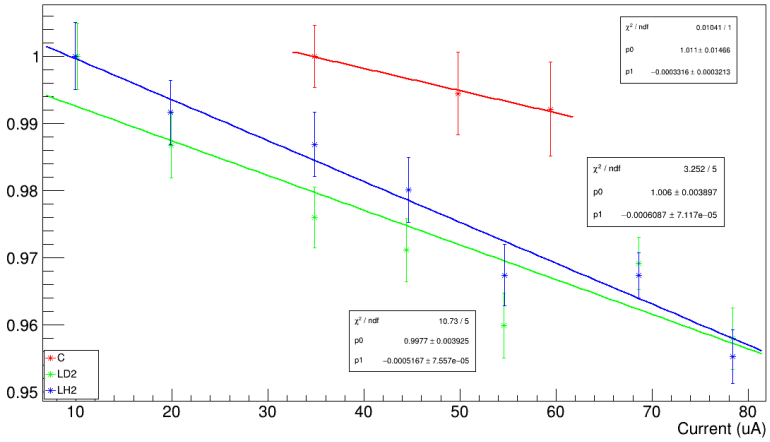


**Figure 4.45:** Target density correction for the SHMS, for scattering angle 25 and $E' = 4.4$ GeV.

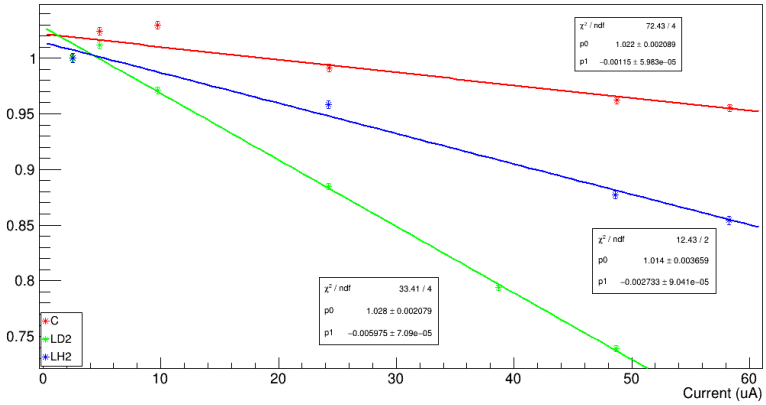


**Figure 4.46:** Target density correction for the HMS, for scattering angle 15 and $E' = 2.0$ GeV.

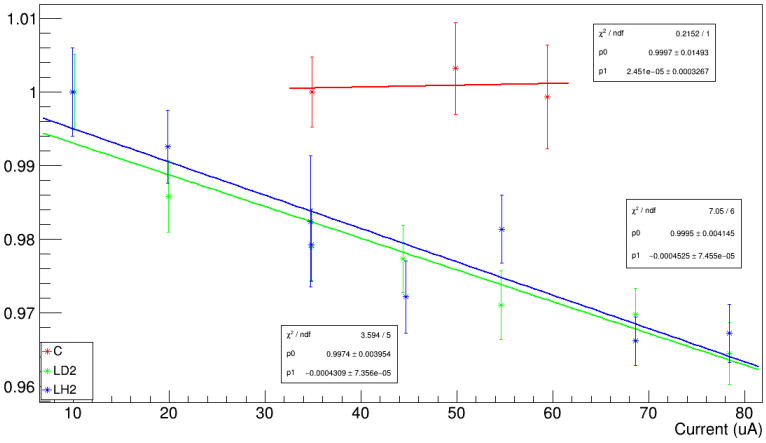


**Figure 4.47:** Target density correction for the HMS, for scattering angle 25 and $E' = 4.4$ GeV.

Broadly, this study suggests that for $\theta = 25, E' = 4.4GeV$, target boiling as been accounted for, as the carbon target does not see a strong dependence on the current. However, it may be that the remaining kinematic setting requires more analysis.

## 4.6 Cross Section and $F_2$ Extraction

In order to extract cross sections from the E12-10-002 experimental data we employ a method called the Monte Carlo ratio method. First, we may express the electron yield as

$$Y(E',\theta) = \frac{N^{e^-} - BG}{\epsilon_{Total}} = L \cdot \sigma_{Data} \cdot (\Delta E' \cdot \Delta\Omega) \cdot A(E',\theta) \tag{4.20}$$

where $N^{e^-}$ is the number of measured electron events, $BG$ are background events, and $\epsilon_{Total}$ is the total efficiency of the spectrometer. Further, $L$ is the total luminosity, $\sigma_{Data}$ is the cross section coming from experimental data, $\Delta E'$ and $\Delta\Omega$ are the energy and angle binning at which the yield is calculated, and $A(E',\theta)$ is the acceptance of the spectrometer. This yield can be additionally calculated via a Monte Carlo simulation, as

$$Y^{MC}(E',\theta) = L \cdot \sigma_{Model} \cdot (\Delta E' \cdot \Delta\Omega) \cdot A_{MC}(E',\theta) \tag{4.21}$$

where here, $\sigma_{Model}$ is the cross section as given by a model using a fitting code developed by E. Christy and Bosted. Likewise, the acceptance is modeled in the Monte Carlo. Assuming the acceptance can be accurately modeled, we take the ratio of the two yields.

$$\frac{Y(E',\theta)}{Y^{MC}(E',\theta)} = \frac{L \cdot \sigma_{Data} \cdot (\Delta E' \cdot \Delta\Omega) \cdot A(E',\theta)}{L \cdot \sigma_{Model} \cdot (\Delta E' \cdot \Delta\Omega) \cdot A_{MC}(E',\theta)} \tag{4.22}$$

We solve for $\sigma_{Data}$ and find,

$$\sigma_{Data} = \sigma_{Model} \frac{Y(E',\theta)}{Y^{MC}(E',\theta)} \tag{4.23}$$

Thus, the final data cross sections depend on modeled cross sections, measured yields, and modeled yields.

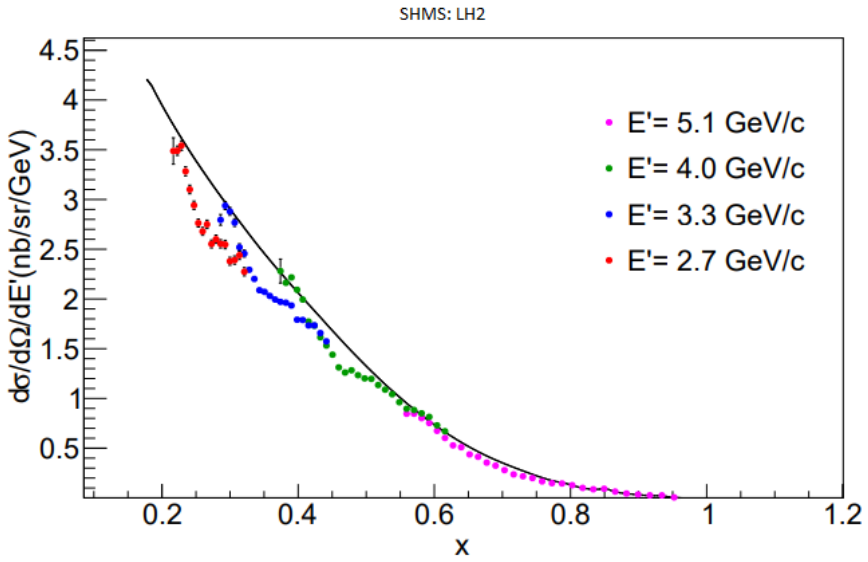


**Figure 4.48:** Data and Monte Carlo cross section comparison as a function of $x$ for LH2 in the SHMS, for 21 degree scattering angle.

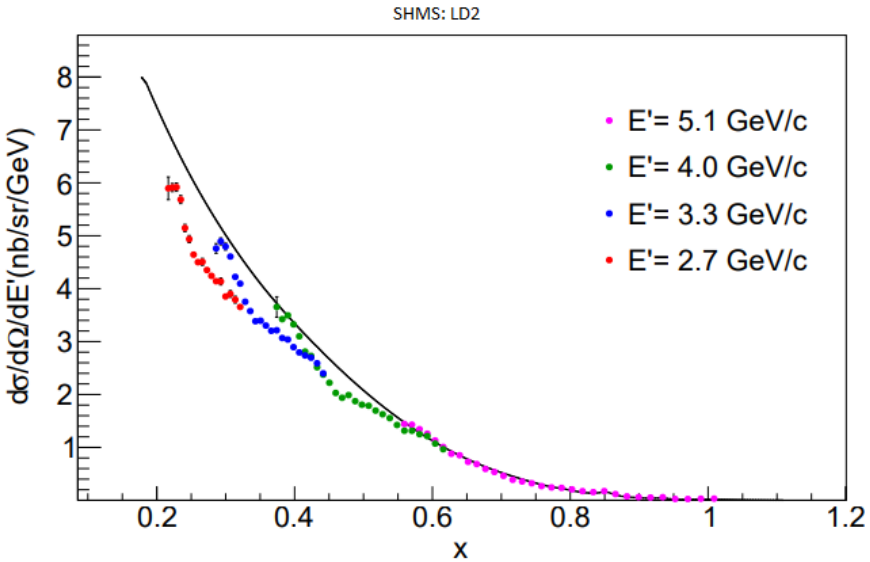


**Figure 4.49:** Data and Monte Carlo cross section comparison as a function of $x$ for LD2 in the SHMS, for 21 degree scattering angle.

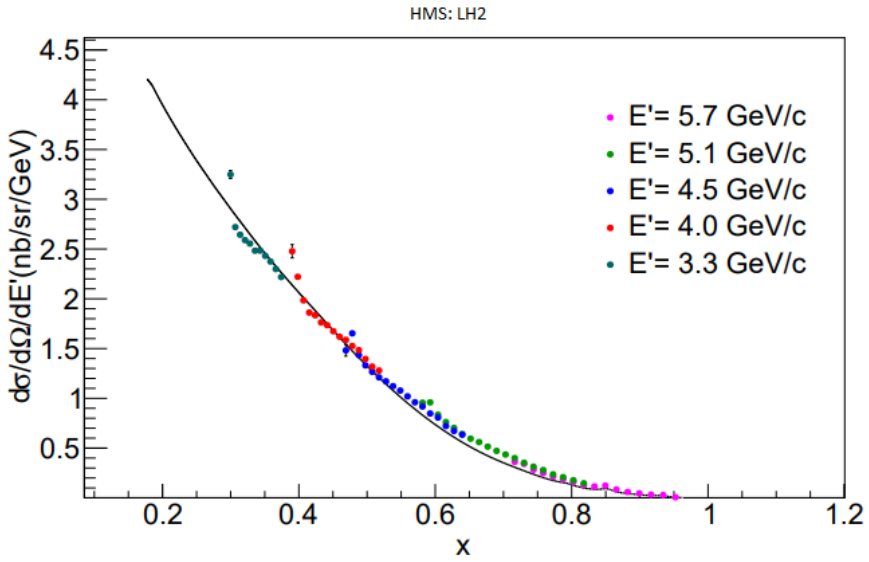


**Figure 4.50:** Data and Monte Carlo cross section comparison as a function of $x$ for LH2 in the HMS, for 21 degree scattering angle.

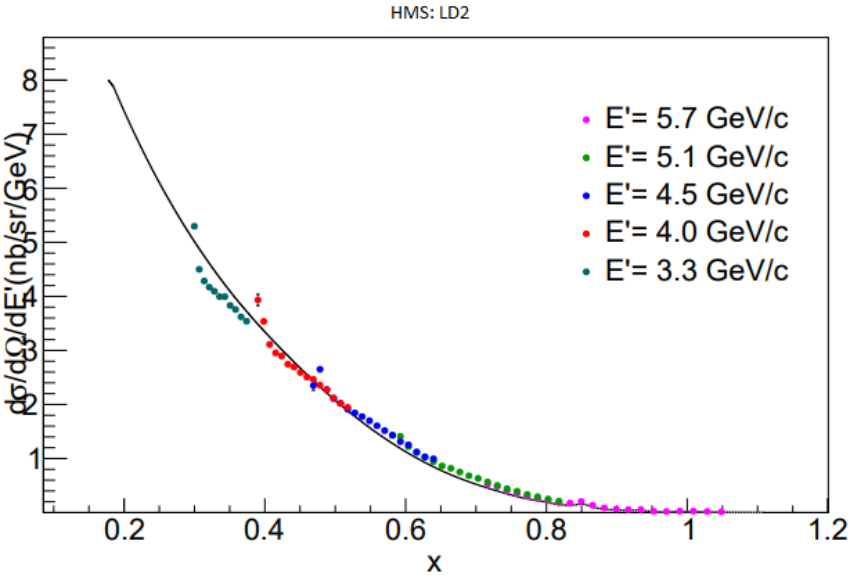


**Figure 4.51:** Data and Monte Carlo cross section comparison as a function of $x$ for LD2 in the HMS, for 21 degree scattering angle.

The cross section is extract by using the fitting code from Christy and Bosted and the esults are shown in figures 4.48 through 4.51 [PB08]. This cross section is modeled by fitting to precision empirical data on inclusive electron proton scattering data, in particular in the resonance regions. In particular, their methodology involves fitting the transverse

and longitudinal photo-absorption cross sections components discussed in section 2.2. T reduced cross section can be written in terms of the transverse and longitudinal cross section,

$$\sigma_R = \frac{1}{\Gamma}\frac{d\sigma}{d\Omega dE'} = \sigma_T(W^2, Q^2) + \epsilon\sigma_L(W^2, Q^2), \tag{4.24}$$

where $\Gamma$ is the flux of virtual photons and $\epsilon$ is relative flux of longitudinal photons. The data sets used to produce this model are listed in table 4.3.

| Data Set | $Q^2_{Min}\ GeV^2$ | $Q^2_{Max}\ GeV^2$ | # Data Points |
|---|---|---|---|
| E94-110 | 0.18 | 5 | 1259 |
| E00-116 | 3.6 | 7.5 | 256 |
| E00-002 | 0.06 | 2.1 | 1346 |
| SLAC DIS | 0.6 | 9.5 | 296 |
| Photoproduction (Old) | 0 | 0 | 242 |
| Photoproduction (DAPHNE) | 0 | 0 | 57 |

**Table 4.3:** Data sets used to model cross sections.

When such fits were done in the past, they did not have sufficient data to constrain both $\sigma_T$ and $\sigma_L$, and therefore the determination of the ratio $R = \sigma_L/\sigma_T$ was extrapolated. With the addition of high precision data, it is now possible to fit and parameterize $\sigma_T(W^2, Q^2)$ and $\sigma_L(W^2, Q^2)$ independently. The parameterization constitutes 75 free parameters: 7 parameters are attributed to the resonance mass, 7 parameters are for the resonance widths, 25 to describe the $Q^2$ dependence on the transverse form factors, 18 parameters for the $Q^2$ dependence on the longitudinal form factors, 10 and 7 parameters to account for non-resonant contribution to $\sigma_T$ and $\sigma_L$ respectively, and 1 dampening parameter for the delta resonance.

Of course, because we are attempting to model data from E12-10-002 that contains nuclear resonances, it is important to model these resonances appropriately as well. This relies on three properties about the cross sections. First, the cross section is the incoherent

sum of two terms; $\sigma^R$ which accounts for contributions from resonance production, and $\sigma^{NR}$, which accounts for a non-resonant background. Second, the resonance production contributions are described by relativistic Breit-Wigner forms that include $Q^2$ dependent amplitudes coming from each resonance. Finally, the non-resonant background depends on $W^2$ smoothly. Thus, we can write,

$$\sigma_{T,L}(W^2, Q^2) = \sigma^R_{T,L}(W^2, Q^2) + \sigma^{NR}_{T,L}(W^2, Q^2) \tag{4.25}$$

and, the resonant contribution can be written in terms of Breit-Wigner forms as,

$$\sigma^R_{T,L}(W^2, Q^2) = W \sum_{i=1}^{7} BW^i_{T,L}(W^2) \cdot [A^i_{T,L}(Q^2)]^2 \tag{4.26}$$

,

where,

$$BW^i = \frac{K_i K_i^{cm}}{K K^{cm}} \cdot \frac{\Gamma_i^{tot}\Gamma_i^{\gamma}}{\Gamma_i[(W^2 - M_i^2)^2 + (M_i\Gamma_i^{tot})^2]} \tag{4.27}$$

with,

$$K = \frac{W^2 - M_p^2}{2M_p} \tag{4.28}$$

$$K^{cm} = \frac{W^2 - M_p^2}{2W} \tag{4.29}$$

$$k_i = K^{cm}|M_i \tag{4.30}$$

where $K$ and $K^{cm}$ are the energies of the photon in the lab and center of mass frame respectively, and $K_i$ and $K_i^{cm}$ are the photon energies in the lab and center of mass frame evaluated at the $i^{th}$ resonance. And the total decay width $\Gamma_i^{tot}$ is given by,

$$\Gamma_i^{tot} = \sum_{j=1}^{3} \beta_i^j \Gamma_i^j \tag{4.31}$$

where $\beta_j^i$ is the branching ration of the $i^{th}$ resonance to the $j^{th}$ decay mode.

In order to perform the fit for the transverse and longitudinal cross sections, seven resonant contributions were included, however, only the pion, double-pion, and eta decay modes were considered, whose branching ratios are shown in table 4.4.

| I | State | $\beta_{1\pi}$ | $\beta_{2\pi}$ | $\beta_{\eta}$ |
|---|---|---|---|---|
| 1 | $P_{33}(1232)$ | 1.0 | 0.0 | 0.0 |
| 2 | $S_{11}(1535)$ | 0.45 | 0.10 | 0.45 |
| 3 | $D_{13}(1520)$ | 0.65 | 0.35 | 0.0 |
| 4 | $F_{15}(1680)$ | 0.65 | 0.35 | 0.0 |
| 5 | $S_{15}(1650)$ | 0.4 | 0.5 | 0.1 |
| 6 | $P_{11}(1440)$ | 0.65 | 0.35 | 0.0 |
| 7 | $l = 3$ | 0.5 | 0.5 | 0.0 |

**Table 4.4:** Resonances and branching ratios included in the fit.

For the transverse cross section, these resonances were fit using the following form,

$$A_T^i(Q^2) = \frac{A_T^i(0)}{(1+Q^2/0.91)^{c_i}} \cdot (1 + \frac{a_i Q^2}{1+b_i Q^2}) \tag{4.32}$$

and for the longitudinal cross section, the fits were given by,

$$A_L^i(Q^2) = A_L^i(0) \cdot \frac{Q^2}{1+d_i Q^2} e^{-eQ^2} \tag{4.33}$$

We note that these forms are chosen such that at large $Q^2$, $A_T^i(Q^2)$ reduces to a dipole form,

$$A_T^i(Q^2) = \frac{A_T^i(0)}{(1+Q^2/0.91)^{c_i}} \cdot \frac{a_i}{b_i} \tag{4.34}$$

and as $Q^2$ approaches zero, the transverse resonance transition amplitude approaches $A_T^i(0)$. As mentioned previously, a non-resonant background also contributes to the total cross section, and these contributions must be fit as well. For the transverse cross section,

the non-resonant contribution is fit using,

$$\sigma_T^{NR} = x' \sum_{i=1}^{2} \frac{\sigma_T^{NR,i}(0)}{Q^2 + a_i^T[b_i^T + c_i^T Q^2 + d_i^T Q^4]} (\Delta W)^{i+\frac{1}{2}} \tag{4.35}$$

where,

$$x' = (1 + \frac{W^2 - (M_p + m_\pi)^2}{Q^2 + Q_0^2})^{-1} \tag{4.36}$$

and $m_\pi$ is the pion mass, $Q_0^2 = 0.05\ GeV^2$ and $\Delta W = W - m_\pi$. For the longitudinal cross section, the non-resonant background is fit by,

$$\sigma_L^{NR} = \sum_{i=1}^{1} \sigma_L^{NR}(0) \frac{(1-x')[a_i^L t + b_i^L]}{(1-x)} \frac{(Q^2)^{c_i^L}}{(Q^2 + Q_0^2)^{(1+c_i^L)}} \cdot (x')^{[d_i^L + e_i^L t]} \tag{4.37}$$

where $t$ is a slowly varying function of $Q^2$ given by,

$$t = \frac{\log(\log(\frac{[(Q^2)^{c_i^L}]}{0.33^2}))}{\log(\frac{m_0}{0.33^2})} \tag{4.38}$$

and $Q^2 = 0.125\ GeV^2$, and $m_0 = 4.2802\ GeV^2$. The different data sets constrain the fit in different regions. For the region $0.18 < Q^2 < 4.5$, the fit is mostly dominated by the E94-110 experimental data shown in figure 4.52, with an associated systematic uncertainty of less than 2%.

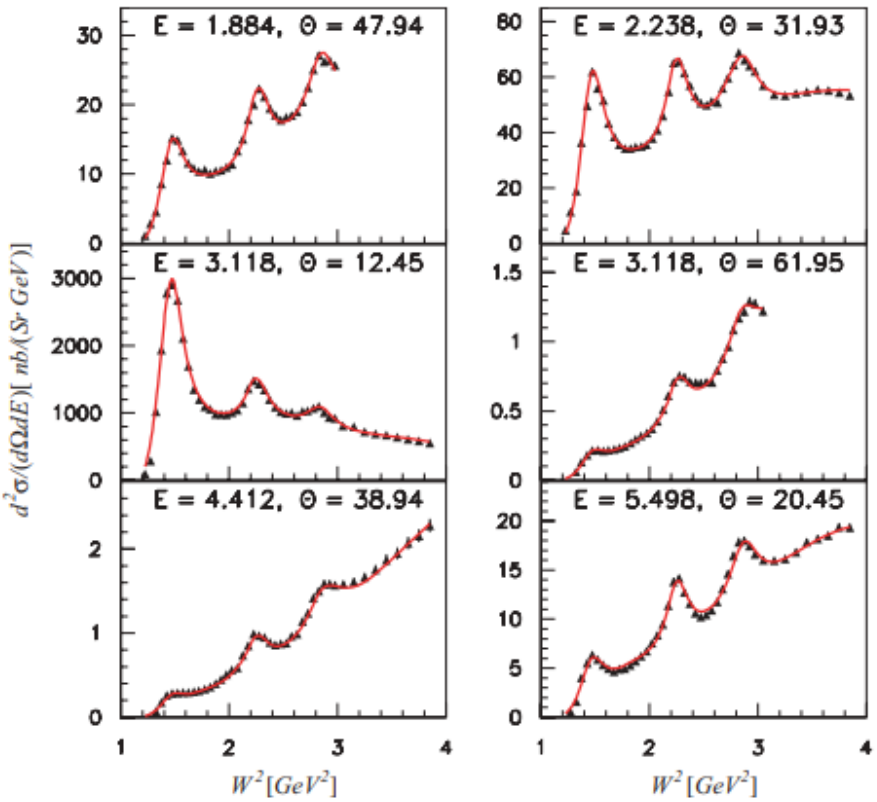


**Figure 4.52:** Cross section data versus $W^2$ for the E94-110 data. Red curve is the fit and black triangles are the data.

In the region $4.5 < Q^2 < 7.5$, the fit is constrained largely by the E00-116 data set, where the statistical uncertainty dominates over the systematic uncertainty. Additionally, the E00-002 data set was used to constrain the fit down to 0.05 $GeV^2$, while data from DAPHNE was used to constrained the fit at $Q^2 = 0$ $GeV^2$, shown in figure 4.53.

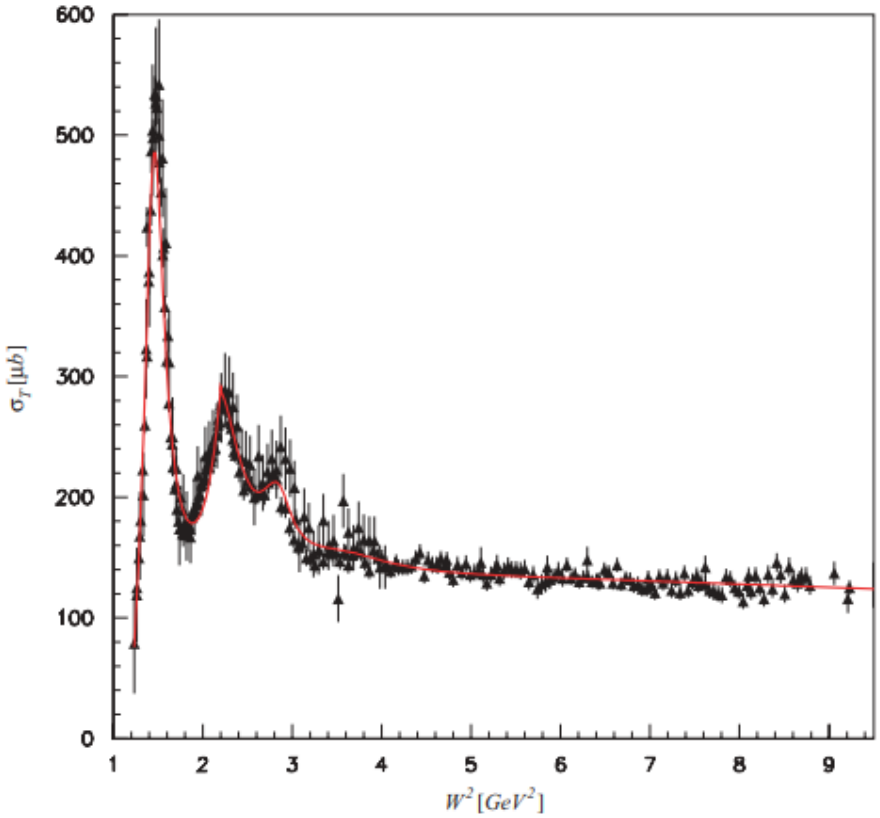


**Figure 4.53:** Cross section data versus $W^2$ for the photoproduction data. Red curve is the fit and black triangles are the data.

From this, one now has access to the modeled cross section. These cross sections can now be used as input for a global PDF analysis.

# Chapter 5

# Results and Discussion

## 5.1 CTEQ-JLab Global PDF Analysis

In Chapter 2, the motivation for a global PDF analysis was briefly discussed. Here we give a more in-depth presentation. As previously mentioned, a global PDF analysis uses a combination of perturbative QCD and world data in order to determine the $Q^2$ and Bjorken $x$ dependence of the PDFs. Perturbative QCD, in particular the DGLAP equations give us access to the $Q^2$ dependence but it is not able to give us the functional dependence of the PDFs on Bjorken $x$. Thus, before we can evolve the PDFs from some energy scale $Q_0^2$ to an arbitrary $Q^2$, we must first map out the $x$ dependence through fitting of the data. Most fitting groups rely on DIS data, mainly from the HERA collider from $e^- - p$ collisions, the Tevatron, and CERN but also including data from fixed-target experiments. As one might imagine, properly fitting a set of data sets has its challenges. One must carefully choose which data sets to include. For example, fixed-target experiments using nuclear targets heavier than deuterium typically are not used due to the difficulty in accounting for the fact that the nucleons are not free and constitute a bound state subject to nuclear effects. It is also useful to consider what sorts of results a global PDF analysis can offer us. Firstly, we gain access to parton distribution functions over a kinematic range that is commensurate with the kinematic range of our data, and indeed, with uncertainty bands that are commensurate with the data. Having just the knowledge about properly constrained PDFs is enough to make scientific progress on a number of fronts. In particular with regards to the relatively unconstrained PDFs of the down quark and the

gluon. Specifically, as was discussed in section 2.4 and demonstrated in figures 2.7 and 2.7, the uncertainties for these PDFs grows as $x$ increases.

We move now from the general motivation of a global PDF analysis to discuss the specific PDF fit used in this analysis. We made use of the latest PDF sets from the CTEQ-JLab collaboration, CJ15. CJ15 sought to fit, among other data sets, $6GeV$ era JLab experimental data, many of which include cross section measurements on deuterium at relatively low $Q^2$ and $W^2$. This made CJ15 a natural candidate to explore the impact of the E12-10-002 experiment to a global PDF analysis, given that E12-10-002 made measurements at large $x$ and which also venture into the resonance region where PDFs, such as the down quark and gluon distributions remain relatively unconstrained. This reflects the lack of precision data in this region, which E12-10-002 seeks to alleviate, at least with regards to the down quark. The expected impact of the E12-10-002 data set on the gluon uncertainty is expected to be minimal, considering CJ15 fits $F_2$ rather than cross sections directly, and whose constraint on the gluon comes only through DGLAP evolution. Nonetheless, in section 5.2.1 we discuss the importance of reducing the gluon uncertainty in relation to beyond standard model physics searches and connect this to the impact that the Electron Ion collider (EIC) may provide for the future. We also explore how reducing the uncertainty in the down quark can lead to greater constraints in $\frac{d}{u}$ at large $x$, and how its behavior as $x \to 1$ can allow us to explore the spin-flavor dynamics of the nucleons.

However, issues may arise when one includes data at relatively low $Q^2$ and $W^2$. In particular at low $Q^2$, and when the kinematic cut on $W^2$ is relaxed, one begins to approach the non-perturbative resonance region discussed in section 4.6. Here, nuclear effects introduce subleading power corrections in $\frac{1}{Q^2}$. These corrections include target mass corrections and nuclear off-shell corrections, which will be discussed in the following section[AA10].

As previously mentioned, the choice of data sets used to produce a fit is of some importance. For this reason, it is instructive to briefly discuss the data sets used in

the CJ15 PDF fit. To begin, the large bulk of the data sets used to produce the CJ15 fit include vector boson, jet production, charged lepton, and W-asymmetry data from the Tevatron, and DIS data from HERA, SLAC, CERN, and JLab. Each data set is important in its own right, and each play roles in the analysis. For example, in the case of constraining the down quark distribution, much of the data sets from the Tevatron, D0, CDF, and W-asymmetries, have direct access to the down quark distribution. However, this data is at high $Q^2$ and $W^2$, and constitutes a relatively small data set. On the other hand, the JLab BoNuS experiment took measurements on a nearly model independent neutron, but its kinematic coverage is at low $Q^2$ and $W^2$. And finally, the addition of the 6 $GeV$ JLab DIS data could form a large data set and extends the kinematic coverage from several experiments, but requires nuclear corrections.

The CJ15 fits include two additional data sets over its previous iteration CJ12. First we discuss the W-boson asymmetry data from the Tevatron. The W-boson asymmetry data sets are largely responsible for constraining the $d/u$-quark and down quark parton distribution functions. This is due to the fact that the $W^{\pm}$ bosons are produced with an asymmetry in $p\bar{p}$ collisions. Because the proton has two up quarks, on average, the up quarks carry more of the proton momentum than the down quarks. This means that $W^+$ bosons tend to be produced in the direction of the proton while $W^-$ bosons are produced in the direction of the anti-proton. This is the source of the W-asymmetry and studying this asymmetry can be directly related to the up and down quark distributions in the proton. Indeed, CJ15 explored the impact of this data set particularly on the down quark and found that its uncertainties were significantly reduced at large $x$[AA16]. Further, the charge asymmetry of the of the produced bosons can be written as,

$$A_W(y) = \frac{d\sigma(W^+)/dy - d\sigma(W^-)/dy}{d\sigma(W^+)/dy + d\sigma(W^-)/dy} \tag{5.1}$$

which can be expressed approximately as,

$$A_W(y) \approx \frac{u(x_1)d(x_2) - d(x_1)u(x_2)}{u(x_1)d(x_2) - d(x_1)u(x_2)} \tag{5.2}$$

and this can be further reduced to,

$$\frac{R(x_2) - R(x_1)}{R(x_2) + R(x_1)} \tag{5.3}$$

where $R(x) = d(x)/u(x)$[GD].

Another clear example that illustrates the interplay between the constraining power of data sets is that of measurements taken on neutrons, such as in the BONuS experiment, and measurements on deuterium. Measurements on nearly free neutrons are able to directly access the down quark distribution of the neutron. And if the down quark distribution can be precisely determined, the knowledge of this PDF can be used in conjunction with deuterium data in order to constrain the off-shell correction $\delta f^N$, discussed in section 5.1.2, for some given deuteron wave function.

However, data sets may overlap in their kinematic coverage and therefore it is possible for them to disagree, causing tension in the fit. For that reason, it is useful to look at the $\chi^2$ value of the data set; if two data sets disagree with each other, the $\chi^2$ of one will change depending on whether the other is included in the fit or not. In this way, we are able to explore the impact of including a new data set into the fit. Tables 5.1 and 5.2 show the whole set of data used to produce the CJ15 fits with the addition of the E12-10-002 data labelled as "e12dhp015".

| Data Set | $\chi^2$ | signd | resid | npts | $\chi^2 pts$ |
|---|---|---|---|---|---|
| e12dhp015 | 341.0 | 94.7 | -331.4 | 550 | 0.62 |
| jl00106$F_2$p | 162.8 | -28.2 | 49.7 | 136 | 1.26 |
| jl00106$F_2$d | 119.2 | -13.8 | 261.7 | 136 | 0.91 |
| Her$F_2$pCut | 45.3 | -10.2 | 0.7 | 37 | 1.12 |
| Her$F_2$dCut | 39.3 | -9.9 | 35.7 | 37 | 0.97 |
| slac_p | 437.0 | 19.0 | 2.9 | 564 | 0.75 |
| slac_d | 406.8 | -20.8 | 746.5 | 582 | 0.64 |
| Bcd$F_2$pCor | 440.4 | 2.9 | 30.5 | 351 | 1.26 |
| Bcd$F_2$dCor | 287.9 | 0.9 | 41.2 | 254 | 1.15 |
| Nmc$F_2$pCor | 404.1 | -15.6 | -17.6 | 275 | 1.48 |
| NmcRatCor | 171.4 | -6.7 | 563.1 | 189 | 0.92 |
| H2_NC_em | 241.6 | -1.8 | 3.7 | 159 | 1.52 |
| H2_NC_ep_1 | 580.2 | 35.2 | 42.5 | 402 | 1.45 |
| H2_NC_ep_2 | 94.5 | -11.1 | 195.3 | 75 | 1.27 |
| H2_NC_ep_3 | 248.4 | 27.6 | 11.4 | 259 | 0.96 |
| H2_NC_ep_4 | 227.9 | -4.3 | 18.4 | 209 | 1.09 |
| H2_CC_em | 46.5 | 2.4 | -133.3 | 42 | 1.09 |
| H2_CC_ep | 50.4 | -1.9 | 44.9 | 39 | 1.29 |

**Table 5.1:** Data sets included in the CJ15 plus E12-10-002 with 1.5% systematic, as well as the total $\chi^2$, the signed $\chi^2$, the residual, the number of data points, and the $\chi^2$ over number of data points.

| Data Set | $\chi^2$ | signd | resid | npts | $\chi^2 pts$ |
|---|---|---|---|---|---|
| BNS_$F_2$nd | 213.2 | -1.4 | -17.1 | 191 | 1.11 |
| e866pp06xf | 138.5 | -22.1 | 5.2 | 121 | 1.15 |
| e866pd06xf | 147.1 | 34.5 | 4.5 | 129 | 1.14 |
| cdfLasy05 | 12.4 | 8.3 | -13.2 | 11 | 1.13 |
| d0Lasy_e15 | 29.2 | -26.0 | 38.3 | 13 | 2.18 |
| d0Lasy13 | 17.1 | 0.9 | -62.7 | 10 | 1.72 |
| CDF_Wasy | 16.8 | -15.4 | 128.5 | 13 | 1.34 |
| D0_Wasy | 12.8 | 12.7 | -343.2 | 14 | 0.79 |
| CDF_Z | 28.6 | 3.4 | 9.9 | 28 | 1.00 |
| D0_Z | 16.0 | 1.6 | -7.3 | 28 | 0.57 |
| d0run2cone | 20.1 | 3.4 | 14.2 | 110 | 0.18 |
| CDFrun2jet | 14.7 | -6.0 | 18.0 | 72 | 0.21 |
| d0_gamjet1 | 6.7 | 5.8 | -41.9 | 16 | 0.42 |
| d0_gamjet2 | 16.4 | 16.3 | -89.2 | 16 | 1.02 |
| d0_gamjet3 | 25.0 | -20.1 | 75.7 | 12 | 2.09 |
| d0_gamjet4 | 13.0 | -4.6 | 29.1 | 12 | 1.07 |

**Table 5.2:** Continuation of data sets included in the CJ15 fit, as well as the total $\chi^2$, the signed $\chi^2$, the residual, the number of data points, and the $\chi^2$ over number of data points.

Now that we have established the general motivation and method of a global PDF analysis, as well as the specialization of the CTEQ-JLab collaboration to introduce large $x$ data sets subject to nuclear corrections, we will next discuss the choice of parameterization for the parton distribution functions.

### 5.1.1 Parton Distribution Parameterization

The parameterization for CJ15 is a five parameter function of the form

$$xf(x,Q_0^2) = a_0 x^{a_1}(1-x)^{a_2}(1+a_3\sqrt{x}+a_4 x) \tag{5.4}$$

that describes the valence quarks $u_v = u - \bar{u}$ and $d_v = d - \bar{d}$, the light sea quark $\bar{u} + \bar{d}$, and the gluon $g$. An additional modification is made to the $d$-quark parameterization to allow mixture with the $u$-quark. There are several reasons for this modification.

First, it allows for the phenomenological control of the ratio $\frac{d_v}{u_v}$. Indeed, an SU(6) spin-flavor symmetry treats $u$-quarks and $d$-quarks identically and one would expect $\frac{d}{u} \to \frac{1}{2}$. Of course, this SU(6) symmetry is not exact and is in fact broken. Unfortunately, experimental data is currently lacking in order to properly characterize the behavior of this ratio. However, there exist phenomenological models that attempt to answer the question. If one considers the dominant spectator quark interaction to be gluon mediated, the $d$-quark distribution is suppressed and $\frac{d}{u} \to 0$ as $x \to 1$. If instead one considers a model where the interaction is helicity-dependent, then $\frac{d}{u} \to \frac{1}{5}$ as $x \to 1$. Additionally, allowing a mixture for the $d$-quark leads to a less restrictive, less biased parameterization [AA11]. This mixture is introduced in the form

$$d_v \to a_0^{d_v}\left(\frac{d_v}{a_0^{d_v}} + bx^c u_v\right) \tag{5.5}$$

where two additional parameters, $b$ and $c$ are introduced. Consequently, $\frac{d_v}{u_v} \to a_0^{d_v} b$ as $x \to 1$ as long as $a_2^{d_v} > a_2^{u_v}$. Due to an isopsin asymmetry in the sea quarks, the ratio $\frac{\bar{d}}{\bar{u}}$ is parameterized independently as

$$\frac{\bar{d}}{\bar{u}} = a_0 x^{a_1}(1-x)^{a_2} + a_3 x(1-x)^{a_4} + 1 \tag{5.6}$$

and this ensures $\frac{\bar{d}}{\bar{u}} \to 1$ as $x \to 1$. Lastly, the $s$-quark PDF is assumed to be proportional to the light sea quark distributions through the following relation, which imposes flavor independence in the sea quarks

$$(s + \bar{s}) = \kappa(\bar{u} + \bar{d}), \tag{5.7}$$

and where $\kappa = 0.4$ is taken in accordance with previous CTEQ-JLab studies. The case

for a asymmetric $s$-quark distributions can be studied through neutrino-nucleus DIS data, however, this involves processes that are not well known theoretically, such as energy loss of the scattered charm quarks while travelling through the nucleus. For this reason, a more detailed analysis of sea quark flavor independence is left for future studies.

### 5.1.2 Nuclear Corrections

Nuclear and off-shell corrections account for the difference between structure functions for a free nucleon, such as in hydrogen, and bound nucleons in heavier nuclei. These corrections were extensively studied by Kulagin and Petti, who employed a phenomenological method whereby corrections to the structure functions were parameterized. The parameters were then fit and fixed using existing nuclear data. Additionally, sum rules can be used to link off-shell correction effects in different kinematic regions. For example. the baryon sum rule is used to link nuclear-shadowing and off-shell corrections. Indeed, this analysis demonstrates that the off-shell corrections are responsible for the cancellation of nuclear-shadowing effects to the valence quark PDFs. The most recent CTEQ-JLab analysis has made improvements in the implementation of these corrections over previous analyses. In previous procedures the corrections were applied to extracted structure functions, but now nuclear corrections are implemented at the partonic level. Therefore the corrections are applicable to any interaction involving quarks and gluons.

#### Nuclear Smearing and Off-shell Corrections

Parton distributions relating to the deuteron are typically treated using the impulse approximation. The approximation is given by taking a convolution of the parton's distribution and the distribution of the nucleons $f_{\frac{N}{d}}$ [WM94]. This is expressed as

$$q^d(x,Q^2) = \int \frac{dz}{z} dp^2 f_{\frac{N}{d}}(z,p^2)\tilde{q}^N(\frac{x}{z},p^2,Q^2) \tag{5.8}$$

where z is the nucleon momentum fraction in the deuteron, $z = \frac{M_d}{M}\frac{p\dot{q}}{p_d\dot{q}}$ and $\tilde{q}^N$ is

the distribution of the parton in the off-shell deuteron. The variable $p^2$ represents the virtuality of the off-shellness of the nucleon. Due to the fact that off-shell effects in the deuteron are small, one can expand the distribution around the on-shell distribution

$$\tilde{q}^N(\frac{x}{z}, p^2, Q^2) = \tilde{q}^N(\frac{x}{z}, Q^2)\left[(1 - \frac{p^2 - M^2}{M^2}\delta f^N(x, Q^2))\right] \tag{5.9}$$

and where

$$\delta f^N(x, Q^2) = \frac{\partial f^N(x, p^2, Q^2)}{\partial p^2}\Big|_{p^2=M^2} \tag{5.10}$$

is the coefficient of the off-shell term. Inserting this into the convolution equation, we get two terms, one on-shell and one off-shell

$$q^{d(on)}(x, Q^2) = \int \frac{dz}{z} f^{(on)}(z) q^N(\frac{x}{z}, Q^2) \tag{5.11}$$

$$q^{d(off)}(x, Q^2) = \int \frac{dz}{z} f^{(off)}(z) \delta f^N(\frac{x}{z}, Q^2) q^N(\frac{x}{z}, Q^2) \tag{5.12}$$

where $f^{(on)}$ and $f^{(off)}$ are referred to as the smearing functions and are the same for protons and neutrons[SK95]. They are given by

$$f^{(on)}(z) = \int dp^2 f_{\frac{N}{d}}(z, p^2) \tag{5.13}$$

$$f^{(off)}(z) = \int dp^2 \frac{p^2 - M^2}{M^2} f_{\frac{N}{d}}(z, p^2) \tag{5.14}$$

The smearing functions can be calculated under several models of the nucleon wave function. These wave functions are produced through fits from nucleon-nucleon scattering data. In particular, the CTEQ-JLab analysis makes use of AV18, CD-Bonn, WJC-1, and WJC-2 wave functions, obtained by fitting around 3,000 data points[RW95],[Mac01]. However, to make full use of the previous result, one must first attempt to fully understand

$\delta f^N(x, Q^2)$, which encodes the off-shell nuclear corrections.

In an attempt to reduce model dependency, the CJ analysis makes use of a phenomenological fit method by Kulagin and Petti. The off-shell nuclear corrections are parameterized as

$$\delta f^N = C(x - x_0)(x - x_1)(1 + x_0 - 1) \tag{5.15}$$

and, the form of the off-shell corrections is motivated by the fact that

$$\int_0^1 dx \delta f^N(x)[q(x) - q(\bar{x})] = 0 \tag{5.16}$$

which suggests that $\delta f(x)$ has at least one zero. Additional pion nuclear corrections suggest there are two zeroes, and so the the functional form of $\delta f(x)$ is explicitly defined with these features[SK06].

## 5.2 $F_2$ Structure Functions

Now that nuclear corrections have been addressed, we are ready to present the $F_2$ structure functions extracted from the E12-10-002 experimental cross section data and compare them to structure functions produced from the CJ15 fit with the additional E12-10-002 data set. As mentioned previously, the $F_2$ extraction from experimental data is done with a separate code that uses the Rosenbluth separation technique combined with fitting from experimental data.

It is noted that CJ15 provides the option to fit experimental data given as the ratio of the deuterium and hydrogen structure functions $\frac{F_2^D}{F_2^p}$, rather than fitting $F_2^D$ and $F_2^p$ separately. There are a few reasons to fit the PDFs from the ratio of the structure functions rather than fitting the structure functions independently. Using $\frac{F_2^D}{F_2^p}$ as input to CJ15 may circumvent the several systematics that have yet to be fully accounted for in the cross section data, particularly pion contamination and the charge symmetric background.

And secondly, fitting the ratio of structure functions can help to avoid fitting biases. For these reasons, we choose to provide $\frac{F_2^D}{F_2^p}$ as the quantity to fit. Finally we present the $\frac{F_2^D}{F_2^p}$ structure function ratio for all available SHMS kinematic settings. Figures 5.1 through 5.18 show a comparison between $\frac{F_2^D}{F_2^p}_{Data}$ and $\frac{F_2^D}{F_2^p}_{CJ15+E12}$. That is, we are comparing the initial experimental data, $\frac{F_2^D}{F_2^p}_{Data}$, which is extracted independently from CJ15, and comparing this to the theory calculation produced by CJ15 when the E12-10-002 data is included.

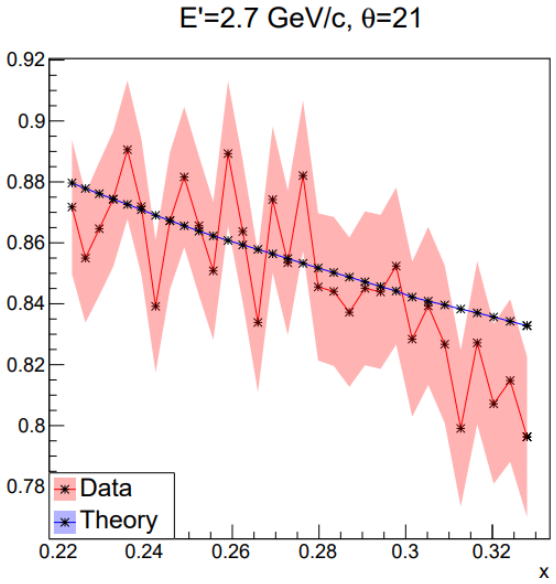


**Figure 5.1:** $\frac{F_2^D}{F^p}$ as a function of Bjorken $x$, for $E' = 2.7\ GeV/c$ and $\theta = 21$. Data refers to $\frac{F_2^D}{F_2^p}_{Data}$ and theory refers to the theory calculation of $\frac{F_2^D}{F_2^p}_{CJ15+E12}$

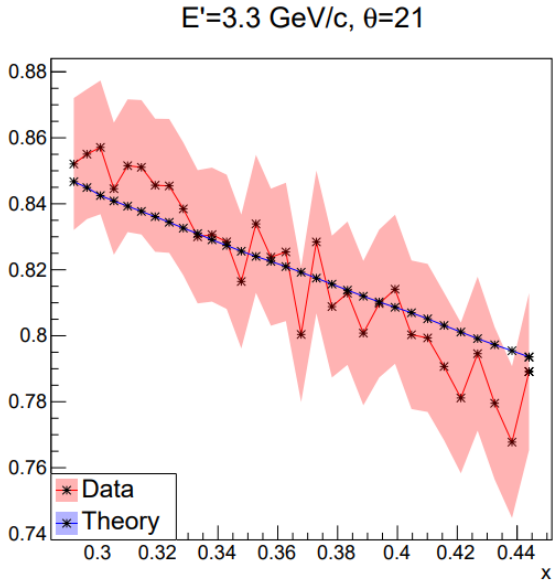


**Figure 5.2:** $\frac{F_2^D}{F^p}$ as a function of Bjorken $x$, for $E' = 3.3\ GeV/c$ and $\theta = 21$. Data refers to $\frac{F_2^D}{F_2^p}_{Data}$ and theory refers to the theory calculation of $\frac{F_2^D}{F_2^p}_{CJ15+E12}$

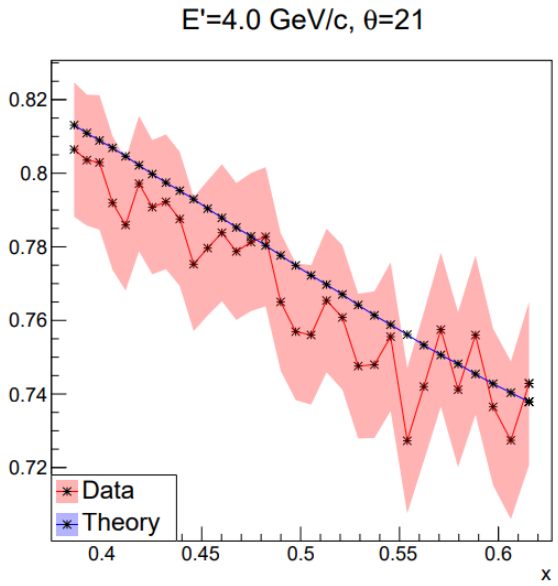


**Figure 5.3:** $\frac{F_2^D}{F^p}$ as a function of Bjorken $x$, for $E' = 4.0\ GeV/c$ and $\theta = 21$. Data refers to $\frac{F_2^D}{F_2^p}_{Data}$ and theory refers to the theory calculation of $\frac{F_2^D}{F_2^p}_{CJ15+E12}$

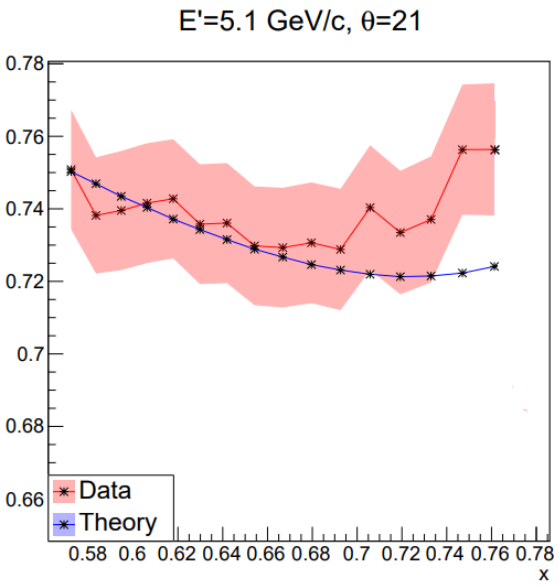


**Figure 5.4:** $\frac{F_2^D}{F^p}$ as a function of Bjorken $x$, for $E' = 5.1\ GeV/c$ and $\theta = 21$. Data refers to $\frac{F_2^D}{F_2^p}_{Data}$ and theory refers to the theory calculation of $\frac{F_2^D}{F_2^p}_{CJ15+E12}$

We begin by discussing figures 5.1 through 5.4, which constitute the lowest angle setting at $\theta = 21$. This angle setting ranges in $x$ from about $x = 0.22$ to $x = 0.76$. Largely, we see good agreement between $\frac{F_2^D}{F_2^p}_{Data}$ and $\frac{F_2^D}{F_2^p}_{CJ15+E12}$ with some discrepancy at the highest $E'$ value, $E' = 5.1 GeV/c$. We don't expect this discrepancy to be caused either by the pion contamination background or the charge symmetric background. This is due to the fact that at $E'$, we expect the number of pions to be suppressed relative to the number of electrons. Secondly, the charge symmetric background is expected to be largest at high scattering angles and low scattering energies. Given the fact that for a given scattering angle, the Bjorken $x$ range is advanced with increasing $E'$, we might expect resonances to play a bigger role in this large $x$ region.

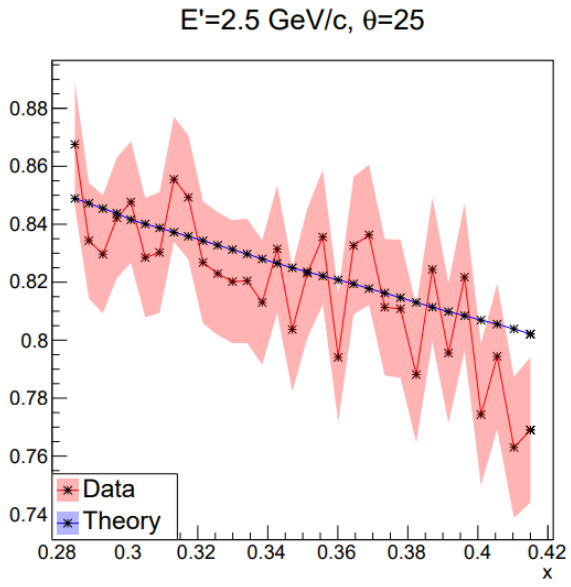


**Figure 5.5:** $\frac{F_2^D}{F^p}$ as a function of Bjorken $x$, for $E' = 2.5\ GeV/c$ and $\theta = 25$. Data refers to $\frac{F_2^D}{F_2^p}_{Data}$ and theory refers to the theory calculation of $\frac{F_2^D}{F_2^p}_{CJ15+E12}$

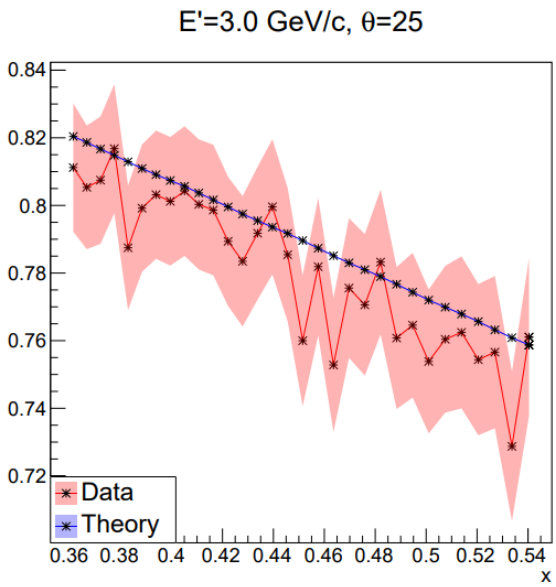


**Figure 5.6:** $\frac{F_2^D}{F^p}$ as a function of Bjorken $x$, for $E' = 3.0\ GeV/c$ and $\theta = 25$. Data refers to $\frac{F_2^D}{F_2^p}_{Data}$ and theory refers to the theory calculation of $\frac{F_2^D}{F_2^p}_{CJ15+E12}$

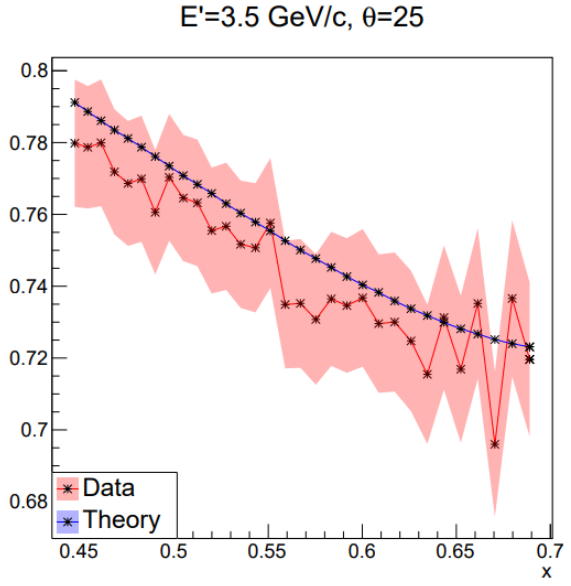


**Figure 5.7:** $\frac{F_2^D}{F^p}$ as a function of Bjorken $x$, for $E' = 3.5\ GeV/c$ and $\theta = 25$. Data refers to $\frac{F_2^D}{F_2^p}_{Data}$ and theory refers to the theory calculation of $\frac{F_2^D}{F_2^p}_{CJ15+E12}$

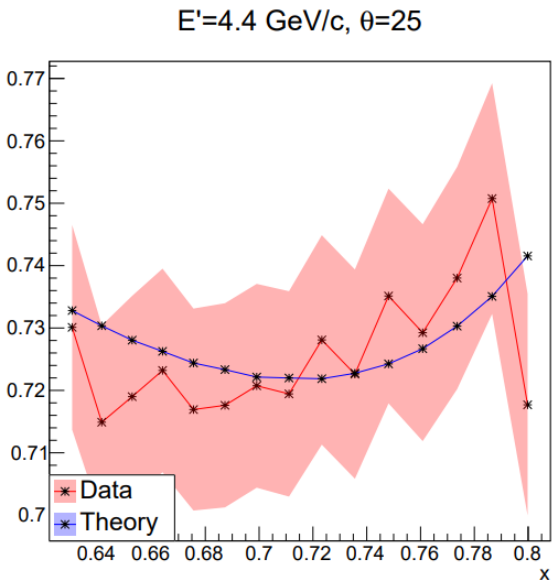


**Figure 5.8:** $\frac{F_2^D}{F^p}$ as a function of Bjorken $x$, for $E' = 4.4\ GeV/c$ and $\theta = 25$. Data refers to $\frac{F_2^D}{F_2^p}_{Data}$ and theory refers to the theory calculation of $\frac{F_2^D}{F_2^p}_{CJ15+E12}$

Figures 5.5 through 5.8 show $\frac{F_2^D}{F_2^p}_{Data}$ and $\frac{F_2^D}{F_2^p}_{CJ15+E12}$ for $\theta = 25$, and $x$ extends from about $x = 0.28$ to $x = 0.8$. Here, we see the general trend that as $\theta$ increases, the highest $E'$ scan larger values of $x$. The comparisons at this angle largely follow the observations of the previous angle, $\theta = 21$. Mostly, $\frac{F_2^D}{F_2^p}_{Data}$ and $\frac{F_2^D}{F_2^p}_{CJ15+E12}$ agree within uncertainties, however, we do observe that the theory calculations tend to sit just above the data points corresponding to $\frac{F_2^D}{F_2^p}_{Data}$. A possible explanation for this may be related to a normalization error present when this study was first carried out. Recent discussions with the JLab $F_2$ group suggest that this normalization has been corrected in the most up-to-date cross section data.

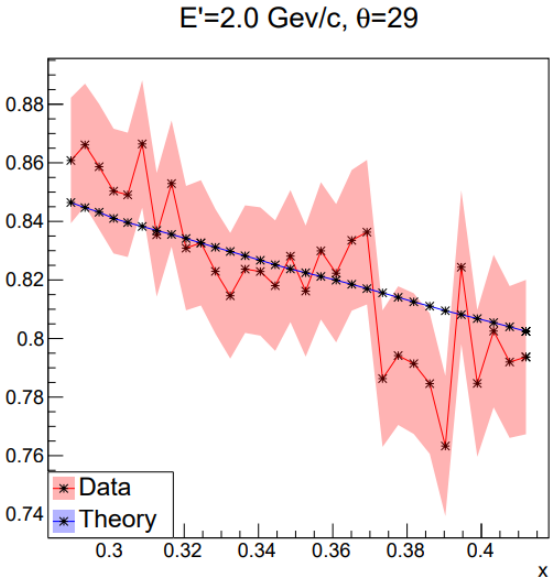


**Figure 5.9:** $\frac{F_2^D}{F^p}$ as a function of Bjorken $x$, for $E' = 2.0\ GeV/c$ and $\theta = 29$. Data refers to $\frac{F_2^D}{F_2^p}_{Data}$ and theory refers to the theory calculation of $\frac{F_2^D}{F_2^p}_{CJ15+E12}$

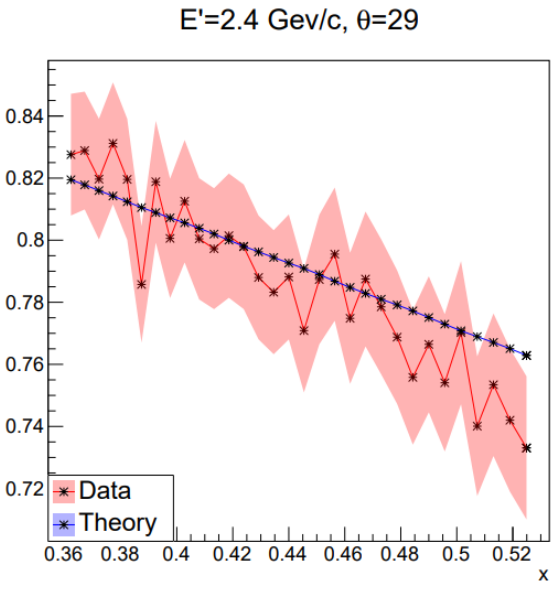


**Figure 5.10:** $\frac{F_2^D}{F^p}$ as a function of Bjorken $x$, for $E' = 2.4\ GeV/c$ and $\theta = 29$. Data refers to $\frac{F_2^D}{F_2^p}_{Data}$ and theory refers to the theory calculation of $\frac{F_2^D}{F_2^p}_{CJ15+E12}$

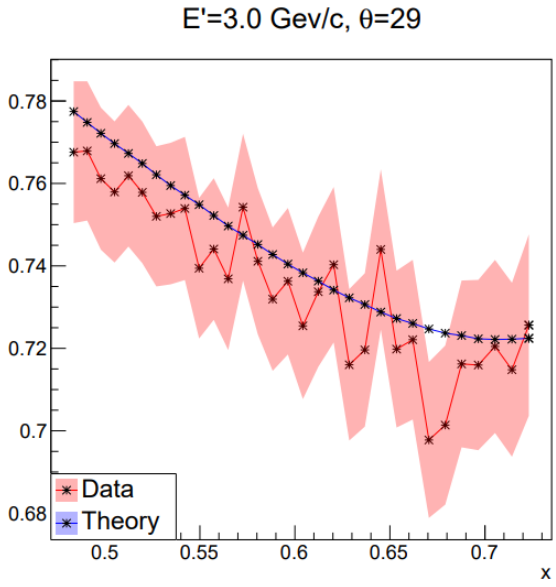


**Figure 5.11:** $\frac{F_2^D}{F^p}$ as a function of Bjorken $x$, for $E' = 3.0\ GeV/c$ and $\theta = 29$. Data refers to $\frac{F_2^D}{F_2^p}_{Data}$ and theory refers to the theory calculation of $\frac{F_2^D}{F_2^p}_{CJ15+E12}$

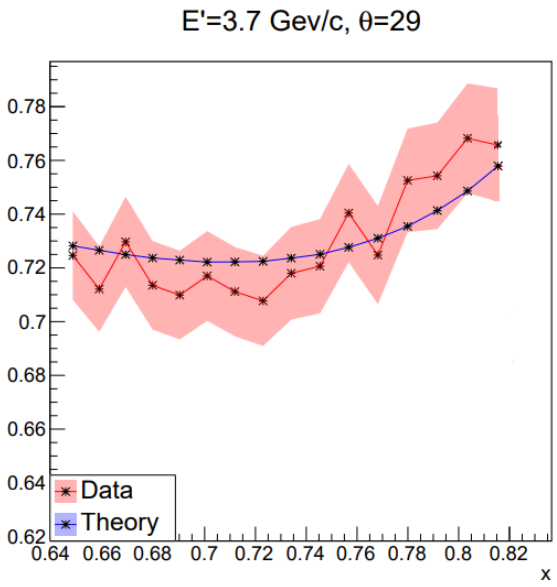


**Figure 5.12:** $\frac{F_2^D}{F^p}$ as a function of Bjorken $x$, for $E' = 3.7\ GeV/c$ and $\theta = 29$. Data refers to $\frac{F_2^D}{F_2^p}_{Data}$ and theory refers to the theory calculation of $\frac{F_2^D}{F_2^p}_{CJ15+E12}$

Figures 5.9 through 5.12 demonstrate the comparison between $\frac{F_2^D}{F_2^p}_{Data}$ and $\frac{F_2^D}{F_2^p}_{CJ15+E12}$ for $\theta = 29$. We notice that perhaps with the exception of 5.11, the theory data points no longer sit so far above $\frac{F_2^D}{F_2^p}_{Data}$. As mentioned previously, the pion contamination and charge symmetric background are generally expected to have a greater effect at lower scattering energies $E'$, and it appears that these contributions are beginning to grow.

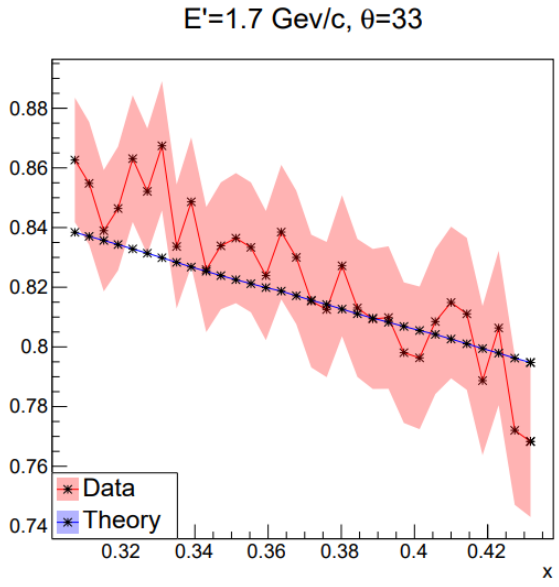


**Figure 5.13:** $\frac{F_2^D}{F^p}$ as a function of Bjorken $x$, for $E' = 1.7\ GeV/c$ and $\theta = 33$. Data refers to $\frac{F_2^D}{F_2^p}_{Data}$ and theory refers to the theory calculation of $\frac{F_2^D}{F_2^p}_{CJ15+E12}$

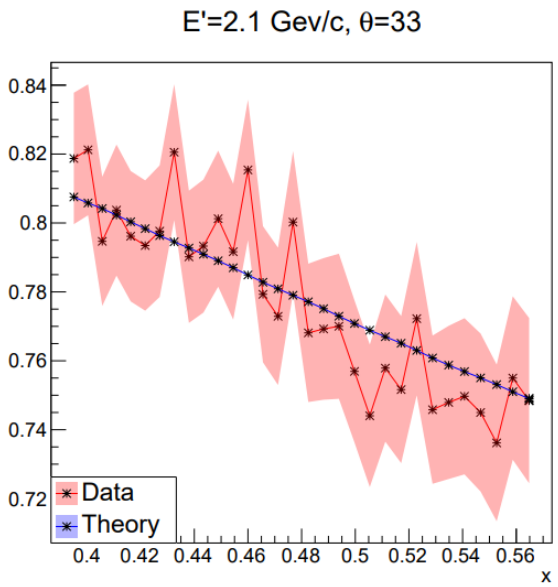


**Figure 5.14:** $\frac{F_2^D}{F^p}$ as a function of Bjorken $x$, for $E' = 2.1\ GeV/c$ and $\theta = 33$. Data refers to $\frac{F_2^D}{F_2^p}_{Data}$ and theory refers to the theory calculation of $\frac{F_2^D}{F_2^p}_{CJ15+E12}$

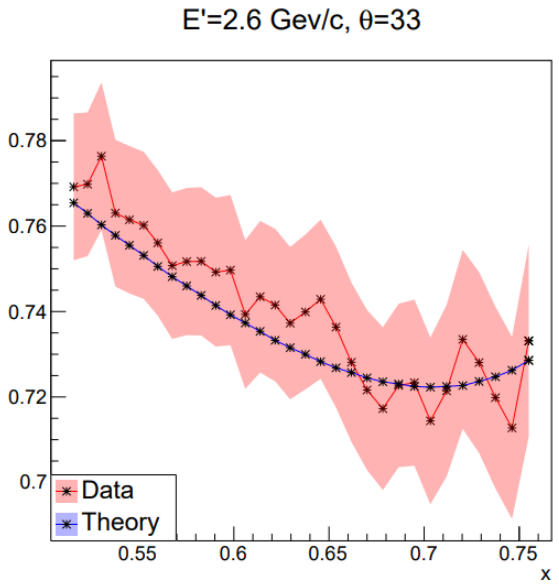


**Figure 5.15:** $\frac{F_2^D}{F^p}$ as a function of Bjorken $x$, for $E' = 2.6\ GeV/c$ and $\theta = 33$. Data refers to $\frac{F_2^D}{F_2^p}_{Data}$ and theory refers to the theory calculation of $\frac{F_2^D}{F_2^p}_{CJ15+E12}$

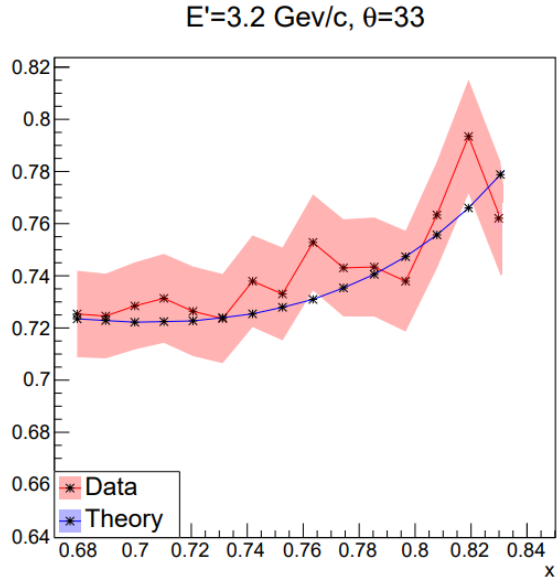


**Figure 5.16:** $\frac{F_2^D}{F^p}$ as a function of Bjorken $x$, for $E' = 3.2\ GeV/c$ and $\theta = 33$. Data refers to $\frac{F_2^D}{F_2^p}_{Data}$ and theory refers to the theory calculation of $\frac{F_2^D}{F_2^p}_{CJ15+E12}$

Figures 5.13 through 5.16 show the comparison between data and theory at $\theta = 33$. Here, we note a reversal of the trend we were seeing before. Whereas at lower $\theta$ we saw that $\frac{F_2^D}{F_2^p}_{Data}$ tended to be below $\frac{F_2^D}{F_2^p}_{CJ15+E12}$, now we see at $\theta = 33$ that it is above $\frac{F_2^D}{F_2^p}_{CJ15+E12}$. It is possible that this can be explained by the pion contamination and charge symmetric background. As discussed previously, these backgrounds are expected to make larger contributions at higher scattering angles $\theta$, and we see that indeed $\frac{F_2^D}{F_2^p}_{Data}$ tends to overshoot $\frac{F_2^D}{F_2^p}_{CJ15+E12}$. And as we will see, this effect continues up to the last scattering angle.

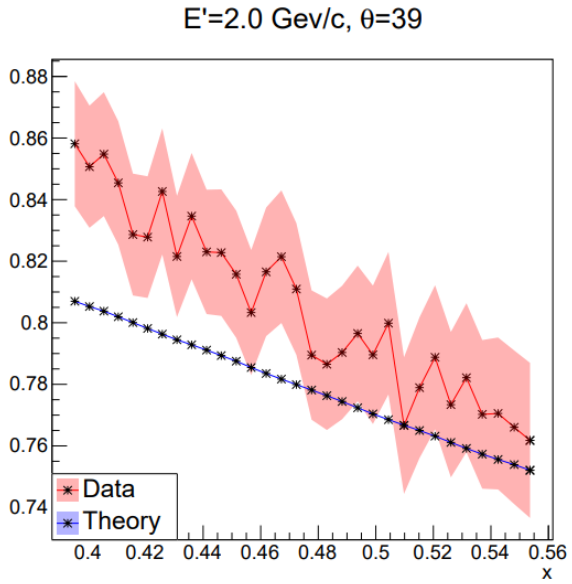


**Figure 5.17:** $\frac{F_2^D}{F^p}$ as a function of Bjorken $x$, for $E' = 2.0\ GeV/c$ and $\theta = 39$. Data refers to $\frac{F_2^D}{F_2^p}_{Data}$ and theory refers to the theory calculation of $\frac{F_2^D}{F_2^p}_{CJ15+E12}$

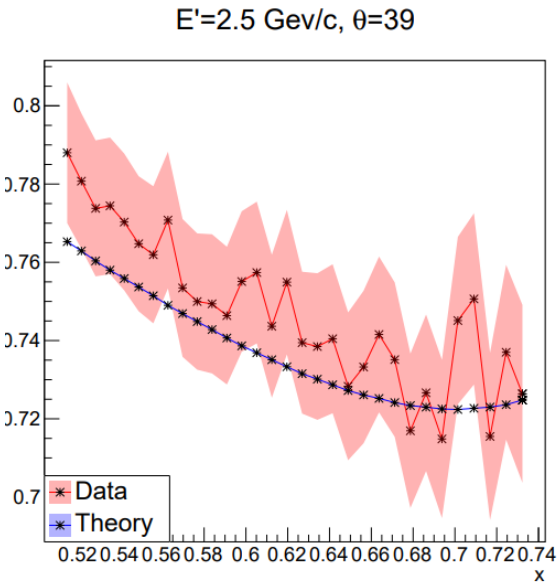


**Figure 5.18:** $\frac{F_2^D}{F^p}$ as a function of Bjorken $x$, for $E' = 2.5\ GeV/c$ and $\theta = 39$. Data refers to $\frac{F_2^D}{F_2^p}_{Data}$ and theory refers to the theory calculation of $\frac{F_2^D}{F_2^p}_{CJ15+E12}$

For the last scattering angle $\theta = 39$, we see notice a continuation and worsening of the discrepancy between $\frac{F_2^D}{F_2^p}_{Data}$ and $\frac{F_2^D}{F_2^p}_{CJ15+E12}$. Indeed, for 5.17, the discrepancy even extends outside of the uncertainties at low $x$. As previously stated, this is likely caused by the pion contamination and charge symmetric backgrounds that are most prominent at low $E'$ and high $\theta$. Indeed, we notice in 5.18 that as we go higher in $E'$, the agreement improves relatively, but the discrepancy is still apparent.

To conclude, we find that on the whole, $\frac{F_2^D}{F_2^p}_{Data}$ and $\frac{F_2^D}{F_2^p}_{CJ15+E12}$ largely agree for most kinematic settings. And even those which suffer most from systematic backgrounds tend to agree with $\frac{F_2^D}{F_2^p}_{CJ15+E12}$ within uncertainties. And finally, we emphasize again that it was the ratio $\frac{F_2^D}{F_2^p}$ that was used as an input to the CJ fit, rather than the separate structure functions. It is reiterated that this was done in part to try to mitigate the effects of the systematic background that appears in the previous figures. And to verify that this was the case, $F_2^D$ and $F_2^p$ were added into the CJ fit as separate inputs and it was observed that the discrepancy was far higher – the $\chi^2$ value was about was about 3.31 and 2.43 for $F_2^D$ and $F_2^p$ respectively. This is in comparison to the $\chi^2$ value of 0.75 when $\frac{F_2^D}{F_2^p}$ was used as the input.

### 5.2.1 Importance of Gluon Uncertainties

With the confirmation that $\frac{F_2^D}{F_2^p}_{Data}$ is in well agreement with the CJ calculation, we are ready to proceed with the fit and produce a new set of PDFs. However, before we do this, it will be useful to briefly discuss a very general but important application of global PDF analyses with data in the large-x region. This will help give context to the content presented in the following section, and will help us interpret their results. In particular, we discuss the role of PDFs and specifically the gluon distribution in beyond the standard model (BSM) physics. The importance of gluon uncertainties in BSM physics search can be succinctly summarized by the consideration that for these studies, QCD constitutes a background. Generally, it is absolutely necessary for any experiment to have a good determination of its backgrounds, lest its result be lost in them. The difficulty in this case is that QCD, with all of its unresolved uncertainties, must be better understood than the new physics for which one is searching. Large gluon uncertainties, in particular at large $x$, often plague many high energy cross sections attempting to study BSM physics. At the moment, gluon uncertainties in many global PDF analyses are mostly indirectly constrained by momentum sum rules. That is to say, the total momentum of

the partons in a nucleon must remain constant. DIS data may also constrain the gluon uncertainty indirectly through the study of scaling violations, and directly from inclusive jet production. However, this has not been sufficient to reduce the gluon uncertainty. It is one of the stated goals of the E12-10-002 experiment to help remedy this problem by contributing experimental data at large $x$ to directly constrain the gluon distribution.

Indeed, at the LHC top quark production cross sections suffer from three main sources of uncertainties; proton gluon uncertainties, the value of strong coupling $\alpha_s$, and the value of the top quark mass $m_t$.

| | TeVatron | LHC 7 TeV | LHC 8 TeV | LHC 14 TeV |
|---|---|---|---|---|
| $gg$ | 15.4% | 84.8% | 86.2% | 90.2% |
| $qg + \bar{q}g$ | -1.7% | -1.6% | -1.1% | 0.5% |
| $qq$ | 86.3% | 16.8% | 14.9% | 9.3% |

**Figure 5.19:** Relative contribution of branching ratios at different LHC energies

Figure 5.19 demonstrates that gluon-gluon scattering dominates with increasing energy, exactly where BSM physics could be found[MC13]. Indeed, many BSM predictions are gluon-initiated interactions, and therefore, any final states produced through gluon scattering will benefit from a decrease in gluon uncertainties.

In particular, as briefly mentioned, studying $t\bar{t}$ production is in fact intimately connected to a lot of BSM physics. This is due to the fact that the mass of the top quark is close to the mass scale of electroweak symmetry breaking, and thus, is strongly coupled to the Higgs boson. Indeed, BSM models have been proposed to explain the mechanism by which the Higgs mass is stabilized; the presence of the top quark radiative corrections contributes negatively to the Higgs mass, and therefore, an explanation is required for why the Higgs has the mass that is observed. Such mechanisms also require the existence of supersymmetric scalar particles. Additionally, BSM models predict graviton Kaluza-Klein resonances that couple strong to the third generation quarks, and in particular, the top quark[RF09].

### 5.2.2 Parton Distribution Functions

It is re-iterated that the final systematic uncertainty of the E12-10-002 experimental data sets have yet to be finalized as of the writing of this thesis. For this reason, we present the data set with three estimated systematic uncertainties; .75%, 1.5%, and 2%. Through talks and discussion with the $F_2$ group at JLab, the final systematic uncertainty is expected to be below 1%, but here we present more conservative estimates. In the following plots, we compare a ratio of the "CJ15_e12_ratio" and CJ15 fits, where the "CJ15_e12_ratio" data have three different systematic uncertainties included. Thus, the red line in the plot corresponds to the ratio between "CJ15" and itself, and so the line is equal to one across $x$. The uncertainty bands correspond to the relative uncertainty of the fits.

Finally, before the PDFs are presented, it is useful to have in mind the kinematic coverage of the E12-10-002 data set. We see in figure 5.20, that E12-10-002 covers and $x$ range from about $x = 0.2$ to about $x = 0.85$. This will help us interpret the results of the fit and allow us to cross-reference where any improvements are made with where in $x$ the data applies.

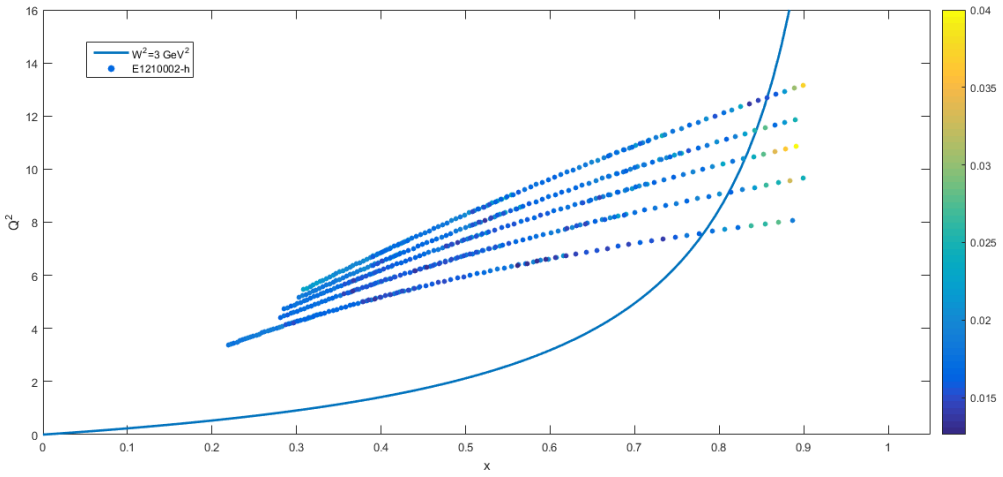


**Figure 5.20:** Kinematics plot of data measured for the Hydrogen target. The color scale indicates the relative uncertainty of the data point.

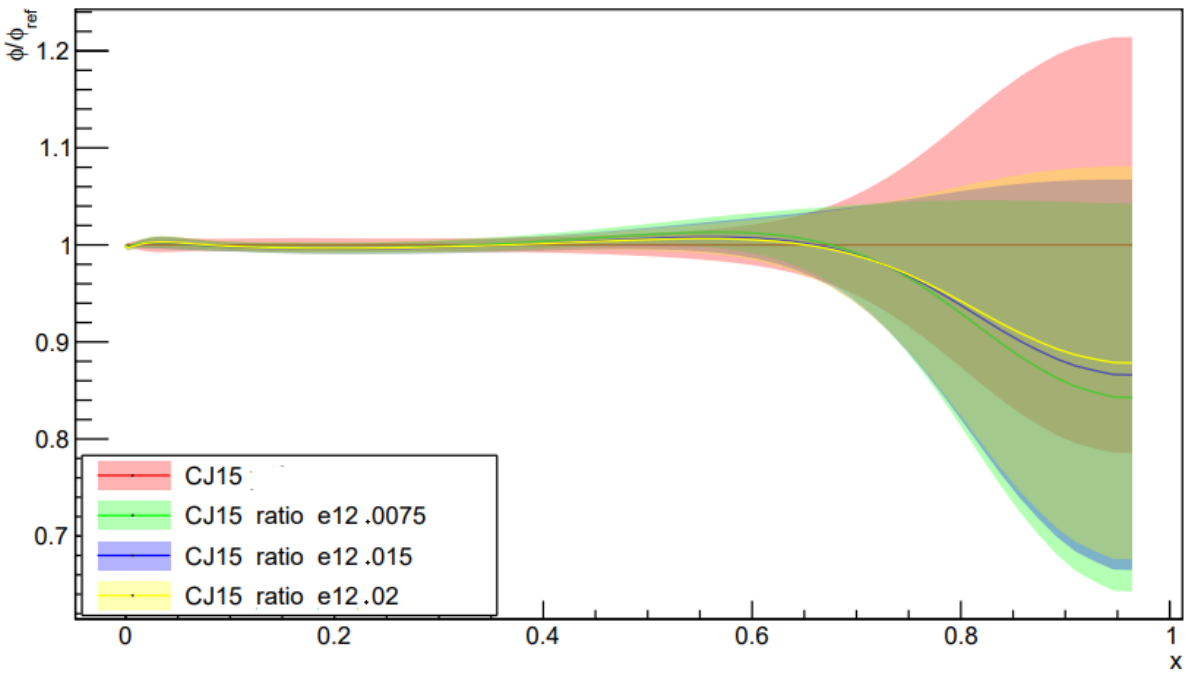


**Figure 5.21:** Parton distribution function ratios for d-quark over u-quark ratio as a function of x.

Figure 5.21 shows the ratio of the central values $\frac{\phi}{\phi_{ref}}$, where $\phi$ refers to the PDF fit of $\frac{d}{u}$ and $\phi_{ref}$ refers to the reference PDF of $\frac{d}{u}$, which is the fit produced by the standard CJ15 fit. As we can see, the addition of the E12-10-002 data appears to soften $\frac{d}{u}$ at large $x$, but still agrees with the CJ15 reference fit within uncertainty bands. We also note the impact of E12-10-002 is not heavily dependent on the systematic uncertainty added to the data set. As discussed previously, behavior of $\frac{d}{u}$ as $x \to 1$ is of some interest regarding a study of the spin-flavor dynamics in nucleons, and we note the effect of E12-10-002 to reduce this ratio at large $x$ by about 10% compared with the CJ15 fit.

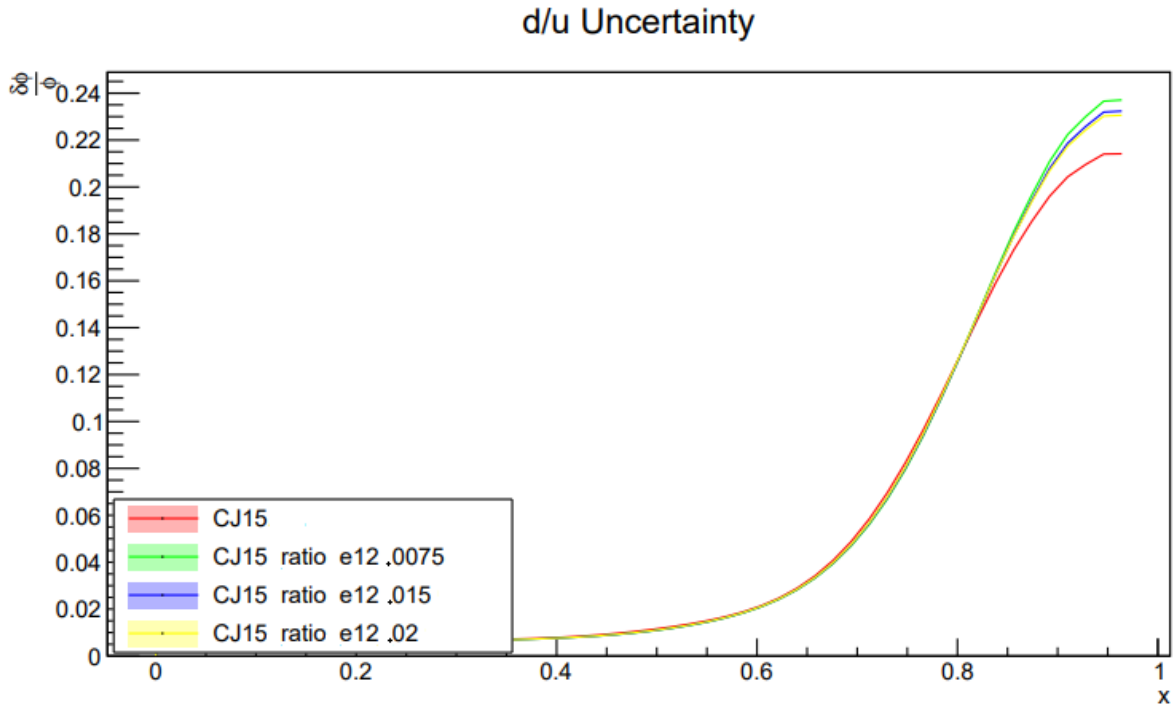


**Figure 5.22:** Parton distribution function uncertainty for d-quark over u-quark ratio as a function of x.

Figure 5.22 shows the relative uncertainty $\frac{\delta\phi}{\phi}$ for the different PDF fits of $\frac{d}{u}$. In fact, we are primarily interested in the uncertainty plots, as studying these will help us determine whether or not the E12-10-002 has a positive impact in reducing the uncertainties of the PDFs. Here, we note that unfortunately, E12-10-002 does not appear to make any significant impact at large $x$. In fact, it appears to make the uncertainties larger at the highest $x$ of about $x = 0.9$. We will see this can be attributed to an increased uncertainty in the down quark in the following figures.

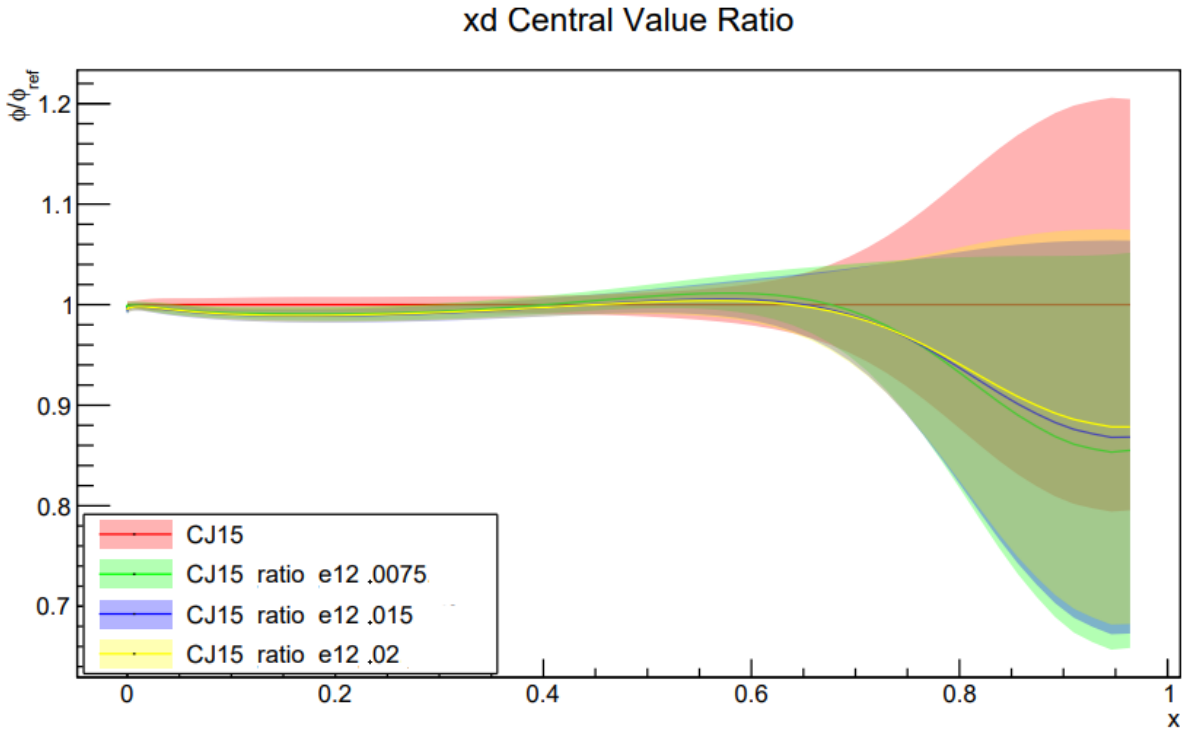


**Figure 5.23:** Parton distribution function ratios for the d-quark as a function of x.

Figure 5.23 again shows the central value ratio of $\frac{\phi}{\phi_{ref}}$, but this time for the down quark distribution. We notice that this figure is qualitatively similar as the one for $\frac{d}{u}$. This is largely expected, as the up quark distribution is relatively well constrained compared to the down quark, and therefore E12-10-002 is not expect to make a significant impact for the up quark. Thus, the behavior of $\frac{d}{u}$ follows closely from the behavior of the down quark.

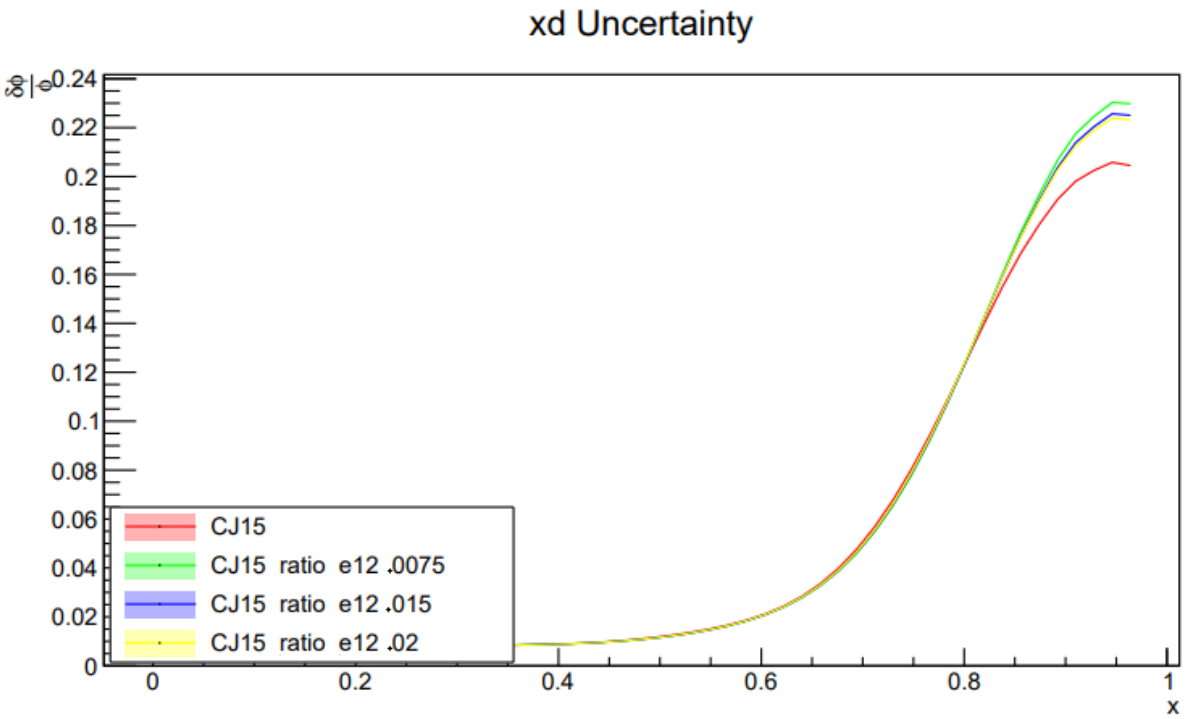


**Figure 5.24:** Parton distribution function uncertainty for the d-quark ratio as a function of x.

Figure 5.24 shows the relative uncertainty $\frac{\delta\phi}{\phi}$ for the down quark distribution. As before, the qualitative behavior of the down quark largely determines the behavior of $\frac{d}{u}$, and previous observations apply. The origin of discrepancy seen at about $x = 0.9$ is still not entirely clear, but cross referencing with the kinematic coverage of E12-10-002 shown in figure 5.20, we notice this discrepancy is just outside of the range where E12-10-002 covers. We are left to conclude that the aforementioned systematics may be playing some role in the discrepancy, but their position in $x$ suggests another explanation.

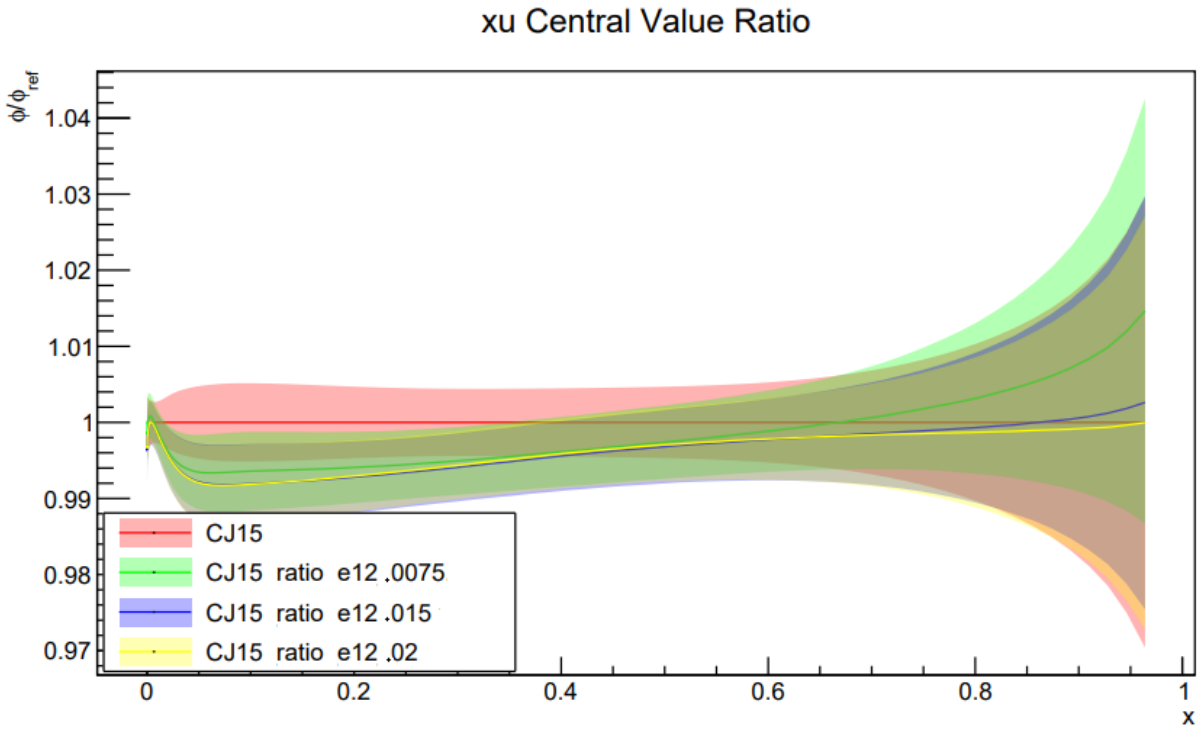


**Figure 5.25:** Parton distribution function ratios for the u-quark as a function of x.

Figure 5.25 shows $\frac{\phi}{\phi_{ref}}$ for the up quark distribution. As previously discussed, E12-10-002 was not expected to provide significant constraining power on the up quark. We do notice the inclusion of E12-10-002 induces a reduction in the distribution at low $x$ and an increase at large $x$, but these changes are well within uncertainty bands and amount to only a few percent difference in the central value.

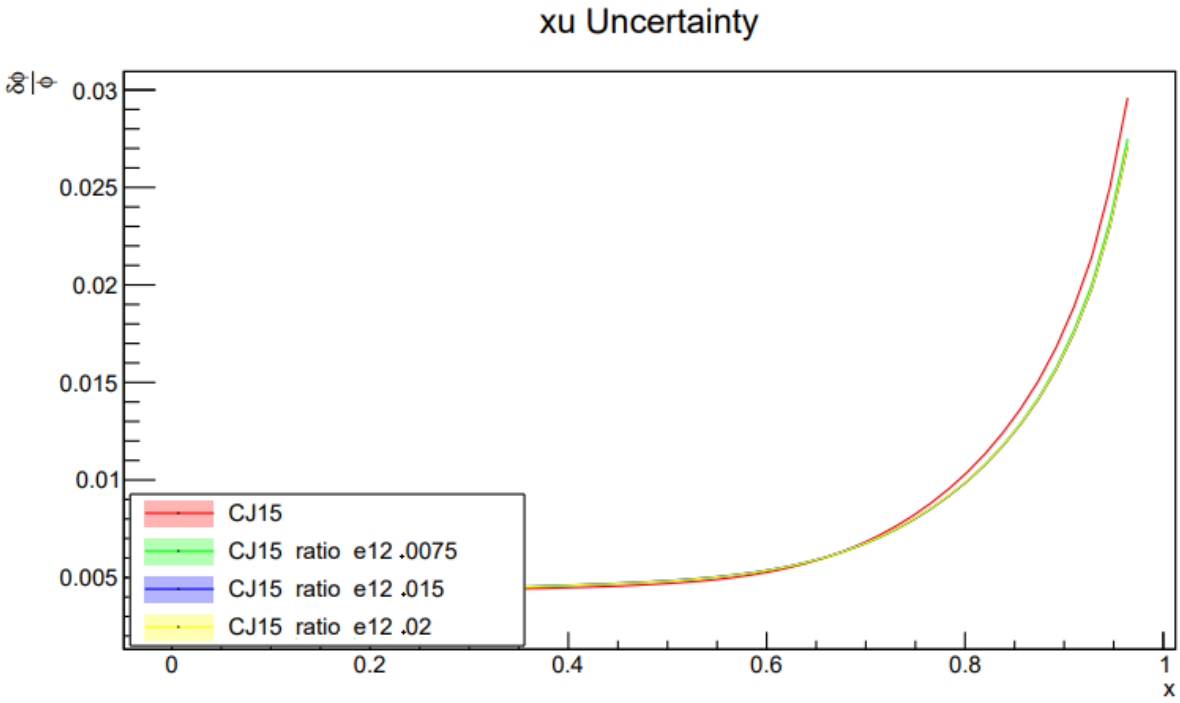


**Figure 5.26:** Parton distribution function uncertainty for the u-quark as a function of x.

Figure 5.26 plots the relative uncertainty $\frac{\delta\phi}{\phi}$ for the up quark distribution. Here, we are not surprised by the relatively low impact of E12-10-002.

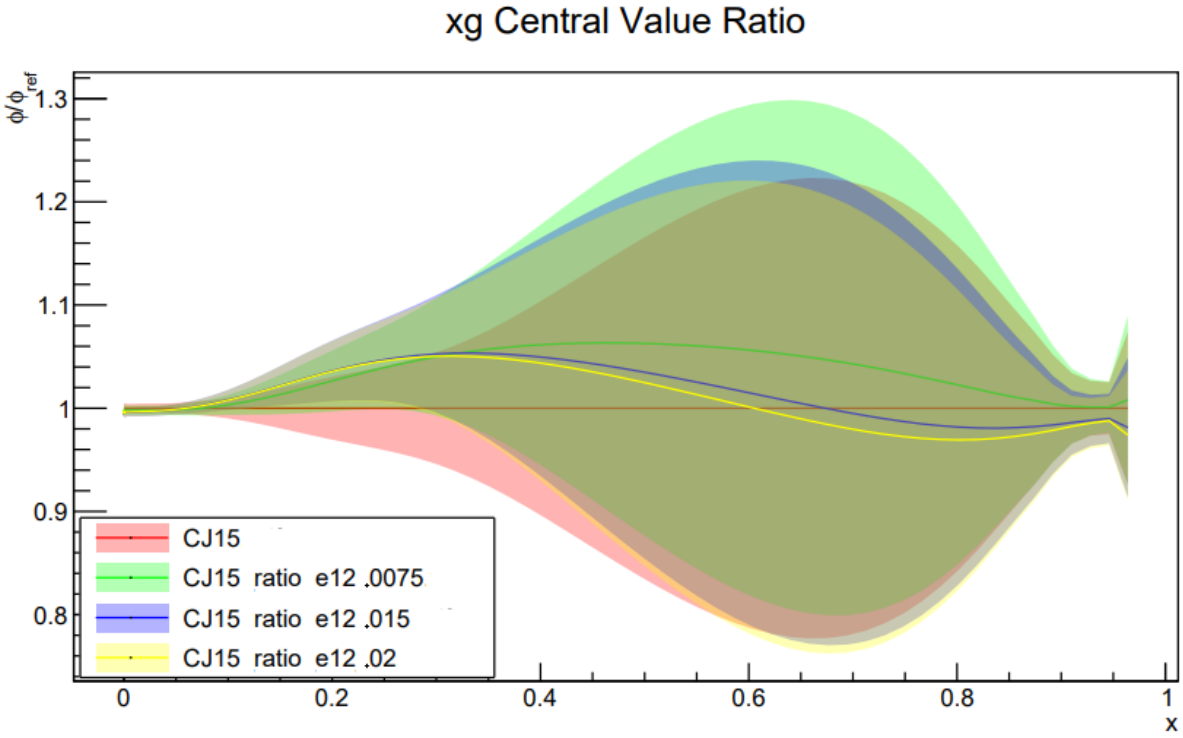


**Figure 5.27:** Parton distribution function ratios for the gluon as a function of x.

Finally, figure 5.27 corresponds to the ratio of the central value, $\frac{\phi}{\phi_{ref}}$, for the gluon. We see some variation in the central value but it is all within uncertainties.

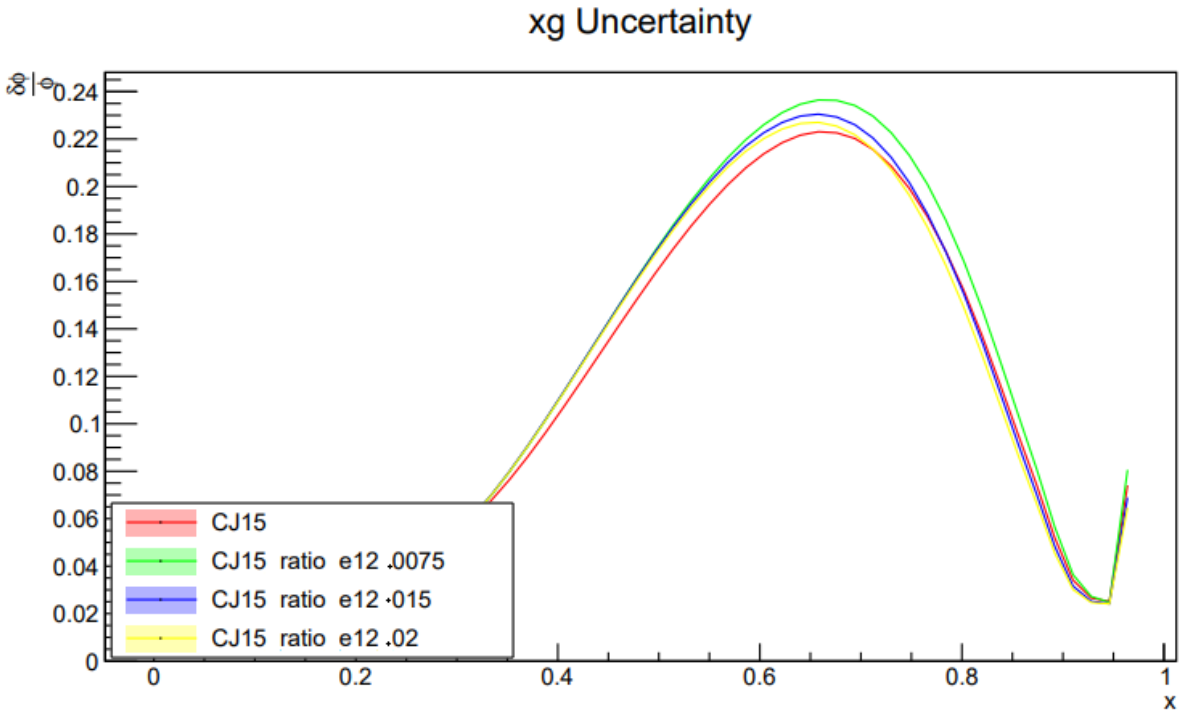


**Figure 5.28:** Parton distribution function uncertainty for the gluon as a function of x.

Figure 5.28 shows the relative uncertainty $\frac{\delta\phi}{\phi}$ for the gluon. Here, we also expect minimal impact from E12-10-002 on constraining the gluon. This is due to the fact that we are fitting the structure functions $F_2$ rather than the cross sections, which contains the full nuclear information about the nucleons. Thus, the constraint on the gluon from E12-10-002 comes only from DGLAP evolution. However, because we have fit the ratio of structure functions $\frac{F_2^D}{F_2^P}$ it is largely expect that the QCD evolution effects will cancel between the numerator and denominator. We do note the inclusion of the E12-10-002 data appears to increase the uncertainty in the gluon around $x = 0.6$. In light of the explanation for why E12-10-002 is not expect to impact the gluon uncertainty, one possible explanation could be that there is some tension between E12-10-002 and one or more data sets with regards to the gluon.

We finish by concluding that the impact of the E12-10-002 data set on the up quark, down quark, and gluon distribution is minimal. However, as will be explored in the following section, there is an argument to be made about considering E12-10-002 as one

of many JLab experiments that, when taken as a whole, may provide the impact we are seeking.

### 5.2.3 JLab 6 GeV + 12 GeV

While we have presented only the impact of the 12 GeV E12-10-002 data on CJ15, it is perhaps better to speak about the inclusion of this data in the greater context of previous JLab experimental data from the 6 GeV era. Indeed, there are five additional 6 GeV data sets that have yet to be included into the CJ15 fit.

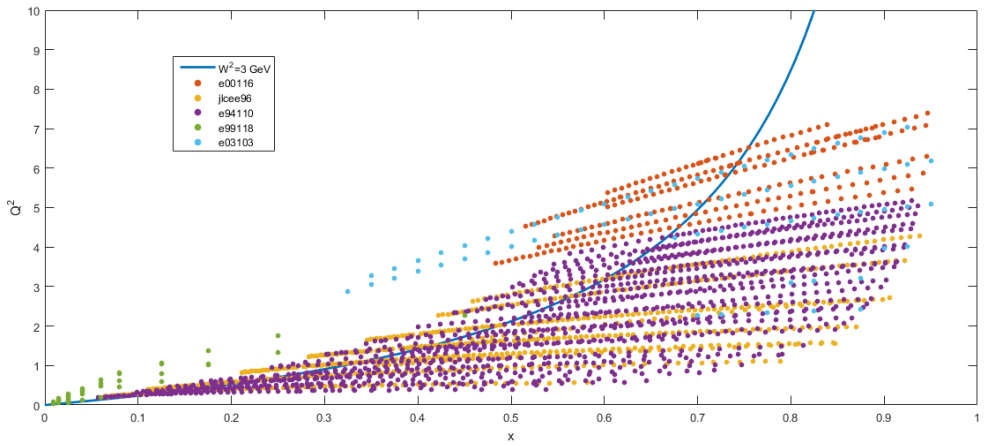


**Figure 5.29:** Bjorken x and $Q^2$ coverage of additional JLab 6 GeV data sets. The $W^2 = 3\ GeV$ line delineates the data points included in the CJ15 kinematic cuts; only points to the left of the $W^2$ line are fit.

The $jlcee96$, $e94110$, $e06009$, $e00116$, and $e03103$ data sets constitute previously unused data sets in the context of global PDF fitting and their combined kinematic coverage is shown in figure 5.29. In order to assess the impact of including the JLab data into CJ15, we plot the relative uncertainty of the two fits. It is also noted that the fits are plotted in the $x$ range for which the data has applicability; that is, from $0.2 - 0.8$ in $x$.

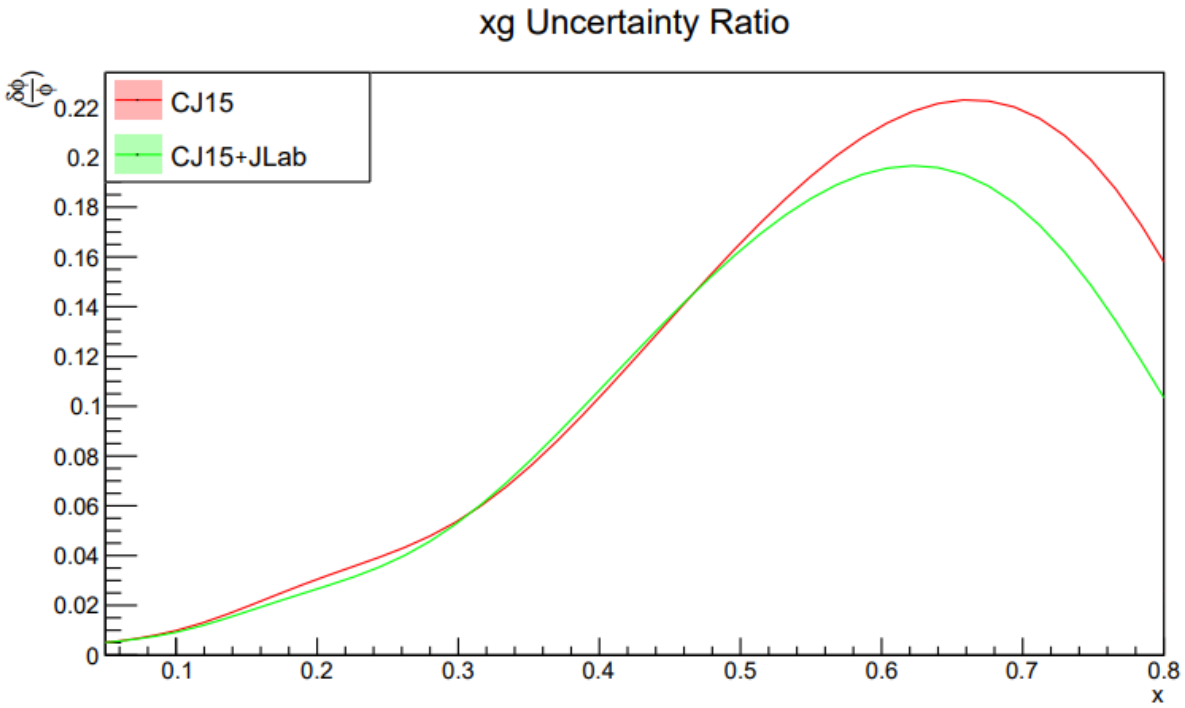


**Figure 5.30:** Plot of relative gluon uncertainty comparing CJ15 with CJ15 plus the 6 GeV data sets and the 12 GeV E12-10-002 data set.

We see in figure 5.30 that the inclusion of the 6 GeV data sets along with E12-10-002 can help to reduce the systematic uncertainty in the gluon, particularly in the region $x = 0.6$ to $x = 0.8$, by almost 20%. Additionally, it was found in a separate analysis by the CTEQ-JLab collaboration at JLab, that the inclusion of the 6 and 12 GeV data sets significantly reduce the uncertainties of the off-shell parameters discussed in section 5.1.2. A tighter constraint on the off-shell parameters leads directly to a better constraint on $\frac{d}{u}$. Indeed, the large $x$ behavior of $\frac{d}{u}$ is of great theoretical importance and reducing its uncertainty can help to exclude several models that make predictions about its asymptotic value. At large $x$, one may approximate $F_2^p$ and $F_2^n$ as,

$$F_2^p \approx \frac{4}{9}u + \frac{1}{9}d \tag{5.17}$$

$$F_2^n \approx \frac{4}{9}d + \frac{1}{9}u \tag{5.18}$$

so solving for $\frac{d}{u}$, we find

$$\frac{d}{u} \approx \frac{4 - \frac{F_2^n}{F_2^p}}{4\frac{F_2^n}{F_2^p} - 1} \tag{5.19}$$

For example, assuming an SU(6) symmetry, as $x \to 1$, one has $u(x) = 2d(x)$. Thus,

$$SU(6) : \frac{d}{u} \to \frac{1}{2} \tag{5.20}$$

A different model assumes a scalar diquark dominance at high-x. Since only $u$-quarks couple to scalar diquarks,

$$\frac{F_2^n}{F_2^p} \to \frac{1}{4} \tag{5.21}$$

and thus,

$$Diquark : \frac{d}{u} \to 0 \tag{5.22}$$

Yet another model predicts that hard gluon exchange dominates the large-x behavior of $\frac{d}{u}$. Here,

$$\frac{F_2^n}{F_2^p} \to \frac{3}{7} \tag{5.23}$$

and so,

$$Hard\ Gluon\ Exchange : \frac{d}{u} \to \frac{1}{5} \tag{5.24}$$

The current CJ15 fit puts this ratio below these predictions, at about 0.09, and the addition of the JLab data sets brings it down a little more, as shown as shown in figures 5.31 and 5.32. However, this is still in agreement with the previous CJ15 value within uncertainty bands.

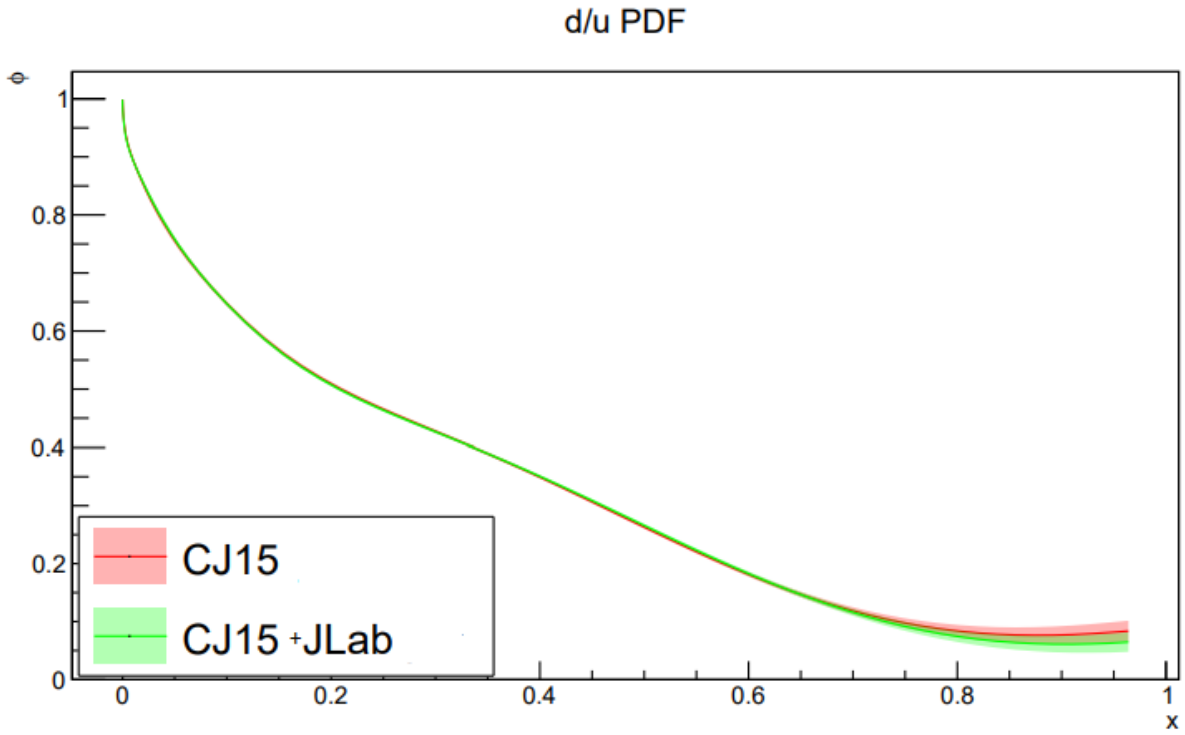


**Figure 5.31:** Parton distribution function for $\frac{d}{u}$ for CJ15 and CJ15 plus the 6 GeV JLab data sets and the 12 GeV E12-10-002 data set with 1.5% systematic uncertainty.

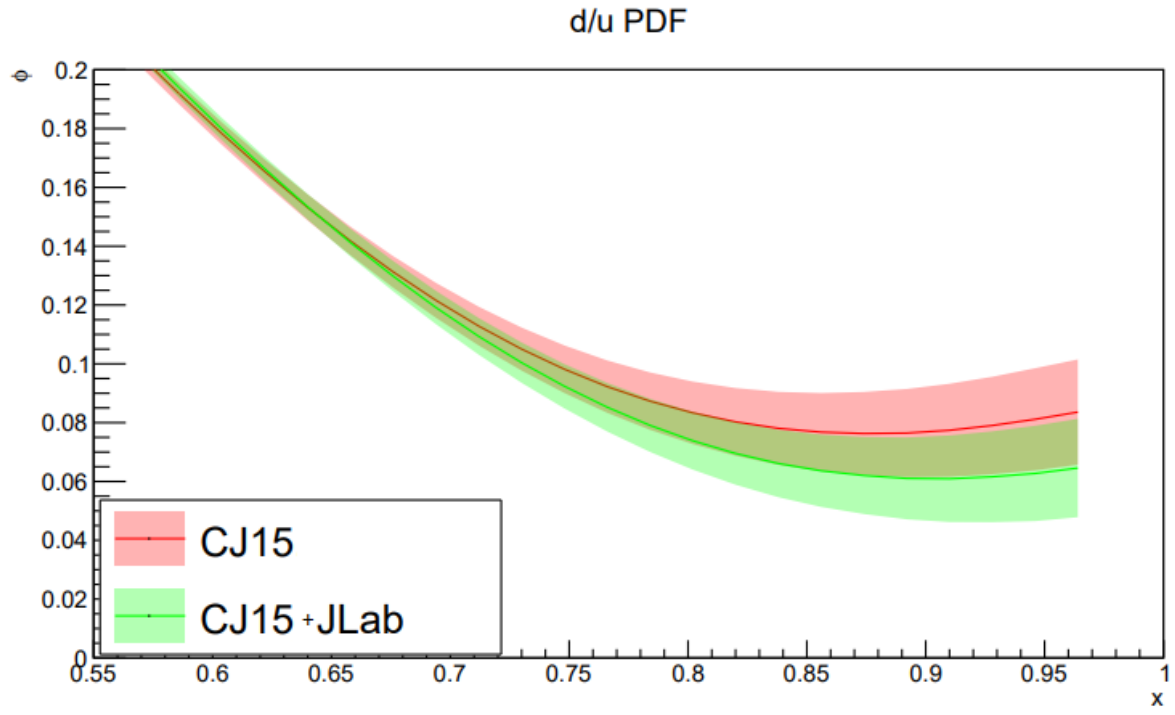


**Figure 5.32:** Inset of the $\frac{d}{u}$ parton distribution function to better illustrate the large x behavior.

In addition to the E12-10-002 data, we may also make use of preliminary results from another 12 GeV JLab experiment called MARATHON. The MARATHON experiment ran concurrently with E12-10-002 in Hall A. It sought to take measurements on tritium and helium-3 targets. The choice of such targets relies on the clever observation that a ratio of these measurements can be made in such a way to cancel out the nuclear effects that often plague measurements on the neutron. Indeed, tritium is composed of 2 neutrons and 1 proton, while helium-3 is composed of 1 neutron and 2 protons. Thus, we can form the ratio,

$$R_{3H} = \frac{F_2^{3H}}{2F_2^n + F_2^p} \tag{5.25}$$

and

$$R_{3He} = \frac{F_2^{3He}}{F_2^n + 2F_2^p} \tag{5.26}$$

Further, if we define the so-called super-ratio as,

$$R^* = \frac{R_{3He}}{R_{3H}} \tag{5.27}$$

we may express $F_2^n/F_2^p$ as

$$\frac{F_2^n}{F_2^p} = \frac{2R^* - F_2^{3He}/F_2^{3H}}{2(F_2^{3He}/F_2^{3H}) - R^*} \tag{5.28}$$

Thus, by measuring $F_2^{3He}/F_2^{3H}$ one has direct access to $F_2^n/F_2^p$ with relatively small nuclear effects. Indeed, referencing figure 5.33, we can see how independently the spectral functions of tritium and helium-3 have an imprint of large nuclear effects, while the super-ratio is relatively flat across a large range of Bjorken x.

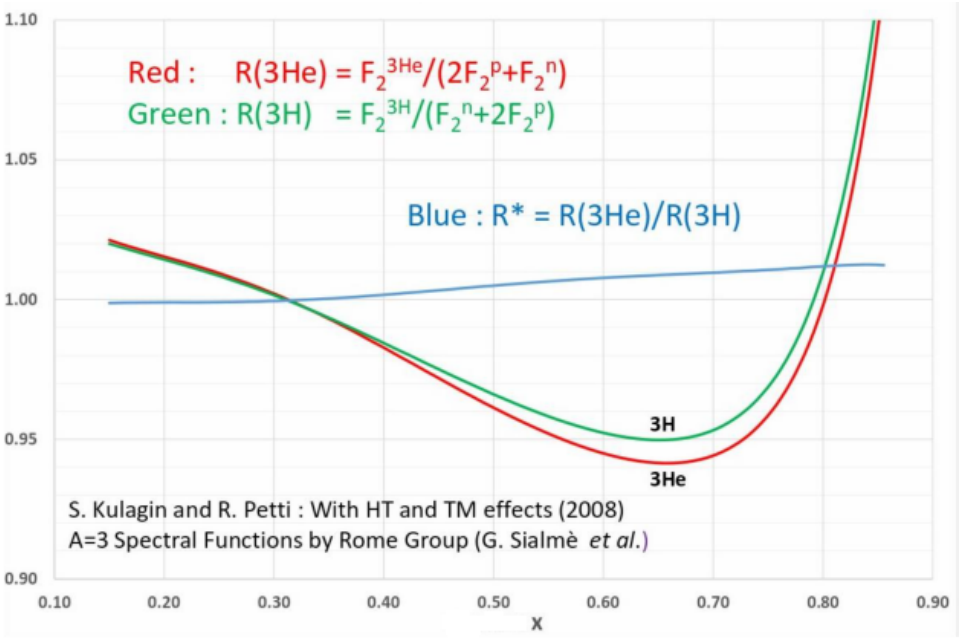


**Figure 5.33:** Spectral functions as a function of Bjorken x. Image: Tung Su

Preliminary results for $F_2^n/F_2^p$ are presented in figure 5.34.

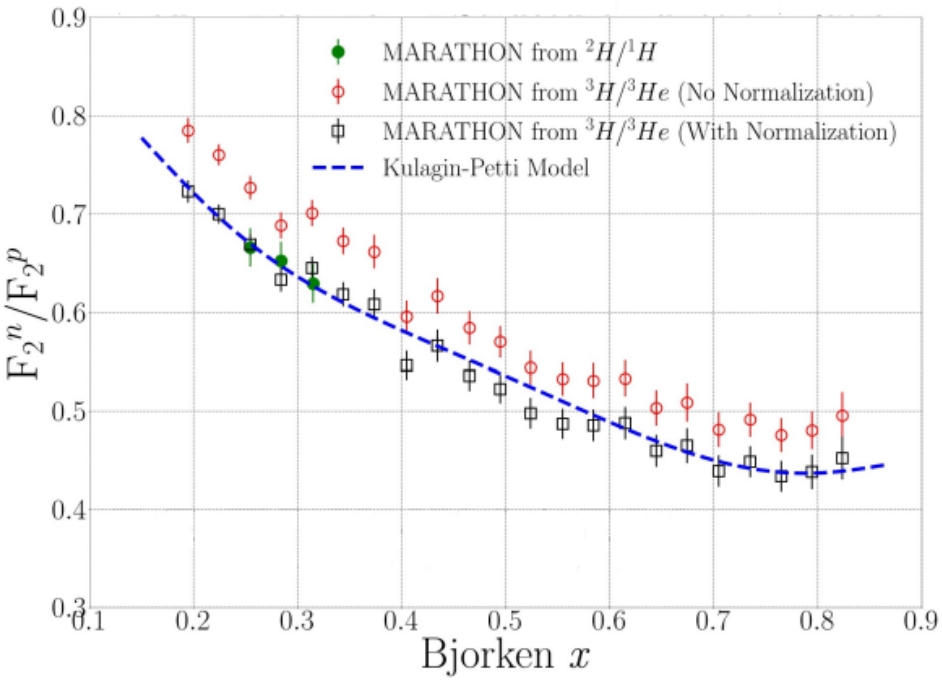


**Figure 5.34:** $F_2^n/F_2^p$ as a function of Bjorken x

These results can further be compared to the previous seminal measurements of $F_2^n/F_2^p$ from SLAC and the accompanying fit by Bodek et al in figure 5.35.

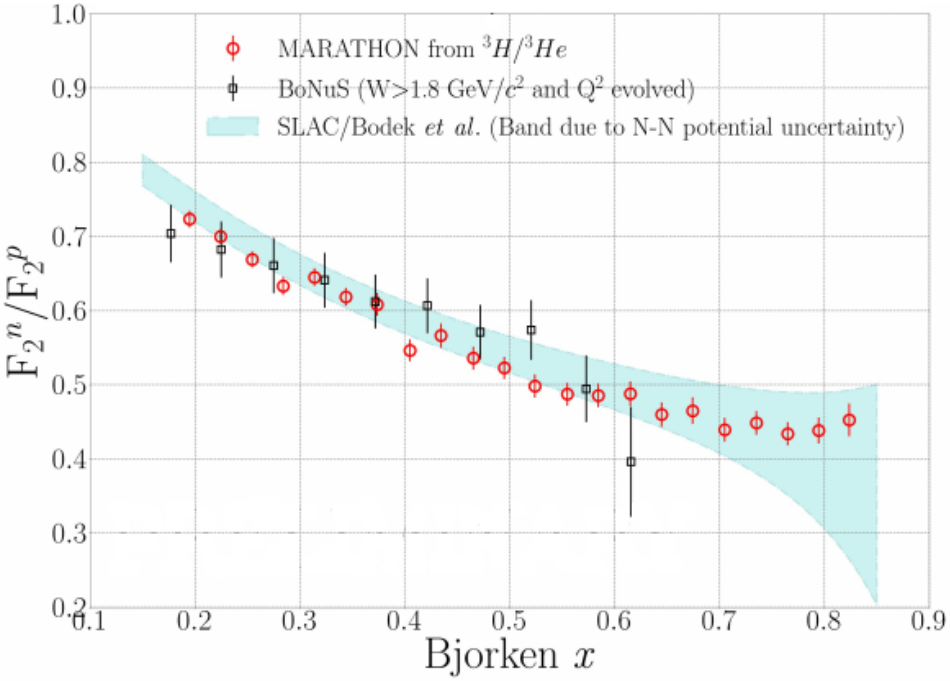


**Figure 5.35:** Comparison of $F_2^n/F_2^p$ against SLAC analysis as a function of Bjorken x, as well as BoNuS data.

Finally, while a direct comparison between the limit behavior of $\frac{d}{u}$ between E12-10-002 and MARATHON is not yet available, we are given a hint at their agreement by the comparison of $\sigma_D/\sigma_H$. In figure 5.36 we see that E12-10-002 and MARATHON largely agree. We also note that there is a discrepancy in the E12-10-002 39 degree data. This is due to the fact that the charge symmetric background is particularly large at this kinematic setting and has yet to be subtracted.

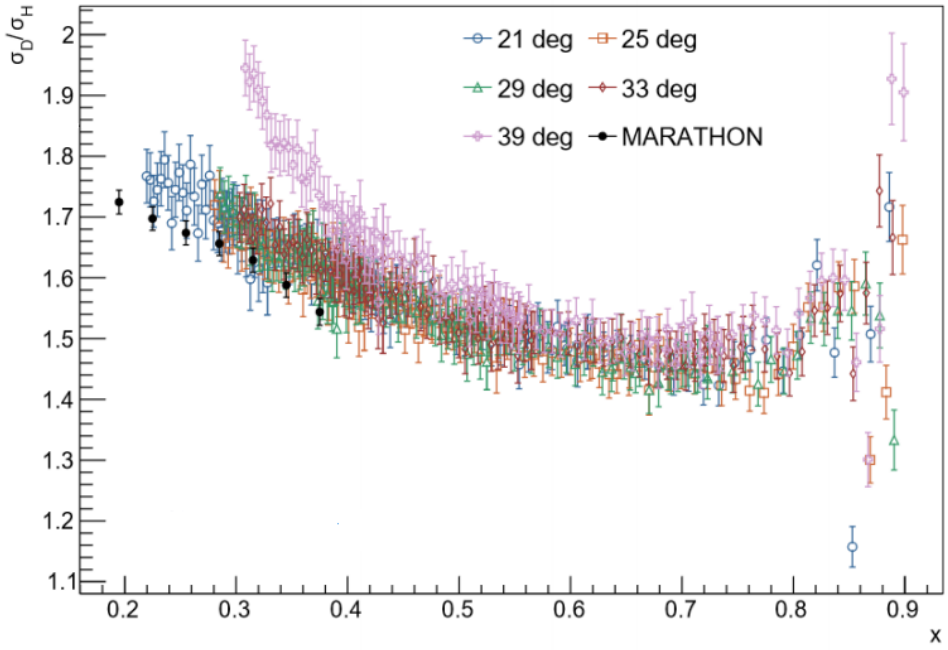


**Figure 5.36:** Ratio of $\sigma_D/\sigma_H$ as a function of Bjorken x for E12-10-002 and MARATHON data.

### 5.2.4 A Future Perspective and the EIC

The Electron Ion Collider (EIC) represents the next generation of high-energy, high-luminosity, polarized collider in the world. Brookhaven National Laboratory was recently chosen as the location of the new EIC, where the infrastructure of RHIC will serve as the backbone to the EIC. A preliminary design of the EIC is shown in figure 5.37.

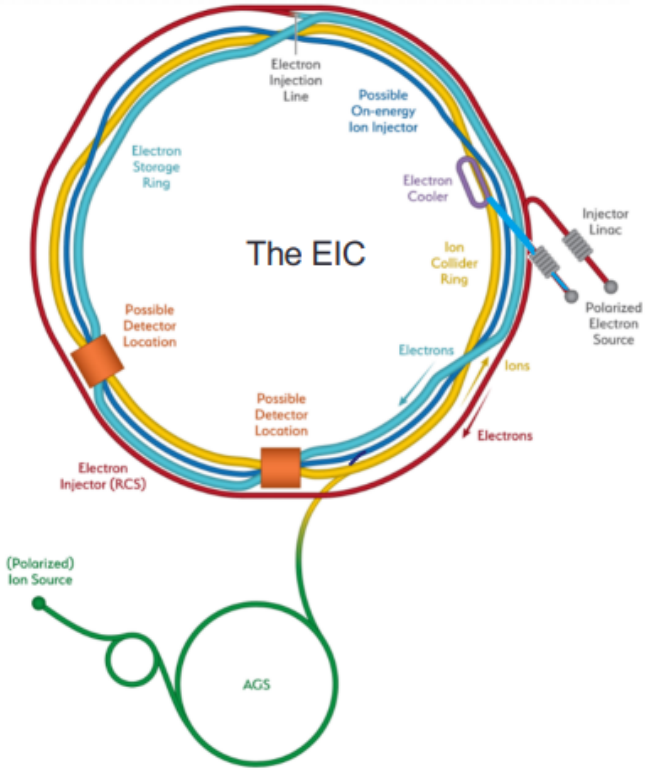


**Figure 5.37:** Preliminary design of the EIC at Brookhaven

Among other topics, the EIC seeks to answer fundamental questions about the spin of the proton; both its origin and how it is connected to the spin-$\frac{1}{2}$ quarks and the spin-1 gluons. To this end, the EIC is proposed to make precision measurements of the $g_1$ polarized structure function as proposed in figure 5.38.

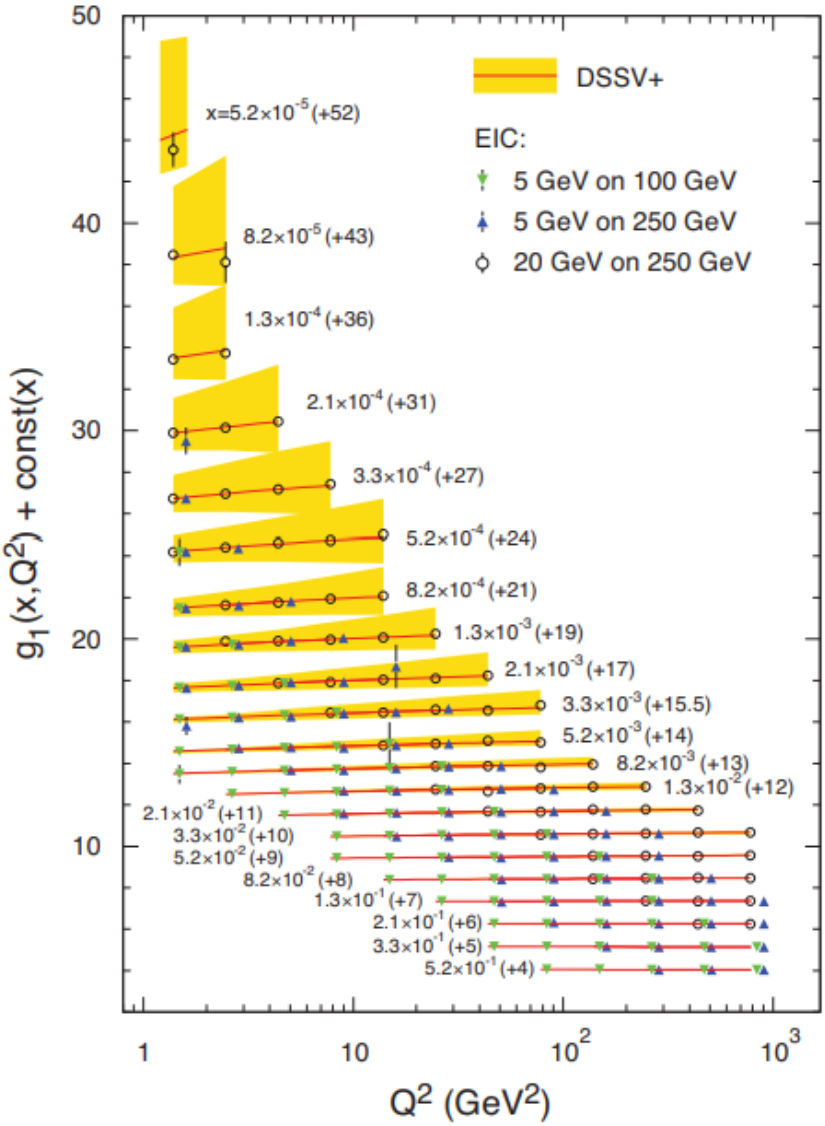


**Figure 5.38:** Simulated EIC data of the $g_1$ polarized structure function for different electron and proton beam energies respectively. Uncertainty bands correspond to a separate analysis[Flo08]

For this reason, the design goals of the EIC require it to achieve polarized beams of up to 70% polarization. In addition to a polarized electron beam, the EIC is will also make use of polarized proton, deuteron, and helium beams. Further, the EIC will address a wide range of phenomenon that operate at different energy scales. On one hand, the EIC will attempt to study nuclear matter at extremely high densities; possibly where gluonic matter saturates. On the other hand, it will also study the origin of sea quarks and gluons in the nucleons at low $Q^2$ – one may naively assume that only valence quarks matter in

this regime, however, experimental data suggests that even at low resolution sea quarks are an important part of the puzzle that is hadronic matter. In order to address these and other questions, the EIC will be capable of accessing a large center-of-mass energy range, from $20 - 100\ GeV$, with the capability to reach 140 $GeV$.

Figure 5.39 demonstrates how the kinematic coverage of the EIC will allow for a wider and more comprehensive study of nuclear matter. Indeed, the coverage of the EIC spans across a large range of $Q^2$; this allows for a direct study of model-independent $Q^2$ evolution. It's coverage in x is also unprecedented, allowing for simultaneous studies of valance and low-x physics.

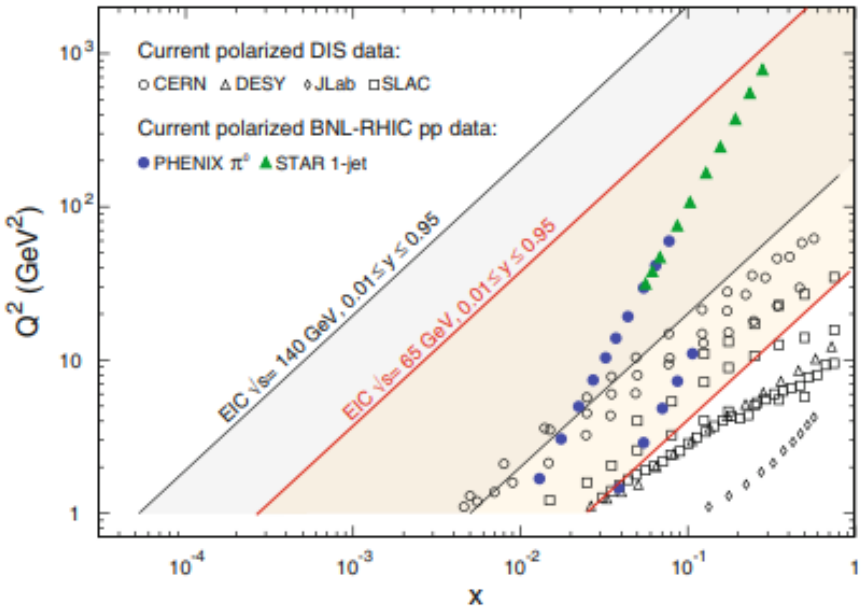


**Figure 5.39:** Kinematic coverage in $x$ and $Q^2$ for various polarized DIS data.

Of course, it is not sufficient to only access these energy regimes, it is important that the measurements be precise. Thus, the EIC is proposed to reach a luminosity of $10^{33-34} cm^{-2} s^{-1}$ as shown in figure 5.40.

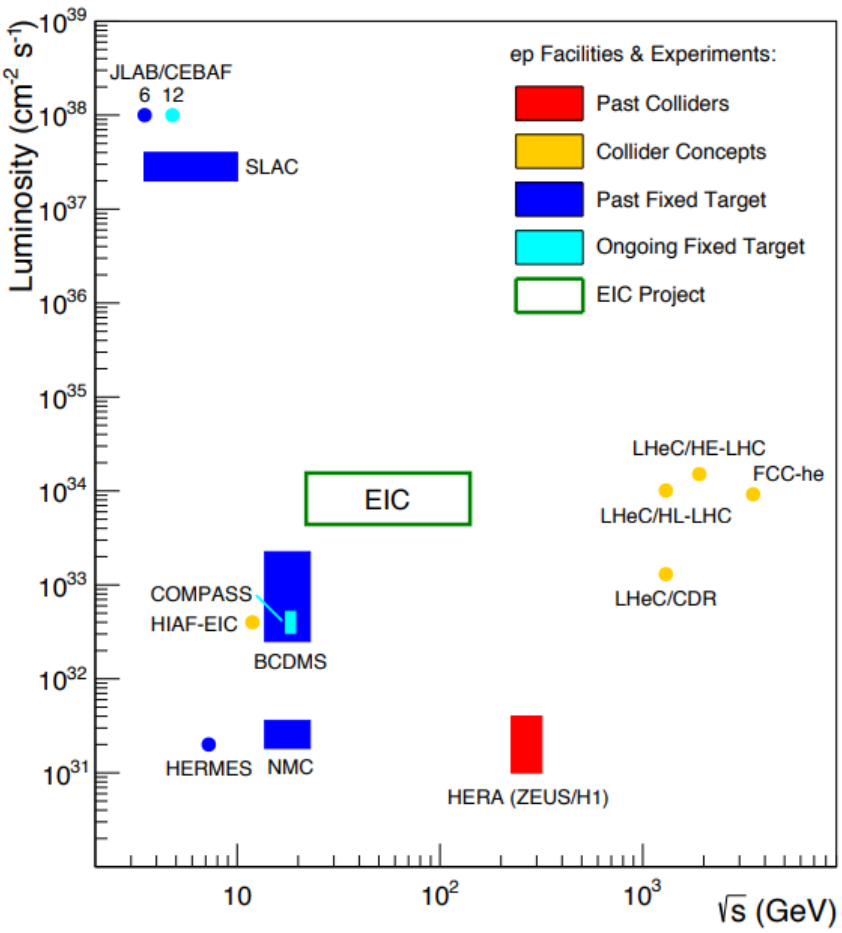


**Figure 5.40:** Luminosity and center-of-mass energies of the EIC as well as past experiments and proposed facilities.

The EIC is poised to address some of the most fundamental questions about nuclear physics that still remain today. For example, it is still not completely understood how the spin of the proton is related to the polarization and orbital angular momentum of its partons. It has been shown that the net polarization associated with quarks and anti-quarks can only account for about 30% of the spin of the proton[Hag10]. Further, lattice QCD calculations have suggested that the remaining 70% can not be attributed to the orbital angular momentum of the quarks. In addition, results from RHIC suggest that gluon polarization may play a large role instead. The EIC has the chance to weigh in on this fundamental question, and simulated EIC data suggests it can lay the groundwork towards a definitive answer. Figure 5.41 demonstrates how the uncertainties in the net

gluon polarization, $\Delta g$, is reduced by the inclusion of simulated EIC data, in particular, at low-x.

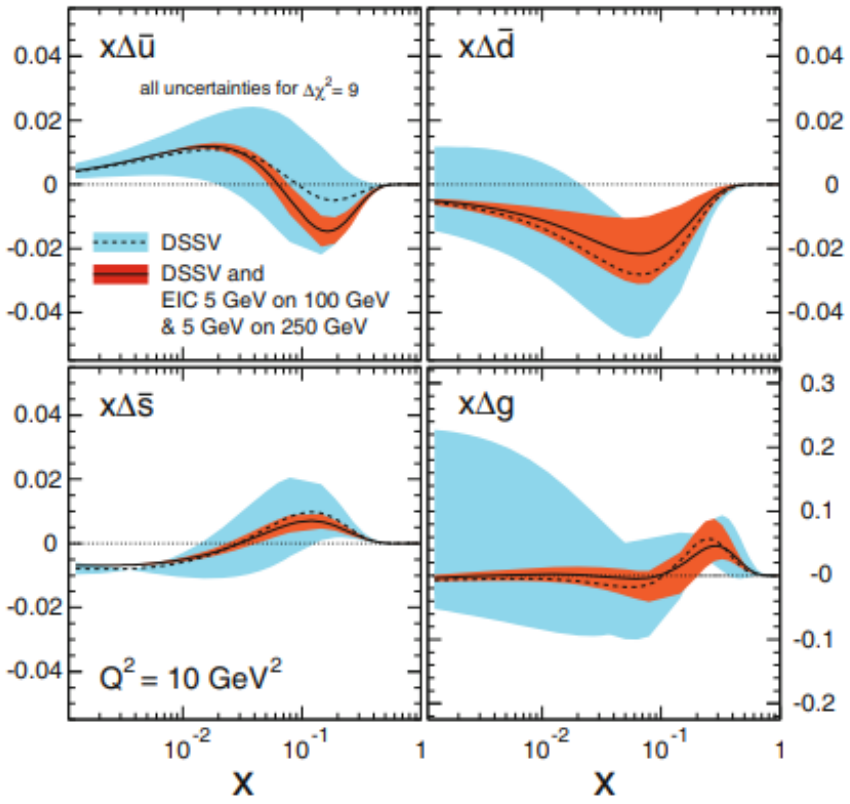


**Figure 5.41:** Impact of EIC data on net parton polarization, and in particular, $\Delta g$, on top of a DSSV analysis[Flo08]

In addition, a global PDF fitting program has the potential to make significant contributions to future EIC results. In order to explore what these contributions may be, we may apply the same global PDF fitting techniques to simulated unpolarized EIC data. First, we present the kinematic coverage of a simulated data set for the EIC in figure 5.42.

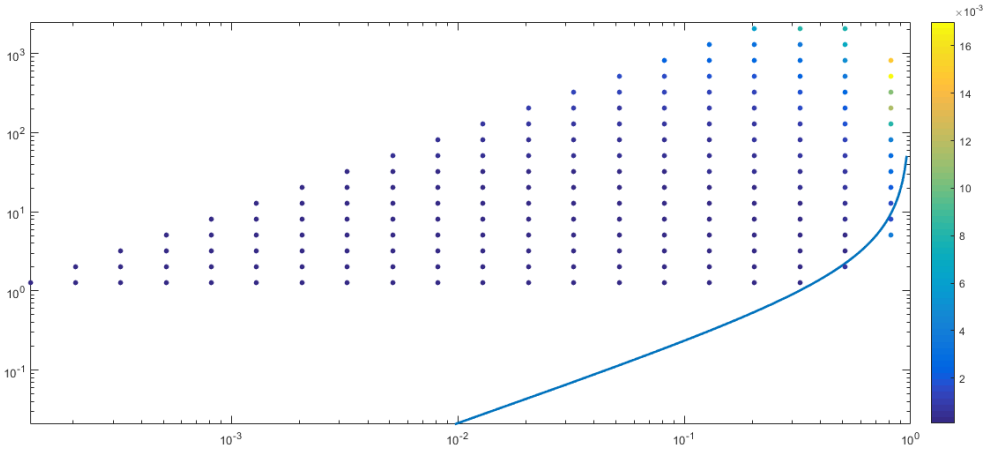


**Figure 5.42:** Kinematic coverage of simulated EIC data. The y-axis is in log-scale to better visualize the data. The plotted line denotes the $W^2 = 3\ GeV^2$ lower-bound kinematic cut in CJ15; only data above the line is fit. The color scale indicates the statistical uncertainty.

As before, we plot the relative uncertainties to get a better sense of the impact of EIC pseudo data; only the statistical uncertainty is included. But first, the procedure for producing the pseudo data will be briefly explained.

The pseudo data in its raw form is given as the number of expected physics events binned in Bjorken x. The statistical uncertainty is given simply by $\frac{1}{\sqrt{N}}$, where $N$ is the number of events. Then, the CJ code is used to calculate the relevant quantities of interest. In this case, we calculate the $F_2$ structure function from proton as well as neutron interactions, $F_2^p$ and $F_2^n$. Finally, these quantities are assigned a statistical uncertainty given by $\frac{1}{\sqrt{N}}$. We note that when including pseudo data into a global PDF fit, the most important quantity becomes the uncertainty associated with the structure function, rather than the central value of the structure function itself. For this reason, it is permissible to use a CJ calculation of $F_2^p$ and $F_2^n$, as we are attempting to explore the affect of an ideal measurement with realistic experimental uncertainties. It is worth noting that the EIC is in a position to implement neutron tagging. In particular, the possible extraction of $F_2^n$ will make significant impact to the uncertainty reduction in the $\frac{d}{u}$ and $d$ parton distribution functions. This is due to the fact that there is a lack of $F_2^n$ measurements

historically, given the difficulty in designing an experiment with this kind of capability.

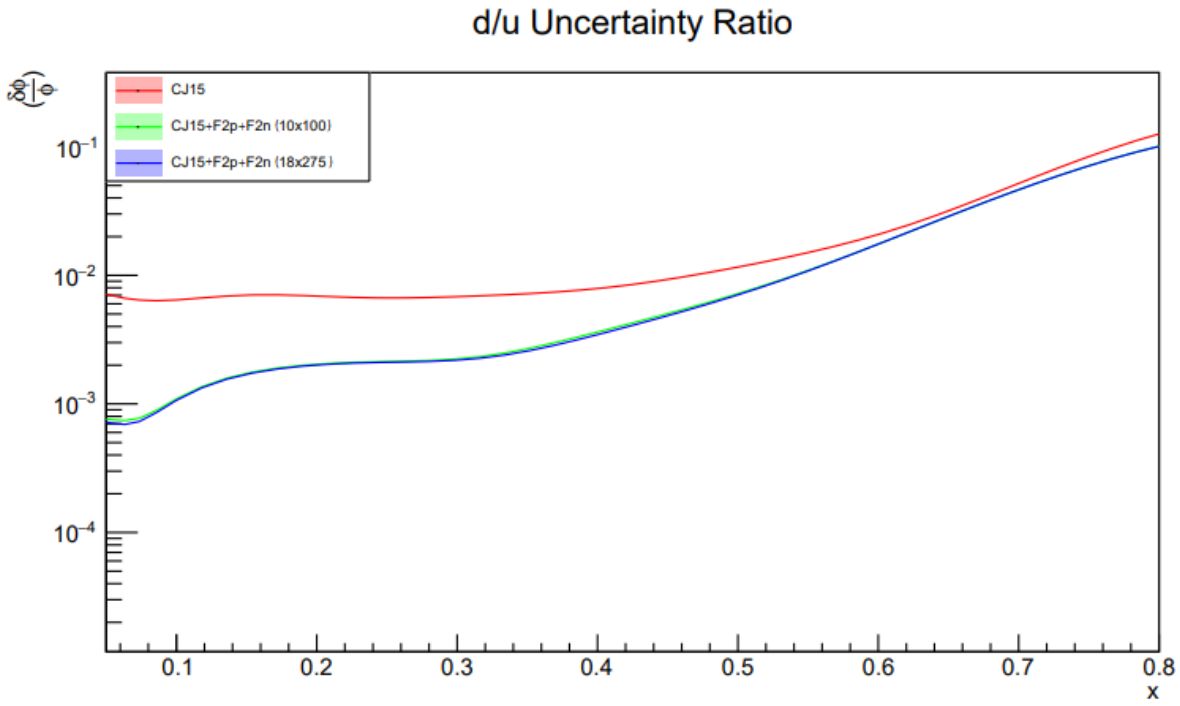


**Figure 5.43:** Plot of relative $\frac{d}{u}$ uncertainty comparing CJ15 with CJ15 plus the simulated EIC $F_2^p$ and $F_2^n$ data. One data set was generated with a 10 $GeV$ electron on a 100 $GeV$ proton; the other was generated with a 18 $GeV$ electron on a 275 $GeV$ proton.

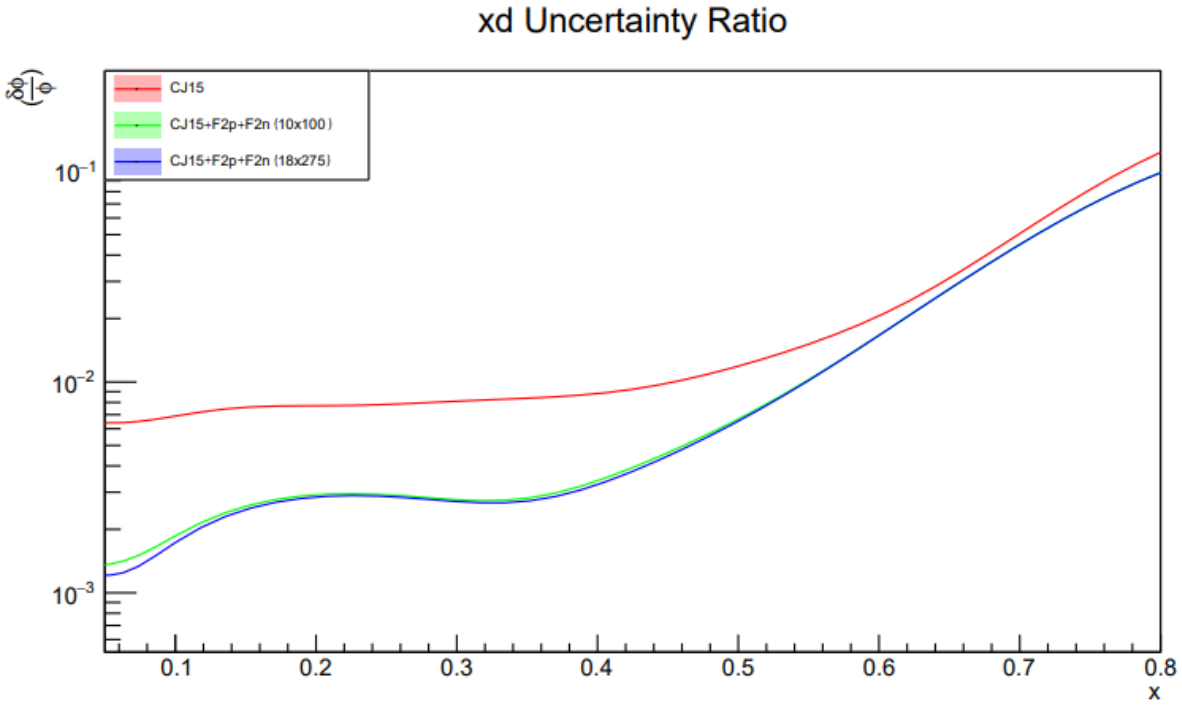


**Figure 5.44:** Plot of relative $d$-quark uncertainty comparing CJ15 with CJ15 plus the simulated EIC $F_2^p$ and $F_2^n$ data. One data set was generated with a 10 $GeV$ electron on a 100 $GeV$ proton; the other was generated with a 18 $GeV$ electron on a 275 $GeV$ proton.

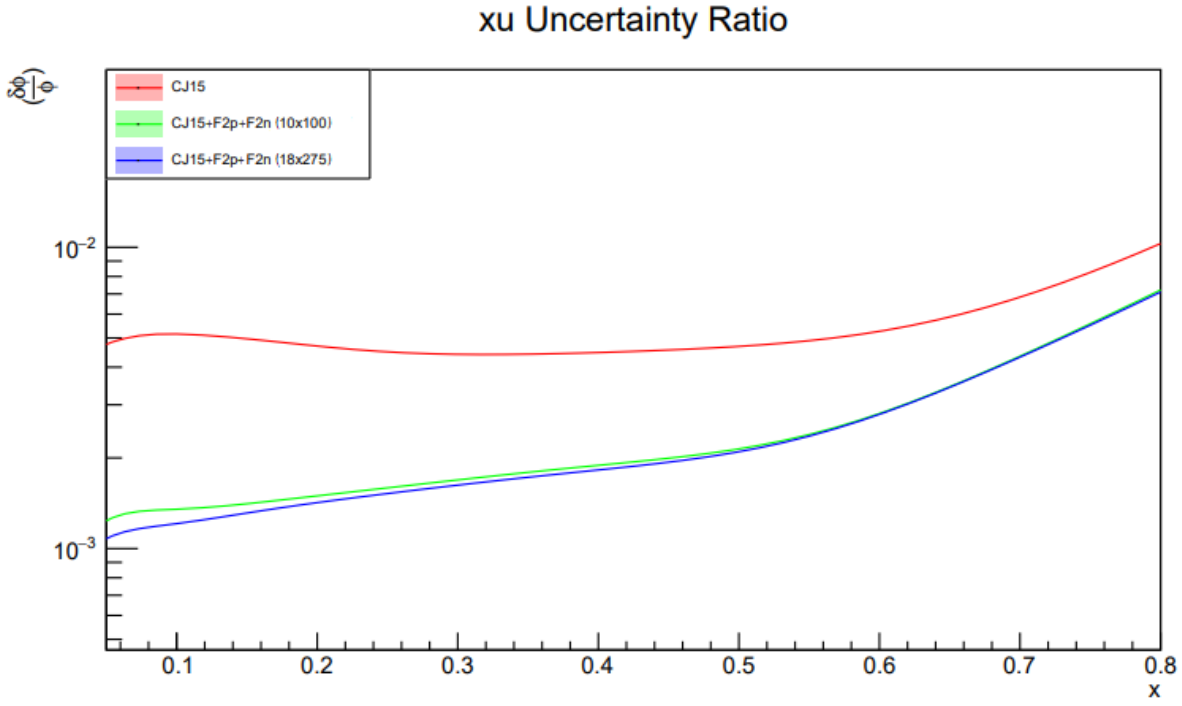


**Figure 5.45:** Plot of relative $u$-quark uncertainty comparing CJ15 with CJ15 plus the simulated $F_2^p$ and $F_2^n$ EIC data. One data set was generated with a 10 $GeV$ electron on a 100 $GeV$ proton; the other was generated with a 18 $GeV$ electron on a 275 $GeV$ proton.

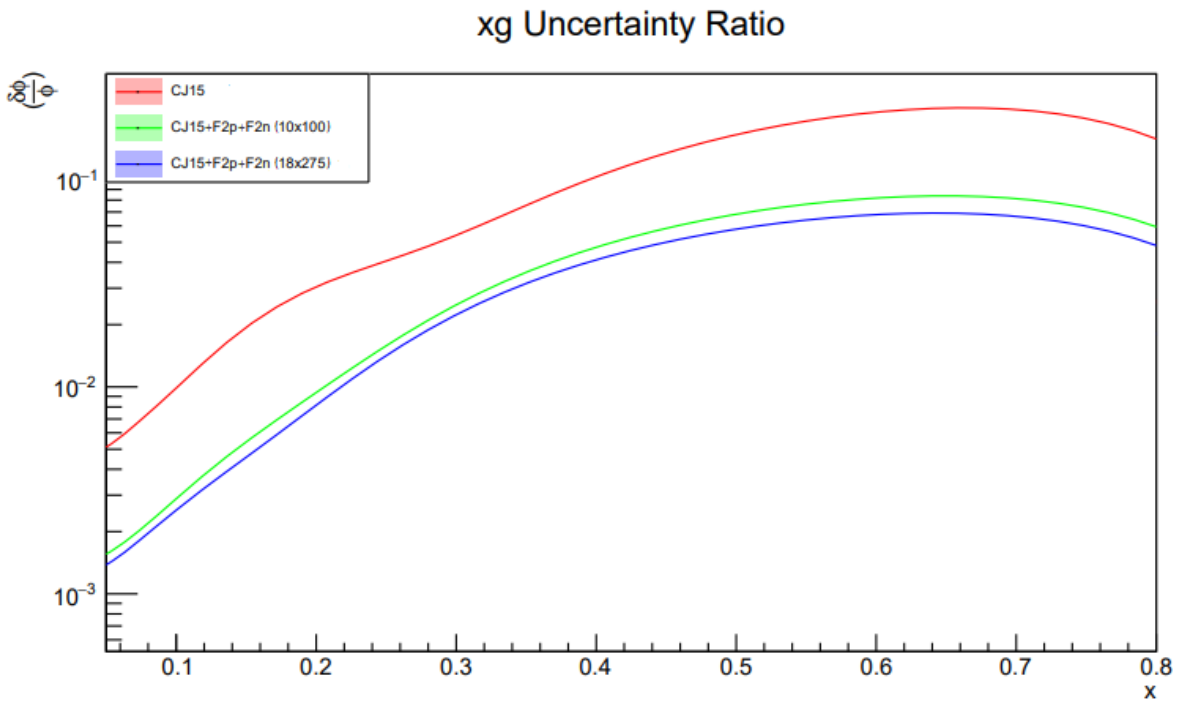


**Figure 5.46:** Plot of relative gluon uncertainty comparing CJ15 with CJ15 plus the simulated EIC $F_2^p$ and $F_2^n$ data. One data set was generated with a 10 $GeV$ electron on a 100 $GeV$ proton; the other was generated with a 18 $GeV$ electron on a 275 $GeV$ proton.

From figure 5.42, we can see that most of the pseudo data is at low Bjorken $x$. This is reflected in the relative ratio plots, figures 5.43 through 5.45, where the biggest impact in the uncertainty reduction is at low $x$. Indeed, this analysis suggests that the EIC may provide near 90% uncertainty reduction at low $x$ for $\frac{d}{u}$, $d$, and $u$ parton distribution function, while the gluon uncertainty is reduced by about 70% across a broad range in $x$.

### 5.2.5 Discussion

There remains much more analysis to be done in order to confidently present a full result of the E12-10-002 data set. As was evident in the presentation of the $F_2$ structure function figures, the data at low $E^{'}$ and high $\theta$ demonstrated a visible discrepancy between the CJ15 theoretical predictions. As mentioned, this is largely due to the presence of the charge symmetric background in the data. Further, the results presented are derived only from the SHMS spectrometer. The analysis for HMS lagged behind and was not suitable

for a global PDF study. However, despite the preliminary nature of these results, one may still draw some conclusions about the impact of E12-10-002. In particular, the CJ15 global PDF analysis demonstrated that by itself, E12-10-002 unfortunately does not significantly reduce the uncertainties in the down quark or the gluon – two parton distributions that remain relatively unconstrained at large Bjorken $x$. However, it was emphasized that the E12-10-002 experiment represents only one in many experiments at JLab with the express goal of populating the large $x$ kinematic range with precision measurements. Indeed, even the spirit of a global PDF analysis depends on the appropriate inclusion of a wide variety of data sets, each with their own kinematic coverage and parton constraints. To this end, the formerly excluded 6 GeV JLab experiments together with E12-10-002 show about an 8% reduction in the gluon uncertainty in the Bjorken $x$ range spanning $x = 0.5$ to $x = 0.8$. Further, together with MARATHON, we are provided with a foothold towards the resolution of the limit behavior of $\frac{d}{u}$. Here, MARATHON is in position to make a more definitive statement, while E12-10-002 may serve as a possible cross-check via a global PDF analysis. Nevertheless, preliminary results of $\sigma_D/\sigma_H$ confirm that MARATHON and E12-10-002 are in relative agreement. This result bodes well for the promise of unraveling the spin-flavor dynamics of the nucleons that the $\frac{d}{u}$ PDF provides. Finally, we conclude with a look towards the future, in the already approved EIC/eRHIC at Brookhaven. This facility will greatly extend both the scope of the fundamental questions one can ask about nuclear matter as well as the precision of the answers it can provide. Questions about the origin of the proton's spin, its mass, and the interface between partonic and hadronic degrees of freedom are all on the table. But not only will the EIC be able to elucidate questions that have remained since the beginning of the field of nuclear physics, its precision will also facilitate a possible next step in the standard model. Indeed, the gluon represents a large stumbling block for many BSM models, and the EIC is a facility largely dedicated to solving this mystery. The potential for the EIC to provide insight into the most simple and fundamental questions about nuclear matter is unprecedented, but it should not be forgotten that this hope for the future is owed to every result, big or

small, that came before it.

# Appendix A

# Appendix

We present the raw cross section data accumulated for the E12-10-002 experiment. As mentioned previously, the complete systematic uncertainty has yet to be determined for the data sets, therefore, only the statistical uncertainty is shown.

| x | $Q^2$ | $\frac{\sigma_D}{\sigma_H}$ | E (GeV) | Stat | E' | $\theta$ |
|---|---|---|---|---|---|---|
| 0.219809 | 3.38283 | 0.874257 | 10.602 | 0.021828 | 2.40196 | 21 |
| 0.22296 | 3.42021 | 0.871757 | 10.602 | 0.022025 | 2.4285 | 21 |
| 0.226131 | 3.45759 | 0.854983 | 10.602 | 0.021179 | 2.45505 | 21 |
| 0.229322 | 3.49496 | 0.864641 | 10.602 | 0.021892 | 2.48158 | 21 |
| 0.232535 | 3.53234 | 0.874314 | 10.602 | 0.022188 | 2.50812 | 21 |
| 0.235769 | 3.56972 | 0.890579 | 10.602 | 0.02272 | 2.53466 | 21 |
| 0.239024 | 3.6071 | 0.871888 | 10.602 | 0.022284 | 2.5612 | 21 |
| 0.242301 | 3.64448 | 0.839148 | 10.602 | 0.021682 | 2.58775 | 21 |
| 0.245599 | 3.68186 | 0.867214 | 10.602 | 0.02251 | 2.61429 | 21 |
| 0.24892 | 3.71924 | 0.88162 | 10.602 | 0.023002 | 2.64083 | 21 |

| | | | | | | |
|---|---|---|---|---|---|---|
| 0.252262 | 3.75662 | 0.865612 | 10.602 | 0.022827 | 2.66737 | 21 |
| 0.255628 | 3.794 | 0.850802 | 10.602 | 0.022629 | 2.69391 | 21 |
| 0.259015 | 3.83138 | 0.889282 | 10.602 | 0.023704 | 2.72045 | 21 |
| 0.262426 | 3.86876 | 0.863715 | 10.602 | 0.023318 | 2.747 | 21 |
| 0.26586 | 3.90614 | 0.833849 | 10.602 | 0.02285 | 2.77354 | 21 |
| 0.269317 | 3.94352 | 0.874197 | 10.602 | 0.023987 | 2.80008 | 21 |
| 0.272798 | 3.9809 | 0.85345 | 10.602 | 0.023707 | 2.82662 | 21 |
| 0.276302 | 4.01827 | 0.882069 | 10.602 | 0.024649 | 2.85315 | 21 |
| 0.279831 | 4.05565 | 0.845516 | 10.602 | 0.024157 | 2.8797 | 21 |
| 0.283384 | 4.09303 | 0.844051 | 10.602 | 0.024455 | 2.90624 | 21 |
| 0.286962 | 4.13041 | 0.837209 | 10.602 | 0.024486 | 2.93278 | 21 |
| 0.290564 | 4.16779 | 0.845081 | 10.602 | 0.025256 | 2.95932 | 21 |
| 0.294192 | 4.20517 | 0.843881 | 10.602 | 0.025277 | 2.98586 | 21 |
| 0.297845 | 4.24255 | 0.852376 | 10.602 | 0.025767 | 3.0124 | 21 |
| 0.301524 | 4.27993 | 0.828384 | 10.602 | 0.025434 | 3.03894 | 21 |
| 0.305228 | 4.31731 | 0.839305 | 10.602 | 0.025929 | 3.06549 | 21 |
| 0.308959 | 4.35469 | 0.826714 | 10.602 | 0.02583 | 3.09203 | 21 |
| 0.312716 | 4.39207 | 0.799069 | 10.602 | 0.025605 | 3.11857 | 21 |

| | | | | | | |
|---|---|---|---|---|---|---|
| 0.3165 | 4.42945 | 0.827172 | 10.602 | 0.02674 | 3.14511 | 21 |
| 0.320311 | 4.46683 | 0.807159 | 10.602 | 0.026252 | 3.17165 | 21 |
| 0.324149 | 4.50421 | 0.814795 | 10.602 | 0.026657 | 3.19819 | 21 |
| 0.328015 | 4.54158 | 0.796297 | 10.602 | 0.026316 | 3.22473 | 21 |
| 0.328015 | 4.54158 | 0.796297 | 10.602 | 0.026316 | 3.22473 | 21 |
| 0.287361 | 4.13457 | 0.862299 | 10.602 | 0.019944 | 2.93573 | 21 |
| 0.291771 | 4.18025 | 0.852055 | 10.602 | 0.019992 | 2.96817 | 21 |
| 0.296218 | 4.22594 | 0.855054 | 10.602 | 0.01968 | 3.00061 | 21 |
| 0.300704 | 4.27162 | 0.857097 | 10.602 | 0.020263 | 3.03304 | 21 |
| 0.305228 | 4.31731 | 0.844569 | 10.602 | 0.020006 | 3.06549 | 21 |
| 0.309792 | 4.36299 | 0.851543 | 10.602 | 0.020119 | 3.09792 | 21 |
| 0.314394 | 4.40868 | 0.851056 | 10.602 | 0.020369 | 3.13036 | 21 |
| 0.319038 | 4.45437 | 0.845617 | 10.602 | 0.020171 | 3.1628 | 21 |
| 0.323721 | 4.50005 | 0.84542 | 10.602 | 0.02029 | 3.19524 | 21 |
| 0.328446 | 4.54574 | 0.838465 | 10.602 | 0.020124 | 3.22768 | 21 |
| 0.333213 | 4.59142 | 0.829997 | 10.602 | 0.02019 | 3.26012 | 21 |
| 0.338022 | 4.63711 | 0.830653 | 10.602 | 0.020309 | 3.29256 | 21 |
| 0.342874 | 4.6828 | 0.828466 | 10.602 | 0.020343 | 3.325 | 21 |

| | | | | | | |
|---|---|---|---|---|---|---|
| 0.347769 | 4.72848 | 0.816438 | 10.602 | 0.020293 | 3.35744 | 21 |
| 0.352709 | 4.77417 | 0.833913 | 10.602 | 0.020901 | 3.38988 | 21 |
| 0.357693 | 4.81985 | 0.823808 | 10.602 | 0.020769 | 3.42231 | 21 |
| 0.362722 | 4.86554 | 0.825414 | 10.602 | 0.020973 | 3.45475 | 21 |
| 0.367797 | 4.91122 | 0.800389 | 10.602 | 0.020486 | 3.48719 | 21 |
| 0.372919 | 4.95691 | 0.828443 | 10.602 | 0.02162 | 3.51963 | 21 |
| 0.378088 | 5.0026 | 0.808835 | 10.602 | 0.02149 | 3.55207 | 21 |
| 0.383304 | 5.04828 | 0.812893 | 10.602 | 0.021719 | 3.58451 | 21 |
| 0.388569 | 5.09397 | 0.800797 | 10.602 | 0.021877 | 3.61695 | 21 |
| 0.393884 | 5.13965 | 0.809747 | 10.602 | 0.022411 | 3.64938 | 21 |
| 0.399247 | 5.18534 | 0.814099 | 10.602 | 0.022588 | 3.68183 | 21 |
| 0.404662 | 5.23103 | 0.800302 | 10.602 | 0.02252 | 3.71427 | 21 |
| 0.410128 | 5.27671 | 0.799336 | 10.602 | 0.022438 | 3.7467 | 21 |
| 0.415645 | 5.3224 | 0.790673 | 10.602 | 0.022364 | 3.77915 | 21 |
| 0.421216 | 5.36808 | 0.781143 | 10.602 | 0.022831 | 3.81158 | 21 |
| 0.42684 | 5.41377 | 0.794574 | 10.602 | 0.023323 | 3.84402 | 21 |
| 0.432518 | 5.45945 | 0.77954 | 10.602 | 0.023074 | 3.87646 | 21 |
| 0.438251 | 5.50514 | 0.767762 | 10.602 | 0.023001 | 3.9089 | 21 |

| | | | | | | |
|---|---|---|---|---|---|---|
| 0.44404 | 5.55083 | 0.789154 | 10.602 | 0.023765 | 3.94134 | 21 |
| 0.44404 | 5.55083 | 0.789154 | 10.602 | 0.023765 | 3.94134 | 21 |
| 0.379112 | 5.01159 | 0.80443 | 10.602 | 0.018061 | 3.55846 | 21 |
| 0.385452 | 5.06697 | 0.806454 | 10.602 | 0.018265 | 3.59778 | 21 |
| 0.391865 | 5.12235 | 0.80356 | 10.602 | 0.0178 | 3.6371 | 21 |
| 0.39835 | 5.17773 | 0.802926 | 10.602 | 0.018281 | 3.67642 | 21 |
| 0.404909 | 5.2331 | 0.791933 | 10.602 | 0.018176 | 3.71574 | 21 |
| 0.411544 | 5.28848 | 0.785941 | 10.602 | 0.017833 | 3.75506 | 21 |
| 0.418255 | 5.34386 | 0.797177 | 10.602 | 0.018384 | 3.79438 | 21 |
| 0.425044 | 5.39923 | 0.790761 | 10.602 | 0.018231 | 3.8337 | 21 |
| 0.431913 | 5.45461 | 0.792237 | 10.602 | 0.018308 | 3.87302 | 21 |
| 0.438862 | 5.50999 | 0.78757 | 10.602 | 0.018228 | 3.91234 | 21 |
| 0.445894 | 5.56536 | 0.775279 | 10.602 | 0.018193 | 3.95166 | 21 |
| 0.453009 | 5.62074 | 0.779656 | 10.602 | 0.018333 | 3.99098 | 21 |
| 0.460209 | 5.67612 | 0.783822 | 10.602 | 0.018596 | 4.0303 | 21 |
| 0.467496 | 5.73149 | 0.778725 | 10.602 | 0.018606 | 4.06962 | 21 |
| 0.474872 | 5.78687 | 0.781294 | 10.602 | 0.018761 | 4.10894 | 21 |
| 0.482337 | 5.84225 | 0.782737 | 10.602 | 0.018922 | 4.14826 | 21 |

| | | | | | | |
|---|---|---|---|---|---|---|
| 0.489893 | 5.89762 | 0.765015 | 10.602 | 0.018686 | 4.18758 | 21 |
| 0.497543 | 5.953 | 0.756943 | 10.602 | 0.018604 | 4.2269 | 21 |
| 0.505288 | 6.00838 | 0.756048 | 10.602 | 0.018955 | 4.26622 | 21 |
| 0.51313 | 6.06375 | 0.765407 | 10.602 | 0.019526 | 4.30554 | 21 |
| 0.52107 | 6.11913 | 0.760806 | 10.602 | 0.019603 | 4.34486 | 21 |
| 0.52911 | 6.17451 | 0.747579 | 10.602 | 0.019654 | 4.38418 | 21 |
| 0.537253 | 6.22988 | 0.747962 | 10.602 | 0.01993 | 4.4235 | 21 |
| 0.5455 | 6.28526 | 0.755581 | 10.602 | 0.0202 | 4.46282 | 21 |
| 0.553854 | 6.34064 | 0.727275 | 10.602 | 0.019782 | 4.50214 | 21 |
| 0.562315 | 6.39601 | 0.742011 | 10.602 | 0.020182 | 4.54146 | 21 |
| 0.570888 | 6.45139 | 0.757501 | 10.602 | 0.020918 | 4.58078 | 21 |
| 0.579573 | 6.50677 | 0.741167 | 10.602 | 0.021059 | 4.6201 | 21 |
| 0.588373 | 6.56214 | 0.756017 | 10.602 | 0.021636 | 4.65942 | 21 |
| 0.59729 | 6.61752 | 0.736504 | 10.602 | 0.02128 | 4.69874 | 21 |
| 0.606327 | 6.6729 | 0.72741 | 10.602 | 0.021446 | 4.73806 | 21 |
| 0.615486 | 6.72827 | 0.742859 | 10.602 | 0.022183 | 4.77738 | 21 |
| 0.615486 | 6.72827 | 0.742859 | 10.602 | 0.022183 | 4.77738 | 21 |
| 0.561358 | 6.38978 | 0.751109 | 10.602 | 0.01643 | 4.53703 | 21 |

| | | | | | | |
|---|---|---|---|---|---|---|
| 0.572291 | 6.46039 | 0.750826 | 10.602 | 0.016511 | 4.58717 | 21 |
| 0.583409 | 6.53099 | 0.738177 | 10.602 | 0.016019 | 4.6373 | 21 |
| 0.594714 | 6.6016 | 0.739543 | 10.602 | 0.016429 | 4.68744 | 21 |
| 0.606213 | 6.6722 | 0.741572 | 10.602 | 0.016515 | 4.73756 | 21 |
| 0.617911 | 6.74281 | 0.742778 | 10.602 | 0.016428 | 4.7877 | 21 |
| 0.629811 | 6.81342 | 0.735767 | 10.602 | 0.016504 | 4.83784 | 21 |
| 0.641921 | 6.88402 | 0.73607 | 10.602 | 0.016548 | 4.88797 | 21 |
| 0.654245 | 6.95463 | 0.729798 | 10.602 | 0.016374 | 4.9381 | 21 |
| 0.666789 | 7.02523 | 0.729299 | 10.602 | 0.016501 | 4.98823 | 21 |
| 0.679559 | 7.09584 | 0.730638 | 10.602 | 0.016657 | 5.03837 | 21 |
| 0.692561 | 7.16644 | 0.728802 | 10.602 | 0.016722 | 5.0885 | 21 |
| 0.705802 | 7.23705 | 0.740344 | 10.602 | 0.017183 | 5.13863 | 21 |
| 0.719288 | 7.30765 | 0.733445 | 10.602 | 0.017027 | 5.18876 | 21 |
| 0.733027 | 7.37826 | 0.73707 | 10.602 | 0.017384 | 5.2389 | 21 |
| 0.747024 | 7.44886 | 0.75632 | 10.602 | 0.01795 | 5.28903 | 21 |
| 0.761289 | 7.51947 | 0.75641 | 10.602 | 0.018219 | 5.33917 | 21 |
| 0.775827 | 7.59007 | 0.670743 | 10.602 | 0.016366 | 5.38929 | 21 |
| 0.790648 | 7.66068 | 0.611594 | 10.602 | 0.015244 | 5.43943 | 21 |

| | | | | | | |
|---|---|---|---|---|---|---|
| 0.80576 | 7.73128 | 0.721603 | 10.602 | 0.018427 | 5.48956 | 21 |
| 0.821171 | 7.80189 | 0.817321 | 10.602 | 0.021281 | 5.5397 | 21 |
| 0.83689 | 7.8725 | 0.739343 | 10.602 | 0.020297 | 5.58983 | 21 |
| 0.852927 | 7.9431 | 0.623073 | 10.602 | 0.017944 | 5.63996 | 21 |
| 0.869292 | 8.01371 | 0.875974 | 10.602 | 0.026542 | 5.6901 | 21 |
| 0.885993 | 8.08431 | 1.05579 | 10.602 | 0.034908 | 5.74023 | 21 |
| 0.281 | 4.41838 | 0.861224 | 10.602 | 0.020791 | 2.22404 | 25 |
| 0.284941 | 4.46721 | 0.867539 | 10.602 | 0.021438 | 2.24861 | 25 |
| 0.288905 | 4.51603 | 0.834335 | 10.602 | 0.019953 | 2.27319 | 25 |
| 0.292893 | 4.56485 | 0.829651 | 10.602 | 0.020375 | 2.29776 | 25 |
| 0.296904 | 4.61367 | 0.842208 | 10.602 | 0.020756 | 2.32234 | 25 |
| 0.300939 | 4.66249 | 0.847647 | 10.602 | 0.020937 | 2.34691 | 25 |
| 0.304998 | 4.71131 | 0.828499 | 10.602 | 0.020576 | 2.37149 | 25 |
| 0.309082 | 4.76014 | 0.830251 | 10.602 | 0.020814 | 2.39606 | 25 |
| 0.31319 | 4.80896 | 0.855517 | 10.602 | 0.021556 | 2.42064 | 25 |
| 0.317322 | 4.85778 | 0.849282 | 10.602 | 0.0214 | 2.44521 | 25 |
| 0.32148 | 4.9066 | 0.826806 | 10.602 | 0.021069 | 2.46979 | 25 |
| 0.325663 | 4.95542 | 0.822948 | 10.602 | 0.021183 | 2.49436 | 25 |

| | | | | | | |
|---|---|---|---|---|---|---|
| 0.329871 | 5.00425 | 0.820195 | 10.602 | 0.021209 | 2.51894 | 25 |
| 0.334105 | 5.05307 | 0.820463 | 10.602 | 0.021469 | 2.54351 | 25 |
| 0.338365 | 5.10189 | 0.813044 | 10.602 | 0.021489 | 2.56809 | 25 |
| 0.342652 | 5.15071 | 0.83148 | 10.602 | 0.022035 | 2.59266 | 25 |
| 0.346964 | 5.19953 | 0.803691 | 10.602 | 0.021458 | 2.61724 | 25 |
| 0.351303 | 5.24836 | 0.823068 | 10.602 | 0.022331 | 2.64181 | 25 |
| 0.355669 | 5.29718 | 0.835586 | 10.602 | 0.023266 | 2.66639 | 25 |
| 0.360062 | 5.346 | 0.794085 | 10.602 | 0.022274 | 2.69096 | 25 |
| 0.364483 | 5.39482 | 0.832637 | 10.602 | 0.023736 | 2.71554 | 25 |
| 0.368931 | 5.44364 | 0.836328 | 10.602 | 0.024178 | 2.74011 | 25 |
| 0.373407 | 5.49247 | 0.811343 | 10.602 | 0.023523 | 2.76469 | 25 |
| 0.377911 | 5.54129 | 0.810835 | 10.602 | 0.023817 | 2.78926 | 25 |
| 0.382444 | 5.59011 | 0.788122 | 10.602 | 0.023566 | 2.81384 | 25 |
| 0.387005 | 5.63893 | 0.824408 | 10.602 | 0.024846 | 2.83841 | 25 |
| 0.391595 | 5.68775 | 0.795563 | 10.602 | 0.024161 | 2.86299 | 25 |
| 0.396215 | 5.73657 | 0.821739 | 10.602 | 0.025484 | 2.88756 | 25 |
| 0.400864 | 5.7854 | 0.774339 | 10.602 | 0.024443 | 2.91214 | 25 |
| 0.405542 | 5.83422 | 0.794404 | 10.602 | 0.025144 | 2.93671 | 25 |

| | | | | | | |
|---|---|---|---|---|---|---|
| 0.410251 | 5.88304 | 0.762999 | 10.602 | 0.024326 | 2.96129 | 25 |
| 0.414991 | 5.93186 | 0.769036 | 10.602 | 0.025056 | 2.98586 | 25 |
| 0.414991 | 5.93186 | 0.769036 | 10.602 | 0.025056 | 2.98586 | 25 |
| 0.356107 | 5.30206 | 0.822693 | 10.602 | 0.018835 | 2.66884 | 25 |
| 0.361385 | 5.36065 | 0.811202 | 10.602 | 0.018982 | 2.69834 | 25 |
| 0.366703 | 5.41923 | 0.805345 | 10.602 | 0.018283 | 2.72782 | 25 |
| 0.372061 | 5.47782 | 0.807474 | 10.602 | 0.018848 | 2.75732 | 25 |
| 0.377459 | 5.53641 | 0.816794 | 10.602 | 0.019068 | 2.78681 | 25 |
| 0.382898 | 5.59499 | 0.787476 | 10.602 | 0.018409 | 2.81629 | 25 |
| 0.388379 | 5.65358 | 0.799195 | 10.602 | 0.018831 | 2.84579 | 25 |
| 0.393901 | 5.71216 | 0.803184 | 10.602 | 0.018959 | 2.87527 | 25 |
| 0.399466 | 5.77075 | 0.801223 | 10.602 | 0.019015 | 2.90476 | 25 |
| 0.405073 | 5.82934 | 0.804254 | 10.602 | 0.019169 | 2.93426 | 25 |
| 0.410724 | 5.88792 | 0.800312 | 10.602 | 0.019246 | 2.96374 | 25 |
| 0.416418 | 5.94651 | 0.798634 | 10.602 | 0.019324 | 2.99324 | 25 |
| 0.422157 | 6.0051 | 0.789367 | 10.602 | 0.019094 | 3.02273 | 25 |
| 0.427941 | 6.06368 | 0.783466 | 10.602 | 0.019288 | 3.05221 | 25 |
| 0.43377 | 6.12227 | 0.79178 | 10.602 | 0.019634 | 3.08171 | 25 |

| | | | | | | |
|---|---|---|---|---|---|---|
| 0.439645 | 6.18085 | 0.799594 | 10.602 | 0.019992 | 3.11119 | 25 |
| 0.445566 | 6.23944 | 0.785428 | 10.602 | 0.019719 | 3.14068 | 25 |
| 0.451535 | 6.29803 | 0.75998 | 10.602 | 0.019344 | 3.17018 | 25 |
| 0.457551 | 6.35661 | 0.781878 | 10.602 | 0.0203 | 3.19966 | 25 |
| 0.463615 | 6.4152 | 0.752807 | 10.602 | 0.019826 | 3.22916 | 25 |
| 0.469727 | 6.47379 | 0.775563 | 10.602 | 0.020651 | 3.25865 | 25 |
| 0.475889 | 6.53237 | 0.770582 | 10.602 | 0.02093 | 3.28813 | 25 |
| 0.482101 | 6.59096 | 0.78324 | 10.602 | 0.021401 | 3.31763 | 25 |
| 0.488364 | 6.64954 | 0.760779 | 10.602 | 0.020988 | 3.34711 | 25 |
| 0.494677 | 6.70813 | 0.764581 | 10.602 | 0.02142 | 3.3766 | 25 |
| 0.501043 | 6.76672 | 0.753848 | 10.602 | 0.021266 | 3.4061 | 25 |
| 0.50746 | 6.8253 | 0.760414 | 10.602 | 0.021691 | 3.43558 | 25 |
| 0.513931 | 6.88389 | 0.762461 | 10.602 | 0.02248 | 3.46507 | 25 |
| 0.520455 | 6.94248 | 0.754378 | 10.602 | 0.022344 | 3.49457 | 25 |
| 0.527034 | 7.00106 | 0.756597 | 10.602 | 0.022522 | 3.52405 | 25 |
| 0.533668 | 7.05965 | 0.728745 | 10.602 | 0.02208 | 3.55355 | 25 |
| 0.540358 | 7.11824 | 0.761057 | 10.602 | 0.023296 | 3.58304 | 25 |
| 0.540358 | 7.11824 | 0.761057 | 10.602 | 0.023296 | 3.58304 | 25 |

| | | | | | | |
|---|---|---|---|---|---|---|
| 0.440137 | 6.18574 | 0.781838 | 10.602 | 0.01735 | 3.11365 | 25 |
| 0.447054 | 6.25409 | 0.779815 | 10.602 | 0.017705 | 3.14806 | 25 |
| 0.454035 | 6.32244 | 0.778685 | 10.602 | 0.017033 | 3.18246 | 25 |
| 0.461082 | 6.39079 | 0.779928 | 10.602 | 0.01764 | 3.21687 | 25 |
| 0.468195 | 6.45914 | 0.771841 | 10.602 | 0.017442 | 3.25127 | 25 |
| 0.475374 | 6.52749 | 0.768624 | 10.602 | 0.017383 | 3.28568 | 25 |
| 0.482621 | 6.59584 | 0.769919 | 10.602 | 0.017567 | 3.32008 | 25 |
| 0.489937 | 6.66419 | 0.760574 | 10.602 | 0.017299 | 3.35449 | 25 |
| 0.497323 | 6.73254 | 0.770324 | 10.602 | 0.017653 | 3.38889 | 25 |
| 0.50478 | 6.80089 | 0.764561 | 10.602 | 0.01758 | 3.4233 | 25 |
| 0.512308 | 6.86924 | 0.763221 | 10.602 | 0.017618 | 3.4577 | 25 |
| 0.51991 | 6.93759 | 0.755486 | 10.602 | 0.017524 | 3.49211 | 25 |
| 0.527585 | 7.00594 | 0.756691 | 10.602 | 0.017717 | 3.52651 | 25 |
| 0.535335 | 7.0743 | 0.751684 | 10.602 | 0.017747 | 3.56092 | 25 |
| 0.543162 | 7.14265 | 0.750687 | 10.602 | 0.017975 | 3.59532 | 25 |
| 0.551065 | 7.211 | 0.757601 | 10.602 | 0.018087 | 3.62973 | 25 |
| 0.559047 | 7.27935 | 0.734893 | 10.602 | 0.017765 | 3.66413 | 25 |
| 0.567109 | 7.3477 | 0.735224 | 10.602 | 0.017928 | 3.69854 | 25 |

| | | | | | | |
|---|---|---|---|---|---|---|
| 0.575251 | 7.41605 | 0.730746 | 10.602 | 0.018172 | 3.73294 | 25 |
| 0.583475 | 7.4844 | 0.736476 | 10.602 | 0.018661 | 3.76735 | 25 |
| 0.591783 | 7.55275 | 0.73461 | 10.602 | 0.018736 | 3.80175 | 25 |
| 0.600175 | 7.6211 | 0.736766 | 10.602 | 0.019151 | 3.83616 | 25 |
| 0.608653 | 7.68945 | 0.729576 | 10.602 | 0.019264 | 3.87056 | 25 |
| 0.617218 | 7.7578 | 0.730029 | 10.602 | 0.019372 | 3.90497 | 25 |
| 0.625871 | 7.82615 | 0.724765 | 10.602 | 0.019558 | 3.93937 | 25 |
| 0.634614 | 7.8945 | 0.715468 | 10.602 | 0.01938 | 3.97378 | 25 |
| 0.643449 | 7.96285 | 0.731276 | 10.602 | 0.020054 | 4.00818 | 25 |
| 0.652376 | 8.0312 | 0.716888 | 10.602 | 0.020442 | 4.04258 | 25 |
| 0.661397 | 8.09956 | 0.735196 | 10.602 | 0.020945 | 4.07699 | 25 |
| 0.670514 | 8.16791 | 0.695985 | 10.602 | 0.020139 | 4.1114 | 25 |
| 0.679728 | 8.23626 | 0.736593 | 10.602 | 0.021762 | 4.1458 | 25 |
| 0.689041 | 8.30461 | 0.719589 | 10.602 | 0.021461 | 4.18021 | 25 |
| 0.689041 | 8.30461 | 0.719589 | 10.602 | 0.021461 | 4.18021 | 25 |
| 0.619558 | 7.77635 | 0.727248 | 10.602 | 0.016212 | 3.9143 | 25 |
| 0.630481 | 7.86228 | 0.730105 | 10.602 | 0.016414 | 3.95756 | 25 |
| 0.641548 | 7.94821 | 0.714903 | 10.602 | 0.015527 | 4.00081 | 25 |

| | | | | | | |
|---|---|---|---|---|---|---|
| 0.65276 | 8.03413 | 0.719002 | 10.602 | 0.016154 | 4.04406 | 25 |
| 0.664122 | 8.12006 | 0.723201 | 10.602 | 0.016317 | 4.08731 | 25 |
| 0.675635 | 8.20599 | 0.71693 | 10.602 | 0.016186 | 4.13057 | 25 |
| 0.687304 | 8.29191 | 0.717613 | 10.602 | 0.016364 | 4.17382 | 25 |
| 0.69913 | 8.37784 | 0.720742 | 10.602 | 0.016334 | 4.21707 | 25 |
| 0.711118 | 8.46377 | 0.719444 | 10.602 | 0.016461 | 4.26032 | 25 |
| 0.72327 | 8.54969 | 0.728088 | 10.602 | 0.016786 | 4.30357 | 25 |
| 0.735591 | 8.63562 | 0.722612 | 10.602 | 0.016774 | 4.34683 | 25 |
| 0.748083 | 8.72155 | 0.735131 | 10.602 | 0.017211 | 4.39008 | 25 |
| 0.76075 | 8.80747 | 0.72925 | 10.602 | 0.017381 | 4.43333 | 25 |
| 0.773596 | 8.8934 | 0.738006 | 10.602 | 0.017806 | 4.47658 | 25 |
| 0.786625 | 8.97933 | 0.750749 | 10.602 | 0.018489 | 4.51984 | 25 |
| 0.79984 | 9.06525 | 0.717693 | 10.602 | 0.017763 | 4.56308 | 25 |
| 0.813246 | 9.15118 | 0.622553 | 10.602 | 0.015837 | 4.60634 | 25 |
| 0.826847 | 9.23711 | 0.674334 | 10.602 | 0.017452 | 4.64959 | 25 |
| 0.840647 | 9.32303 | 0.799974 | 10.602 | 0.021389 | 4.69284 | 25 |
| 0.85465 | 9.40896 | 0.825582 | 10.602 | 0.023 | 4.73609 | 25 |
| 0.868862 | 9.49489 | 0.665584 | 10.602 | 0.019478 | 4.77935 | 25 |

| | | | | | | |
|---|---|---|---|---|---|---|
| 0.883286 | 9.58081 | 0.834622 | 10.602 | 0.026035 | 4.8226 | 25 |
| 0.897928 | 9.66674 | 1.05199 | 10.602 | 0.035648 | 4.86585 | 25 |
| 0.285664 | 4.7302 | 0.872034 | 10.602 | 0.021229 | 1.77923 | 29 |
| 0.289466 | 4.78246 | 0.860802 | 10.602 | 0.021435 | 1.79889 | 29 |
| 0.293285 | 4.83473 | 0.866127 | 10.602 | 0.020897 | 1.81855 | 29 |
| 0.29712 | 4.887 | 0.858666 | 10.602 | 0.021415 | 1.83821 | 29 |
| 0.300973 | 4.93927 | 0.850336 | 10.602 | 0.021305 | 1.85787 | 29 |
| 0.304843 | 4.99153 | 0.849056 | 10.602 | 0.021225 | 1.87753 | 29 |
| 0.308731 | 5.0438 | 0.866439 | 10.602 | 0.02173 | 1.89719 | 29 |
| 0.312637 | 5.09607 | 0.835419 | 10.602 | 0.021113 | 1.91685 | 29 |
| 0.31656 | 5.14834 | 0.85291 | 10.602 | 0.021553 | 1.93651 | 29 |
| 0.320501 | 5.2006 | 0.830856 | 10.602 | 0.021228 | 1.95617 | 29 |
| 0.32446 | 5.25287 | 0.832676 | 10.602 | 0.021388 | 1.97583 | 29 |
| 0.328437 | 5.30514 | 0.822931 | 10.602 | 0.021262 | 1.99549 | 29 |
| 0.332432 | 5.3574 | 0.814599 | 10.602 | 0.021452 | 2.01515 | 29 |
| 0.336445 | 5.40967 | 0.823703 | 10.602 | 0.021778 | 2.03481 | 29 |
| 0.340477 | 5.46194 | 0.822886 | 10.602 | 0.021899 | 2.05447 | 29 |
| 0.344528 | 5.51421 | 0.818053 | 10.602 | 0.022279 | 2.07413 | 29 |

| | | | | | | |
|---|---|---|---|---|---|---|
| 0.348597 | 5.56647 | 0.828136 | 10.602 | 0.022527 | 2.09379 | 29 |
| 0.352685 | 5.61874 | 0.816186 | 10.602 | 0.022369 | 2.11345 | 29 |
| 0.356793 | 5.67101 | 0.829928 | 10.602 | 0.023435 | 2.13311 | 29 |
| 0.360919 | 5.72328 | 0.822296 | 10.602 | 0.023608 | 2.15277 | 29 |
| 0.365064 | 5.77554 | 0.833517 | 10.602 | 0.024017 | 2.17243 | 29 |
| 0.369229 | 5.82781 | 0.836319 | 10.602 | 0.024675 | 2.19209 | 29 |
| 0.373414 | 5.88008 | 0.786311 | 10.602 | 0.023307 | 2.21175 | 29 |
| 0.377618 | 5.93235 | 0.794173 | 10.602 | 0.023676 | 2.23141 | 29 |
| 0.381842 | 5.98461 | 0.791426 | 10.602 | 0.024029 | 2.25107 | 29 |
| 0.386085 | 6.03688 | 0.784598 | 10.602 | 0.02398 | 2.27073 | 29 |
| 0.390349 | 6.08915 | 0.763298 | 10.602 | 0.023929 | 2.29039 | 29 |
| 0.394633 | 6.14141 | 0.824364 | 10.602 | 0.02622 | 2.31005 | 29 |
| 0.398938 | 6.19368 | 0.784678 | 10.602 | 0.025046 | 2.32971 | 29 |
| 0.403263 | 6.24595 | 0.80254 | 10.602 | 0.026026 | 2.34937 | 29 |
| 0.407608 | 6.29822 | 0.791988 | 10.602 | 0.025921 | 2.36903 | 29 |
| 0.411975 | 6.35048 | 0.793668 | 10.602 | 0.026362 | 2.38869 | 29 |
| 0.411975 | 6.35048 | 0.793668 | 10.602 | 0.026362 | 2.38869 | 29 |
| 0.357204 | 5.67624 | 0.815416 | 10.602 | 0.019082 | 2.13508 | 29 |

| | | | | | | |
|---|---|---|---|---|---|---|
| 0.36216 | 5.73896 | 0.827562 | 10.602 | 0.019606 | 2.15867 | 29 |
| 0.367144 | 5.80168 | 0.828882 | 10.602 | 0.018978 | 2.18226 | 29 |
| 0.372156 | 5.8644 | 0.819669 | 10.602 | 0.019443 | 2.20585 | 29 |
| 0.377196 | 5.92712 | 0.831189 | 10.602 | 0.019634 | 2.22944 | 29 |
| 0.382265 | 5.98984 | 0.819593 | 10.602 | 0.019495 | 2.25304 | 29 |
| 0.387362 | 6.05256 | 0.785736 | 10.602 | 0.018754 | 2.27663 | 29 |
| 0.392489 | 6.11528 | 0.818826 | 10.602 | 0.019607 | 2.30022 | 29 |
| 0.397644 | 6.178 | 0.800584 | 10.602 | 0.019212 | 2.32381 | 29 |
| 0.402829 | 6.24072 | 0.812558 | 10.602 | 0.019721 | 2.3474 | 29 |
| 0.408044 | 6.30344 | 0.800427 | 10.602 | 0.019534 | 2.37099 | 29 |
| 0.413289 | 6.36616 | 0.797262 | 10.602 | 0.019474 | 2.39459 | 29 |
| 0.418564 | 6.42889 | 0.801454 | 10.602 | 0.020012 | 2.41818 | 29 |
| 0.423869 | 6.49161 | 0.797883 | 10.602 | 0.020073 | 2.44177 | 29 |
| 0.429205 | 6.55433 | 0.787982 | 10.602 | 0.019933 | 2.46537 | 29 |
| 0.434573 | 6.61705 | 0.783244 | 10.602 | 0.019975 | 2.48896 | 29 |
| 0.439971 | 6.67977 | 0.788156 | 10.602 | 0.020123 | 2.51255 | 29 |
| 0.445401 | 6.74249 | 0.77086 | 10.602 | 0.019917 | 2.53614 | 29 |
| 0.450863 | 6.80521 | 0.787333 | 10.602 | 0.020865 | 2.55973 | 29 |

| | | | | | | |
|---|---|---|---|---|---|---|
| 0.456358 | 6.86793 | 0.795514 | 10.602 | 0.021465 | 2.58332 | 29 |
| 0.461884 | 6.93065 | 0.774828 | 10.602 | 0.021099 | 2.60692 | 29 |
| 0.467443 | 6.99337 | 0.787489 | 10.602 | 0.02172 | 2.63051 | 29 |
| 0.473036 | 7.05609 | 0.77853 | 10.602 | 0.021754 | 2.6541 | 29 |
| 0.478661 | 7.11881 | 0.768756 | 10.602 | 0.02151 | 2.67769 | 29 |
| 0.484321 | 7.18154 | 0.755814 | 10.602 | 0.021677 | 2.70129 | 29 |
| 0.490014 | 7.24426 | 0.76645 | 10.602 | 0.021912 | 2.72488 | 29 |
| 0.495741 | 7.30698 | 0.754062 | 10.602 | 0.022115 | 2.74847 | 29 |
| 0.501503 | 7.3697 | 0.770207 | 10.602 | 0.023044 | 2.77206 | 29 |
| 0.507299 | 7.43242 | 0.740076 | 10.602 | 0.022471 | 2.79565 | 29 |
| 0.513131 | 7.49514 | 0.753427 | 10.602 | 0.022966 | 2.81924 | 29 |
| 0.518998 | 7.55786 | 0.741997 | 10.602 | 0.023057 | 2.84284 | 29 |
| 0.524901 | 7.62058 | 0.733084 | 10.602 | 0.023055 | 2.86643 | 29 |
| 0.524901 | 7.62058 | 0.733084 | 10.602 | 0.023055 | 2.86643 | 29 |
| 0.476548 | 7.09529 | 0.770655 | 10.602 | 0.017172 | 2.66884 | 29 |
| 0.483611 | 7.1737 | 0.767583 | 10.602 | 0.017204 | 2.69834 | 29 |
| 0.490728 | 7.2521 | 0.767891 | 10.602 | 0.016893 | 2.72783 | 29 |
| 0.497897 | 7.3305 | 0.761165 | 10.602 | 0.017228 | 2.75732 | 29 |

| | | | | | | |
|---|---|---|---|---|---|---|
| 0.505121 | 7.4089 | 0.757926 | 10.602 | 0.017117 | 2.78681 | 29 |
| 0.5124 | 7.4873 | 0.761871 | 10.602 | 0.017177 | 2.8163 | 29 |
| 0.519734 | 7.5657 | 0.757835 | 10.602 | 0.017185 | 2.84578 | 29 |
| 0.527124 | 7.6441 | 0.752017 | 10.602 | 0.017002 | 2.87527 | 29 |
| 0.534571 | 7.7225 | 0.752689 | 10.602 | 0.017164 | 2.90476 | 29 |
| 0.542075 | 7.8009 | 0.753933 | 10.602 | 0.017358 | 2.93425 | 29 |
| 0.549637 | 7.8793 | 0.739431 | 10.602 | 0.01705 | 2.96374 | 29 |
| 0.557257 | 7.95771 | 0.744087 | 10.602 | 0.017177 | 2.99324 | 29 |
| 0.564937 | 8.03611 | 0.736864 | 10.602 | 0.017281 | 3.02273 | 29 |
| 0.572677 | 8.11451 | 0.754238 | 10.602 | 0.017824 | 3.05222 | 29 |
| 0.580477 | 8.19291 | 0.741118 | 10.602 | 0.017741 | 3.08171 | 29 |
| 0.588339 | 8.27131 | 0.731931 | 10.602 | 0.017392 | 3.11119 | 29 |
| 0.596263 | 8.34971 | 0.73628 | 10.602 | 0.017764 | 3.14068 | 29 |
| 0.60425 | 8.42811 | 0.72545 | 10.602 | 0.017761 | 3.17017 | 29 |
| 0.612301 | 8.50651 | 0.733728 | 10.602 | 0.018221 | 3.19966 | 29 |
| 0.620416 | 8.58491 | 0.740288 | 10.602 | 0.018853 | 3.22915 | 29 |
| 0.628596 | 8.66332 | 0.716006 | 10.602 | 0.018363 | 3.25865 | 29 |
| 0.636842 | 8.74172 | 0.719625 | 10.602 | 0.018605 | 3.28814 | 29 |

| | | | | | | |
|---|---|---|---|---|---|---|
| 0.645155 | 8.82012 | 0.74399 | 10.602 | 0.019436 | 3.31763 | 29 |
| 0.653535 | 8.89852 | 0.719814 | 10.602 | 0.019022 | 3.34712 | 29 |
| 0.661984 | 8.97692 | 0.722095 | 10.602 | 0.019365 | 3.37661 | 29 |
| 0.670503 | 9.05532 | 0.697774 | 10.602 | 0.018907 | 3.40609 | 29 |
| 0.679091 | 9.13372 | 0.701379 | 10.602 | 0.019291 | 3.43558 | 29 |
| 0.68775 | 9.21212 | 0.716217 | 10.602 | 0.020233 | 3.46507 | 29 |
| 0.696481 | 9.29052 | 0.715952 | 10.602 | 0.020653 | 3.49456 | 29 |
| 0.705285 | 9.36892 | 0.720463 | 10.602 | 0.020991 | 3.52405 | 29 |
| 0.714162 | 9.44733 | 0.714815 | 10.602 | 0.021097 | 3.55355 | 29 |
| 0.723114 | 9.52573 | 0.725638 | 10.602 | 0.022 | 3.58304 | 29 |
| 0.723114 | 9.52573 | 0.725638 | 10.602 | 0.022 | 3.58304 | 29 |
| 0.637808 | 8.75086 | 0.722972 | 10.602 | 0.01636 | 3.29157 | 29 |
| 0.64808 | 8.84756 | 0.72461 | 10.602 | 0.016508 | 3.32795 | 29 |
| 0.658456 | 8.94425 | 0.712121 | 10.602 | 0.015887 | 3.36432 | 29 |
| 0.668936 | 9.04095 | 0.729701 | 10.602 | 0.016763 | 3.40069 | 29 |
| 0.679522 | 9.13764 | 0.713517 | 10.602 | 0.01648 | 3.43706 | 29 |
| 0.690216 | 9.23434 | 0.709881 | 10.602 | 0.016501 | 3.47343 | 29 |
| 0.701021 | 9.33103 | 0.716987 | 10.602 | 0.016695 | 3.5098 | 29 |

| | | | | | | |
|---|---|---|---|---|---|---|
| 0.711936 | 9.42773 | 0.711174 | 10.602 | 0.016621 | 3.54617 | 29 |
| 0.722965 | 9.52442 | 0.707714 | 10.602 | 0.016761 | 3.58254 | 29 |
| 0.734108 | 9.62111 | 0.717986 | 10.602 | 0.017256 | 3.61891 | 29 |
| 0.745368 | 9.71781 | 0.720619 | 10.602 | 0.017543 | 3.65529 | 29 |
| 0.756747 | 9.8145 | 0.74042 | 10.602 | 0.01827 | 3.69165 | 29 |
| 0.768246 | 9.9112 | 0.724759 | 10.602 | 0.018266 | 3.72803 | 29 |
| 0.779868 | 10.0079 | 0.752552 | 10.602 | 0.01926 | 3.7644 | 29 |
| 0.791613 | 10.1046 | 0.754263 | 10.602 | 0.019831 | 3.80077 | 29 |
| 0.803485 | 10.2013 | 0.768225 | 10.602 | 0.020419 | 3.83715 | 29 |
| 0.815486 | 10.298 | 0.765733 | 10.602 | 0.021056 | 3.87352 | 29 |
| 0.827617 | 10.3947 | 0.644817 | 10.602 | 0.018344 | 3.90989 | 29 |
| 0.83988 | 10.4914 | 0.63649 | 10.602 | 0.018859 | 3.94627 | 29 |
| 0.852278 | 10.5881 | 0.764119 | 10.602 | 0.023804 | 3.98264 | 29 |
| 0.864813 | 10.6848 | 0.826991 | 10.602 | 0.026954 | 4.01901 | 29 |
| 0.877488 | 10.7814 | 0.767568 | 10.602 | 0.026615 | 4.05535 | 29 |
| 0.890304 | 10.8781 | 0.734169 | 10.602 | 0.027199 | 4.09172 | 29 |
| 0.303261 | 5.17348 | 0.855958 | 10.602 | 0.020533 | 1.51235 | 33 |
| 0.307177 | 5.23064 | 0.862648 | 10.602 | 0.020878 | 1.52906 | 33 |

| | | | | | | |
|---|---|---|---|---|---|---|
| 0.311107 | 5.28781 | 0.854814 | 10.602 | 0.020565 | 1.54577 | 33 |
| 0.315052 | 5.34497 | 0.838949 | 10.602 | 0.020328 | 1.56248 | 33 |
| 0.319011 | 5.40214 | 0.846391 | 10.602 | 0.020747 | 1.57919 | 33 |
| 0.322985 | 5.4593 | 0.863097 | 10.602 | 0.021213 | 1.5959 | 33 |
| 0.326974 | 5.51647 | 0.852118 | 10.602 | 0.02107 | 1.61261 | 33 |
| 0.330977 | 5.57363 | 0.867406 | 10.602 | 0.021643 | 1.62932 | 33 |
| 0.334996 | 5.6308 | 0.833654 | 10.602 | 0.020789 | 1.64603 | 33 |
| 0.33903 | 5.68796 | 0.84863 | 10.602 | 0.021593 | 1.66274 | 33 |
| 0.343078 | 5.74513 | 0.825935 | 10.602 | 0.020959 | 1.67946 | 33 |
| 0.347142 | 5.8023 | 0.833882 | 10.602 | 0.021266 | 1.69617 | 33 |
| 0.351221 | 5.85946 | 0.836458 | 10.602 | 0.021799 | 1.71288 | 33 |
| 0.355316 | 5.91663 | 0.83337 | 10.602 | 0.021777 | 1.72959 | 33 |
| 0.359426 | 5.97379 | 0.823897 | 10.602 | 0.021647 | 1.7463 | 33 |
| 0.363551 | 6.03096 | 0.838493 | 10.602 | 0.022532 | 1.76301 | 33 |
| 0.367692 | 6.08812 | 0.830005 | 10.602 | 0.02237 | 1.77972 | 33 |
| 0.371849 | 6.14529 | 0.815359 | 10.602 | 0.022247 | 1.79643 | 33 |
| 0.376022 | 6.20245 | 0.812529 | 10.602 | 0.022662 | 1.81314 | 33 |
| 0.380211 | 6.25962 | 0.827193 | 10.602 | 0.023631 | 1.82985 | 33 |

| | | | | | | |
|---|---|---|---|---|---|---|
| 0.384415 | 6.31679 | 0.813059 | 10.602 | 0.023121 | 1.84657 | 33 |
| 0.388636 | 6.37395 | 0.809366 | 10.602 | 0.023465 | 1.86328 | 33 |
| 0.392873 | 6.43112 | 0.809844 | 10.602 | 0.02388 | 1.87999 | 33 |
| 0.397126 | 6.48828 | 0.798066 | 10.602 | 0.023562 | 1.8967 | 33 |
| 0.401395 | 6.54545 | 0.79633 | 10.602 | 0.023898 | 1.91341 | 33 |
| 0.405681 | 6.60261 | 0.80849 | 10.602 | 0.024291 | 1.93012 | 33 |
| 0.409983 | 6.65978 | 0.814875 | 10.602 | 0.025413 | 1.94683 | 33 |
| 0.414302 | 6.71694 | 0.811085 | 10.602 | 0.025479 | 1.96354 | 33 |
| 0.418638 | 6.77411 | 0.788698 | 10.602 | 0.02497 | 1.98025 | 33 |
| 0.422991 | 6.83127 | 0.806353 | 10.602 | 0.025861 | 1.99696 | 33 |
| 0.427361 | 6.88844 | 0.772044 | 10.602 | 0.024967 | 2.01368 | 33 |
| 0.431747 | 6.94561 | 0.76828 | 10.602 | 0.025283 | 2.03039 | 33 |
| 0.431747 | 6.94561 | 0.76828 | 10.602 | 0.025283 | 2.03039 | 33 |
| 0.38988 | 6.39076 | 0.828128 | 10.602 | 0.019215 | 1.86819 | 33 |
| 0.395122 | 6.46138 | 0.818716 | 10.602 | 0.019078 | 1.88883 | 33 |
| 0.400389 | 6.532 | 0.821229 | 10.602 | 0.018993 | 1.90948 | 33 |
| 0.405681 | 6.60261 | 0.794666 | 10.602 | 0.018735 | 1.93012 | 33 |
| 0.410998 | 6.67323 | 0.803732 | 10.602 | 0.019011 | 1.95076 | 33 |

| | | | | | | |
|---|---|---|---|---|---|---|
| 0.416341 | 6.74384 | 0.79615 | 10.602 | 0.018921 | 1.97141 | 33 |
| 0.421709 | 6.81446 | 0.793451 | 10.602 | 0.018911 | 1.99205 | 33 |
| 0.427103 | 6.88508 | 0.797627 | 10.602 | 0.019096 | 2.01269 | 33 |
| 0.432523 | 6.95569 | 0.820539 | 10.602 | 0.019702 | 2.03333 | 33 |
| 0.437969 | 7.02631 | 0.790181 | 10.602 | 0.019185 | 2.05398 | 33 |
| 0.443442 | 7.09693 | 0.793288 | 10.602 | 0.019295 | 2.07462 | 33 |
| 0.448941 | 7.16754 | 0.801239 | 10.602 | 0.019738 | 2.09526 | 33 |
| 0.454467 | 7.23816 | 0.791653 | 10.602 | 0.019694 | 2.11591 | 33 |
| 0.46002 | 7.30877 | 0.815395 | 10.602 | 0.020367 | 2.13655 | 33 |
| 0.4656 | 7.37939 | 0.779304 | 10.602 | 0.019759 | 2.15719 | 33 |
| 0.471207 | 7.45001 | 0.772909 | 10.602 | 0.019932 | 2.17784 | 33 |
| 0.476842 | 7.52062 | 0.800251 | 10.602 | 0.020598 | 2.19848 | 33 |
| 0.482505 | 7.59124 | 0.768113 | 10.602 | 0.020069 | 2.21912 | 33 |
| 0.488195 | 7.66186 | 0.769247 | 10.602 | 0.02055 | 2.23977 | 33 |
| 0.493914 | 7.73247 | 0.770019 | 10.602 | 0.021058 | 2.26041 | 33 |
| 0.499661 | 7.80309 | 0.756917 | 10.602 | 0.020616 | 2.28105 | 33 |
| 0.505437 | 7.8737 | 0.744033 | 10.602 | 0.020668 | 2.30169 | 33 |
| 0.511241 | 7.94432 | 0.757882 | 10.602 | 0.021351 | 2.32234 | 33 |

| | | | | | | |
|---|---|---|---|---|---|---|
| 0.517075 | 8.01494 | 0.751639 | 10.602 | 0.021334 | 2.34298 | 33 |
| 0.522938 | 8.08555 | 0.772241 | 10.602 | 0.022241 | 2.36362 | 33 |
| 0.52883 | 8.15617 | 0.745807 | 10.602 | 0.021506 | 2.38427 | 33 |
| 0.534752 | 8.22678 | 0.747918 | 10.602 | 0.022225 | 2.40491 | 33 |
| 0.540704 | 8.2974 | 0.749695 | 10.602 | 0.022662 | 2.42555 | 33 |
| 0.546686 | 8.36802 | 0.744992 | 10.602 | 0.02292 | 2.4462 | 33 |
| 0.552698 | 8.43863 | 0.73617 | 10.602 | 0.022721 | 2.46684 | 33 |
| 0.558741 | 8.50925 | 0.754997 | 10.602 | 0.023709 | 2.48748 | 33 |
| 0.564815 | 8.57987 | 0.748432 | 10.602 | 0.023978 | 2.50813 | 33 |
| 0.564815 | 8.57987 | 0.748432 | 10.602 | 0.023978 | 2.50813 | 33 |
| 0.508612 | 7.91237 | 0.773931 | 10.602 | 0.017348 | 2.313 | 33 |
| 0.515823 | 7.9998 | 0.769184 | 10.602 | 0.017196 | 2.33856 | 33 |
| 0.523078 | 8.08723 | 0.769792 | 10.602 | 0.016813 | 2.36411 | 33 |
| 0.530378 | 8.17466 | 0.776355 | 10.602 | 0.017284 | 2.38967 | 33 |
| 0.537724 | 8.26209 | 0.763043 | 10.602 | 0.017194 | 2.41523 | 33 |
| 0.545116 | 8.34952 | 0.761478 | 10.602 | 0.017252 | 2.44079 | 33 |
| 0.552555 | 8.43695 | 0.76018 | 10.602 | 0.017211 | 2.46635 | 33 |
| 0.56004 | 8.52438 | 0.756059 | 10.602 | 0.017046 | 2.4919 | 33 |

| | | | | | | |
|---|---|---|---|---|---|---|
| 0.567572 | 8.61181 | 0.75074 | 10.602 | 0.017158 | 2.51746 | 33 |
| 0.575153 | 8.69924 | 0.751688 | 10.602 | 0.017226 | 2.54302 | 33 |
| 0.582782 | 8.78667 | 0.751751 | 10.602 | 0.017352 | 2.56858 | 33 |
| 0.590459 | 8.8741 | 0.749218 | 10.602 | 0.017431 | 2.59414 | 33 |
| 0.598185 | 8.96153 | 0.749688 | 10.602 | 0.017571 | 2.6197 | 33 |
| 0.605962 | 9.04896 | 0.739308 | 10.602 | 0.017401 | 2.64525 | 33 |
| 0.613788 | 9.13639 | 0.743458 | 10.602 | 0.017742 | 2.67081 | 33 |
| 0.621665 | 9.22382 | 0.741506 | 10.602 | 0.01786 | 2.69637 | 33 |
| 0.629593 | 9.31125 | 0.737285 | 10.602 | 0.017825 | 2.72193 | 33 |
| 0.637572 | 9.39868 | 0.739898 | 10.602 | 0.018123 | 2.74749 | 33 |
| 0.645604 | 9.48611 | 0.742872 | 10.602 | 0.01863 | 2.77304 | 33 |
| 0.653688 | 9.57354 | 0.736346 | 10.602 | 0.018844 | 2.7986 | 33 |
| 0.661825 | 9.66097 | 0.728124 | 10.602 | 0.01864 | 2.82416 | 33 |
| 0.670017 | 9.7484 | 0.721622 | 10.602 | 0.018736 | 2.84972 | 33 |
| 0.678262 | 9.83582 | 0.717261 | 10.602 | 0.01905 | 2.87527 | 33 |
| 0.686562 | 9.92325 | 0.722693 | 10.602 | 0.01913 | 2.90083 | 33 |
| 0.694917 | 10.0107 | 0.723355 | 10.602 | 0.019452 | 2.9264 | 33 |
| 0.703328 | 10.0981 | 0.714397 | 10.602 | 0.019523 | 2.95195 | 33 |

| | | | | | | |
|---|---|---|---|---|---|---|
| 0.711795 | 10.1855 | 0.721436 | 10.602 | 0.020077 | 2.97749 | 33 |
| 0.72032 | 10.273 | 0.733479 | 10.602 | 0.020938 | 3.00307 | 33 |
| 0.728902 | 10.3604 | 0.728048 | 10.602 | 0.021179 | 3.02862 | 33 |
| 0.737542 | 10.4478 | 0.719839 | 10.602 | 0.021273 | 3.05417 | 33 |
| 0.746241 | 10.5353 | 0.712747 | 10.602 | 0.021326 | 3.07975 | 33 |
| 0.754999 | 10.6227 | 0.733153 | 10.602 | 0.022499 | 3.1053 | 33 |
| 0.754999 | 10.6227 | 0.733153 | 10.602 | 0.022499 | 3.1053 | 33 |
| 0.669069 | 9.73831 | 0.737106 | 10.602 | 0.016906 | 2.84677 | 33 |
| 0.679217 | 9.84591 | 0.725356 | 10.602 | 0.016575 | 2.87822 | 33 |
| 0.689448 | 9.95352 | 0.724581 | 10.602 | 0.016231 | 2.90968 | 33 |
| 0.699763 | 10.0611 | 0.728453 | 10.602 | 0.016689 | 2.94113 | 33 |
| 0.710163 | 10.1687 | 0.731363 | 10.602 | 0.017039 | 2.97258 | 33 |
| 0.720649 | 10.2763 | 0.726377 | 10.602 | 0.017174 | 3.00404 | 33 |
| 0.731222 | 10.3839 | 0.723597 | 10.602 | 0.017093 | 3.03549 | 33 |
| 0.741884 | 10.4915 | 0.737941 | 10.602 | 0.017585 | 3.06695 | 33 |
| 0.752635 | 10.5992 | 0.733031 | 10.602 | 0.017788 | 3.09843 | 33 |
| 0.763476 | 10.7068 | 0.752803 | 10.602 | 0.018391 | 3.12988 | 33 |
| 0.77441 | 10.8144 | 0.743037 | 10.602 | 0.018601 | 3.16134 | 33 |

| | | | | | | |
|---|---|---|---|---|---|---|
| 0.785436 | 10.922 | 0.743375 | 10.602 | 0.018989 | 3.19279 | 33 |
| 0.796556 | 11.0296 | 0.737921 | 10.602 | 0.019308 | 3.22425 | 33 |
| 0.807771 | 11.1372 | 0.763334 | 10.602 | 0.020427 | 3.2557 | 33 |
| 0.819083 | 11.2448 | 0.793439 | 10.602 | 0.021828 | 3.28716 | 33 |
| 0.830492 | 11.3524 | 0.762051 | 10.602 | 0.021647 | 3.31861 | 33 |
| 0.842001 | 11.46 | 0.667673 | 10.602 | 0.019689 | 3.35006 | 33 |
| 0.85361 | 11.5676 | 0.661844 | 10.602 | 0.020264 | 3.38152 | 33 |
| 0.86532 | 11.6752 | 0.817803 | 10.602 | 0.026316 | 3.41297 | 33 |
| 0.877133 | 11.7828 | 0.892121 | 10.602 | 0.030305 | 3.44443 | 33 |
| 0.889051 | 11.8904 | 0.797599 | 10.602 | 0.029207 | 3.47588 | 33 |
| 0.39045 | 6.72605 | 0.864823 | 10.602 | 0.020001 | 1.42338 | 39 |
| 0.395442 | 6.80038 | 0.858143 | 10.602 | 0.020302 | 1.43911 | 39 |
| 0.400451 | 6.8747 | 0.850676 | 10.602 | 0.019839 | 1.45484 | 39 |
| 0.405477 | 6.94902 | 0.854767 | 10.602 | 0.020114 | 1.47057 | 39 |
| 0.410521 | 7.02334 | 0.845433 | 10.602 | 0.020046 | 1.4863 | 39 |
| 0.415582 | 7.09766 | 0.828653 | 10.602 | 0.019794 | 1.50202 | 39 |
| 0.420661 | 7.17198 | 0.827805 | 10.602 | 0.019754 | 1.51775 | 39 |
| 0.425757 | 7.2463 | 0.842643 | 10.602 | 0.020474 | 1.53348 | 39 |

| | | | | | | |
|---|---|---|---|---|---|---|
| 0.430871 | 7.32062 | 0.821524 | 10.602 | 0.019697 | 1.54921 | 39 |
| 0.436003 | 7.39494 | 0.834636 | 10.602 | 0.020511 | 1.56494 | 39 |
| 0.430871 | 7.32062 | 0.821524 | 10.602 | 0.019697 | 1.54921 | 39 |
| 0.436003 | 7.39494 | 0.834636 | 10.602 | 0.020511 | 1.56494 | 39 |
| 0.441153 | 7.46926 | 0.823022 | 10.602 | 0.0202 | 1.58066 | 39 |
| 0.44632 | 7.54359 | 0.822778 | 10.602 | 0.020553 | 1.59639 | 39 |
| 0.451506 | 7.61791 | 0.815749 | 10.602 | 0.020652 | 1.61212 | 39 |
| 0.45671 | 7.69223 | 0.803312 | 10.602 | 0.020313 | 1.62785 | 39 |
| 0.461932 | 7.76655 | 0.816542 | 10.602 | 0.020888 | 1.64358 | 39 |
| 0.467173 | 7.84087 | 0.821453 | 10.602 | 0.021537 | 1.6593 | 39 |
| 0.472432 | 7.91519 | 0.810955 | 10.602 | 0.021392 | 1.67503 | 39 |
| 0.47771 | 7.98951 | 0.789501 | 10.602 | 0.021005 | 1.69076 | 39 |
| 0.483006 | 8.06383 | 0.786521 | 10.602 | 0.021362 | 1.70649 | 39 |
| 0.488321 | 8.13815 | 0.790341 | 10.602 | 0.021676 | 1.72222 | 39 |
| 0.493655 | 8.21248 | 0.796517 | 10.602 | 0.022028 | 1.73794 | 39 |
| 0.499008 | 8.2868 | 0.789591 | 10.602 | 0.022474 | 1.75367 | 39 |
| 0.50438 | 8.36112 | 0.799857 | 10.602 | 0.023144 | 1.7694 | 39 |
| 0.509771 | 8.43544 | 0.76659 | 10.602 | 0.02219 | 1.78513 | 39 |

| | | | | | | |
|---|---|---|---|---|---|---|
| 0.515181 | 8.50976 | 0.778916 | 10.602 | 0.02286 | 1.80086 | 39 |
| 0.520611 | 8.58408 | 0.788785 | 10.602 | 0.023399 | 1.81658 | 39 |
| 0.52606 | 8.6584 | 0.773392 | 10.602 | 0.023615 | 1.83231 | 39 |
| 0.531529 | 8.73272 | 0.782148 | 10.602 | 0.024195 | 1.84804 | 39 |
| 0.537018 | 8.80704 | 0.770235 | 10.602 | 0.02414 | 1.86377 | 39 |
| 0.542526 | 8.88136 | 0.770535 | 10.602 | 0.02468 | 1.87949 | 39 |
| 0.548054 | 8.95569 | 0.766051 | 10.602 | 0.024952 | 1.89522 | 39 |
| 0.553602 | 9.03001 | 0.761778 | 10.602 | 0.025185 | 1.91095 | 39 |
| 0.553602 | 9.03001 | 0.761778 | 10.602 | 0.025185 | 1.91095 | 39 |
| 0.507747 | 8.40757 | 0.787645 | 10.602 | 0.017536 | 1.77923 | 39 |
| 0.514504 | 8.50047 | 0.787996 | 10.602 | 0.017969 | 1.79889 | 39 |
| 0.521291 | 8.59337 | 0.780737 | 10.602 | 0.017314 | 1.81855 | 39 |
| 0.528109 | 8.68627 | 0.773779 | 10.602 | 0.01738 | 1.83821 | 39 |
| 0.534957 | 8.77917 | 0.774433 | 10.602 | 0.01745 | 1.85787 | 39 |
| 0.541836 | 8.87207 | 0.770293 | 10.602 | 0.017485 | 1.87753 | 39 |
| 0.548747 | 8.96498 | 0.764739 | 10.602 | 0.017259 | 1.89719 | 39 |
| 0.555688 | 9.05788 | 0.761915 | 10.602 | 0.01752 | 1.91685 | 39 |
| 0.562661 | 9.15078 | 0.770785 | 10.602 | 0.017465 | 1.93651 | 39 |

| | | | | | | |
|---|---|---|---|---|---|---|
| 0.569666 | 9.24368 | 0.753453 | 10.602 | 0.017614 | 1.95617 | 39 |
| 0.576703 | 9.33658 | 0.74997 | 10.602 | 0.017416 | 1.97583 | 39 |
| 0.583771 | 9.42948 | 0.749384 | 10.602 | 0.017779 | 1.99549 | 39 |
| 0.590873 | 9.52238 | 0.746372 | 10.602 | 0.01759 | 2.01515 | 39 |
| 0.598006 | 9.61528 | 0.755094 | 10.602 | 0.017962 | 2.03481 | 39 |
| 0.605173 | 9.70819 | 0.757379 | 10.602 | 0.01811 | 2.05447 | 39 |
| 0.612373 | 9.80109 | 0.743647 | 10.602 | 0.018266 | 2.07413 | 39 |
| 0.619605 | 9.89399 | 0.75493 | 10.602 | 0.018464 | 2.09379 | 39 |
| 0.626872 | 9.98689 | 0.739459 | 10.602 | 0.018124 | 2.11345 | 39 |
| 0.634172 | 10.0798 | 0.738467 | 10.602 | 0.018734 | 2.13311 | 39 |
| 0.641506 | 10.1727 | 0.740463 | 10.602 | 0.019035 | 2.15277 | 39 |
| 0.648874 | 10.2656 | 0.7283 | 10.602 | 0.01889 | 2.17243 | 39 |
| 0.656277 | 10.3585 | 0.733239 | 10.602 | 0.019488 | 2.19209 | 39 |
| 0.663715 | 10.4514 | 0.741549 | 10.602 | 0.019908 | 2.21175 | 39 |
| 0.671187 | 10.5443 | 0.735116 | 10.602 | 0.019734 | 2.23141 | 39 |
| 0.678695 | 10.6372 | 0.716944 | 10.602 | 0.019719 | 2.25107 | 39 |
| 0.686238 | 10.7301 | 0.72665 | 10.602 | 0.020002 | 2.27073 | 39 |
| 0.693816 | 10.823 | 0.714849 | 10.602 | 0.020217 | 2.29039 | 39 |

| | | | | | | |
|---|---|---|---|---|---|---|
| 0.701431 | 10.9159 | 0.745106 | 10.602 | 0.021384 | 2.31005 | 39 |
| 0.709082 | 11.0088 | 0.750635 | 10.602 | 0.021885 | 2.32971 | 39 |
| 0.716769 | 11.1017 | 0.715492 | 10.602 | 0.021348 | 2.34937 | 39 |
| 0.724493 | 11.1946 | 0.737015 | 10.602 | 0.022333 | 2.36903 | 39 |
| 0.732254 | 11.2875 | 0.726374 | 10.602 | 0.02272 | 2.38869 | 39 |
| 0.732254 | 11.2875 | 0.726374 | 10.602 | 0.02272 | 2.38869 | 39 |
| 0.668381 | 10.5095 | 0.733588 | 10.602 | 0.016727 | 2.22405 | 39 |
| 0.677754 | 10.6256 | 0.733456 | 10.602 | 0.016947 | 2.24862 | 39 |
| 0.687183 | 10.7417 | 0.738776 | 10.602 | 0.016675 | 2.27318 | 39 |
| 0.696668 | 10.8578 | 0.727265 | 10.602 | 0.016805 | 2.29775 | 39 |
| 0.706209 | 10.974 | 0.726538 | 10.602 | 0.016823 | 2.32234 | 39 |
| 0.715806 | 11.0901 | 0.719772 | 10.602 | 0.016894 | 2.34691 | 39 |
| 0.725461 | 11.2062 | 0.727403 | 10.602 | 0.017059 | 2.37148 | 39 |
| 0.735174 | 11.3223 | 0.722417 | 10.602 | 0.017205 | 2.39605 | 39 |
| 0.744945 | 11.4385 | 0.733776 | 10.602 | 0.017585 | 2.42064 | 39 |
| 0.754775 | 11.5546 | 0.7387 | 10.602 | 0.018267 | 2.44521 | 39 |
| 0.764665 | 11.6707 | 0.750611 | 10.602 | 0.01867 | 2.46978 | 39 |
| 0.774614 | 11.7869 | 0.750365 | 10.602 | 0.019042 | 2.49437 | 39 |

| | | | | | | |
|---|---|---|---|---|---|---|
| 0.784624 | 11.903 | 0.745674 | 10.602 | 0.019164 | 2.51894 | 39 |
| 0.794695 | 12.0191 | 0.733301 | 10.602 | 0.019264 | 2.54351 | 39 |
| 0.804828 | 12.1352 | 0.770989 | 10.602 | 0.020769 | 2.56808 | 39 |
| 0.815023 | 12.2514 | 0.787074 | 10.602 | 0.022113 | 2.59267 | 39 |
| 0.82528 | 12.3675 | 0.798124 | 10.602 | 0.022863 | 2.61724 | 39 |
| 0.835601 | 12.4836 | 0.793655 | 10.602 | 0.023486 | 2.64181 | 39 |
| 0.845986 | 12.5997 | 0.761724 | 10.602 | 0.023705 | 2.66638 | 39 |
| 0.856435 | 12.7159 | 0.665312 | 10.602 | 0.02181 | 2.69097 | 39 |
| 0.86695 | 12.832 | 0.717505 | 10.602 | 0.024602 | 2.71554 | 39 |
| 0.87753 | 12.9481 | 0.83034 | 10.602 | 0.030022 | 2.74011 | 39 |
| 0.888176 | 13.0642 | 0.952609 | 10.602 | 0.037128 | 2.76468 | 39 |
| 0.89889 | 13.1804 | 0.835378 | 10.602 | 0.035039 | 2.78927 | 39 |

**Table A.1:** Table of E12-10-002 cross section ratio data. Only the statistical uncertainty is available at the time of this writing.

# References


[AA10] C.E. Keppel W. Melnitchouk P. Monaghan J.G. Morfin J.F. Owens A. Accardi, M.E. Christy. New parton distributions from large-x and low-$q^2$ data. *Physical Review D*, 81(3), February 2010.

[AA11] C.E. Keppel W. Melnitchouk J.G. Morfin J.F. Owens L. Zhu A. Accardi, M.E. Christy. Uncertainties in determining parton distributions at large x. *Physical Review D*, 84(1), July 2011.

[AA16] W. Melnitchouk J.F. Owens N. Sato A. Accardi, L.T. Brady. Constraints on large-x parton distributions from new weak boson production and deep-inelastic scattering data. *Physical Review D*, 93(11), June 2016.

[Cha32] J. Chadwick. Possible existence of a neutron. *Nature*, 1932.

[CL01] G.A. Krafft C.W. Leemann, D.R. Douglas. The continuous electron beam accelerator facility: Cebaf at the jefferson laboratory. *Annual Review of Nuclear and Particle Science*, 51, December 2001.

[Col79] PLUTO Colaboration. Jet analysis of the $\gamma(9.46)$ decay into charged hadrons. *Physics Letters B*, 82(3), April 1979.

[DJG73] F. Wilczek D. J. Gross. Ultraviolet behavior of non-abelian gauge theories. *The Physical Review*, 30(26), June 1973.

[Dok77] Y. Dokshitser. Calculation of the structure functions for deep inelastic scattering and e+ e- annihilation by perturbation theory in quantum chromodynamics. *Sov. Phys. JETP*, October 1977.

[EF49] C.N. Yang Enrico Fermi. Are mesons elementary particles? *The Physical Review*, 76(12), December 1949.

[FG64] A. Radicati F. Gursey. Spin and unitary sping independence of strong interactions. *The Physical Review*, 13(5), August 1964.

[Flo08] D. Florian. Global analysis of helicity parton densities and their uncertainties.

*Physical Review Letters*, 2008.

[Fow64] W.B. Fowler. The omega minus experiment. *Scientific American*, 1964.

[GA77] G. Parisi G. Altarelli. Aymptotic freedom in parton language. *Nuclear Physics B*, 126(2):298–318, August 1977.

[GD] M. Schmelling G. Dissertori, I.G. Knowles. Quantum chromodynamics: High energy experiments and theory.

[GM61] Murray Gell-Mann. Symmetries of baryons and mesons. *The Physical Review*, 125(16), March 1961.

[GPSO47] C. F. Powell G. P. S. Occhialini. Nuclear disintegrations produced by slow charged particles of small mass. *Nature*, 159:186–190, February 1947.

[Gre64] O. W. Greenberd. Spin and unitary-spin independence in a paraquark model of baryons and mesons. *The Physical Review*, 13(20), November 1964.

[Gre15] O. W. Greenberg. The origin of quark color. *The Physical Review*, 68(1), January 2015.

[Hag10] P. Hagler. Hadron structure from lattice quantum chromodynamics. *Physics Reports*, 2010.

[JC89] G. Sterman J.C. Collins, D.E. Soper. Factorization of hard processes in qcd. *Adv.Ser.Direct.High Energy Phys*, 5, 1989.

[JDB69] E. A. Pachos J. D. Bjorken. Inelastic election-proton and $\gamma$-proton scattering, and the structure of the nucleon. *The Physical Review*, 185(5), September 1969.

[Mac01] R. Machleidt. High-precision, charge-dependent bonn nucleon-nucleon potential. *Physical Review C*, 63(2), February 2001.

[MC13] A. Mitovb J. Rojob M. Czakon, M.L. Mangano. Constraints on the gluon pdf from top quark pair production at hadron colliders. *Journal of High Energy Physics*, 2013.

[MYH65] Y. Nambu M. Y. Han. Three-triplet model with double su(3). *The Physical*

*Review*, 139(4B), August 1965.

[PB08] E. Christy P.E. Bosted. Empirical fit to inelastic electron-deuteron and electron-neutron resonance region transverse cross sections. *Physical Review C*, 77(6), June 2008.

[RF09] F. Maltoni R. Frederix. Top pair invariant mass distribution: a window on new physics. *Journal of High Energy Physics*, 2009.

[Ros50] M.N. Rosenbluth. High energy elastic scattering of electrons on protons. *Physical Review*, 79(4), August 1950.

[Rut19] E. Rutherford. Collision of a particle with light atoms. *Philosophical Magazine*, 1919.

[RW95] R. Schiavilla R.B. Wiringa, V.G.J Stoks. Accurate nucleon-nucleon potential with charge-independence breaking. *Physical Review C*, 51(1), January 1995.

[SK95] G. Piller W. Weise S.A. Kulagin, W. Melnitchouk. Spin-dependent nuclear structure functions: General approach with application to the deuteron. *Physical Review D*, 52(2), August 1995.

[SK06] R. Petti S.A. Kulagin. Global study of nuclear structure functions. *Nuclear Physics A*, 765(1), January 2006.

[SW16] Hall C Staff S.A. Wood. Jefferson lab hall c standard equipment manual. *https://hallcweb.jlab.org/safety-docs/current/Standard-Equipment-Manual.pdf*, 2016.

[Tin74] C.C. Ting. Experimenal observation of a heavy particle j. *The Physical Review*, 33(23), December 1974.

[Uns91] K.B. Unser. The parametric current transformer, a beam current monitor developed for lep. *CERN, CH-1211 Geneva 23 (Switzerland)*, 1991.

[VG72] L.N. Lipatov V.N. Gribov. Deep inelastic ep scattering in perturbation theory. *Sov. J. Nuclear Physics*, 1972.

[WM94] A.W. Thomas W. Melnitchouk, A.W. Scheiber. Deep-inelastic scattering from off-shell nucleons. *Physical Review D*, 49(3), February 1994.

[Yan03] C. Yan. Description of the hall c raster systems. *(Unpublished)*, 2003.

[Yuk35] Hideki Yukawa. On the interaction of elementary particles. *Progress of Theoretical Physics Supplement*, 1(1):48–57, January 1935.